UNIVERSITY OF PARDUBICE
FACULTY OF TRANSPORT ENGINEERING

PROPOSAL OF A COMPUTER MODEL FOR SIMULATION OF CAR TIRES UNDER DYNAMIC LOADS

A thesis submitted in fulfillment of the requirements
for the the degree of Doctor of Philosophy

2025

Ing. Sadjiep Tchuigwa Baurice Sylvain

Program of Study:
P0788D040002 - Transport Means and Infrastructure

Branch of study:
Transport Means

Dissertation Title:
Proposal of a computer model for simulation of car tires under dynamic loads

Author:
Ing. Sadjiep Tchuigwa Baurice Sylvain

Principal Supervisor:
Prof.Ing. Jan Krmela, Ph.D

Specialist Supervisor:
Ing. Jan Pokorny, Ph.D

The dissertation has arisen at the supervising:
Faculty of Transport Engineering, Department of Transport Means and Diagnostics.

Declaration of Authorship

I declare:
The thesis entitled ***proposal of a computer model for simulation of car tires under dynamic loads*** is my own work. All literary sources and information that I used in the thesis are referenced in the bibliography. I have been acquainted with the fact that my work is subject to the rights and obligations arising from Act No. 121/2000 Sb., On Copyright, on Rights Related to Copyright and on Amendments to Certain Acts (Copyright Act), as amended, especially with the fact that the University of Pardubice has the right to conclude a license agreement for the use of this thesis as a school work under Section 60, Subsection 1 of the Copyright Act, and that if this thesis is used by me or a license to use it is granted to another entity, the University of Pardubice is entitled to request a reasonable fee from me to cover the costs incurred for the creation of the work, depending on the circumstances up to their actual amount.

I acknowledge that in accordance with Section 47b of Act No. 111/1998 Sb., On Higher Education Institutions and on Amendments to Other Acts (Act on Higher Education Institutions), as amended, and the Directive of the University of Pardubice No. 7/2019 Rules for Submission, Publication and Layout of Theses, as amended, the thesis will be published through the Digital Library of the University of Pardubice.

Signed:

Date:

In:

Ing. Sadjiep Tchuigwa Baurice Sylvain

Acknowledgements

I would like to express my profound thanks to my supervisor, **Prof. Ing. Jan Krmela, Ph.D.**, for his unwavering support, insightful consultations, and guidance since the beginning of my studies. His extensive knowledge and expertise in tire computational modeling and testing have greatly guided my work.

I also wish to extend my gratitude to my specialist supervisor, **Ing. Jan Pokorny, Ph.D.**, for his valuable advice and support with all laboratory-related and administrative matters.

I am grateful to **Ing. Jakub Vágner, Ph.D.**, the head of the Department of Transport Means and Diagnostics, for his support in the laboratory with materials and experiments.

My sincere thanks go to **doc. Ing. Petr Voltr, Ph.D.**, the head of the Educational and Research Centre in Transport, for providing access to the computer room during weekdays and weekends for my computational tasks.

I want to thank **doc. Ing. Krmelová Vladimíra, Ph.D.**, for her support during my research, especially in facilitating my internship at the Alexander Dubček University of Trenčín.

I likewise hold in high regard all the lecturers and researchers of the faculty who have enriched my knowledge through their lectures and consultations.

I want to thank all the laboratory technicians and workers at the Educational and Research Centre in Transport, for their help with experiments.

I would also like to convey my gratitude to my parents, **Tchuigwa J. M.** and **Djomen J.**, and to my family at large, for their emotional support, encouragement and unwavering love.

Finally, I would like to acknowledge the funding provided by the University of Pardubice through the SGS grants, as well as the Cultural and Educational Grant Agency of the Slovak Republic (KEGA), project No. KEGA 003TnUAD-4/2022.

Abstract

Doctoral thesis

Proposal of a computer model for simulation of car tires under dynamic loads

by Ing. Sadjiep Tchuigwa Baurice Sylvain

UNIVERSITY OF PARDUBICE
Faculty of Transport Engineering
Department of Transport Means and Diagnostics
Supervisor: Prof.Ing. Jan Krmela, Ph.D

2025, 213 pages

This study focuses on the modeling and simulation of car tires subjected to dynamic loads. As an essential part of the vehicle suspension system, tires ensure a proper transfer of loads to the ground and absorb rolling-induced vibration. In operating conditions, these loads are highly dynamic. However, the analysis of tires under these conditions has not been thoroughly explored in the literature. Therefore, the objective of this work is to address this gap. To achieve this, both the review of the experimental response of tire components in cyclic dynamic tests and the review of the existing tire models are conducted. Afterward, the methodology of a Finite element-based model that is consistent with material dynamic properties and dynamic load is proposed. An insightful strategy for the creation of the geometry, material parameter identification, choice of topology, boundary conditions, and solution scheme is proposed. In order to validate this model, simulations and experiments were conducted on a selected tire in static, dynamic and free vibration setups. The comparison of results, specifically the vertical deflection, contact area, mode shapes, and natural frequencies, demonstrates the model's accuracy. Furthermore, extensive responses such as steady-state rolling, vibration analysis, transient rolling, and steady-state dynamic were examined. Compared to static response, the results bring new findings regarding the effect of dynamic loads on the deformation and stress state in the tire. Moreover, this model is versatile and can be extended to investigate more responses, such as the acoustic, thermomechanical, aquaplaning and coupled noise, vibration, and harshness analyses. This work contributes to the advancement of the tire industry and highlights the significance of considering dynamic loads in the tire design phases for improving tire design, durability, and safety.

Keywords: Finite Element Method, Tire Simulation, Dynamic Load, Steady State Dynamic, Vibration, Transient Rolling.

Anotace

Dizertační práce

Návrh počítačového modelu pro simulaci pneumatik automobilu při dynamickém zatížení

UNIVERZITA PARDUBICE
Dopravní Fakulta Jana Pernera
Katedra Dopravních Prostředků a Diagnostiky
Školitel: Prof.Ing. Jan Krmela, Ph.D
2025, 213 stran

Tato studie se zaměřuje na modelování a simulaci pneumatik automobilů vystavených dynamickému zatížení. Jakožto základní součást systému odpružení vozidla zajišťují pneumatiky správný přenos zatížení na zem a absorbují vibrace vyvolané odvalováním. V provozních podmínkách jsou tato zatížení vysoce dynamická. Analýza pneumatik za těchto podmínek však v literatuře nebyla důkladně prozkoumána. Cílem této práce je proto tuto mezeru zaplnit. Za tímto účelem je proveden jak přehled experimentální odezvy komponent pneumatik v cyklických dynamických testech, tak i přehled stávajících modelů pneumatik. Následně je navržena metodologie modelu založeného na metodě konečných prvků, která je v souladu s dynamickými vlastnostmi materiálu a dynamickým zatížením. Je navržena propracovaná strategie pro vytvoření geometrie, identifikaci parametrů materiálu, volbu topologie, okrajových podmínek a schéma řešení. Pro validaci tohoto modelu byly provedeny simulace a experimenty na vybrané pneumatice ve statickém, dynamickém a volném vibračním nastavení. Porovnání výsledků, konkrétně vertikální výchylky, kontaktní plochy, tvaru kmitů a vlastních frekvencí, demonstruje přesnost modelu. Dále byly zkoumány rozsáhlé odezvy, jako je ustálené odvalování, vibrační analýza, přechodné odvalování a ustálená dynamika. Ve srovnání se statickou odezvou výsledky přinášejí nové poznatky týkající se vlivu dynamického zatížení na deformaci a stav napětí v pneumatice. Tento model je navíc všestranný a lze jej rozšířit tak, aby zkoumal více odezev, jako jsou akustické, termomechanické, aquaplaningové a související analýzy hluku, vibrací a drsnosti. Tato práce přispívá k rozvoji pneumatikářského průmyslu a zdůrazňuje význam zohlednění dynamického zatížení ve fázích návrhu pneumatik pro zlepšení konstrukce, životnosti a bezpečnosti pneumatik.

Klíčová slova: Metoda konečných prvků, simulace pneumatik, dynamické zatížení, ustálená dynamika, vibrace, přechodné odvalování.

Contents

List of Figures

List of Tables

List of Abbreviations

ALE	**A**rbitrary **L**agrange **E**ulerian
BEM	**B**oundary **E**lment **M**ethod
CFD	**C**omputational **F**luid **D**ynamics
CNORMF	**C**ontact force distribution
CPRESS	**C**ontact **P**ressure distribution
C3H8RH	**3D** continuum **8**-node **H**exahedral solid **H**ybrid element with **R**educed integration
EU	**E**uropean **U**nion
FE	**F**inite **E**lment
FEM	**F**inite **E**lment **M**ethod
GDP	**G**ross **D**omestic **P**roduct
GHG	**G**reen **H**ouse **G**az
GHO	**G**lobal **H**ealth **O**bservatory
HM	**H**yper- **P**seudo-**E**lastic
JATMA	**J**apan **A**utomobile **T**ire **M**anufacturers **A**ssociation
LI	**L**oad **I**ndex
$\mathcal{M}$	**S**pace of square matrices
H	Sobolev space
MR	**M**ooney **R**ivlin
RP	**R**eference **P**oint
RRC	**R**olling **R**esistance **C**lass
RVE	**R**epresentative **V**olume **E**lement
VH	**V**isco- **H**yperelastic

Physical Constants

Acceleration due to gravity $g = 9.81\,\mathrm{m\,s^{-2}}$

List of Symbols

$a = (a_x, a_y, a_z)$	Acceleration vector field	$\mathrm{m\,s^{-2}}$
$\overrightarrow{A_\alpha}$	Fibers orientation unit vectors	
$\mathcal{C}_{IJKL}$	Fourth-order elasticity tensor	MPa
$C_i,\ c_{0i}$	Material constants	MPa
C	right Cauchy-Green deformation tensor	
D_i	Compressibility parameters	$\mathrm{MPa^{-1}}$
$E_{I\ \epsilon\{1,2,3\}}$	Basis coordinate vectors associated with X_I	
$e_{i\ \epsilon\{1,2,3\}}$	Basis coordinate vectors associated with x_i	
E	Green-Lagrange strain tensor	
E	Young's modulus	MPa
F	Deformation gradient	
F_{cx}, F_{cy}, F_{cz}	Resulting force components at tire-road interface	N
F_{wx}, F_{wy}, F_{wz}	Force components at wheel's center	N
g_i	Relaxation/creep moduli	
$I_{i\ \epsilon\{1,2,3\}}$	Principal invariants of C	
$\overline{I}_{i\ \epsilon\{1,2,3\}}$	Reduced principal invariants of C	
J	Jacobean determinant	
$k_x, k_y, k_z, C_\alpha, C_\gamma$	tire handling stiffness	$\mathrm{N\,m^{-1}}$,$\mathrm{N\,^{\circ -1}}$, $\mathrm{N\,m\,^{\circ -1}}$
M_{cx}, M_{cy}, M_{cz}	Resulting moment components at tire-road interface	N
M_{wx}, M_{wy}, M_{wz}	Moment components at wheel's cente	$\mathrm{N\,m}$
P	First Piola-Kirchhoff stress tensor	MPa
$\underline{p}$	Hydrostatic pressure	MPa
p_n	Contact pressure	MPa
p_{in}	Tire inflation pressure	MPa
r, m, η	Mullins damage parameters	
R_{drum}	Drum radius	m
$R_{r,in}$	Rim radius	m
$R_{t,in}$	Tire radius	m
S	Second Piola-Kirchhoff stress tensor	MPa
t	Time variable	s
$\mathcal{T}$	Piola-Kirchhoff stress tensor	MPa

$u = (u_x, u_y, u_z)$	Displacement vector field	m
$\mathcal{U}$	Volumetric strain energy density function	J
$U_{I,J}$	right stretch tensor	
$v_t = (v_{tx}, v_{ty}, v_{tz})$	Velocity vector field	$\mathrm{m\,s^{-1}}$
V_0	Initial volume of Ω_0	$\mathrm{m^3}$
v	Volume of Ω_t at ant time	$\mathrm{m^3}$
W	Strain energy density function	J
$\hat{W}$	Deviatoric strain energy density function	J
$W_{contact}$	Contact energy	J
W_{ext}	External energy	J
W_{int}	Internal energy	J
W_{kine}	Kinetic energy	J
$x_{i\ \epsilon\{1,2,3\}}$	Eulerian coordinate variable	m
$X_{I\ \epsilon\{1,2,3\}}$	Lagrangian coordinate variable	m
ε	small strain tensor	
η	Viscosity	$\mathrm{m\,s^{-1}}$
ω	Angular frequency	rad
κ	Bulk modulus	MPa
σ	Cauchy stress tensor	MPa
γ	Camber angle	$^\circ$
ρ	Density	$\mathrm{kg\,m^{-3}}$
μ_{dyn}	Dynamic friction coefficient	
Ω	Non-empty Bounded domain	
$\lambda_{i\ \epsilon\{1,2,3\}}$	Principal stretches	
ν	Poisson's ratio	
$\varnothing_i$	Reinforcement's diameter	mm
τ_{ij}	Shear stress	MPa
α	Slip angle	$^\circ$
μ_s	Static friction coefficient	
Δt_{stable}	Stable time increment	s
θ	Temperature	$^\circ\mathrm{C}$
Δt	Time increment	s
σ_{VH}	Von Mixes stress	MPa

To the glory of the almighty God…

To my late grandparents…

To my loving parents…

1 Introduction

1.1 Context

Tires are key structural components in both road and air transport that play a paramount role in mobile structure integrity and stability. They not only transfer loads from the moving structure (car, truck, aircraft, etc.) to the supporting ground, but they also absorb shocks due to road roughness or disparities such as peeling, rutting, or feathering on the road, or any other pathologies that affect the structural morphology of the road surface. Therefore, they significantly contribute to providing comfort, stability, and safety in various operating conditions. As per the usage, one distinguishes many types of tires:

- Passenger and light truck tires: PT/LT;
- Bicycle tires;
- Motorcycle tires;
- Agricultural tires;
- Aero tires;
- Racing tires;
- Truck and bus tires.

These tires vary by their design and bearing capacity. This is why the improvement in tire design and manufacturing processes is at the heart of manufacturers' and governments' quest. This quest constantly stimulates research efforts to enhance the tire according to the nature of the various stresses it is subjected to and the conditions in which it operates. Although the tire's current complex structure is the fruit of great evolution and poignant progress, the fact remains that its structural optimization is still necessary in view of the material resources required and the ecological and economic stakes involved. In the current dynamically changing modern world, where the problems of rational use of natural resources and mitigation of the environmental impact of human activities are becoming ever more acute, the demands for sustainability and performance are ever greater. This, in turn, raises the need to develop more sophisticated and accurate simulation models that will allow manufacturers to better apprehend the behavior of tires and foster the design of higher-performance products.

1.2 Research motivations

Given the dynamic loads that tires are subjected to throughout their service life, developing a computer model to simulate tires under these loads is of paramount importance from both a scientific and industry perspective. Such a model will close the current gap in dynamic tire modeling, providing manufacturers with a more advanced modeling roadmap for product design and optimization. These motivations are highlighted in Figure 1.1.

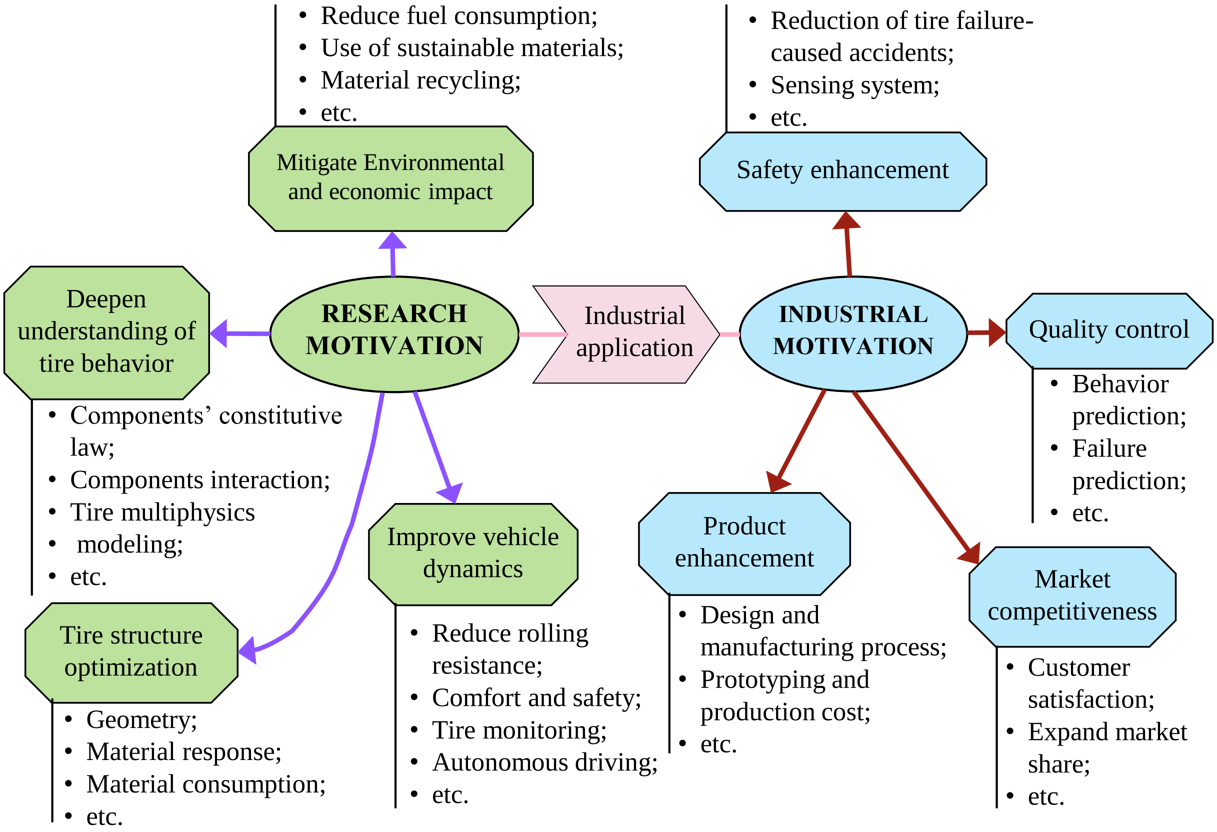

Figure 1.1: Motivation for the improvement of tire modeling.

1.2.1 Environmental and sustainability reasons:

In today's climate of fossil fuel scarcity [1] and skyrocketing energy prices, coupled with rising energy demands for the world's production systems due to a growing population, the issue of resource and energy sustainability has emerged as one of the major concerns of this century and has increasingly been catching the attention of decision-makers worldwide. By pursuing sustainable policies, governments [2] are encouraging businesses and research centers to develop less energy-intensive systems that will make it easier for the effective transition from fossil fuels to green or eco-friendly energy to occur. In this respect, the transport sector [2], [3], [4] stands as one of the most polluting industries in terms of vehicle oil consumption and energy consumption for vehicle parts manufacturing. Like the aerodynamic shape of a vehicle, tire

rolling resistance plays an important role in determining fuel consumption and consequently increasing greenhouse gas emissions (carbon monoxide, etc.).
The structure of modern tires is the result of decades of continuous research and innovation in the automotive and chemical industries. Originally, only natural polymers were used, but later, with technological advances in chemistry, synthetic polymers began to be combined with natural polymers in order to produce tires with improved performance and lower costs. Depending on the tire's usage and requirements [5] (mechanical, environmental, financial, etc.) involved, several compositions may be considered (see Figure 1.2).

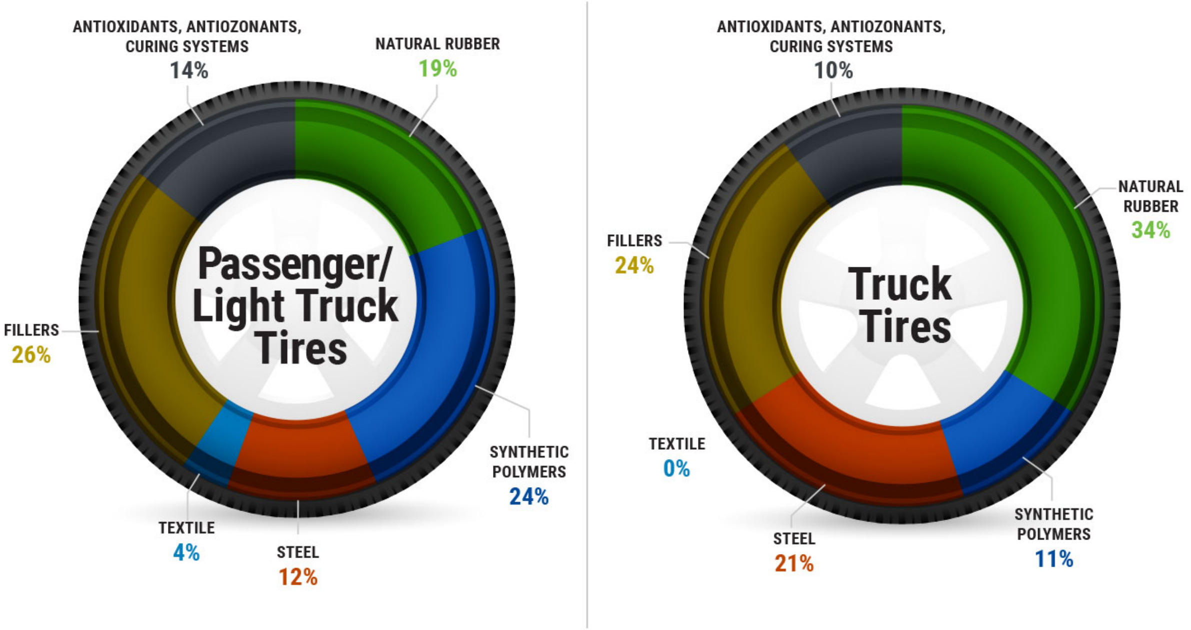

Figure 1.2: Average composition of passenger, light truck and truck tires [6].

As we might expect, heavy truck tires require more reinforcements (on average, twice as much) and more natural polymers because of their much higher load-bearing capacity. However, a primary principle of sustainable development is that waste products must be recycled and reintroduced into production cycles. For instance, a study conducted in 2021 by the Japan Automobile Tire Manufacturers Association (JATMA) [7] revealed that only around 16% of used tires are recycled, while around 64% are used for energy recovery, which raises serious pollution concerns, as the latter is accompanied by significant greenhouse gas (GHG) emissions. Recalling meanwhile that tires' lifecycle can be roughly divided into four stages highlighted in

Figure 1.3.

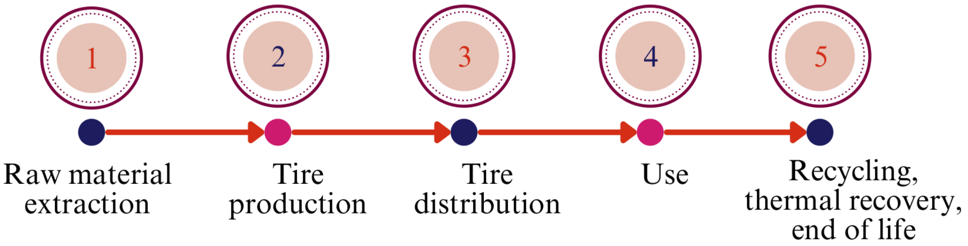

Figure 1.3: Tire life cycle.

According to the same study, over the entire lifecycle of tires, more than 80% of GHG emissions occur during the usage stage due to rolling resistance with the road surface.(see Figure 1.4).

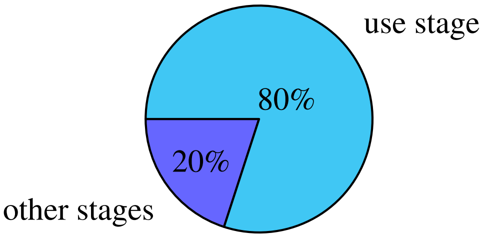

Figure 1.4: Greenhouse gas emissions throughout tire lifecycle (from extraction, production, usage to recycling) [7].

Rolling resistance is a very relevant phenomenon in vehicle dynamics, as it dictates how tires interact with the road during motion. It is roughly defined as the tendency of the tire in contact with the road to resist movement in the direction of travel. According to Clark and Dodge [8], the primary cause of rolling resistance is hysteresis, induced by the viscoelastic constitutive behavior of rubber compounds in the tires. In the same vein, there exists a categorization in the tire industry that rates tire rolling efficiency based on their rolling resistance class(RRC). This coefficient is a useful indicator since it is directly related to the vehicle's fuel consumption. Simply put, the higher the rolling resistance class, the more fuel the vehicle will consume. In concomitant rolling situations, tires generate noises, for which the value measured in decibels must comply with certain requirements aimed at reducing noise pollution. Another indicator of no less importance is the wet braking performance, which measures the braking capacity of the tire on wet roads. In this rating, the best tires require 30% less braking distance than the worst ones [9].

As of 2021, the European Comission [9] has adopted a new ranking system for rating tire *fuel efficiency*, *wet braking performance*, and *noise emittance* in replacement of the former system. In this classification system, tires are sorted from A to E for the first two indicators and from A to C for the noise rating, both in descending order. This rating is presented in an overview in Figure 1.5.

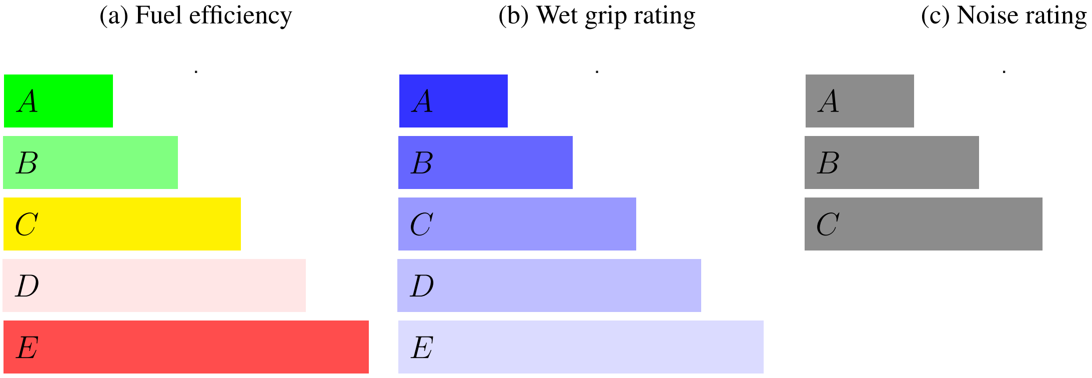
(a) Fuel efficiency
(b) Wet grip rating
(c) Noise rating

Figure 1.5: E.U.labeling system of tires as per environment and safety criteria.

Before being granted access to the EU market, manufacturers must prove that their products have been tested and approved by the relevant authorities to meet environmental and safety requirements.

In view of the above-mentioned environment and resource challenges, it is essential to adopt solutions oriented toward the circular economy concept. This concept is based on the 4R principle: *Renew, Reuse, Reduce and Recycle*. In this regard, Michelin[10] and Continental[11] have announced they have invested in R&D to reach a circularity rate of 100% by 2050. Achieving this goal of replacing raw materials with fully sustainable materials demands a deeper understanding of the material behavior from both the chemical and mechanical perspectives.

1.2.2 Economic motivations:

According to surveys conducted by Research [12], Promodo [13], and Statista [14], the global automotive tire market was estimated at \$126.78 billion in 2022 and is expected to reach \$154.4 billion by 2027 (see Figure 1.6).

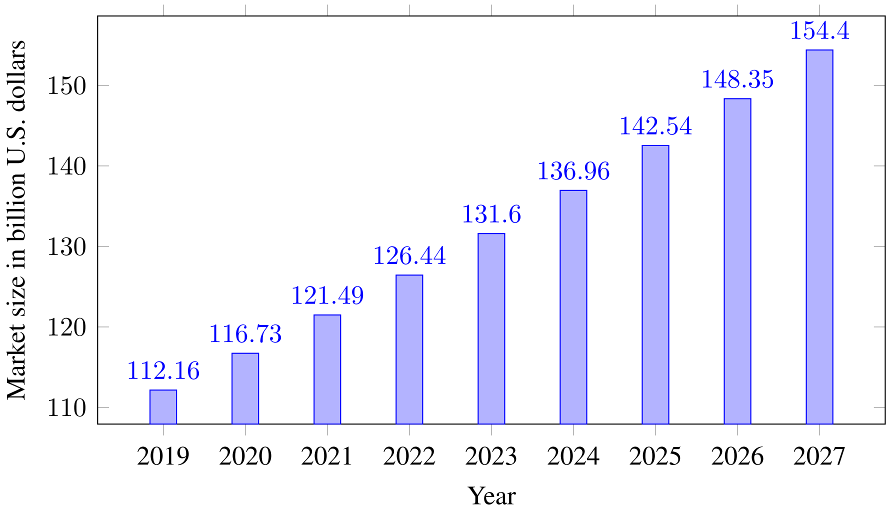

Figure 1.6: Revenue in the automotive tire market [13], [14].

In the 2023 annual report released by Statista [14], in 2019, the automotive tire market was valued at $112.6 billion. This basically means that this section of the market is expected to grow with a compound annual growth rate (CAGR) of circa 4% yearly until 2027. Compared with the figures in 2000, the value of the global automotive tire market has almost doubled and has significantly grown in terms of competitiveness and product quality. Among the world's leading tire manufacturers, companies such as Bridgestone, Michelin, Continental and Goodyear stand out of the crowd with approximately 66% of the market revenue in 2020. In this market, the largest demand is concentrated in the Asia-Pacific region, with about 45% of the global value. Bearing in mind that this region is home to about 60.2% of the world's population, demography and living standards meaningfully drive the rise in the market demand for tires. Meanwhile, the increase in the world's road infrastructures within the last 25 years speaks eloquently to the rise in demand for transportation and underlines its importance for human beings, both individually and collectively in society. For instance, between 2005 and 2014, 32 million kilometers of built roads were reported by the World Road Statistics (WRS) database[15]. Consequently, the tire market is a very lucrative market segment with a bright future ahead. This brief overview of the automotive tire market's monetary value helps understand why tire producers have been massively investing in research and development to enhance the quality and design of their products.

1.2.3 Tire performance and durability motivations:

Alongside purely environmental and safety aspects, there are also requirements (see Figure 1.7) related to the structural performance of tires.

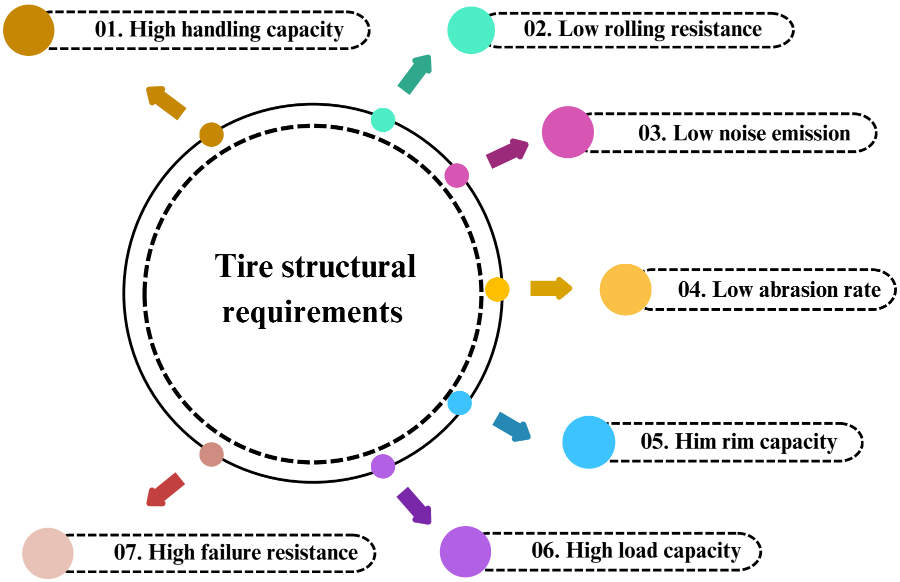

Figure 1.7: Structural requirements for tire.

Tire *stability* and *durability* are key requirements that demand an advanced structural analysis during the design process and thorough verification during the testing phase. Such an in-depth analysis stresses the tire's handling characteristics and, more broadly, examines its behavior in various short-, medium- and long-term scenarios. It also helps detect and prevent sudden tire failures such as wear, tear, delamination, and blowout, which are responsible for many car traffic crashes worldwide, as inventoried by Freeman and Leith [16], Chen et al. [17], Gent and Walter [18] and Gardner and Queise [19]. The assessment for structural integrity and stability of the tire is more generally conducted on a model that encompasses the geometry of the tire and its constituents, material constitutive laws, boundary conditions and initial conditions, loads, and solution schemes. Throughout the years, the tire industry has witnessed the emergence of numerous tire models developed by researchers and engineers to capture tire behavior in diverse scenarios. These models vary in their level of detail, complexity, accuracy, and applicability and can be categorized into three main groups: empirical, semi-analytical, and theoretical. While empirical models solely rely on experimental measurement data, semi-analytical models combine experimental data with mathematical equations to predict tire response. On the top of the above models stand theoretical models, which are the most sophisticated and use advanced mathematical formulation to simulate tire performance. Out of these models, only the latter allows for rigorous modeling of tire components as highlighted by Sadjiep Tchuigwa et al. [20].

Deepening tire response understanding is the ground-to-efficient tire enhancement, and it spans from the characterization of components' materials behavior to modeling techniques, passing through components interactions and model parameters such as intra-components interface and road contact interactions. Thus, proposing a tire model that can rigorously tackle any possible structural analysis in static and dynamic scenarios is relevant. In addition, it can also serve as a base for thermal, acoustic, and aquaplaning studies and, more generally, for multiphysics analysis.

1.2.4 Holistic simulation of vehicle dynamics:

When approaching vehicle dynamics from a holistic point of view, the incorporation of the tire model as a subroutine function to integrate tire response in the vehicle model is of industrial importance. Realistic and more insightful modeling of vehicle handling and crashworthiness can be unveiled in such a context. Furthermore, the combination of such a model with sensors and the integration of artificial intelligence will help reinforce vehicles' reliability and safety. In line with this futurist aim, Bridgestone Bridgestone Corporation [21] announced in 2019, a research project for the development of smart tires for safer driving. In the fast-paced pursuit of self-driving vehicles, holistic vehicle simulation[22], [23] has become more important than ever. This approach allows for the systematic capture and consideration of all vehicle systems, providing a real-time, in-depth understanding of the vehicle behavior. Again, it makes enhanced monitoring and assisted control feasible via artificial intelligence models. More explicitly, once the numerical model has been validated based on experiments, it can be utilized to run large-scale simulations and collect the data necessary for training the machine learning model. The trained model may then be deployed in driverless cars to enable tire response monitoring and driving assistance.

1.2.5 Enhancement of tire design via topology optimization:

Once an in-depth insight into tire modeling has been gathered, it becomes easier to perform structural optimization for rational utilization of material resources. For sustainable management of available material resources, the lightweight design of the tires is necessary to fine-tune the current tire design so that fewer material is utilized while fulfilling the same structural requirements. Significant breakthroughs in topological optimization techniques [24], [25] over the last three decades have made it possible. By way of example, this is the methodology powering current research into non-pneumatic tires as studied in [26]. Many variants of topology optimization approaches in the literature are based on two pioneering formulations: the Bidirectional Evolutionary Structural Optimization (BESO) method and the Solid Isotropic Material with Penalisation method (SIMP), respectively developed by Yang et al. [27] and Bendsøe [28]. However, there is no known method that tackles topology optimization involving geometrical, material, and contact nonlinearities. Nevertheless, there are promising advances in this regard with the recent studies by Zhang [29], Habashneh and Movahedi Rad [30] and Frederiksen et al. [31].

1.3 Problem statement

As highlighted above, improving the tire modeling and analysis process for dynamic scenarios is substantial for a better understanding of tire response and mitigating the ecological footprint of tire production and use. In recent years, FEM (Finite Element Method) has established itself as a sophisticated technique for the simulation of a wide variety of boundary value problems, including tire simulation. Thanks to cutting-edge technological advancement in computer architecture, FEM is gaining more and more ground. With its ability to address both linear and nonlinear problems in static as well as dynamic, it can be efficiently used to solve mechanical problems involving geometrical, material, contact and follower force nonlinearities. Furthermore, because of its transdisciplinary capabilities, FEA allows fluid, thermal, acoustic, mechanical and multi-physics simulations to be carried out. The accuracy of the FE model to simulate tires relies on the appropriate choice of material constitutive laws, the definition of the topology (geometry) via image acquisition and computer-aided modeling, appropriate application of loads, prescription of boundary conditions, as well as a proper choice of a solver scheme. However, as far as dynamic loads are concerned, the existing computer models cannot be utilized in their current states, as they would become, in this case, inconsistent with regard to material behavior and load variation. Also, given the nonlinearities involved and the level of meshing required to obtain acceptable results, the high computational cost is a major drawback. Nonetheless, the FE models are way more powerful than the analytical and semi-analytical tire models.

1.4 Research aim

In real-life usage, tires are exposed to dynamic loads that have to be taken into account during the design phase to ensure safe usage, durability, and comfort of vehicle occupants. The dynamic response of a tire to these loads is closely conditioned by the mechanical properties of its constituents. However, there is currently no existing tire model that can comprehensively capture the actual dynamic response of materials so that both reversible and irreversible phenomena inherent to tire constituents are regarded. Nor is it intended for the dynamic simulation of tires in dynamic scenarios. Therefore, the aim of this thesis is to **propose a material-consistent and computationally stable FEM-based model for modeling and simulating tires under dynamic loads**. This model should allow a better mechanical characterization of tire components and provide an efficient modeling strategy, as well as an optimal choice of solver properties for ensuring stable and accurate solutions.

In light of the above-mentioned motivations and the limitations of existing tire models, the aim of this thesis is to develop an innovative tire model that can accurately predict tire behavior under dynamic loads, considering the consistent dynamic response of tire materials.

1.5 Research objective

In order to achieve the aim of this thesis, the following activities were carried out:

- **Literature review on tire models** (assumptions, inputs, limitations, purpose): The purpose of this work is to comprehensively explore existing tire models considering various aspects such as the underlying assumptions they are built on, the inputs (material properties, geometry and mesh creation, boundary conditions, loads, solver) required for their implementations, the inherent limitations they may possess, and the specific purposes they serve within the field of automotive engineering.

- **A detailed analysis of component behavior laws and identification of the parameters that influence the tire's dynamic response**: this study assesses the effective material response to dynamic loads and related material parameter identification procedure.

- **Mechanical characterization, testing and calibration of tire parts**: in this part, experimental tests and material laws calibration are performed on tire parts from a tire selected for validation.

- **Development of a numerically stable modeling process**: The purpose of this work is to design and optimize an efficient modeling workflow and procedure for tire modeling. This work serves as proof of concept to show that the chosen material model is also accurate under static loads.

- **Experimental static and dynamic testing of a selected tire**: In this work, real laboratory full-scale tests, namely the static test on the static adhesor, the static and dynamic test on the dynamic adhesor, and the unloaded tire modal vibration test, are carried out.

- **Validation of the numerical model based on experimental results**: this part is devoted to the application and validation of the developed modeling process.

- **Simulation of various tire operational scenarios**: extensive analyses, including steady-state rolling, post-steady-state rolling vibration, steady-state dynamic, and transient rolling, are investigated.

1.6 Manuscript outline

The structure of this thesis is organized as follows:

Chapter 2 provides a general presentation and state-of-the-art knowledge of tire modeling. More precisely, a brief introduction to tire functions, parts, and mechanical characteristics is presented, along with a systematic literature review on tire models. Among the reviewed tire parts and models, an emphasis is placed on finite element-based tire models, which are the inspiration for the current research.

Chapter 3 explores kinematics and possible material constitutive models for tire components, namely rubber compounds (inner liner, apex, sidewall, tread, undertread, etc.), steel cords, textile cords and carcass. These models range from the simplest in small strain to the most complex in finite strain. Additionally, existing contact formulations pertaining to tire-road interaction are examined.

In Chapter 4, the proposed FE-based tire model is constructed. First of all, a more realistic experimental-inspired material model is chosen, and the material parameter identification is outlined. Then, the modeling process includes the topology, boundary conditions, methodology, assumptions and kinematic description of the problem are presented.

In Chapter 5, the influence of the rubber compound material law on the static response of a selected tire is studied in detail. Also, a vectorized and generalized algorithm was introduced to optimally reduce computational time.

In Chapter 6, the validation of numerical results against experimental results in static and dynamic setups is thoroughly investigated in terms of deformation, contact pressure, and contact patch. Further analyses, including steady-state rolling, steady-state dynamic, random vibration, post-steady-state rolling frequency analysis, and transient rolling, are explored.

In Chapter 7, findings, model limitations, future recommendations and concluding remarks are discussed and highlighted.

2 Presentation and state of art on tire models

Tires in their current design are the outcome of decades of engineering improvement and evolution. Their complex structure has evolved ever since in terms of material and design techniques. The aim of this chapter is first to present the tire structure and its characteristics. Secondly, to review the literature on tire simulation models and identify their limitations.

2.1 Definition and functions

The tire is a composite structure resulting from a sophisticated disposition of elastomer and reinforcements to ensure contact, rolling and load transfer between the moveable system with which it is associated and a rolling surface (pavement, tarmac or airfield). Tires are used in a variety of applications, notably on aircraft landing gears, where they ensure safe take-off and landing, on trucks of all types (construction equipment, etc.), and on passenger vehicles. To each of these applications corresponds a particular design and structure in terms of material composition and assembly. In the scope of this thesis, the focus is solely on car tires.

In automotive engineering, beyond the primary function of the tire abovementioned, the tire is one of the most important parts of a vehicle system and is designed not only to transfer the vehicle's loads to the tarmac but is also expected to respond to the driver's maneuvers through the steering system. In a much more precise fashion, three major functions are ideally expected in the design process of an optimal tire from a driving perspective illustrated in Figure 2.1

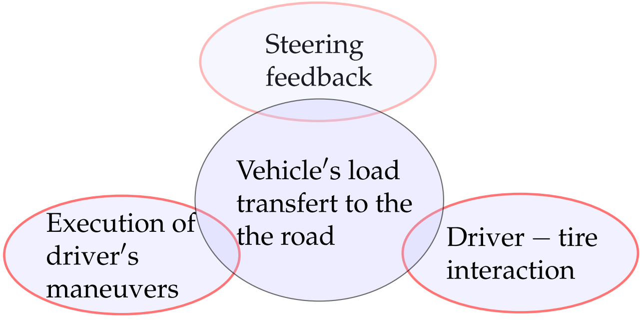

Figure 2.1: Tire's major functions.

2.1.1 Terminology and tire mechanical characteristics

There exist two distinct designs of car tires, namely radial tires and bias tires (see Figure 2.3). While radial tires are made with respectively 0° and 90° oriented plies toward the longitudinal direction of the tire, bias tires are made with plies unaligned following the longitudinal and transversal direction.

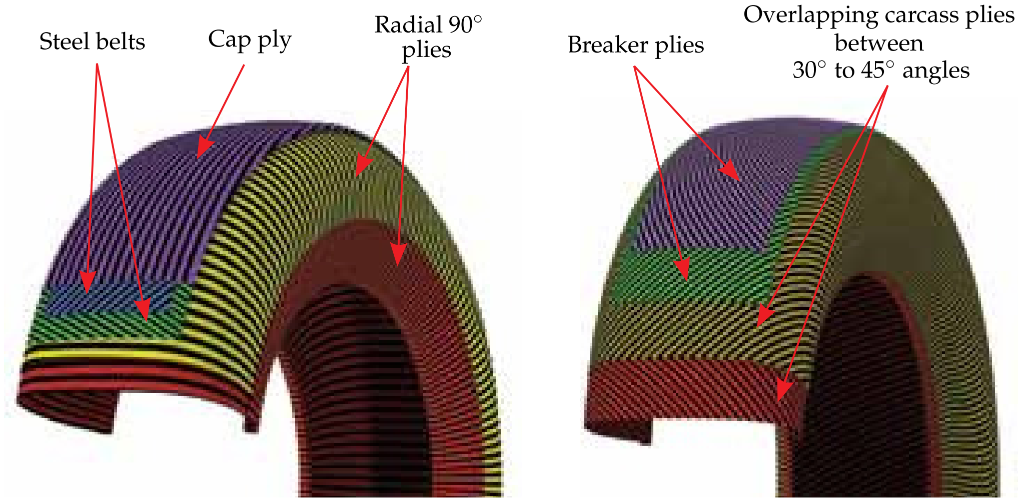

Figure 2.2: radial tire casing (left) versus bias tire casing (right) [32].

Tire components definition and functions:

A cross-section on a tire reveals a combination of different components (see Figure 2.3) of various properties. It is this complex design that makes the tire such a special structure, as each of its components is judiciously positioned and chosen.

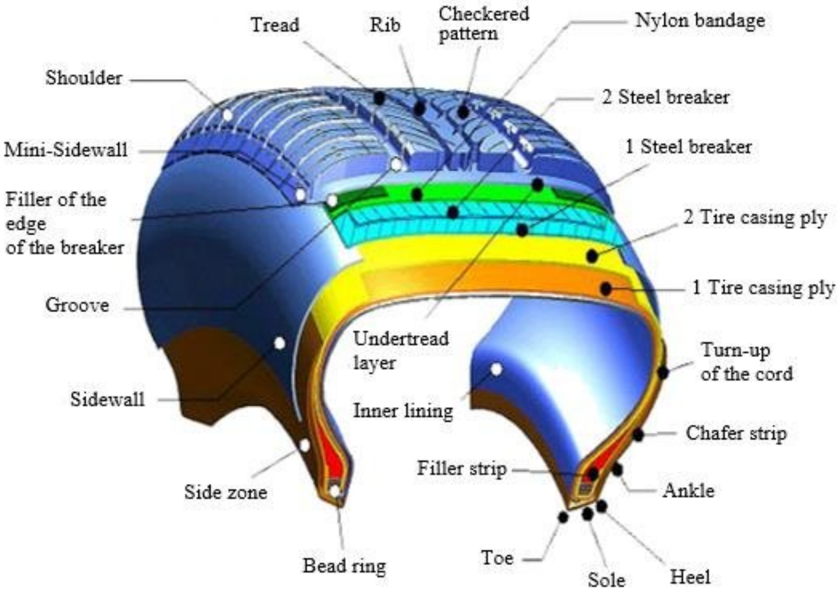

Figure 2.3: Tire casing parts [33].

Beads are a bundle of steel wires(see Figure 2.4(a)) and are much stiffer than rubber from bead filler, it prevents the tire from sliding out of the rim in high soliciting operational situations like sudden short turns, cornering, lateral sliding, or braking. Meanwhile, in the technology with tubeless tires characterized by a higher safety and stability than those with separate inner tubes, bead helps avoid the leak of pressurized air in the tire by constraining the tire to remain in the parts of the rim called bead rests and located between the flanges (inboard and outboard) and mounting humps as shown in Figure 2.4(b).

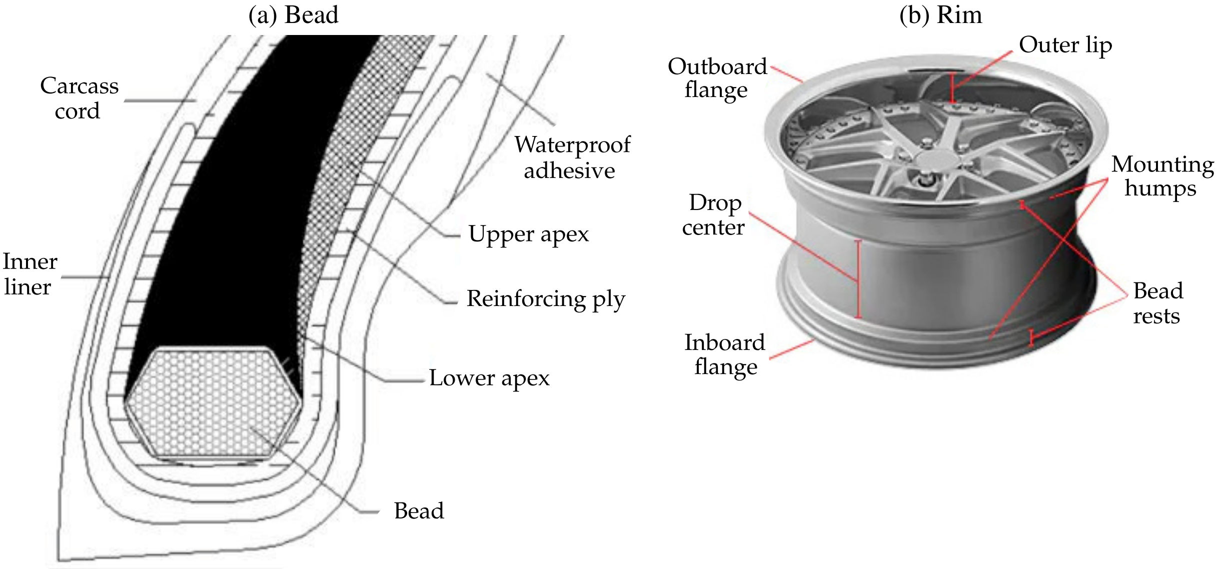

Figure 2.4: Bead structure [34] and rim's parts [35].

Tread is the tire part directly in contact with the road surface and is important for transferring wheel loads to the soil, steering response/traction, and assuring quality handling vehicle and rolling contact. Typical tire tread usually has many parts, which are ribs, grooves, blocks, shoulders, and sipes, as depicted in Figure 2.5.

Figure 2.5: Tire tread parts [36].

The shape, size, and features of treads are the result of an optimization process that stringently depends upon tarmac surface properties (i.e., friction coefficient, roughness) and the environment (temperature, humidity, etc.) in which the vehicle operates. It is also important to note that tread patterns can either be symmetrical, asymmetrical, or directional depending on the level of handling performance expected when driving over a given type of pavement with given surface characteristics.

Due to this, winter tire treads differ in shape and size from summer tires. An optimal tread size means a suitable contact patch and less slippage, resulting in a better transmission of traction force and faster braking. In the rolling configuration, they are also subjected to wear, which is the material deterioration of the ribs as a consequence of frictional contact with grips present on the tarmac. Owing to this unavoidable wear caused by the permanent contact, several regulations define tread depth requirements [37] for different tire types and regulate tire design and manufacturing processes. Treadwear can manifest itself in a variety of patterns depending on the underlying causes, such as alignment issues, excessive air pressure, balancing issues, insufficient air pressure, and suspension concerns. For that reason, treadwear features are often examined to diagnose and detect possible faults in the vehicle's steering and suspension systems.

Inner liner is the most internal rubber layer in a tire that helps preserve or reduce the loss of inflation pressure of air trapped between the inner cavity of the tire and the rim.

Carcass are thin textile fiber cords that are glued into the rubber and sit on top of the inner lining. They strengthen tire body and help maintain inflation pressure.

Textile belts are placed under the tread and help reinforce the rubber under stress while allowing the tread to grip the road properly.

Steel cords provide tires with the rigidity needed to withstand heavy stresses under the tread.

Inner filler or inner liner is the innermost part of the tire and is designed to be waterproof and helps prevent air loss. It is usually made of synthetic rubber.

Each of the above-mentioned components has to fulfill a set of requirements [5], [20], including structural, handling, comfort, and safety aspects. Which are expected for the resulting tire to comply with transport regulations.

2.2 Static and dynamic characteristics of tires

Before jumping into the structural properties of the tire as a whole, it is imperative to establish a suitable coordinate system that helps accurately define acting forces and torques. In the context of tire dynamics, three different coordinate systems are important for several reasons (defining load application, boundary conditions, and results probe).

- *Earth-fixed coordinate system* $\Re_{\mathrm{O}}$: The earth-fixed coordinate system is the reference coordinate system from which the material points of the tire and road geometry are defined. It does not change throughout the simulation. In commercial software such as ABAQUS® [38] or ANSYS® [39], it coincides with the default coordinate system of the software. Dynamically speaking, accurate tire response analysis in a rolling state requires a global fixed coordinate located on the road, from where important quantities like deformation, speed, acceleration, slip distance, forces, torques, etc., can be recorded or probed. Such a coordinate system is important for reliably measuring data needed for validation of the model on the basis of experiments;
- *Rim center coordinate system* $\Re_w$ (also called *wheel coordinate system*):

  This coordinate system is attached to the center of the rim. In chapter 4, the use of such a coordinate system is of good relevance since it enables to apply quantities like the ratio of the vehicle self-weight, the yaw torque, the self-aligning torque, etc., transmitted to the wheel through the rim. In this coordinate system, the origin (here noted w) coincides with the center of the wheel;
- *Tire coordinate system* $\Re_{\mathrm{T}}$:

  The coordinate system $\Re_{\mathrm{T}}$ has its center located at the contact with road and is characterized by its vertical axis, which remains collinear to that of $\Re_{\mathrm{O}}$. Forces and torques obtained in this coordinate are very usual for handling analysis of tires as extensively investigated in the literature.

With these three definitions of coordinate systems at hand, it is much easier to cinematically and dynamically define a tire as a single body based on resultant quantities. In the tridimensional space, a tire, as a single body, is cinematically defined in terms of six degrees of freedom, namely three translations and three rotations. To this, cinematic quantities are associated with three forces and three moments or torques. In tire simulation, these quantities are commonly defined according to the standard SAE coordinate system (see Figure 2.6), where are reported three forces, namely the normal or radial force F_z, the longitudinal force F_x and the lateral force F_y; and three moments namely the rolling resistance moment M_r, the overturning moment M_o and the yaw moment or aligning torque M_z. From the above three torques, the associated angular velocity, the angular speed and the yaw rate can be readily derived with respect to their specific acting directions. Figure 2.6 shows a clear visualization of the system of coordinates and cinematic quantities.

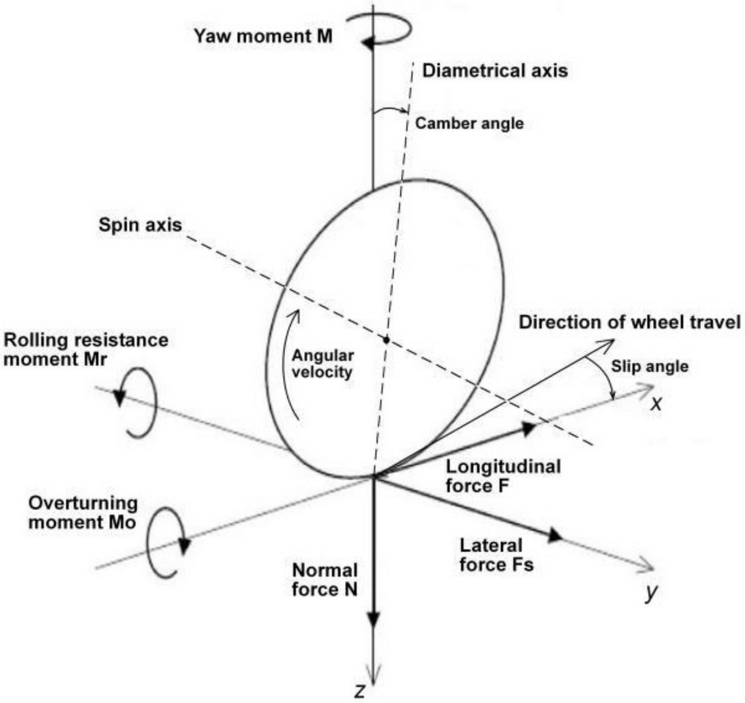

Figure 2.6: Tire handling coordinate system [40].

Radial stiffness

The radial stiffness k_z [in kN/m or N/mm] of a tire is physically defined as its resistance to deformation in the radial direction when subjected to vertical load and is mathematically given as

$$k_z = \frac{\partial F_z}{\partial u_z} \tag{2.1}$$

It is commonly obtained after calculating the tangents of the curve $F_z(u_z)$ at all loading points. In laboratory, u_z is measured by performing a static test, which involves applying different values of F_z to the tire and measuring its radial or vertical deformation.

Longitudinal stiffness

Analogously, the longitudinal stiffness k_x [in kN/m or N/mm] measures the tire's ability to withstand deformation in the longitudinal direction under the effect of an applied force $F_x \leq F_f = \mu_s (F_z + P_w)$.

$$k_x = \frac{\partial F_x}{\partial u_x} \tag{2.2}$$

Where μ_s is the static friction coefficient, F_f is the friction force in Newton and P_w is the weight of the tire in Newton.

Remark. *If we apply a force $F_x > F_f$, the static friction will be broken, leading to an activation of motion toward the direction of F_x as illustrated in Figure*

In the static test, the tire to be tested is installed on the testing apparatus, preloaded vertically up to a certain value, and then longitudinally loaded at the center of the rim. This process is repeated for a particular inflation pressure. Afterwards, the derivative (k_x) of the curve $F_x$versus u_x is readily calculated.

Lateral stiffness

The lateral stiffness k_y [in kN/m or N/mm] measures the tire's ability to withstand deformation in the radial direction under the effect of a force F_y

$$k_y = \frac{\partial F_y}{\partial u_y} \tag{2.3}$$

This procedure is identical to the one that was outlined for determining k_x.

Cornering stiffness

The rate at which the lateral force changes in relation to the slip angle is known as the cornering stiffness C_α [in kN/rad]. This is mathematically given by the formula

$$C_\alpha = \frac{\partial F_y}{\partial \alpha} \tag{2.4}$$

Torsional stiffness

The torsional stiffness C_γ [in kN.m/rad or N.mm/rad] is defined as the ratio between the yaw moment M_z and the camber angle γ:

$$C_\gamma = \frac{\partial M_z}{\partial \gamma} \tag{2.5}$$

Remark. *In the expressions of k_z, k_x, k_y, C_α and C_γ, we stringently use partial derivatives since despite appearances, they are dependent on a variety of other variables such as the temperature, coefficient of friction, the speed, etc. Furthermore, the procedure is practically the same in dynamic situations, the only difference being that the tire is assigned an angular velocity $\dot{\omega}$.*

Apart from the pure scenarios defined above, it is possible to combine the loading sequence so as to obtain combined cases in which lateral and longitudinal forces are combined as mathematically defined in Eq. (2.6).

$$F_y(F_z, F_x, \alpha,\ T, \gamma, V, \mu_f, \varsigma, p_c,\ p_{in}) \text{ or } F_x(F_z, F_y, \alpha,\ T, \gamma, V, \mu_f, \varsigma, p_c,\ p_{in}) \tag{2.6}$$

So it can be with variables amongst the outputs in Figure 2.7. In the existing handling models in the literature, several authors [41], [42], [43], [44] have investigated the dependence of F_x, F_y, M_x, M_y and M_z as functions of other variables than F_z, α and γ. However, a description of the model with all the key dependent variables stated in Figure is experimentally very costly as it requires a consistent sensing system to measure all deformations, forces/moments (F_x, F_y, M_x, M_y, M_z) and contact pressure in the course of measurement.

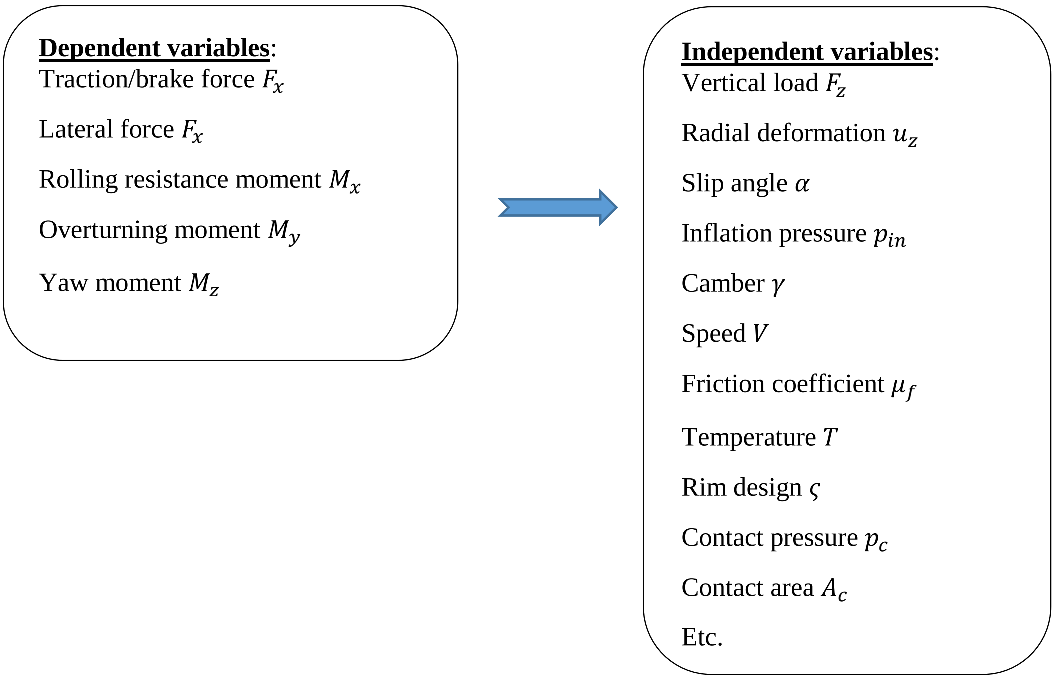

Figure 2.7: Dependent and independent variables for tire handling analysis.

2.3 Literature review

2.3.1 Review of experimental data from tire component testing:

Bearing in mind that the holistic response of the tire is intrinsically linked to that of each of its components, we first start with the observation, interpretation and analysis of laboratory tests of tire components in the following. Nevertheless, it is essential to note that the identification of these parameters is not always straightforward since it often involves purchasing expensive testing equipment and specimens.

Steel cords:

According to experimental results of tensile tests carried out by many researchers such as Korunović et al. [45] and Wei and Olatunbosun [46], steel cords are predominantly solicited in the lower region of the stress-strain where Hooke's law suffices to account for their contribution. Thus, no plastic deformation is expected here as depicted in Figure 2.8. In this regard, a simple uniaxial tensile test is enough to determine Young's modulus (E_{steel}) and Poisson's ratio (ν_{steel}), which are the only parameters needed to account for its contribution.

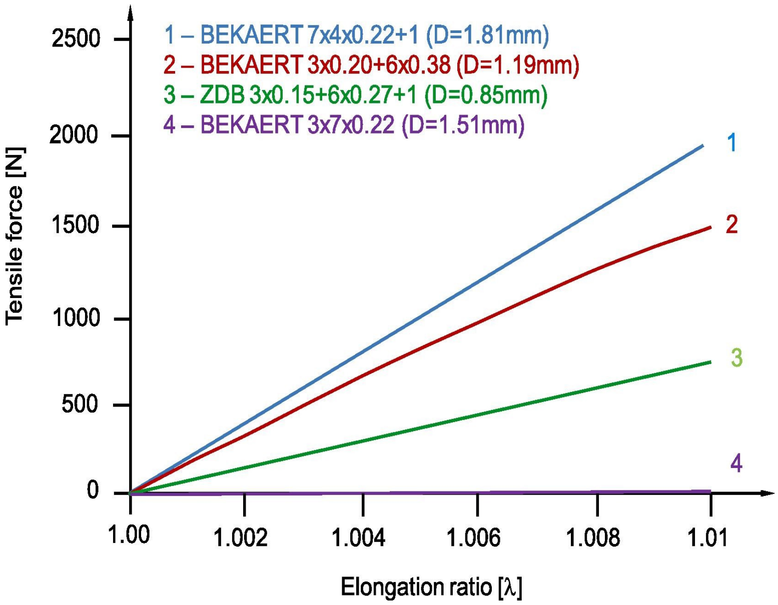

Figure 2.8: Tensile test results of several steel cords[45].

Rubber compounds:

Rubber compounds used for tire making exhibit in uniaxial tensile test, a very large deformation [47], [48], [49] whilst still remaining in the elastic region as depicted in Figure 2.9(a). In a cyclic tensile test[50], they rather depict a combination of hysteresis and stress softening response, as shown in Figure 2.9.

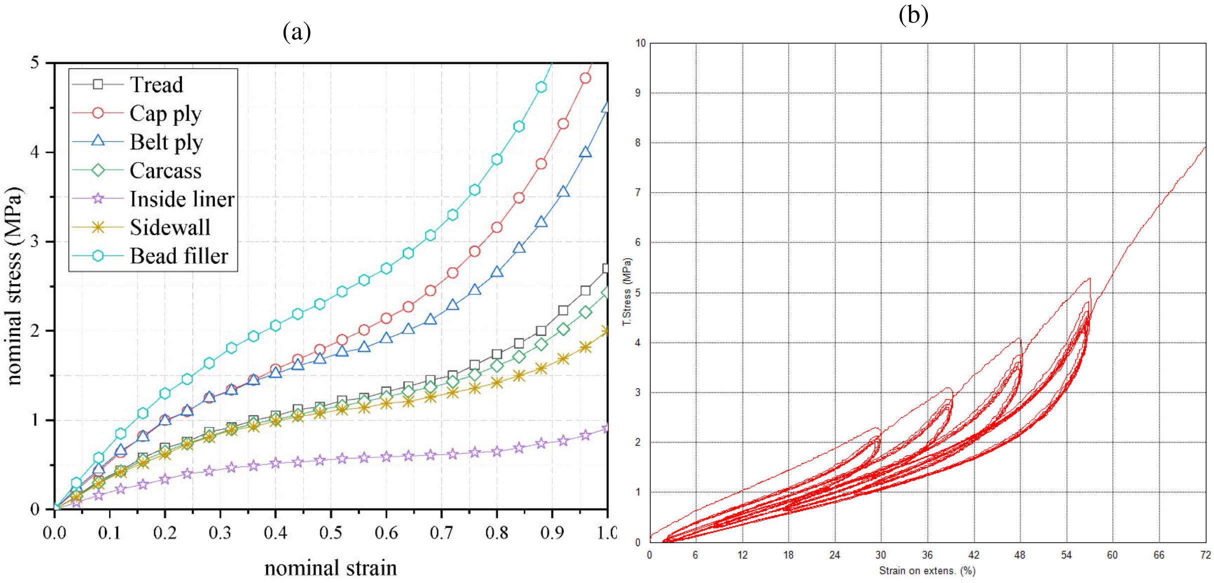

Figure 2.9: Rubber compounds response. (a) in uniaxial tensile test [51], (b) in uniaxial tensile cyclic test [52].

Upon thoroughly examining the cyclic response of the rubber, it can be noted that in addition to hyperelasticity, tire rubber exhibits a combined occurrence of hysteresis and stress-softening response. Since these two phenomena are at the core of tires' damping characteristics, their characterization is relevant. We can spot hysteresis by noting that in every cycle, the loading and unloading paths do not coincide. This feature is induced by material viscoelasticity. On the other hand, it can be observed that the loading path in the current cycle differs from the unloading path of the previous cycle, resulting in stress softening, also known as the Mullins effect. This observation indicates that there is a memory effect in the rubber. The memory effect in rubber means that the material retains some memory of its previous deformation.

Much research has been devoted to investigating these phenomena from both the material and the structural point of view. From the material perspective, Mullins [53],[54] demonstrated that the inclusion of filler in rubber composition significantly increases this effect. In tire rubber formulation, silica and carbon black fillers are added to improve strength and abrasion resistance. From the structural perspective, two groups of mechanical models have been developed: the micro and macromechanical-inspired. The micromechanical model was initially proposed by Bueche [55], who postulated that stress softening is due to the breakage of the molecular bonds between rubber and fillers. This approach was improved by many authors successively up to its most enhanced form suggested by Govindjee and Simo [56]. On the other hand, the macromechanical-based model of Mullins damage was suggested by the pioneering work by Ogden and Roxburgh [57], who adapted the existing damage concepts by Lemaitre [58] and Neto et al. [59] to characterize Mullins damage in filled rubber. Owing to this approach, Dorfmann and Ogden [60] proposed the most used model for accounting Mullins effect for any given loading-unloading process. A decade later on, Göktepe [61] proposed a unified micro-macromechanical approach for characterizing rubber.

However, for computational simplicity, the micromechanical approach is disregarded in this thesis, and the relevant approach is briefly presented in Section 3.2.2

Textile cords:

Laboratory cyclic tensile tests of tire textile cords carried out by [52] and many other researchers [62], [63], [64], [65], [66] reveal, as illustrated in Figure 2.10, that in addition to the slightly hyperelastic response under monotonic tensile load (resulting in the so-called virgin curve), textile cords also exhibit a very tiny viscoelastic+Mullins damage response under cyclic tensile test. However, in comparison to rubber compounds, the hysteresis loops of textile cords are very small and can be neglected for computational simplicity. Thus, textile cords can be assumed to behave as linear elastic materials.

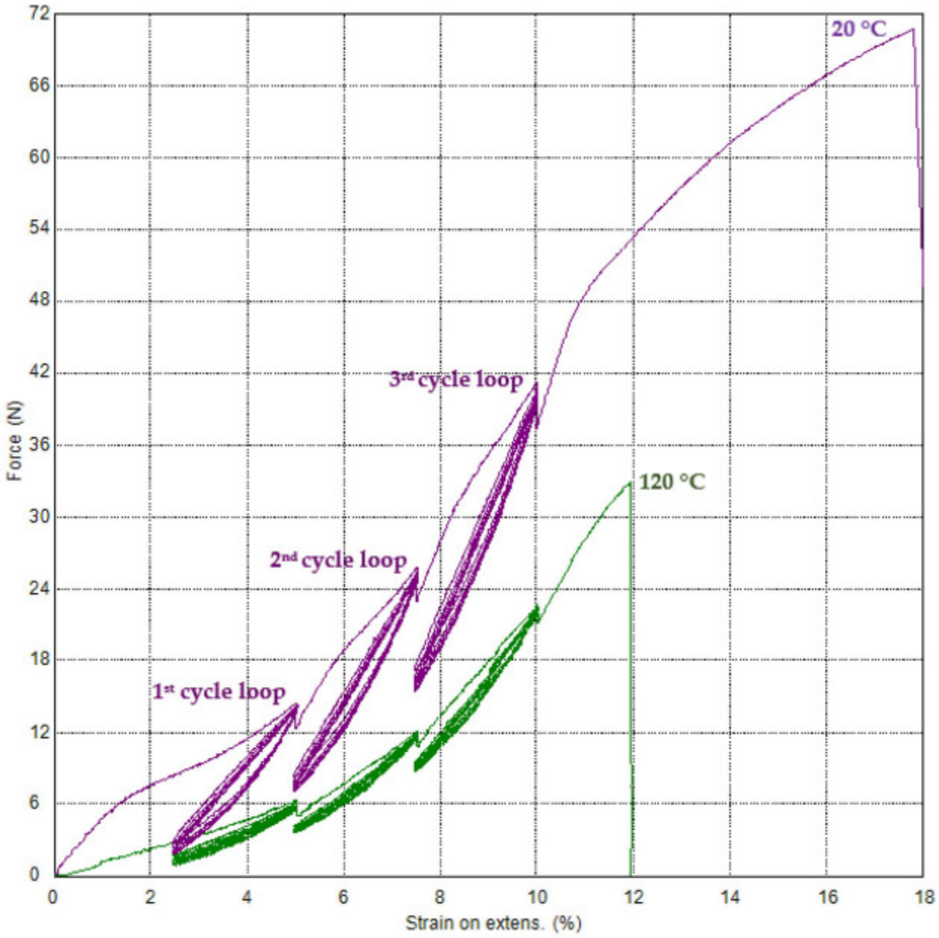

Figure 2.10: Stress-strain dependence of PA66 in cyclic tensile test at 20°C and 120°C [52].

2.3.2 Literature review on tire models

Over the decades, the tire industry has seen a number of tire models emerge from the research and engineering community to simulate tire behavior in different contexts. These models vary in their levels of detail, complexity, accuracy and applicability. Furthermore, they are utilized to for a specific target such as handling, comfort or structural analysis. *Handling models*, for instance, are designed to capture the maneuverability characteristics of a tire, such as its lateral and longitudinal slip, cornering stiffness, and self-aligning torque. These models are commonly used in vehicle dynamics simulations to evaluate the performance of different tire designs and optimize the vehicle's handling and stability. *Comfort models*, on the other hand, focus on the ability of tires to provide passengers with a smooth and stable ride. These models account for factors such as the natural frequency of the tire, the damping ratio, and the contact patch area. Comfort models are often used in vehicle noise and vibration simulations to assess vehicles' acoustic and tactile comfort under different road conditions. *Structural models* delve into the internal behavior of tires, including their deformation, stress, and strain patterns. These models are typically used in tire design and testing to optimize tire durability, safety, and performance. Structural models can also help identify potential failure modes and design solutions to mitigate them.

In the literature, tire models are ranked into three categories, namely empirical, semi-theoretical, and purely theoretical models as depicted in Figure 2.11.

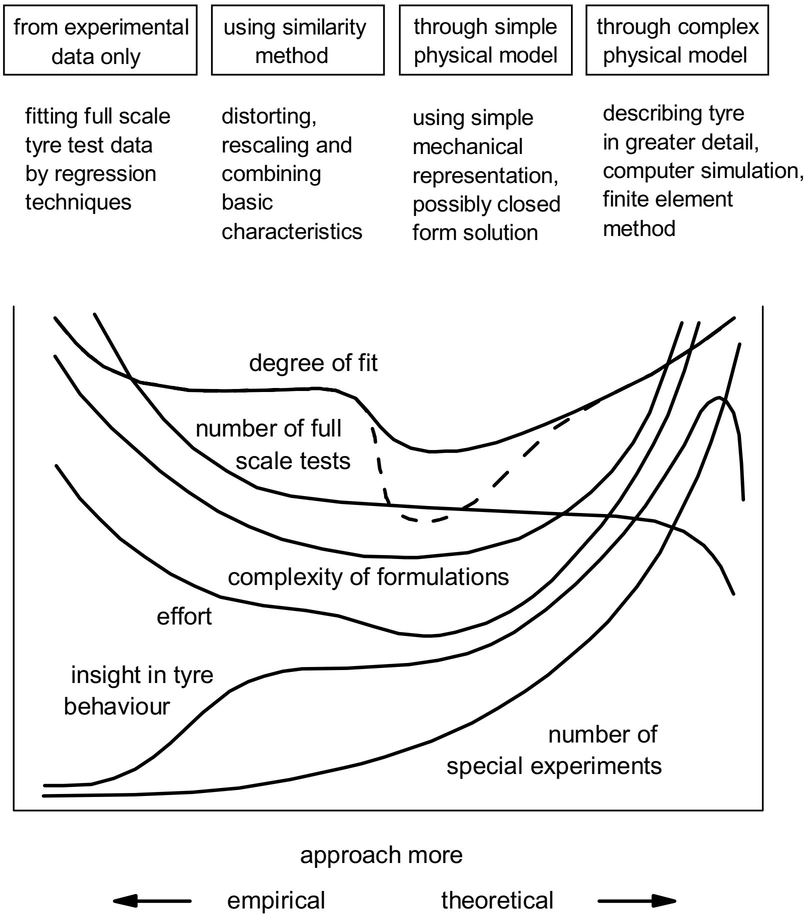

Figure 2.11: Types of tire modeling approaches [67].

Empirical tire models

Among empirical tire models, we can mention

- Developed by Pacejka [67], the Magic Formula tire model is a mathematical expression (see Eq.(2.7)) that describes tire handling characteristics as a function of parameters such as the slip ratio, applied force, slip angle, and camber angle.

$$y = D \cdot \sin(C \cdot \arctan[Bx - E \cdot (Bx - \arctan(Bx))]) \tag{2.7}$$

Where:

  - x is the independent variable (such as slip rate, applied force, etc.).
  - y is the dependent variable (representing force or moment).
  - B, C, D, and E are constants.

These constants are determined by fitting the formula to experimental data.

- Fiala tire model [68] represents the tire belt as a thin circular disk in a single point contact with the road surface. This model is defined in terms of three formulas that describe tire force/moment as a function of the slip rate, slip angle, vertical applied force, and the friction coefficient.

These models are constructed using experimental data from real tire tests. Although these models offer simplicity and computational efficiency, they also have limitations in terms of accuracy and the need for extensive experimental data. Furthermore, structural analysis, modal vibration, or transient analysis can not be investigated with these models.

Semi-empirical tire models

For the sake of tackling the lack of physical considerations in empirical models,semi-empirical models were developed. Among these models, we can mention:

- The Brush Tire Model [69] is used in vehicle dynamics to analyse tire steady state rolling. In this model, a series of flexible bristles is used to model tire tread. These bristles are attached to a rigid carcass. An illustration of this model is shown in Figure 2.12.

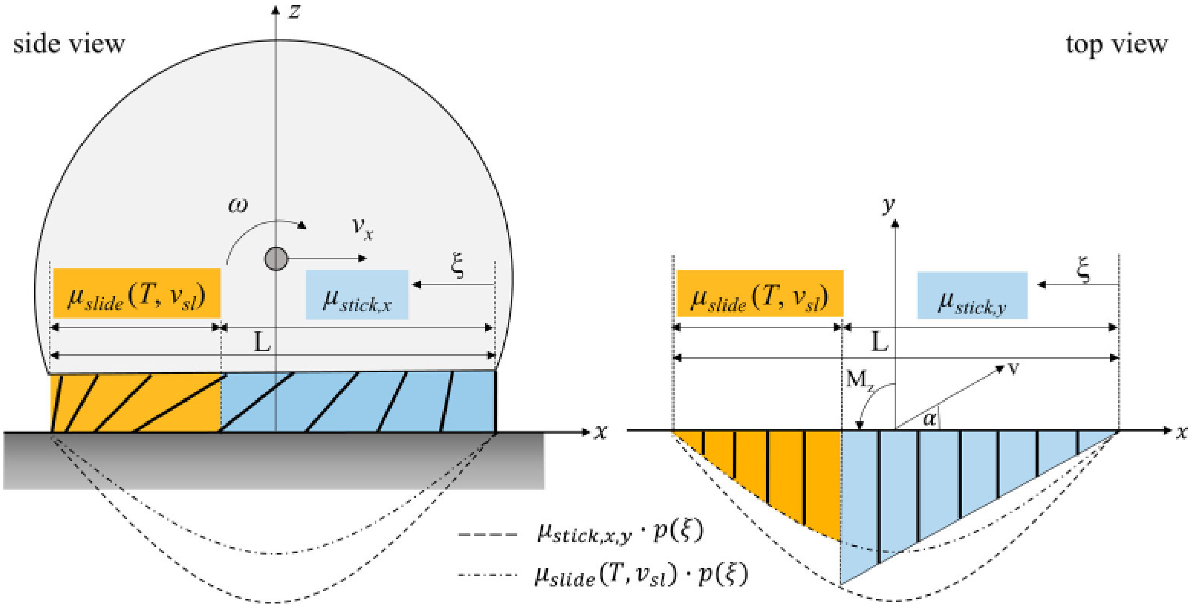

Figure 2.12: Brush model [70].

- The brush-string model [67] is an enhancement of the original brush tire model. This improved model incorporates string elements to account for the stiffness of the tire carcass belt. It was developed to improve the contact patch and to analyze local deformation during lateral maneuvers and combined slip.

- The rigid ring model [71] models tire tread as a rigid ring and sidewall with a combination of springs and dashpots. Tire slip is accounted for using an elastic spring.

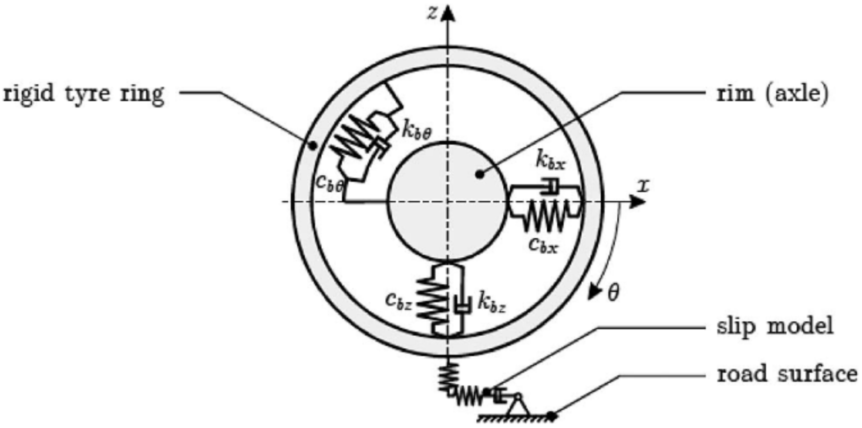

Figure 2.13: Rigid ring model [72].

- Unlike the rigid ring tire model, the Flexible Ring Tire Model [73] proposes a model with deformable tread represented with elastic springs.

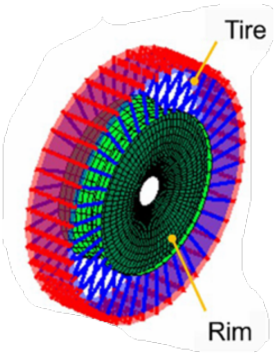

Figure 2.14: Flexible ring tire model [74].

- Lopez et al. [75] proposed a semi-analytical approach to derive Green's functions for simulating the vibration and acoustic emission of a rotating tire with a noise up to 500 Hz. Basically, considering a linear elastic model, a homogeneous tire cross-section, and a frictionless road surface, the FE method is employed to compute the eigenvalues and eigenvectors. Subsequently, tire impulse response or Green's function is derived using the eigenfunction expansion method.

Theoretical tire models

Theoretical tire models are highly regarded for their precision and ability to address intricate physical challenges. With the aid of numerical methods like the Finite Element Method (FEM), extensive research has been carried out, incorporating more realistic factors. Below, we highlight some noteworthy studies in this area.

- Noor et al. [76] proposed possible shell-based linear elastic orthotropic and anisotropic models exploiting tire axisymmetry for fast computation. This model does not take into account material nonlinearities and only treats static loads.

- Shokouhfar et al. [77] proposed a simplified tire model with a shell element with homogenized linear elastic and orthotropic (reinforced belt) law. This model was validated under a static load and used for steady-state rolling.

- Shida et al. [78] studied the rolling resistance of a tire using static finite element analysis. In their model, the rubber components were represented as brick elements with linear elastic material properties, while the rubber layers with reinforcements were treated as a homogenized linear elastic material. The axial loads applied in this study were purely static.

- Burke and Olatunbosun [79] laid down a good theoretical framework for modeling static tire-road interaction. A gap element-based formulation was selected to suitably model the contact. The obtained Numerical results showed a good agreement with the numerical ones calculated in the FE commercial software MSC/NASTRAN.

- Alkan et al. [80] investigated a static tire model with hyperelastic rubber compounds and linear isotropic laminate layers. This model was experimentally validated in four scenarios: on a flat surface, on a flat surface with a rectangular cleat, on a flat surface with a circular cleat, and on a flat surface with a triangular cleat.

- Relying also on a hyperelastic material model of type Money-Rivlin, Golbakhshi and Namjoo [81] appraised the effect of air inflation pressure, speed, and temperature on tire rolling resistance. Also, the dependence of the rolling resistance on the axial load was studied. During the footprint analysis, the static load is applied in a ramp manner.

- Phromjan and Suvanjumrat [82] studied the effect of belt layers (number and position) on the performance and stiffness of non-pneumatic tires using Finite Element Analysis. A visco-hyperelastic material model was used to fit the experimental data of the tested specimen extracted in the tire.

- Mohsenimanesh et al. [83] constructed a truck tire model (with nearly linear elastic rubber compounds and orthotropic reinforced layers) to analyze off-road tire-road static interaction.

- Fontaine et al. [84] incorporated linear orthotropic belt layers in their tire model with hyperelastic (Money-Rivlin) rubber compounds and a linear elastic steel belt layer. This model was evaluated under static load.

- Wei and Olatunbosun [46] proposed a dynamic explicit model for predicting tire cornering performance and relaxation length at a constant slip angle in rolling conditions. The rubber components are modeled using visco-hyperelastic material, while the reinforcements have linear elastic properties.

- Tielking [85] created a shell model intended to predict the influence of design variables such as nylon and polyester properties on the deformation of a four-ply bias tire under vertical load.

- A few years later, Noor [86] introduced two shell-based nonlinear tire strategies, in axisymmetry and 3D, with contact constraints enforced using the perturbed Lagrange method. This strategy showed satisfying results in predicting both the mechanical and thermal response in tire-pavement interaction with friction.

Another advantage of FEM is its capability to deal with very impact or crash tests. For instance,

- Baranowski and Malachowski [87] developed a numerical model to study a tire from a military vehicle that is subjected to a mine blast. The carcass belt was modeled using a linear orthotropic material law, while the steel cords were represented as truss elements incorporating a simplified version of the Johnson-Cook (JC) model. Additionally, the rubber was modeled with brick elements using the Ogden material law.

- Baranowski et al. [88] designed a tire model and an experimental validation process for assessing tire quasi-static and dynamic response under tread blast and free drop. In this work, Ogden's material law is utilized for the rubber components, while the cords are modeled using a simplified Johnson-Cook (JC) model that accounts for isotropic hardening and strain rate effects. Regarding the topology, the cords are represented as truss elements, whereas the rubber components are meshed using linear brick elements. In terms of loads, the static test was performed under a monotonic load.

- Based on the same model, the same authors [89] proposed a dynamic explicit model for modeling tire blast loading, considering the so-called Simplified Rubber Material (SRM) model for rubber (meshed with C3H8RH) and simplified Johnson-Cook reinforcements (meshed with truss elements). They adopted the penalty approach developed by Abu-Odeh [90] and implemented by Hallquist [91] in LS-DYNA [92] to constrain reinforcements (steel and textile wires) to remain in their rubber layers.

  Apart from thermo-mechanical analysis, the FE method also enables to perform acoustic analysis as extensively studied by many authors Cho et al. [93]. Rafei et al. [62]

suggested a frictional and temperature-dependent FE tire model to evaluate tire handling characteristics such as cornering and aligning properties.

Kuraishi et al. [94] recently introduced a new CFD model called ST-SI-TC-IGA (Space-Time Slip Interface Topology Change Isogeometric Analysis) for investigating with high accuracy and reasonable computational cost, tire aerodynamics while rolling on a rough road covered with a fluid film.

In summary, we have extracted key notes regarding material properties, load types, and the purpose of the study from the literature review. In Table 2.1 are reported the important comments that have oriented this work.

Table 2.1: Comparison of selected FEA Tire Models.

FEA tire model	**Topic**	**Topology and material constitutive laws**	**Observations**
Burke and Olatunbosun [79]	Static analysis	Linear elastic shell composite elements	- No monotonic load. -No rubber visco-hyperelasticity.
Shida et al. [78]	Rolling resistance	Laminate shell elements with linear viscoelastic behavior.	- No dynamic test. - No rubber hyperelasticity. -Static load.
Alkan et al. [80]	tire rolling(with and without cleat)	Hyperelastic rubber and linear elastic shell (belt).	-No rubber viscoelasticity. - No monotonic load. -No dynamic test.
Golbabakhshi and Naimi, 2015	rolling resistance	Hyperelastic and linear orthotropic shell elements (belts.	-No rubber viscoelasticity. -Constant load -No dynamic test.
Krmela and Krmelova [95]	Static analysis	Mooney-Rivlin hyperelastic with and without orthotropic reinforcing layers (shell elements)	-No rubber viscoelasticity. - No monotonic load. No dynamic test.
Ali [96]	static/rolling analysis	Visco-hyperelastic and linear elastic shell (belt).	- No monotonic load. -No dynamic test.
Shokouhfar et al. [77]	static/steady state rolling	linear elastic rubber and orthotropic belt	-No, rubber visco-hyperelasticity. -No, dynamic test. -No monotonic load.
Golbakhshi and Namjoo [81]	rolling resistance	Hyperelastic-Money Rivlin linear elastic shell belt	-No dynamic test. - No viscoelasticity. -Monotonic load.
Phromjan and Suvanjumrat [82]	rolling resistance	visco-hyperelastic rubber linear elastic shell belt.	-No monotonic load. -No dynamic test.
Fontaine et al. [84]	rolling resistance	Hyperelastic rubber orthotropic belt	-No monotonic load. -No dynamic test. -No viscoelasticity.

2.4 Research gap

While a commensurable number of material constitutive laws are in the literature, as reviewed above, rubber compounds' contribution is approximated as linear, hyperelastic, or visco-hyperelastic. However, we note from the brief review of experimental cyclic tests of rubber that the dynamic response of rubber components shows a more complex constitutive law: **visco-hyperelastic with Mullins effect**. This behavior drives tire response when exposed to low-, medium-, and high-frequency loadings or operating scenarios. Thus, the realistic response of tires in rolling, cornering, and braking scenarios heavily depends on the damping contribution of materials' constitutive laws for absorbing various sources of excitations resulting from the weight of the vehicle and occupants, as well as shocks due to contact with road obstacles and asperities.

As highlighted in the literature review, existing research on mechanical modeling of tires considers only a monotonic applied force. However, in a real use scenario, tires are exposed to dynamic loads. When fluctuating loads (dynamic loads) are concerned, the consistency of the model requires the use of material parameters obtained from the cyclic test of tire components. Since we observe that experimentally, in dynamic loading, tire compounds such as rubber exhibit a constitutive response of type visco-hyperelastic with Mullins damage. Therefore, the purpose of this thesis is to address these limitations. That is to say, to **propose a FEM-based model for simulating tires under dynamic loads**. Such *a model takes into account the dynamic properties of the tire components and allows for accurate simulation of tires under dynamic loads.*

2.5 Benefits of the proposed model

By coupling the potential of the Finite Element Method (FEM) with recent advances in material parameter identification, computational mechanics, and available simulation tools (ABAQUS® [38], MATLAB®[97], and PYTHON[98]), the proposed model is based entirely on physics-driven consideration. The main targeted benefits of the proposed model are as follows:

- **Consistency and accuracy of the material models**: The constitutive laws considered for the constituent materials of the tire elements are driven by the assessment of experimental data collected during tests on the elements extracted from the tires and a review of recent material parameters identification schemes in the literature. As a result, they capture the response of each element as accurately as possible within the validation constraints set during the calibration phase;

- **Toward realistic holistic vehicle simulation**: Although complex and computer resource-demanding, holistic modeling is the most effective technique automakers use to design, analyze, and test their prototype vehicles during the design and testing phases. Because of its integrative nature, each vehicle's system is represented by a module responsible for reproducing its response as faithfully as possible. In this regard, the current model can be integrated to simulate tire response.

- **General applicability**: Even though the field of study of tires in this thesis is limited to passenger vehicle tires, the application of the model remains the same for other tire classes (for light and heavy trucks, aircraft, tanks, etc.). Since the major difference lies in the geometry, the casing structure and the chemical composition of rubber compounds;
- **Cost efficiency**: The consistent procedure for identifying material parameters adopted here condenses material testing requirements to a single cyclic tensile test, in contrast to the ordinary procedure in the literature, which requires three types of tests for rubber compound characterization. The result is a significant gain in cost, computational effort, and reliability of material response.
- **Adaptability**: Given the perpetual need to improve tire design and performance in a rapidly changing global context, it is useful to have an adaptable approach that can evolve with new or future tire designs in terms of geometry and material constituents. Therefore, it makes it easy to add new material constitutive laws, new simulation techniques or new physical principles (acoustic, thermal, etc.) and improve the model for continuous innovation and development in the field.

The proposed model can be utilized in future work to validate the experimental works in tire acoustics and thermomechanics, such as the one conducted by Hu et al. [99] on acoustic resonance noise in the tire-rim under different inflation pressures.

3 Kinematics and mechanical properties of tire materials

An effective and objective approach to gaining a deeper understanding of the tire as a whole necessitates a certain knowledge and understanding of the constitutive laws of the components involved, as well as how they all interact to give the tire characteristics and performance observed under operating conditions. Thereby, in this chapter, possible constitutive laws of tire compounds are presented and outlined with the aim of capturing appropriate behavior that combines a good balance between accuracy and computational cost for each of the tire's components.

3.1 Kinematics:

In the following, let us consider a continuum body that initially (at $t = 0$) occupies the domain $\Omega_0 \subset \mathbb{R}^d{}_{|d\in\langle 1,\ 2,\ \ 3\rangle}$ in the reference configuration and $\Omega_t \subset \mathbb{R}^d{}_{|d\in\langle 1,\ 2,\ \ 3\rangle}$ in the current configuration as illustrated in Figure 3.1.
Where the reference configuration denoted by $\mathcal{R}_0 = (\overrightarrow{E_1}, \overrightarrow{E_2}, \overrightarrow{E_3})$ is chosen arbitrarily to provide the easiest possible description of the problem. A trivial choice is to set it as being identical to the physical space $\mathbb{R}^d{}_{|d\in\langle 1,\ 2,\ \ 3\rangle}$ with normal unit vectors $\overrightarrow{\imath}$, $\overrightarrow{\jmath}$ and $\overrightarrow{k}$. Thus before the body Ω_0 deforms, any material point $M \in \Omega_0$ is defined in $\mathcal{R}_0$ as follows

$$\begin{aligned} M : \Omega_0 &\longrightarrow \mathbb{R}^3 \\ M &\longmapsto \overrightarrow{X} \end{aligned} \tag{3.1}$$

Here $\overrightarrow{X}$ is called position vector of $M \in \Omega_0$ with respect to $\mathcal{R}_0$ and can be written in term of the basis vectors $\overrightarrow{E_1}, \overrightarrow{E_2}$ and $\overrightarrow{E_3}$ by

$$\overrightarrow{X}(M) = \sum_{i=1}^{d} X_i \overrightarrow{E_i},\ d \in \langle 1, 2, 3\rangle \tag{3.2}$$

For the sake of simplicity, we consider the convention of repeated indices of Einstein so we can write the eq. in a simpler form

$$\overrightarrow{X}(M) = X_i \overrightarrow{E_i}\ ,\ d \in \langle 1, 2, 3\rangle \tag{3.3}$$

When the body Ω_0 deforms, the reference configuration $\mathcal{R}_0$ is transformed into the current configuration $\mathcal{R}_t$, which is basically the configuration attached to the body Ω_t at any time $t > 0$ and defined by the orthonormal basis$(\overrightarrow{e_1}, \overrightarrow{e_2}, \overrightarrow{e_3})$. Then, any material point $M \in \Omega_t$ can be located with its position vector $\overrightarrow{x}\,(M)$ in $\mathcal{R}_t$ by the relation

$$\overrightarrow{x}\,(M) = \sum_{i=1}^{d} x_i \overrightarrow{e_i},\; d \in \langle 1, 2, 3 \rangle \tag{3.4}$$

Or simply

$$\overrightarrow{x} = x_i \overrightarrow{e_i},\; i \in \langle 1, 2, 3 \rangle \tag{3.5}$$

Lagrangian, Eulerian and Arbitrary Lagrangian-Eulerian (ALE) configurations:

We define the mapping $\overrightarrow{\varphi}$ (see Figure 3.1) that links the position of $\forall\, M_0 \in \Omega_0$ in the reference configuration to its position M_t in the current configuration as follows

$$\begin{aligned} \overrightarrow{\varphi} : \Omega_t \times [0, \mathrm{T}] \;&\longrightarrow \mathbb{R}^3 \\ \overrightarrow{X} \longmapsto \overrightarrow{x} &= \overrightarrow{\varphi}(\overrightarrow{X}, t) \end{aligned} \tag{3.6}$$

It should be noted that $\overrightarrow{\varphi}$ is bijective such that its inverse exists and is unique. From the sketch in Figure 3.1, we can decompose the vector $\overrightarrow{x}$ in the sum of $\overrightarrow{X}$ and the displacement vector $\overrightarrow{u} \in \mathbb{R}^d{}_{|d \in \langle 1,\ 2,\ \ 3 \rangle}$ as follows

$$\begin{aligned} \overrightarrow{x} = \overrightarrow{\varphi}(\overrightarrow{X}, t) &= \overrightarrow{X} + \overrightarrow{u}(\overrightarrow{X}, t) \\ \overrightarrow{X} &= \overrightarrow{\varphi}^{-1}(\overrightarrow{x}) \end{aligned} \tag{3.7}$$

In Eq. (3.6), the definition of $\overrightarrow{x}$ as a function of $\overrightarrow{X}$ is referred to as the Eulerian description, while the inverse is called to the Lagrangian description. In both the reference and current configuration, we can write out $\overrightarrow{u}$ in terms of basis components

$$\overrightarrow{u} = u_i \overrightarrow{E_i} = u_i \overrightarrow{e_i} \tag{3.8}$$

Where with emphasize that u_i and u_i are the components of $\overrightarrow{u}$ in $\mathcal{R}_0$ and $\mathcal{R}_t$, respectively.
From now on, we adopt space vector convention for the notation of vectors without arrows (e.g., E_i instead of $\overrightarrow{E}_i$) so that

$$x = \varphi\,(X, t) = X + u(X, t) \tag{3.9}$$

When deformation is very large, like in hyperelastic materials, it is more convenient to use the so-called Arbitrary Lagrange-Eulerian(ALE) configuration to circumvent mesh distortion issues. Thus, a composition can be set as illustrated in Figure 3.1.

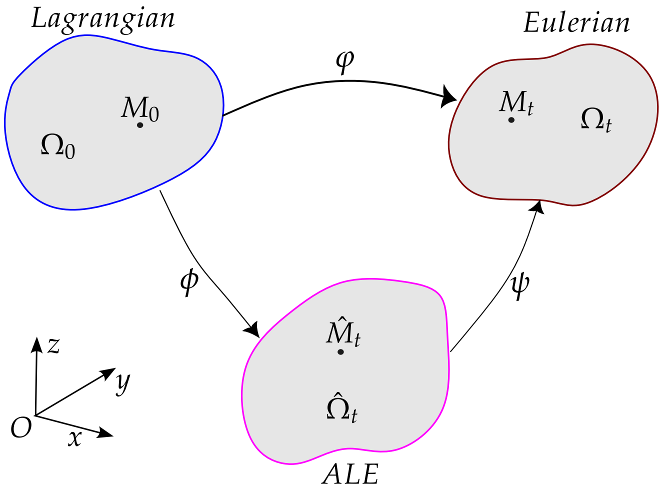

Figure 3.1: Lagrangian, Eulerian and Arbitrary Lagrangian-Eulerian(ALE) configurations.

Deformation measures:

Let us now, define the deformation gradient $F \in \mathcal{M}^{d \times d}$ by deriving φ with respect to X

$$\begin{gathered} F = \frac{\partial \varphi}{\partial X} = \frac{\partial}{\partial X}\left(X + u\left(X, t\right)\right) \\ F = \boldsymbol{I} + \nabla_X u \quad or \quad F_{\imath J} = \delta_{\imath J} + u_{\imath, J} \end{gathered} \tag{3.10}$$

Where indices that follow a comma stand for space derivative with respect to X. $\boldsymbol{I}$ is the identity matrix associated with the basis$(\overrightarrow{E_1}, \overrightarrow{E_2}, \overrightarrow{E_3})$, $\delta_{\imath J} = \begin{cases} 1 \text{ if } \imath = J \\ 0 \text{ otherwise } \imath \neq J \end{cases}$ is the Kronecker delta symbol and $\nabla_X u = \dfrac{\partial u}{\partial X}$ is the gradient of displacement field u with respect to the reference configuration. It should be also noted that lowercase indices (i.e. $\imath, \jmath \in \{1, \ldots, d\}$) live in the current configuration whereas uppercase indices (i.e. $\mathrm{I}, \mathrm{J} \in \{1, \ldots, d\}$) in the reference configuration $\mathcal{R}_0$ and $\mathcal{R}_t$, which is very useful for eulerian description. Another stability condition to be verified by F to hold is to satisfy

$$\forall F \mid F \in \mathcal{M}^{d \times d},\ det\left(F\right) > 0 \tag{3.11}$$

Particularly, when there is no deformation, F must verify $F = \boldsymbol{I}$, which is a rigid body (J=$det\left(F\right) = 1$). As a consequence, we introduce J the Jacobean of the transformation, which measures the proportion of volume change of the body under the bijection φ and is obtained by the formula

$$J = det\left(F\right),\ F \in \mathcal{M}^{d \times d} \tag{3.12}$$

With F at hand and using the chain rule, we can derive transport formulas in Table 3.1

Table 3.1: Transport formulas

Names	**Transport formula**
Vector transport	$dx = F\ dX$
Surface transport	$ds = J\ F^{-T} dS$
Volume transport	$dv = J\ dV$

Given that deformations that structures undergo need to be quantitively measured, it is more practical to have an expression that expresses the deformations in terms of metrics. This is achieved by calculating the right Cauchy Green deformation tensor C through the formula

$$C = F^T F \quad \text{or} \quad C_{ij} = F_{Ki} F_{jK} \tag{3.13}$$

Then with respect to the reference configuration, we define the Green-Lagrange strain tensor E by the following

$$\mathrm{E} = \frac{1}{2}(\nabla_X u +^T \nabla_X u + \nabla_X u^T \nabla_X u) = \frac{1}{2}(C - I) \tag{3.14}$$

Apart from the definition of the strain tensor from Eq. (3.14), many others exist in the literature [100], and we report in Table 3.2 only the most frequently used.

Table 3.2: A family of strain tensors

Name of the strain tensor	**Expression**
Green-Lagrange strain	$\mathrm{E} = \frac{1}{2}(C - I)$
Logarithmic Lagrange strain	$\mathrm{E} = \frac{1}{2}\ln(C)$
Seth–Hill strain family	$\mathrm{E}^{(\mathfrak{n})} = \frac{1}{2\mathfrak{n}}\left(U^{2\mathfrak{n}} - \mathrm{I}\right), \mathfrak{n} \in \mathbb{N}^+$
Power strain family	$\mathrm{E}^{(\mathfrak{n})} = \frac{1}{\mathfrak{n}+\mathfrak{m}}\left(U^{\mathfrak{m}} - U^{-\mathfrak{n}}\right), \mathfrak{n}, \mathfrak{m} \in \mathbb{N}^+$

Where U is the right stretch tensor, obtained from the polar decomposition of F (ie. $F = RU$). $\mathbb{N}^+$ is the set of natural numbers.

A variety of stress measures:

Under certain prescribed boundary conditions, applied external forces/moments generate internal forces/moments that cause material displacements, resulting in deformations which spontaneously induce stresses in any representative volume of the body. Conversely, applied stresses in turn cause the material to react and deform, creating a feedback loop that further affects the body's response to its external environment.

The flowchart in Fig highlights the duality that exists at any point $M \in \Omega_t$ between the stress and the strain in any chosen RVE. Consequently, any change in stress results in a change in strain and vice versa. In fact, the material's response at any given time during the loading/unloading course is governed by the stress-strain relationship, also known as *constitutive laws*. Several constitutive behaviors for different material responses exist in the literature and range from reversible to irreversible depending on the hypothesis of small deformations or large deformations with either small or large rotations. It is important to emphasize that this section does not include all the constitutive laws in the literature but focuses only on those concerned with materials involved in tire structure.

Before jumping into constitutive laws, we need to define stress and strain. In the current configuration, the Cauchy stress tensor σ is fully described in terms of its 9 components of which 3 are normal components (σ_{xx}, σ_{yy} and σ_{zz}) and 6 are shear components ($\sigma_{xy}, \sigma_{yx}, \sigma_{xz}, \sigma_{zx}, \sigma_{yz}$ and σ_{zy}). In terms of these components, the matricial representation of σ reads as follows

$$\sigma = \begin{bmatrix} \sigma_{xx} & \sigma_{xy} & \sigma_{xz} \\ \sigma_{yx} & \sigma_{yy} & \sigma_{yz} \\ \sigma_{zx} & \sigma_{zy} & \sigma_{zz} \end{bmatrix} \tag{3.15}$$

Where shear components $\{\sigma_{ij}\}_{i \neq j = x,y,z}$ are usually referred to as $\{\tau_{ij}\}_{i \neq j = x,y,z}$. Each column of σ stands for the components of the stress state in the directions of the basis (O, x, y, z). For further details about this kinematics, the reader is referred to [100], [101], [102]. In addition to the Cauchy stress tensor, many other definitions exist depending on the configuration where the force and the area of action are expressed. Furthermore, these definitions are essential and are employed for deriving the variational formulation of the boundary value problems in a given configuration. In that regard, Table 3.3 summarizes the expression of the other definitions of stress tensors.

Table 3.3: A family of stress tensors.

Stress	**formula**	**Definition**
Piola–Kirchhoff stress tensor $\boldsymbol{\mathcal{T}}$	$\mathcal{T} = J\sigma$	$\equiv \frac{(\mathcal{F})_{\mathcal{R}_t}}{(\mathcal{A})_{\mathcal{R}_t}}$
First Piola–Kirchhoff stress tensor $\boldsymbol{P}$	$P = J\sigma F^{-T}$	$\equiv \frac{(\mathcal{F})_{\mathcal{R}_t}}{(\mathcal{A})_{\mathcal{R}_0}}$
Second Piola–Kirchhoff stress tensor $\boldsymbol{S}$	$S = F^{-1}\sigma F^{-T}$	$\equiv \frac{(\mathcal{F})_{\mathcal{R}_0}}{(\mathcal{A})_{\mathcal{R}_0}}$
Nominal stress tensor $\boldsymbol{N}$	$N = P^T$	$\equiv \frac{(\mathcal{F})_{\mathcal{R}_t}}{(\mathcal{A})_{\mathcal{R}_0}}$

Where the expression $P \equiv \dfrac{(\mathcal{F})_{\mathcal{R}_0}}{(\mathcal{A})_{\mathcal{R}_0}}$ means that the targeted tensor relates a force in the spatial configuration $\mathcal{R}_t$ to an area $\mathcal{A}$ in the reference configuration $\mathcal{R}_0$ and so on for other tensors (S, $\mathcal{T}$ and N).

3.2 Material constitutive models

3.2.1 In small strain

Linear elasticity

In the hypothesis of infinitesimal strain, the second order term $\frac{1}{2}\nabla_X u^T \nabla_X u$ from eq. of the Green-Lagrange tensor E can be neglected such that E reduces to the small strain tensor ε.

$$\varepsilon = \frac{1}{2}(\nabla_X u + \nabla_X u^T) \tag{3.16}$$

Where we recall that ε has three normal components (ε_{xx}, ε_{yy} and ε_{zz}) and six shear components ($\varepsilon_{xy}, \varepsilon_{yx}, \varepsilon_{xz}, \varepsilon_{zx}, \varepsilon_{yz}$ and ε_{zy}) organized in the matricial form as

$$\varepsilon = \begin{bmatrix} \varepsilon_{xx} & \varepsilon_{xy} & \varepsilon_{xz} \\ \varepsilon_{yx} & \varepsilon_{yy} & \varepsilon_{yz} \\ \varepsilon_{zx} & \varepsilon_{zy} & \varepsilon_{zz} \end{bmatrix} \tag{3.17}$$

Since ε and σ are symmetric tensors, it is possible to reduce their order with fewer number of components using Voight notation as follows

$$\left\{ \begin{array}{l} \{\varepsilon\} = \left(\varepsilon_{xx}, \varepsilon_{yy}, \varepsilon_{zz}, \varepsilon_{yz}, \varepsilon_{xz}, \varepsilon_{xy}\right)^T \\ \{\sigma\} = \left(\sigma_{xx}, \sigma_{yy}, \sigma_{zz}, \sigma_{yz}, \sigma_{xz}, \sigma_{xy}\right)^T \end{array} \right. \tag{3.18}$$

In order to get an insight into the real nature of the effects of loads in the matter, it is a common practice to decompose the stress tensor in its volumetric and deviatoric parts. The idea behind this transformation is justified by the fact that the failure in some materials is driven by either the volumetric changes or excessive shear (for instance, in elastoplastic materials). By definition, the deviatoric and volumetric components of a nth-order tensor A is given by the linear mappings $\wp_{sph}$ and $\wp_{dev}$ such that

$$\left\{ \begin{array}{l} A^{sph} = \wp_{sph} : A \\ A^{dev} = \wp_{dev} : A \end{array} \right. \tag{3.19}$$

Where the symbol : is the double inner product and the $2 * n^{th}$-order tensors ($\wp_{sph}$ and $\wp_{dev}$) are formulated in terms of the second-order unit tensor I and the fourth-order unit tensor II, associated with the basis $(\overrightarrow{e_1}, \overrightarrow{e_2}, \overrightarrow{e_3})$

$$\left\{ \begin{array}{r} \wp_{sph} = \dfrac{1}{n} I \odot I \\ \wp_{dev} = II - \dfrac{1}{n} \mathbf{I} \odot I \end{array} \right. \tag{3.20}$$

$\wp_{sph}$ and $\wp_{dev}$ are called the spherical and deviatoric projection tensors, respectively. Replacing these two expressions in Eq. (3.20) leads to

$$\left\{ \begin{array}{r} A^{sph} = \dfrac{1}{n} tr\left(A\right) I \\ A^{dev} = A - \dfrac{1}{n} tr\left(A\right) I \end{array} \right. \tag{3.21}$$

So for $A = \sigma$, with the help of the equality $\sigma = II : \sigma$, the decomposition of the Cauchy Stress tensor reads as

$$\left\{ \begin{array}{r} \sigma^{sph} = \dfrac{1}{3} tr\left(\sigma\right) I \\ \sigma^{dev} = \sigma - \dfrac{1}{3} tr\left(\sigma\right) I \end{array} \right. \tag{3.22}$$

Where σ^{sph} and σ^{dev} are also called hydrostatic or volumetric stress tensor and isochoric stress tensors, respectively. This same decomposition can be applied to the strain tensor and material tensor to find out the contribution of their volumetric and isochoric components.

Isotropic elastic materials: Mechanical properties of such materials are the same at any point $M \in \Omega_t$, in all the direction of space (isotropy) and the stress state remains linearly related to the strain state

$$\sigma = \overline{\overline{\mathcal{C}}} : \varepsilon \ \text{ or } \varepsilon = \overline{\overline{\mathcal{D}}} : \sigma \tag{3.23}$$

Where $\overline{\overline{\mathcal{C}}}$ and $\overline{\overline{\mathcal{D}}}$ are material tensor and the compliance tensor, respectively. The former and the latter are fourth-order tensors with 9x9 components. In Voight notation, this equation reads as

$$\{\sigma\} = \mathcal{C}\,\{\varepsilon\} \ \text{ or } \{\varepsilon\} = \mathcal{D}\,\{\sigma\} \tag{3.24}$$

Where $\{\sigma\}$ is Cauchy stress or true stress vector, $\{\varepsilon\}$ is the strain vector, $\mathcal{C}$ is the material tensor and $\mathcal{D}$ the complicance tensor. Due to the linear isotropy and homogeneity of the media, material and compliance tensors ($\overline{\overline{\mathbb{C}}}$ and $\overline{\overline{\mathcal{D}}}$) described in eq. we end up in 3D with only 12 components, so they can be reduced to two-order tensors ($\mathcal{C}$ and $\mathcal{D}$) in Voight notation.

$$\mathcal{D} = \begin{bmatrix} 1/E & -\nu/E & -\nu/E & 0 & 0 & 0 \\ -\nu/E & 1/E & -\nu/E & 0 & 0 & 0 \\ -\nu/E & -\nu/E & 1/E & 0 & 0 & 0 \\ 0 & 0 & 0 & 1/2G & 0 & 0 \\ 0 & 0 & 0 & 0 & 1/2G & 0 \\ 0 & 0 & 0 & 0 & 0 & 1/2G \end{bmatrix} \tag{3.25}$$

Wherein, $\lambda = \dfrac{E\nu}{(1-2\nu)(1+\nu)}$ and $G = \dfrac{E}{2(1+\nu)}$ are Lamé's first parameter and shear modulus, respectively. It is worth noting that the definition of this constitutive law is based entirely on the determination of two parameters, namely the Young's modulus E and Poisson's ratio ν, which are commonly obtained via simple tests like tensile or compression tests.

Transversely isotropic materials: As shown in fig., the mechanical properties of such materials are characterized by symmetry with respect to a chosen direction that is orthogonal to the plane of the material's isotropy. The material responds differently in the direction of isotropy than it does in the other two orthogonal directions as a result of this oriented local anisotropy. Therefore, two distinct Young modulus and Poisson's ratio are needed to fully characterize the model. Let us assume that $\overrightarrow{e_1}$ is the direction of isotropy, so we have $E_1 \neq E_2 = E_3$ and

$\nu_{23} \neq \nu_{12} = \nu_{13}$ making that

$$\mathcal{D} = \begin{bmatrix} 1/E_1 & -\nu_{12}/E_1 & -\nu_{12}/E_1 & 0 & 0 & 0 \\ -\nu_{12}/E_1 & 1/E_2 & -\nu_{23}/E_2 & 0 & 0 & 0 \\ -\nu_{12}/E_1 & -\nu_{23}/E_2 & 1/E_2 & 0 & 0 & 0 \\ 0 & 0 & 0 & 1/G_{23} & 0 & 0 \\ 0 & 0 & 0 & 0 & 1/G_{12} & 0 \\ 0 & 0 & 0 & 0 & 0 & 1/G_{12} \end{bmatrix} \tag{3.26}$$

Where $G_{ij} = \left.\frac{E_j}{2(1+\nu_{ij})}\right|_{i \neq j \in \{1,2,3\}}$ is the shear moduli in the plane (i, j).
This constitutive model is typically observed in composite materials in which a material A also called matrix, is unidirectional reinforced with stiffer material called fibers or reinforcements. In order to set this model, the material has to be tested at least in two directions:

- The direction of isotropy (by $\overrightarrow{e_1}$)
- and either with respect to $\overrightarrow{e_2}$ or $\overrightarrow{e_3}$

Orthotropic linear elastic materials: Due to the fact that this type of materials has at least two planes of isotropy or symmetry, the material response varies from one direction to the others depending on what direction you observe. Therefore, Young moduli and Poisson's ratios are all different in the three main directions ox, oy and oz; that is to say $E_1 \neq E_2 \neq E_3$ and $\nu_{23} \neq \nu_{12} \neq \nu_{13}$. The compliance tensor of such materials is given by

$$\mathcal{D} = \begin{bmatrix} 1/E_1 & -\nu_{21}/E_2 & -\nu_{31}/E_3 & 0 & 0 & 0 \\ -\nu_{12}/E_1 & 1/E_2 & -\nu_{32}/E_3 & 0 & 0 & 0 \\ -\nu_{13}/E_1 & -\nu_{23}/E_2 & 1/E_3 & 0 & 0 & 0 \\ 0 & 0 & 0 & 1/G_{23} & 0 & 0 \\ 0 & 0 & 0 & 0 & 1/G_{13} & 0 \\ 0 & 0 & 0 & 0 & 0 & 1/G_{12} \end{bmatrix} \tag{3.27}$$

Where $G_{ij} = \left.\frac{E_j}{2(1+\nu_{ij})}\right|_{i \neq j}$ is the shear moduli in the plane(i, j). Taking into account the fact that $\mathcal{D}$ has to be symmetric ($\mathcal{D}^T = \mathcal{D}$), three conditions have to be verified:

$$\frac{\nu_{12}}{E_1} = \frac{\nu_{21}}{E_2}, \quad \frac{\nu_{13}}{E_1} = \frac{\nu_{31}}{E_3}, \quad \frac{\nu_{23}}{E_2} = \frac{\nu_{32}}{E_3} \tag{3.28}$$

The construction of such a constitutive law requires to perform experimental tests with respect to all three main directions [103], which is sometimes very cost-consuming or even difficult to achieve for composites whose at least one dimension is very thin.

Linear viscoelasticity:

Under the effects of an external prescribed displacement/force, certain materials exhibit both an elastic and viscous response, which means that at any time $t \in [0, T]$, the stress state at any point $M \in \Omega_t$ is fully described in terms of both the strain and the strain rate; and vice versa. In order words, the stress/strain states in such media are time-dependent and do not immediately vanish after the external load or excitation is removed. As a result of this, irreversible phenomena occur and are revealed by a decrease in stress (stress relaxation), an increase in strain (creep), or a rise in temperature (hysteresis, etc...). Experimentally, this behavior can easily be put into evidence by analyzing the stress-strain curve of the specimen loaded in cyclic tension or cyclic compression. In such tests, the stress-strain dependence of both the loading and unloading course do not coincide (see Figure 3.2). This observation is a result of an activation of internal rearrangement of long molecular chains, which itself is a source of *dissipation*. Basically, the material adapts its molecular structure to accommodate the newly imposed excitation. The cause of this is hysteresis.

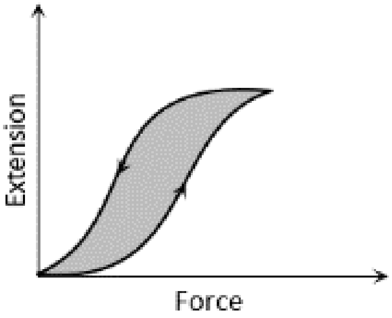

Figure 3.2: Typical hysteresis loop in a rubber material [104].

In virtue of the fact that the unloading path in the stress-strain curve is not identical to the loading path, more energy is needed to deform the material throughout the loading course than it is released mechanically during the unloading course. As a consequence, the energy of the inner part in the hysteresis loop [105] is not instantly released by the material at the end of the unloading but is rather converted and released by molecular friction as thermal energy: *hysteric losses*. Keeping in mind that rubber behavior is highly influenced by the temperature, this thermal energy impacts mechanical parameters by decreasing them [106], [107]. This phenomenon is more accentuated when the loading and unloading courses are done quickly and we therefore draw that the stress/strain state is heavily rate dependent. The characterization of the viscoelasticity of rubber compounds brings significant insight into understanding their damping properties under dynamic loads. Generally, rheological viscoelastic models are the most common choices for capturing both creep and stress relaxation of materials, which are two dual forms of viscoelasticity manifestations. Before all, we define stress relaxation and creep as follows

stress relaxation

The stress relaxation phenomenon is the observed decay in the stress state in materials under constant strain as illustrated in Figure 3.3. Basically, under a constant imposed field of strain applied (see Figure 3.3(a)) for some time, the material adapts itself at the molecular level through molecular chain rearrangements. Gradually, as the adaptation process evolves, the state of stress decreases (see Figure 3.3(b)) since the progressive changes in molecular arrangements confer the structure a better mobilization of all its molecular potential to withstand instabilities arising in the media.

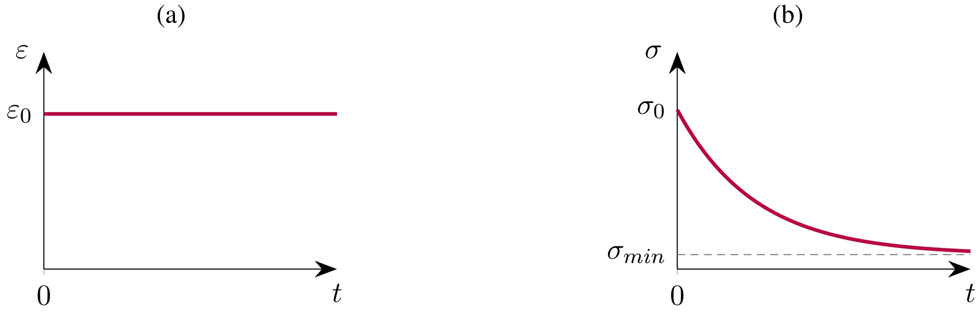

Figure 3.3: Stress relaxation. (a) applied constant strain ε_0, (b) stress response induced

However, the resulting molecular arrangements do not return to their original states once the imposed field of strain is removed. For instance, the physical evidence of this principle can be observed by considering a rubber band pulled from both ends and maintained for a certain time. When the considered time has elapsed, and the strain has been canceled, one can observe that the length has increased and does not instantly retake the initial dimensions. These effects are more pronounced when either the amount of the imposed strain increases or the application time is prolonged. If many levels of strain are applied as depicted in Figure 3.4(a), the material depicts a series of many portions with relaxation decay for each of the prescribed constant strain values as shown in Figure 3.4(b).

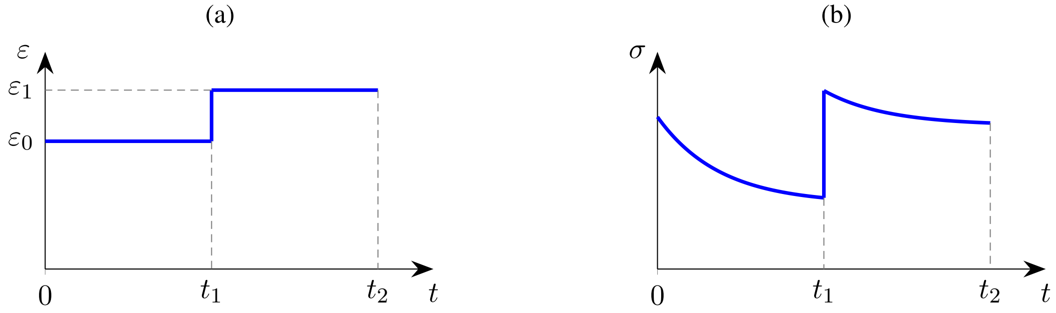

Figure 3.4: Stress relaxation. (a) applied constant strain ε_0, (b) stress response induced.

Creep:

The creep phenomenon illustrated in Figure 3.5 is basically defined as an increase in strain when the material is subjected to a constant field of stress or applied force over a certain time, as illustrated in Figure 5.4(b). Unlike stress relaxation, the strain state increases monotonically over time as long as the load is maintained. However, if the load/stress is indefinitely sustained, it would eventually increase and tend to a maximum value denoted ε_{max} as shown in Figure 5.4(c).

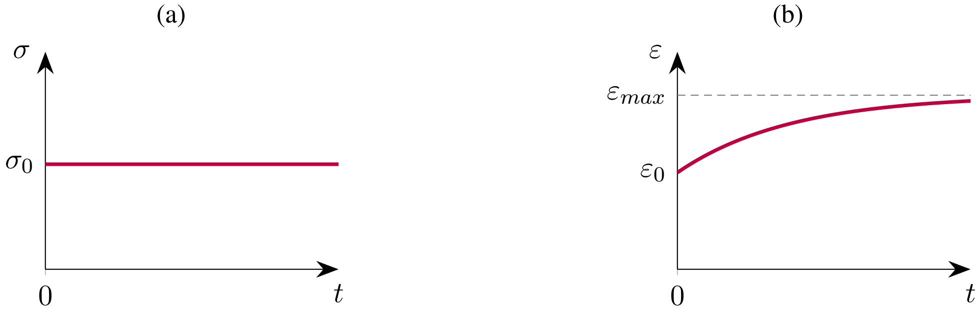

Figure 3.5: Creep process. (a) applied constant stress σ_0, (b) strain response induced.

Similarly, in the case of a series of prescribed constant stress or force, a piecewise smooth increase in strain is obtained as depicted in Figure 4.12.

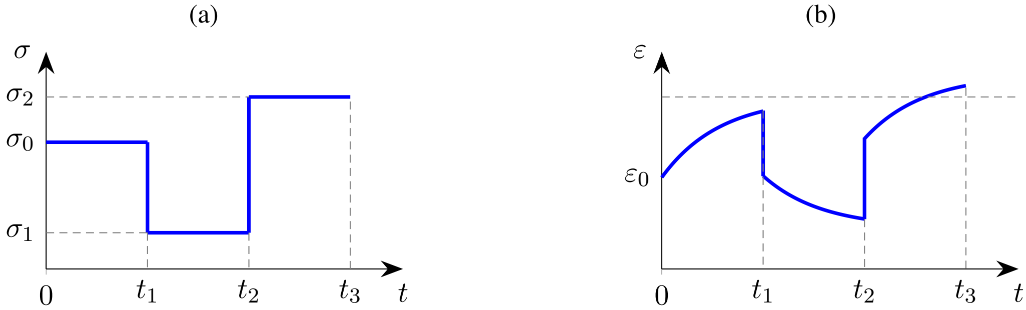

Figure 3.6: Multiple creep process. (a) series of applied constant stress ε_0, ε_0. (b) stress response induced.

In a dynamic load sequence, it is very common to encounter load sequences that can contain both creep and stress relaxation. Nonetheless, they cannot happen simultaneously. Owing to this fact, there is a transfer mapping that links both transformations and is often used to determine parameters of creep from stress relaxation data and vice versa, as we have discussed further in chap experimental.

In regards to these irreversible phenomena occurring in rubber-like materials under dynamic loads due to creep and relaxation, it is thereafter obvious to include corresponding dissipative terms in the general formulation of the problem, since internal damping of rubber materials, as well as temperature changes and friction contact, are one of the major sources of dissipation in tires' performances. Studying the contribution of these underlined phenomena becomes one of the milestones in building up a realistic dynamic response of tires. In order to fully describe the dissipation observed, one needs to define internal variables (from which the free energy function of the system stands) that can capture the evolution of the system from the thermodynamic point of view. Several rheological-based models have been utilized to model simple or relatively complex viscoelastic responses of materials. The main idea behind these rheological models is to combine one or more springs and one or more dashpots in series/parallel to mimic the response of the material as illustrated in Figure 3.7.

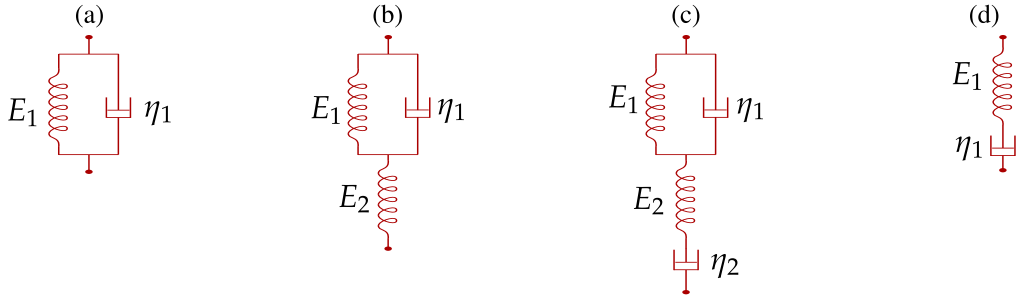

Figure 3.7: Simplest material rheological models. (a) Kevin model, (b) Kelvin-Voigt model, (c) Burgers model, (d) Maxwell model.

Besides the previous basic models, the so-called standard linear solid model (SLS) of Maxwell (see Figure 3.8) is the simplest complete rheological model and is made of a spring assembled in parallel with one internal spring in series with a dashpot portraying the dissipation. This model is the first simple choice that helps make a rough approximation of both creep and stress relaxation phenomena.

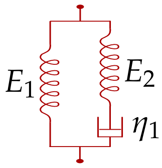

Figure 3.8: Standard Linear Solid (SLS) Maxwell model.

Constitutive law formulation:

Under the hypothesis of small strain and constant temperature, we consider the SLS model shown in Figure 3.8, where the parameter E_1 stands for the purely quasi-static elastic contribution in the strain energy density and E_2 for the internal parameter of the elastic perturbed portion and η is the viscosity of the material represented analogically as a viscous fluid. Recalling that the stress level in a spring component is given by the formula

$$\sigma_{elastic} = E\ \varepsilon_{elastic} \tag{3.29}$$

And the stress in the viscous component in terms of the rate of deformation and the viscosity through

$$\sigma_v = \eta \frac{d\varepsilon_v}{dt} \tag{3.30}$$

We can write the stress in each component of the model as

$$\sigma_1 = E_1\varepsilon_1, \quad \sigma_2 = E_2\varepsilon_2, \quad \sigma_v = \eta\frac{d\varepsilon_v}{dt} \tag{3.31}$$

In parallel, one has the following properties:

$$\begin{cases} \varepsilon = \varepsilon_1 = \varepsilon_2 + \varepsilon_v \\ \sigma = \sigma_1 + \sigma_2 \\ \sigma_2 = \sigma_v \end{cases} \tag{3.32}$$

Where σ and ε are the total stress and strain of the SLS model, respectively. Replacing the terms from Eq. (3.31) into Eq. (3.32), we get

$$\begin{cases} \varepsilon = \varepsilon_1 = \varepsilon_2 + \varepsilon_v & \text{(3.33a)} \\ \sigma = E_1\varepsilon_1 + \eta\dfrac{d\varepsilon_v}{dt} & \text{(3.33b)} \\ \sigma_2 = \sigma - \sigma_1 & \text{(3.33c)} \end{cases}$$

Then, applying time derivative to Eq. (3.33a), we obtain the time derivative of the viscous strain

$$\dot{\varepsilon}_v = \dot{\varepsilon} - \dot{\varepsilon}_2 = \dot{\varepsilon} - \frac{\dot{\sigma}_2}{E_2} \tag{3.34}$$

After replacing the expressions from Eq. (3.31) and Eq. (3.34) into Eq. (3.33) and simplifying so to have only σ and ε as variables, we obtain

$$E_1\varepsilon_1 + \eta\left[\dot{\varepsilon} - \frac{\dot{\sigma}_2}{E_2}\right] = E_1\varepsilon_1 + \eta\left[\dot{\varepsilon} - \frac{\dot{\sigma} - E_1\dot{\varepsilon}}{E_2}\right] \tag{3.35}$$

From Eq. (3.35), we rewrite everything in such a way that stress terms are moved to the left-hand side and the strain expressions on the right-hand side, we end up with the governing equation of the SLS model of Maxwell

$$\sigma + \frac{\eta}{E_2}\dot{\sigma} = E_1\varepsilon + \eta\left[1 + \frac{E_1}{E_2}\right]\dot{\varepsilon} \tag{3.36}$$

In the case of a stress relaxation test, a prescribed constant strain level ε_0 is applied to the specimen, and it implies that the second term of the right-hand side Eq. (3.36) vanishes and we can deduce the governing equation of stress relaxation

$$\sigma + \frac{\eta}{E_2}\dot{\sigma} = E_1\varepsilon_0 \tag{3.37}$$

Similarly, in the case of creep test, a prescribed constant stress σ_0 is applied. Thus Eq. (3.36) would be transformed into

$$\sigma_0 = E_1 \varepsilon + \eta \left[1 + \frac{E_1}{E_2} \right] \dot{\varepsilon} \tag{3.38}$$

Now, given that stress relaxation or creep progressively occurs in the material at different characteristic times instead of at a single time, one needs more branches with springs and dashpots in the SLS model to capture the response of the material as accurately as possible. This requirement is fulfilled with the model introduced by James Clerk Maxwell and E Wiechert [108] and is widely known as the *Generalized Maxwell model*, which takes into account the fact that stress relaxation or creep processes happen at different characteristic times [109]. Physically, this is explained by the fact that the size of molecular chains is not uniformly distributed, and neither are their properties.

Before going further, let us define Carson transform $\mathcal{L}$ [110] that maps a real-value function in time domain onto the Carson domain with parameter p

$$\mathcal{L} : \ \varphi(t) \longmapsto L\varphi' = \varphi^*(p) = p \int_0^{\infty} e^{-pt} \varphi(t) \, dt \tag{3.39}$$

With the properties

$$\begin{gathered}
\varphi \text{ is continuous in } \mathcal{D} \subset \mathbb{R} \\
\forall \, t < 0 \, , \ \varphi = 0 \\
\exists \, \vartheta > 0 \, , \left| e^{-\vartheta t} \varphi(t) \right| < 0 \\
(a * b')^* = a^* * b^* \\
\varepsilon^* = f^* \, \sigma^* \\
\sigma^* = g^* \, \varepsilon^* \\
f^* g^* = 1
\end{gathered} \tag{3.40}$$

Where $\sigma^*$and ε^* are Carson transform notations of stress and strain, respectively; f^* and g^* the associated transfer functions so that

$$\varepsilon = f \, \sigma \text{ and } \sigma = g \, \varepsilon \tag{3.41}$$

- Case of a purely elastic material with modulus E

$$\begin{gathered}
\varepsilon = \frac{1}{E}\sigma \ \rightarrow f = \frac{1}{E} \, y(t) \ \rightarrow f^* = \frac{1}{E} \\
g^* = \frac{1}{f^*} = E \rightarrow g = E \, y(t)
\end{gathered} \tag{3.42}$$

- Case of a purely linear viscous material with viscosity η

$$\begin{gathered}\dot{\varepsilon} = \frac{1}{\eta}\sigma \;\rightarrow \varepsilon = \frac{t}{\eta}\sigma \;\rightarrow\; f = \frac{t}{\eta}\, y\,(t) \;\rightarrow f^* = \frac{1}{\eta p} \\ g^* = \frac{1}{f^*} = \eta p \rightarrow g = \eta\delta\end{gathered} \tag{3.43}$$

In case of a disposition of elements in both parallel and series, the resulting transfer functions (g and f) are calculated by summing up

- In parallel

$$g = \sum_{i=1}^{Nb} g_i \tag{3.44}$$

- In series

$$f = \sum_{i=1}^{Nb} f_i \tag{3.45}$$

Having the expression of the transfer functions for each basic rheological model and knowing how to figure out the case with many rheological components, we can characterize the Generalized model of Maxwell depicted in Figure 3.9.

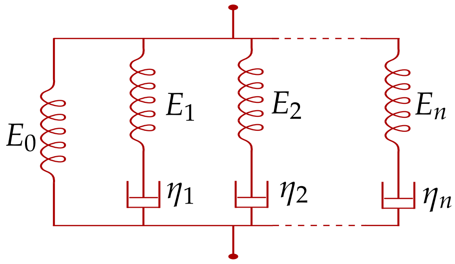

Figure 3.9: Generalize model of Maxwell.

In the first branch ($i = 0$), there is only the spring with parameter $E_0 = E_e$, therefore From Eq. (3.42), the transfer function ${g_0}^*$ of the branch is trivial

$${g_0}^*(p) = E_0 \tag{3.46}$$

As for others, there is a spring and a dashpot connected in series so in virtue of Eq. (3.42), (3.43) and (3.45), for each branch i $(1 \leq i \leq N,\ \mathrm{N\ number\ of\ internal\ branches})$ the corresponding transfer function ${f_i}^*$ in the Carson domain is given by

$${f_i}^*(p) = \frac{1}{E_i} + \frac{1}{\eta_i\, p} \quad \rightarrow\; {g_i}^*(p) = \frac{1}{f^*} = \left(\frac{1}{E_i} + \frac{1}{\eta_i\, p}\right)^{-1} \tag{3.47}$$

With aid of Eq. (3.44), the resulting transfer function g^* of all the branches is obtained

$$g^*(p) = {g_0}^* + \sum_1^N {g_i}^* = E_0 + \sum_1^N \left[\frac{\eta_i \, p \, E_i}{E_i + \ \eta_i \, p} \right] \tag{3.48}$$

At this stage, we need to determine the transfer function g in the time domain instead of in the Carson transform domain. We need for this purpose to rearrange the expression $g^*(p)$

$$g^*(p) = E_0 + \sum_1^N E_i \left[\frac{p}{\dfrac{E_i}{\eta_i} + p} \right] \tag{3.49}$$

This function is called the relaxation modulus of the model in the Carson transform domain and links the stress to the strain through the relation in Eq. (3.40). Writing the inverse transform of that expression leads to

$$\begin{gathered} \mathcal{L}^{-1}(g^*(p)) = g(t) = \mathcal{L}^{-1} \left(E_0 + \sum_1^N E_i \left[\frac{p}{\frac{E_i}{\eta_i} + p} \right] \right) \\ \rightarrow \mathcal{H}(t) = E_0 + \sum_1^N E_{i,rel} \, e^{-\frac{E_i}{\eta_i} t} \end{gathered} \tag{3.50}$$

Then it is often simpler to rather used normalized relaxation modulus $g(t)$, thereby we suppose $E_i = g_i^{(r)} E_0$ such that $g_\infty^{(r)} = 1 - \sum_1^M g_i^{(r)}$(long term relative modulus), thus Eq. (3.50) reduces to

$$H\left(t\right) = E_0 \left(g_\infty^{(r)} + \sum_1^M g_i^{(r)} e^{-\frac{E_i}{\eta_i} t} \right) = E_0 g_r\left(t\right), \ g_r\left(t\right) = g_\infty^{(r)} + \sum_1^M g_i^{(r)} e^{-\frac{E_i}{\eta_i} t}, \tag{3.51}$$

Using the same token for describing creep, the creep and normalized moduli read as

$$\mathcal{G}\left(t\right) = \mathcal{G}_0 \left(g_\infty^{(c)} + \sum_1^M g_i^{(c)} e^{-\frac{E_i}{\eta_i} t} \right), \ g_c\left(t\right) = g_\infty^{(c)} + \sum_1^M g_i^{(c)} e^{-\frac{t}{\mu_i}} \tag{3.52}$$

Where $\mu_i|_{1 \le i \le N}$ are creep times associated with the generalized Maxwell model.
With these moduli at hand, it is then straightforward to derive stress or strain states by applying Volterra theorem [102], [111], for a given time interval

$$\sigma\left(t\right) = E_0 \, \varepsilon\left(t\right) + \int_0^t \mathcal{H}(t - t^{'}) \dot{\varepsilon}(t^{'}) dt^{'} \tag{3.53}$$

The second term in Eq. (3.53) can be simplified by partial integration into

$$\int_0^t \mathcal{H}(t-t^{'})\dot{\varepsilon}(t^{'})dt^{'} = \Big[\mathcal{H}(t-t^{'})\varepsilon(t^{'})\Big]_0^t + \int_0^t \frac{d\mathcal{H}(t-t^{'})}{dt}\varepsilon(t^{'})dt^{'} \tag{3.54}$$

Which is analogous to the form

$$\int_0^t \mathcal{H}(t-t^{'})\dot{\varepsilon}(t^{'})dt^{'} = \mathcal{H}\left(t-t\right)\varepsilon(t) - \mathcal{H}(t-0)\varepsilon\left(0\right) + \int_0^t \frac{d\mathcal{H}(t-t^{'})}{dt}\varepsilon(t^{'})dt^{'} \tag{3.55}$$

In the latter equation, the term $\varepsilon\left(0\right)$ is the residual strain tensor. For simplicity, we assume a strain-free state at $t = 0$. Thence, with the Eq. (3.55), the expression for stress relaxation and creep can be straightforwardly deduced as follows

$$\begin{cases} \sigma(t) = E_0\,\varepsilon(t) + \displaystyle\int_0^t \dot{\mathcal{H}}(t-t^{'})\varepsilon(t^{'})dt^{'} \text{ if stress relaxation} & (3.56a) \\ \varepsilon(t) = \mathcal{G}_0\,\sigma(t) + \displaystyle\int_0^t \dot{\mathcal{G}}(t-t^{'})\sigma(t^{'})dt^{'} \text{ if creep} & (3.56b) \end{cases}$$

Where in the hypothesis of small strain, the strain tensor ε reads as

$$\varepsilon\left(u\right) = \frac{1}{2}\left(\nabla_X u +^T \nabla_X u\right) = \varepsilon^D + \varepsilon^H \tag{3.57}$$

Where $\varepsilon^H = tr(\varepsilon)$ is the hydrostatic or volumetric strain tensor and $\varepsilon^D = \varepsilon - \varepsilon^H$ is the deviatoric strain tensor.

In Eq. (3.56), E_0 and $\mathcal{G}_0$ stands for the instantaneous elastic moduli for creep and relaxation, respectively; $\mathcal{H}$ and $\mathcal{G}$ are relaxation and creep moduli functions, respectively. Futhermore, Eq. (3.56) clearly outlines that creep and relaxation have a dual connection, which essentially means that a single test can be used to define both models under certain assumptions underlined in detail in Chap. Experimental.

For incompressible or nearly incompressible material, it is worth splitting Cauchy stress from Eq. (3.56a) into the volumetric and deviatoric parts.

$$\sigma\left(t\right) = {\sigma_0}^D\left(t\right) + \int_0^t {\sigma_0}^D(t-t^{'})\dot{g}_r(t^{'})dt^{'} + \sigma^H\left(t\right) \tag{3.58}$$

Wherein ${\sigma_0}^D\left(t\right) = E_0{\varepsilon}^D(t)$ and $\sigma^H(t)$ are respectively the deviatoric part of the instantaneous stress tensor and the hydrostatic part of Cauchy stress tensor $\sigma\left(t\right)$. Based on the Eq. (3.58), the extension of the problem to 2D or 3D linear viscoelasticity becomes obvious from Hooke's law

$$\sigma_0\left(u\right) = \overline{\overline{\mathcal{C}}}\,\varepsilon\left(u\right) = \text{dev}\left[\sigma_0\left(u\right)\right] + \sigma_0^H \tag{3.59}$$

Where $\overline{\overline{C}}$ is the fourth-order elasticity or material tensor, see Section 3.2.1.

3.2.2 In finite strain:

Throughout the loading/unloading course, this category of models pertains to materials that exhibit large strains, but in the elastic domain. At any given time t, their material tensor depends on the displacement field. Their behavior is typically described by the strain energy density W and enables to derive the stress-strain relationship. As an example, this model is commonly adopted to model rubber-like materials, as well as soft tissues by fitting the chosen model to experimental data [112], [113].

Hyperelasticity

Hyperelastic materials are materials that exhibit a high level of strain while remaining in the elastic domain. The behaviour of such materials is entirely characterized by the so-called strain energy density function W, which is a scalar-valued tensor function and is defined in such a way that

$$\begin{aligned} W : \Omega_t \ \times \mathcal{M}^{d\times d} \ &\longrightarrow \mathbb{R}^+ \\ (M, F) &\longmapsto W(F) \end{aligned} \tag{3.60}$$

The choice of the mathematical expression of the W is not made arbitrarily since it has to coherently verify certain physical conditions such as:

- Positive definiteness :

  $$\begin{cases} \forall\, M \ \in \ \Omega_t \ , \ F \in \mathcal{M}^{d\times d} \text{ and } det(F) \geq 0 \,|\ W \ (M, F) \ > 0 \ \text{ at any } t > 0 \\ W\,(M, I) = 0 \text{ at } t = 0 \end{cases} \tag{3.61}$$

  Having assumed that there are no residual deformations (implies $F = I$)within the body Ω_0 in the reference frame, the strain energy density function is simply equal to zero at any material point $M_0 \in \Omega_0$ at the initial time $t = 0$. However, for every $t > 0$, the strain energy function must always be positive for this to hold. This mathematical description satisfies the physical interpretation because deformations observed on the body subjected to loads are proof of the existence of a created energy. In purely elastic considerations, this energy is released by the material once the external load is canceled. For the sake of stability, the function W has to fulfill the following properties:

- Principle of material frame indifference:

  $$\forall\, Q \in \ Orth^3, \ M \ \in \ \Omega_t \,|\ W\,(M, QF) = W\,(M, F) \tag{3.62}$$

Where we recall that $Orth^3$ is the space of square orthogonal matrices. This property infers that the strain energy density of the material is independent of the material fiber orientation. If verified, the material is, therefore, said to be isotropic (properties are the same in all directions of the space).

- Polyconvexity: The functional W is polyconvex if and only if there exists a function f that is convex with respect to all its 19 variables arising from F, $adjF$, and J such that.

$$\begin{aligned} W : \Omega_t \ \times \mathcal{M}^{d\times d} \ &\longrightarrow \mathbb{R}^+ \\ (M, F) \longmapsto W(F) &= f(F, adjF, J) \end{aligned} \tag{3.63}$$

  Where $adjF = JF^{-T}$ is the adjoint of the deformation gradient F.

- Thermodynamic Consistency: Another important requirement for the existence of the strain energy density function W is the thermodynamic consistency condition defined within Clausius-Duhem inequality as follows

$$P : \dot{F} - \dot{W} \geqslant 0 \tag{3.64}$$

For further details about the above requirements, the reader is referred to [114], [115].
As a result of Eq. (3.62), W can be fully defined in terms of the deformation gradient tensor F or the right Cauchy-Green deformation tensor C or, equivalently, the left Cauchy-Green tensor B. With:

$$C = F^T F \tag{3.65}$$

One can thence point out that C is symmetric and positive definite. The straightforward consequence of the abovementioned property is that the strain energy density can uniquely be defined either in terms of the eigenvalues ${\lambda^2}_{i \,\epsilon\, \{1,2,3\}}$, principal invariants $I_{i \,\epsilon\, \{1,2,3\}}$ or principal traces of the tensor C.

$$W\left(C\right) = \hat{W}\left(\overline{\lambda}_1^2, \overline{\lambda}_2^2, \overline{\lambda}_3^2\right) = W\left(I_1, I_2, I_3\right) = W\left(trC, trC^2, trC^3\right) \tag{3.66}$$

With aid of [31], we can assume an uncoupling of volumetric and deviatoric responses and introduce the distortion gradient or volume-preserving gradient tensor $\overline{F} = J^{-1/3}F$; in such a way that the strain energy density can be split up into two components: energy due to changes in volume (volumetric component) and energy due to pure stretches under constant volume (isochoric component).

$$W\left(C\right) = \hat{W}\left(\overline{F}\right) + \mathcal{U}\left(J\right) \tag{3.67}$$

In the light of this decomposition, the Jacobean of the new transformation is volume-preserving ($det\left(\overline{F}\right) = 1$). To this distortion gradient, corresponds the right Cauchy-Green tensor $\overline{C} =$

$\overline{F}^T\overline{F}$ with eigenvalues $\overline{\lambda}_1^2, \overline{\lambda}_2^2, \overline{\lambda}_3^2$, and principal invariants $\overline{I}_1, \overline{I}_2, \overline{I}_3$ related as follows:

$$\overline{I}_1 = \overline{\lambda}_1^2 + \overline{\lambda}_2^2 + \overline{\lambda}_3^2,\ \overline{I}_2 = \overline{\lambda}_1^2\overline{\lambda}_2^2 + \overline{\lambda}_2^2\overline{\lambda}_3^2 + \overline{\lambda}_3^2\overline{\lambda}_1^2,\ \overline{I}_3 = \overline{\lambda}_1^2\overline{\lambda}_2^2\overline{\lambda}_3^2 = det\left(\overline{F}\right),\ \overline{I}_1 = J^{-\frac{2}{3}}\, I_1 \quad (3.68)$$

Bearing in mind that the Jacobean of the primal problem is $J = det(F)$ and measures volume changes and getting advantage of this formalization, the volumetric term is quantified by the expression

$$\mathcal{U}\left(J\right) = \sum_{I=1}^{M} \frac{1}{d_i}(J-1)^{2i} \quad (3.69)$$

Where d_i are incompressibility parameters and N the order of the polynomial series of J required to fit the experimental data recorded from the volumetric test. It is, therefore, obvious that for an incompressible or nearly-incompressible material ($J = det\left(F\right) \ = 1$), this term is equal to zero (for Nylon cords, this term is zero). Often in commercial software, the nearly incompressibility is enforced by setting Poisson's ratio to a value in $[0.480,\ 0.4997]$ so as to avoid instability in the course of the simulation[116], [117]. Besides the volumetric energy density function in Eq. (3.69), other forms[118], [119], [120] are also often used and a few are reported in Table 3.4.

Table 3.4: A few volumetric strain energy density functions.

Volumetric strain energy density	**References**
$\mathcal{U}\left(J\right) = \kappa\left(J-1\right)^2$	
$\mathcal{U}\left(J\right) = \frac{\kappa}{4}(logJ)^2$	[120]
$\mathcal{U}\left(J\right) = \frac{\kappa}{4}\left(J^2 - 1 + 2log(J)\right)$	[120]
$\mathcal{U}\left(J\right) = \kappa\left(J - 1 - log(J)\right)$	[119]
$\mathcal{U}\left(J\right) = \boldsymbol{\kappa}\left(1 - J - Jlog(J)\right)$	[118]

Where κ is the bulk modulus.

In the case of incompressible material, the above volumetric energy density functions vanish. This is usually implemented with help of mixte variational formulation with *u-p* verifying the *inf-sup* condition or with stabilization methods [118], [121], [122].

As per the deviatoric parts, several hyperelastic models (mostly phenomenological ones) are most often considered for approximating the rubber contribution of shear effects in the strain energy density. These models are summarized in Table 3.5.

Table 3.5: A few deviatoric strain energy density functions.

Models	**Deviatoric strain energy functions**	**Constants**	**Reference**
Neo-hookean	$\hat{W}\left(\bar{I}_1\right)_{Neo\_h} = C_{01}\left(\bar{I}_1 - 3\right)$	C_{01}	[120]
Mooney Rivlin	$\hat{W}\left(\bar{I}_1, \bar{I}_2\right) = \sum_{i,j=0}^{M} C_{ij}\left(\bar{I}_1 - 3\right)^i \left(\bar{I}_2 - 3\right)^j$	C_{ij}	[123]
Ogden	$\hat{W}\left(\bar{\lambda}\right) = \sum_{i=1}^{M} \frac{\mu_i}{\alpha_i^2}\left(\bar{\lambda}_1^{\alpha_i} + \bar{\lambda}_2^{\alpha_i} + \bar{\lambda}_3^{\alpha_i} - 3\right)$	$\mu_i,\ \alpha_i$	[124]
Yeoh	$\hat{W}\left(\bar{I}_1\right) = \sum_{I=1}^{M} C_{i0}\left(\bar{I}_1 - 3\right)^i$	C_{i0}	[119]
Gent	$\hat{W}\left(\bar{I}_1, \bar{I}_2\right) = C_1\left(\bar{I}_1 - 3\right) + 3C_2 ln(\bar{I}_2)$	C_i	[125], [126]
Polynomial	$\hat{W}\left(\bar{I}_1, \bar{I}_2\right) = \sum_{i,j=1}^{M} C_{ij}\left(\bar{I}_1 - 3\right)^i \left(\bar{I}_2 - 3\right)^j$	C_{ij}	[127]

Anisotropic hyperelasticity

Due to the non-homogeneous structure of the material, characterized by the presence of molecular heterogeneities or fibers (see Figure 3.10), the strain energy density function does not have the same properties in all spatial directions at any M point in the media but remains hyperelastic. As a result, one or more preferential directions generate the anisotropic energy term [113], [128].

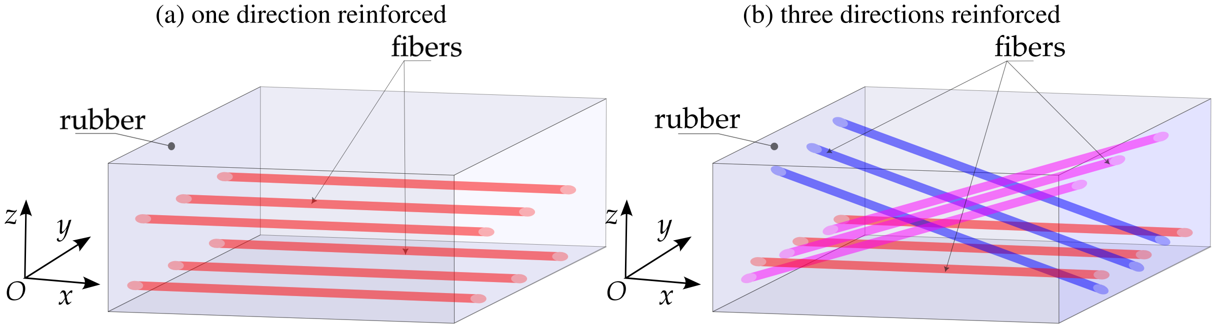
(a) one direction reinforced

(b) three directions reinforced

Figure 3.10: Fiber-reinforced polymer.

Let us define $\overrightarrow{A_\alpha}\Big|_{i\in\langle 1,2,\ \ldots,k\rangle}$ as the k unit vectors of fibers orientation of the material. At any time $t \geq 0$, the functional W is defined as

$$\begin{aligned} W : \Omega_t \times \mathcal{M}^d \times \mathbb{R}^d &\longrightarrow \mathbb{R}^+ \\ (M, F, \overrightarrow{A_\alpha}) &\longmapsto W(M, F, \overrightarrow{A_\alpha}) \end{aligned} \tag{3.70}$$

Where d is the dimension of the problem (i.e. 2 in 2D or 3 in 3D). In this definition, the functional $W(M, F,\overrightarrow{A_\alpha})$ equally has to be positive definiteness as stated in Eq. (3.61); however does not verify the material indifference frame. It is usually admitted a split of $W(M, F,\overrightarrow{A_\alpha})$ into the isotropic term $W^{iso}(F)$ and the anisotropic term $W^{aniso}\left(F, \overrightarrow{A_\alpha}\right)$ as follows

$$W\left(M, F,\overrightarrow{A_\alpha}\right) = W^{iso}(F) + W^{aniso}\left(F, \overrightarrow{A_\alpha}\right) \tag{3.71}$$

Before explicitly introducing the strain density energy of such materials, we need to define more invariants in addition to I_1, I_2 and I_3. Let us consider that the material is reinforced with a family of k groups of fibers, whose each group is oriented following the unit vector $\overrightarrow{A}_{\alpha\ \in(1,2,..,k)}$.

$$I_4^{(\alpha)} = tr\left(C\overrightarrow{A}_\alpha\right) = \overrightarrow{A}_\alpha \cdot C\overrightarrow{A}_\alpha\ ,\ I_5^{(\alpha)} = tr\left(C^2\overrightarrow{A}_\alpha\right) = \overrightarrow{A}_\alpha \cdot C^2\overrightarrow{A}_\alpha \tag{3.72}$$

In some cases, fibers interaction is taken into account by means of coupled invariants $I_8^{(\imath,\jmath)}$ and $I_9^{(\imath,\jmath)}$ given as

$$I_8^{(\imath,\jmath)} = \left(\overrightarrow{A}_\alpha \cdot \overrightarrow{A}_\alpha\right)\left(\overrightarrow{A}_\alpha \cdot C\overrightarrow{A}_\alpha\right); I_9^{(\imath,\jmath)} = \left(\overrightarrow{A}_\alpha \cdot C\overrightarrow{A}_\alpha\right)^2;\ \imath \neq \jmath \in\ (1, 2, \ldots, k) \tag{3.73}$$

This constitutive behavior is of particular interest since there has been an increasing number of research in the last decade making use of it to generate a geometric homogeneous model to reduce the computational complexity of some fiber-reinforced composites. Initially, it was developed to model certain fiber-reinforced soft tissues, but it has recently witnessed wider use. There is a plethora of models in the literature[129] and we report a few of them in Table 3.6

Table 3.6: A few anisotropic-hyperelastic strain energy density functions.

Models	**strain energy density functions**	**constant**	**references**
Humphrey and Yin	$W = c_1\left[exp\left(c_2(I_4-1)^2\right) - 1\right]$	c_1, c_2	[130]
Holzapfel	$W = C_1(I_1-3) + \frac{c_1}{2c_2}[exp(c_2(I_4-1)^2) - 1]$	C_1, c_1, c_2	[131]
Extended Holzapfel	$W = C_1(I_1-3) + \frac{c_1}{2c_2}[exp((1-\kappa)(I_1-3)^2 + \kappa(I_4-1)^2 - 1)]$	C_1, c_1, c_2	[132]

Linear visco-hyperelasticity:

In section 1.2, we have covered the strain energy density functions for hyperelastic materials and unlike linear elastic materials, rubber-like materials exhibit large strain and the deriving Cauchy stress tensor σ is also non-linear and can be split into the hyperelastic component (σ^e) and viscous component (σ^v) [133] as follows

$$\sigma\left(t\right) = \sigma^{D}\left(t\right) + \sigma^{H}\left(t\right) = \sigma^{e}\left(t\right) + \sigma^{v}\left(t\right) \tag{3.74}$$

However, we note this time that expression in Eq. (3.58), which portrays the response (creep or stress relaxation) of a linear viscoelastic material for any given excitations (prescribed stress or prescribed strain), needs to be extended to comply with visco-hyperelastic properties of the material. To do so, we reconsider the generalized Maxwell rheological model in Figure 3.9 and prosny series of the same form as in the last section. Recently, authors in [133] and [134] proposed a modified version of the Cauchy stress tensor without the need to have a different strain density energy for the viscous part [135]. In there, the hydrostatic component σ^H and deviatoric component σ^D of the stress tensor are explicitly given in the relations in Eq. (3.75a) and (3.75a), respectively

$$\begin{cases} \sigma^{D}\left(t\right) = \sigma_0^{D}(t) + \displaystyle\int_0^t F_t^{-1}(t-t^{'})\sigma_0^{D}(t-t^{'})F_t^{-1}(t-t^{'})\dot{g}_r(t^{'})dt^{'} & \text{(3.75a)} \\ \sigma^{H}(t) = \sigma_0^{H}(t) + \displaystyle\int_0^t \sigma_0^{H}(t-t^{'})\dot{g}_r(t^{'})dt^{'} & \text{(3.75b)} \end{cases}$$

Where $F_t(t-t^{'}) = F(t-t^{'})F^{-1}(t)$ is the relative deformation gradient, σ_0^D and $\sigma_0^H$are the instantaneous deviatoric and hydrostatic stress, respectively. We recall from sect. that the strain energy density function of the material undergoing finite deformation can be decomposed into its deviatoric and volumetric components

$$W\left(F(t)\right) = \hat{W}\left(\overline{F}\right) + \mathcal{U}\left(J(t)\right) \tag{3.76}$$

So we can obtain $\sigma_0^D(t)$ and $\sigma_0^H(t)$ from the following

$$\sigma_0^{H}(t) = \frac{\partial U\left(J(t)\right)}{\partial J}\ ,\ \sigma_0(t) = \frac{1}{J}\frac{\partial W\left(F(t)\right)}{\partial F}F^{T}, \sigma_0^{D}(t) = \sigma_0(t) - \sigma_0^{H}(t) \tag{3.77}$$

Where $\sigma_0(t)$ is the instantaneous purely hyperelastic Cauchy stress tensor. For further details about Eq. (3.74), the reader is referred to papers [134], [136] and [137]. Once $\sigma\left(t\right)$ is computed from Eq. (3.74), the first Piola–Kirchhoff stress tensor P, Second Piola–Kirchhoff stress tensor

S and Kirchhoff stress tensor $\mathcal{T}$ can be readily calculated at each time step by the relations

$$\begin{cases} P(t) = J(t)\sigma\,(t)\,F^{-T}\,(t) & (3.78a) \\ S\,(t) = F^{-1}\,(t)\,\sigma\,(t)\,F^{-T}\,(t) & (3.78b) \\ \mathcal{T}\,(t) = J\,(t)\;\;\sigma\,(t) & (3.78c) \end{cases}$$

Depending on the configuration from where energy integrands are evaluated using the discretized form of the weak variational formulation of the boundary value problem, the latter expressions will be of great importance in later chapters.

Nonlinear visco-hyperelasticity:

In the presence of large deformations, the linear viscosity approach described using the Prony series in the Section cannot efficiently capture the nonlinear viscoelastic flow. Now assuming the multiplicative split principle [138] illustrated in Fig, the deformation gradient F is decomposed into its hyperelastic F_e and viscous F_v parts as follows.

$$F = F_e F_v \tag{3.79}$$

Subsequently, it is assumed that viscous deformation takes place in an isochoric process.

$$det\,(F_v) = 1 \tag{3.80}$$

such that the flow rule can be derived as

$$\dot{\varepsilon}_v = \dot{\lambda}\frac{\partial \overline{q}}{\partial \sigma} \tag{3.81}$$

Where $\hat{q} = J\sqrt{\frac{3}{2}\sigma^{dev} : \sigma^{dev}}$ and $\dot{\lambda} = \dot{\varepsilon}^v_{eq}$ are the equivalent deviatoric Cauchy stress and equivalent creep strain rate, respectively. After writing out the derivative in Eq. (3.83), we end up with

$$\dot{\varepsilon}_v = \frac{3\dot{\varepsilon}^v_{eq}}{2}\frac{\sigma^{dev}}{\overline{q}} \tag{3.82}$$

The complete description of the above-defined flow rule is obtained by prescribing $\dot{\varepsilon}^v_{eq}$. In this regard, several creep evolution models exist in the literature, out of which the most famous and efficient one suitable for rubber-like materials was proposed by Bergstrom and Boyce[139] and is known as the BB power-law model, given as

$$\dot{\varepsilon}^v_{eq} = a\,(\lambda_v - 1 + \zeta)^c\,(\tilde{q})^m \tag{3.83}$$

Where $\lambda_v = \sqrt{\frac{1}{3} I : C_v}$. a, ζ, m, c and c are material parameters, usually determined using a nonlinear optimization scheme based on creep test data.

Remark. *It should be noted that in ABAQUS, the flow rule cannot be used in conjunction with Mullins damage. Additionally, ABAQUS explicit does not offer this feature. However, it is possible to utilize this model with the ABAQUS standard solver. Thereby, it is essential to keep in mind that selecting this model implies that the user is limited to running static or dynamic simulations using an implicit scheme.*

This model has efficient capabilities in predicting nonlinear viscous flow in rubber-like materials, as demonstrated in the tire rolling analysis work conducted in [2].

Mullins effect:

The Mullins effect is defined as the progressive softening of the material as the number of cycles increases. Basically, in the current cycle, reloading the material to the first unloading point of the previous cycle requires less energy than loading up to the maximum stretch in the previous cycle [133], [140]. This damage evolves as the number of cycles increases, and we can interpret it as a progressive loss in stiffness, which simply means that at the molecular level, there is some molecular chain damage taking place.

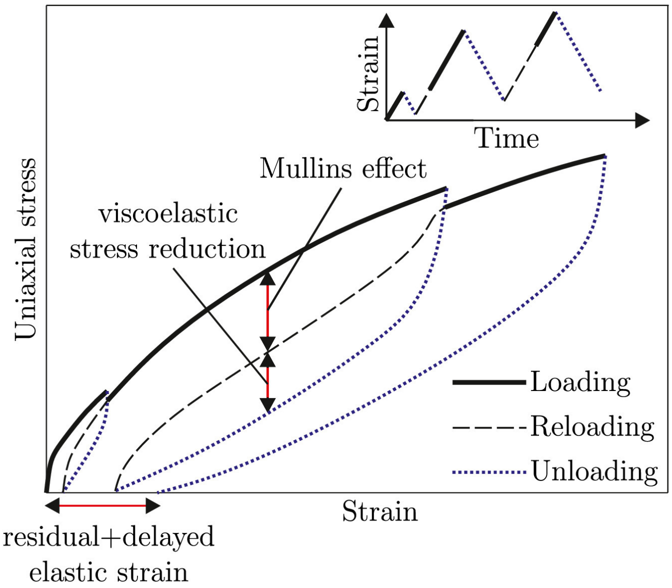

Figure 3.11: Influence of Mullins damage on stress-strain curve [133].

A viscoelastic damage model at finite strain was initially proposed by Simo [141] and consists in introducing a penalty factor $\varphi(\Xi_t)$ to the deviatoric part of the strain energy density $\hat{W}\left(\overline{F}\right)$, since Mullins damages are only due to shear effect in the material [142]. So the derived energy function proposed by Simo [141] reads as

$$W\left(F,\Xi_t\right)=\varphi\left(\Xi_t\right)\hat{W}\left(\overline{F}\right)+\mathcal{U}\left(J\right) \tag{3.84}$$

Where $\varphi\left(\Xi_t\right)\in[0,1]$ is the damage factor, where particularly $\varphi\left(\Xi_t\right)$ is 1 when there is no damage and 0 when the damage is total. However, the definition of damage Ξ_t evolution with this approach is not always easy. A simple formula is given as

$$\Xi_t=\max_{s\in]-\infty,t]}\sqrt{2\hat{W}\left(\overline{F}\right)} \tag{3.85}$$

As for the damage evolution, an exponential-based expression has been proposed by Simo and Taylor [143] and Simo and Taylor [144] and formulated as

$$\varphi_t\left(\Xi_t\right)=\beta+(1-\beta)\,\frac{e^{-\Xi_t/\xi}}{\Xi_t/\xi},\ \beta\in[0,1],\ \xi\in]-\infty,0] \tag{3.86}$$

In this expression, β and ξ are prescribed parameters and usually their choice is not always objective since it should be taken on a justified basis in regards to physics-driven considerations. A more stable augmented form of the pseudo-strain energy density function has been developed by Dorfmann and Ogden [60] and reads as

$$\begin{cases} W\left(F,\eta\right)=\eta\hat{W}\left(\overline{F}\right)+\mathcal{U}\left(J\right)+\psi\left(\eta\right) & \text{(3.87a)}\\ \psi'\left(\eta\right)=-\hat{W}\left(\overline{F}\right) & \text{(3.87b)}\end{cases}$$

Where $\eta\in[0,1]$ is the damage factor. A simple derivative of $\psi\left(\eta\right)$ with respect to η from Eq. (3.87b) was suggested by Ogden and Roxburgh [57] as

$$\psi'\left(\eta\right)=-\left(m+\beta\hat{W}_{max}\right)\mathrm{erf}^{-1}\left(r\left(\eta-1\right)\right)-\hat{W}_{max} \tag{3.88}$$

Where erf is the Gauss error function and the triplet ($m\geq 0,\beta\geq 0,\ r>1$) are positive constant materials. $\hat{W}_{max}$ is the maximal strain energy density at the first point of unloading in the first loading cycle. By replacing $\psi'\left(\eta\right)$ from Eq. (3.88) into Eq. (3.87b), we obtain the damage parameter given in Eq. (3.89)

$$\eta\left(\overline{F}\right)=1-\frac{1}{r}\mathrm{erf}\left(\frac{\hat{W}_{max}-\hat{W}\left(\overline{F}\right)}{m+\beta\hat{W}_{max}}\right) \tag{3.89}$$

The numerical implementation of this latter damage model is quite stringent and is available in many commercial software like ABAQUS, where the user has only to define the triplet ($m,\beta,\ r$) when setting material properties.

3.3 Temperature dependence:

Viscoelastic properties of rubber-like materials are closely susceptible to temperature changes, which can have a significant impact on their simulation accuracy. When the temperature rises, the material loses its stiffness and becomes softer [145], [146], [147], [148], [149], as shown in Figure 3.12. This process is accelerated in the presence of an external source of thermal energy or if the ambient temperature is higher than the reference temperature of the material. Furthermore, the smaller the melting temperature of the material is, the more sensitive it is to small temperature changes.

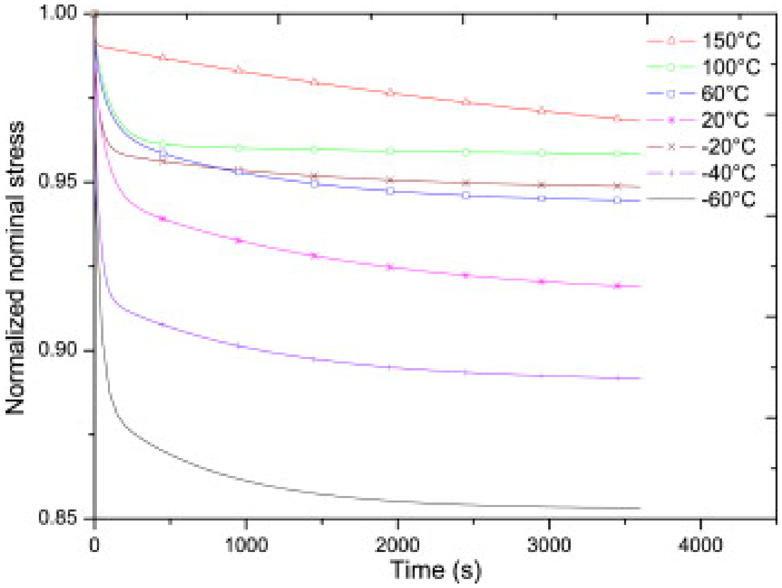

Figure 3.12: Stress relaxation responses for the unfilled silicone rubber for different temperatures [147].

In tire thermodynamics, heat can impact tire performance and longevity. Two major sources of heat generation are predominant, namely external heat exchange and road friction-induced heat generation.

When tires are operating in an environment with higher or lower temperatures, an exchange of temperature progressively takes place between the tire and its surrounding environment, which can vary significantly depending on weather conditions and ambient temperature. On the other hand, permanent frictional contact with the road during rolling generates friction-induced heat. Two factors come into play in this phenomenon: the roughness and the relative speed of the contacting surfaces.

Usually, the simplest approach to account for temperature effects on the viscoelasticity of rubber-like material is to assume that the material is a thermo-rheologically simple material[150] so that the so-called time-temperature superposition principle ([133],[151], [152], [153], [154], [155], [156]) can be applied to determine viscoelasticity parameters at a given temperature θ from their known values at the reference temperature θ_{ref} using the so-called temperature shift factor a_θ. In the literature, there exist two major approximations of a_θ, most often used:

- The Williams–Landel–Ferry approach [152]

$$\log\left(a_\theta\right) = -\frac{C_1(\theta-\theta_{ref})}{C_2+(\theta-\theta_{ref})} \tag{3.90}$$

  Where C_1 and C_2 are material constants that depend on material temperature. θ and $\theta_{ref)}$are temperature in degrees ($°C$)

- The Arrhenius law

$$\ln\left(a_\theta\right) = -\gamma\left(\frac{1}{\theta}-\frac{1}{\theta_{ref}}\right) \tag{3.91}$$

Where γ is a material constant. In this regard, θ and θ_{ref} are temperature in Kelvins. Once the empirical shift function $a_t(T)$ is determined, relaxation modulus at the temperature is given by the formula

$$\forall\,\theta,\ \mathcal{G}\left(\theta_{ref},t\right)\ ,\ \mathcal{G}\left(\theta,t\right)=\mathcal{G}\left(\theta_{ref},\frac{t}{a_t(\theta)}\right) \tag{3.92}$$

Where $t_R = \dfrac{t}{a_\theta(\theta)}$ is the reduced time. This process is summarized in the flowchart in Figure 3.13.

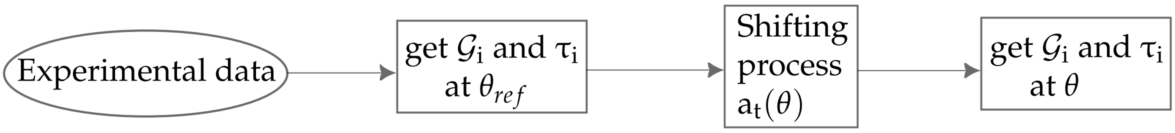

Figure 3.13: Interpolation process of the shifted moduli and relaxation/creep times.

3.4 Wear of tread:

Since treads are directly in contact with the road, they are highly exposed to the effects of contacting surface roughness. With their grooves designed to offer the best possible stability and avoid aquaplaning on a wet road, repeated friction with the road is a source of both heat generation and wear [157], [158], [159], [160], [161]. Wear is the progressive deterioration of the tire part (tread) that is directly in contact with road. This phenomenon is by nature unavoided but becomes abnormal when the damage process is whether too fast or unevenly distributed on grooves and in some cases, reveals imbalance problems with steering and suspension systems for instance [162], [163]. Several wear models have been proposed in the literature for accounting tire wear. The simplest model is called Archard wear equation [160] and reads as

$$Q_{\text{wear}} = \mathcal{K}\frac{F_n d_s}{H} \tag{3.93}$$

Where H is the harness of contacting surface, $\mathcal{K}$ is a constant, F_n is the applied normal force, d_s is the sliding distance, and Q_{wear} is the volume of worn debris. One can note that Archard's model is not directly described in terms of the friction coefficient and footprint area. To alleviate this limitation, many improved versions exist in the literature [164], [165], [166]. Tangential and normal contact constraints are enforced in the computational model by enforcing contact constraints in the potential energy of the structure through the Lagrange multiplier, discretized in the Garlekin space and solved with the Newton-Raphson scheme by iteration after a consistent linearization of the weak form of the variational formulation (see [167], [168], [169], [170]).

3.5 Contact constitutive laws:

As outlined in the introduction section, one of the key roles of a tire is to ensure a stable and smooth transfer of vehicle loads to the ground. This function entails permanent contact between the tire and the road surface. This interaction is a complex phenomenon that can be split into two components, namely tangential and normal, and conveys an entire field of interest for tire manufacturers worldwide, aiming to improve the rolling properties of their products for optimal grip and stability on the road, especially during hazardous weather conditions. Consequently, accurate tire modeling relies closely on the choice of the correct contact algorithm and enforcement of contact-type boundary conditions. In the computational contact mechanics literature [167], [168], [169], [170], researchers have proposed several numerical approaches to solving contact problems between deformable bodies:

- Penalty method:
- Lagrange multiplier:
- Augmented Lagrange multiplier:
- Nitsche's method:

In order to introduce contact laws, let denote by $\Omega^{(1)}$ and $\Omega^{(2)}$ the domains of the space respectively occupied by the tire and the ground at each time. Just for illustration, we assume the longitudinal view in Figure 4.13. Let also the boundaries $\Gamma^{(1)}$ and $\Gamma^{(2)}$, in red (–) and magenta

(–) in Figure 4.13, be the potential contact zones between both bodies.

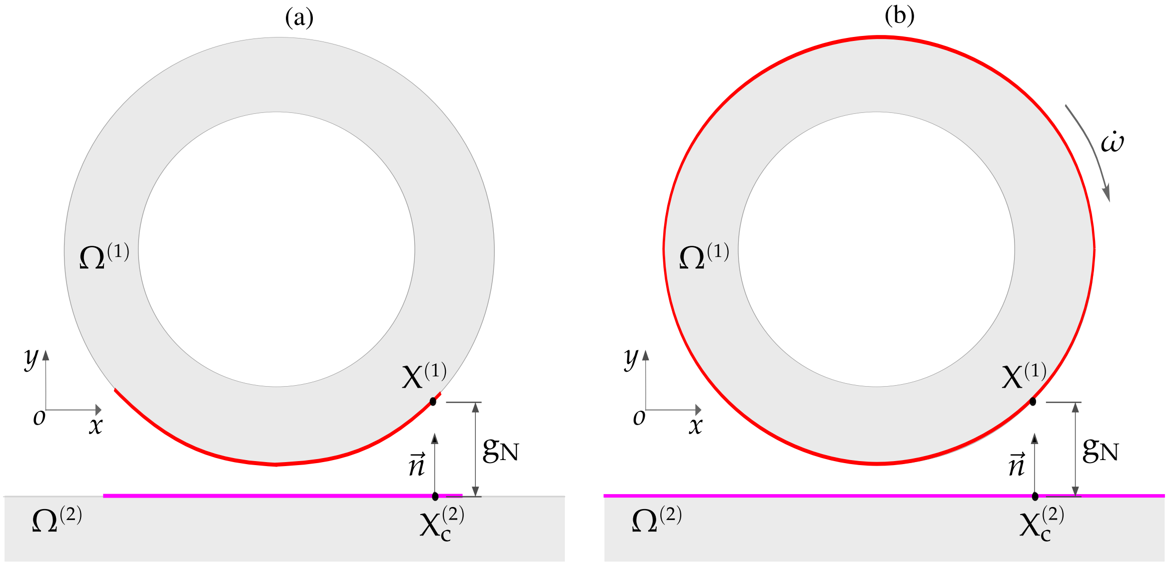

Figure 3.14: Basic representation of the contact gap and potential contact surfaces between the tire and the road. (a) in Static, (b) in rolling.

Whilst in static situations, the potential contact surfaces $\Gamma^{(1)}$ and $\Gamma^{(2)}$ are respectively reduced to just the lower tread part of the tire and the corresponding adjacent surface on the ground as illustrated in Figure 4.13(a), in rolling conditions, the contact surface of the tire is extended to the entire outermost surface of the tread as schematically shown in Figure 4.13(b).
Then, we also denote $\mathrm{x}_c^{(2)}$ the orthogonal projection of a point $\mathrm{x}^{(1)} \in \Gamma^{(1)}$ along the normal $\vec{n}$ onto the surface $\Gamma^{(2)}$.

3.5.1 Normal contact behavior:

At each time step, the compatibility of the normal interaction between the two bodies has to be fulfilled by verifying the contact inequality defined in Eq. (3.94)

$$\begin{cases} \forall\, x^{(1)} \in \Gamma^{(1)} \text{ such that } \exists\, x_c^{(2)} \in \Gamma^{(2)} & \text{(3.94a)} \\ g_N\,(X,t) = \vec{n}\cdot\left[x^{(1)}(X^{(1)},t) - x^{(2)}(X_c^{(2)},t)\right] \geq 0 & \text{(3.94b)} \end{cases}$$

Where g_N is called the gap distance function.
The condition in Eq. (3.94) ensures the enforcement of the non-penetration constraint between the two contacting surfaces throughout the course of the simulation. With the gap function at

hand, the normal contact behavior is outlined in Figure 3.15.

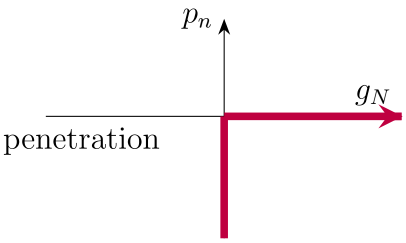

Figure 3.15: Strict normal contact law.

Where p_n is the contact pressure. This normal contact formulation in ABAQUS is named "hard" contact.

It can be noted from this illustration that when the normal gap is closed, that is to say, $g_N\,(X,t) = 0$, the contact pressure has a value different from zero. The overall summarized normal contact conditions based on Eq. (3.94b) and the relationship between g_N and p_n have been proposed by Hertz-Signorini-Moreau, referred to as KKT conditions in contact mechanics literature and given in Eq. (3.95)

$$g_N\,(X,t) \geq 0,\; p_n\,(X,t) \leqslant 0,\; p_n\,(X,t)\, g_N\,(X,t) = 0 \tag{3.95}$$

This formulation of the normal contact law is also relevant for *tied contact* type, which means the contacting surfaces remain tied to each other throughout the simulation. Thus, a more straightforward form of Eq. (3.94b) is obtained in Eq. (3.98) after simplification

$$x^{(1)}(X^{(1)},t) - x^{(2)}(X_c^{(2)},t) = 0 \tag{3.96}$$

Besides the contact behavior depicted in Figure 3.15, other approaches exist, such as the linear and exponential behaviors that allow for a slight violation of the non-penetration condition. Nevertheless, the strict approach outlined herebefore is the most realistic, though computationally a bit more challenging.

3.5.2 Tangential contact behavior:

Whenever two contacting surfaces come into contact, they typically touch each other at some points at which there are forces acting in the tangential plan. These forces are responsible for resisting the motion between the two surfaces. Numerous works in the field of tribology have been devoted to building a computational framework to better understand the complex mechanics involved in surface contact and friction[]. The most widely known is the Coulomb model, which is described by the conditions below.

$$
\begin{cases}
\|t_\tau\| - \mu\,|p_n| \leqslant 0, \quad \text{slip condition} & (3.97a)\\
v_{\tau,rel} + \beta\, t_r = 0, \quad \text{slip rule} & (3.97b)\\
\beta > 0, \quad \text{stick/slip separation} & (3.97c)\\
\beta\,(\|t_\tau\| - \mu|p_n|) = 0 & (3.97d)
\end{cases}
$$

Where $v_{\tau,rel}$ is the relative velocity of the two bodies and given as

$$x^{(1)}(X^{(1)}, t) - x^{(2)}(X_c^{(2)}, t) = 0 \tag{3.98}$$

Graphically, this law is shown in Figure 3.16. Indeed, we distinguish the pure and stiction frictional models. While in the former model, the contacting bodies are stuck when $v_{\tau,rel} = 0$ (ie. $||t_\tau|| < \mu_s|p_n|$), which corresponds to blue segments in Figure 3.16 stated in Eq. (3.97a). However, as soon as $v_{r,rel} \neq 0$, the threshold motion is reached ($||t_\tau|| = \mu_s|p_n|$), leading to a relative frictional slip between the two contacting surfaces and oriented towards the direction of $v_{r,rel}$. In contrast, when the motion threshold is reached in the Coulomb model with stiction (see Fig. 3.16(b)), the relative slip/sliding takes place under the kinematic friction force, which is calculated based on the dynamic friction coefficient $\mu_{dyn} < \mu_s$ (i.e. $||t_{\tau,dyn}|| = \mu_{dyn}|p_n|$).

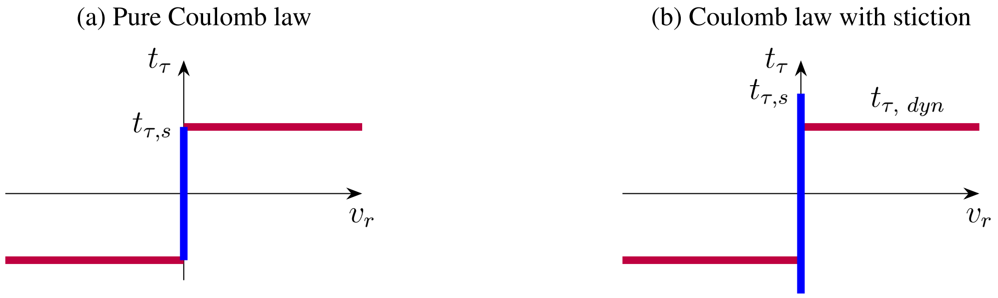
(a) Pure Coulomb law

(b) Coulomb law with stiction

Figure 3.16: Basic Coulomb frictional laws.

Though the numerical implementation of these models may seem relatively simple due to linearity, the jump observed at $v_{\tau,rel} = 0$ makes its convergence quite tedious, given that these laws are non-differentiable at this point. As a solution to alleviate this hindrance, numerous smoothing-based or regularization models such as the Coulomb-Stiction-Stribeck model [171], and many others [172], [173] have been proposed in the literature.

4 Proposed computer model for tire simulation

4.1 Motivation and assumptions

4.1.1 Motivation

Thanks to the tremendous potential offered by scientific computing and cutting-edge architecture of modern computers, dynamic simulation is an integral part of tire development process, as it not only enables manufacturers to carry out in-depth analysis of tire behavior in various scenarios, namely normal and accidental conditions, explosion, impact with an obstacle but also to optimize design and reduce costs and time between design and prototype manufacturing. This technique is based entirely on numerical modeling, which is the computerized emanation of the mathematical description of the mechanical response of tires (see Figure 4.1). To this end, the assumptions underlying the formulation of such a model must integrate as faithfully as possible the parameters of the problem (topology, material constitutive laws, boundary, and initial conditions) while maintaining a certain balance between accuracy, efficiency, and complexity.

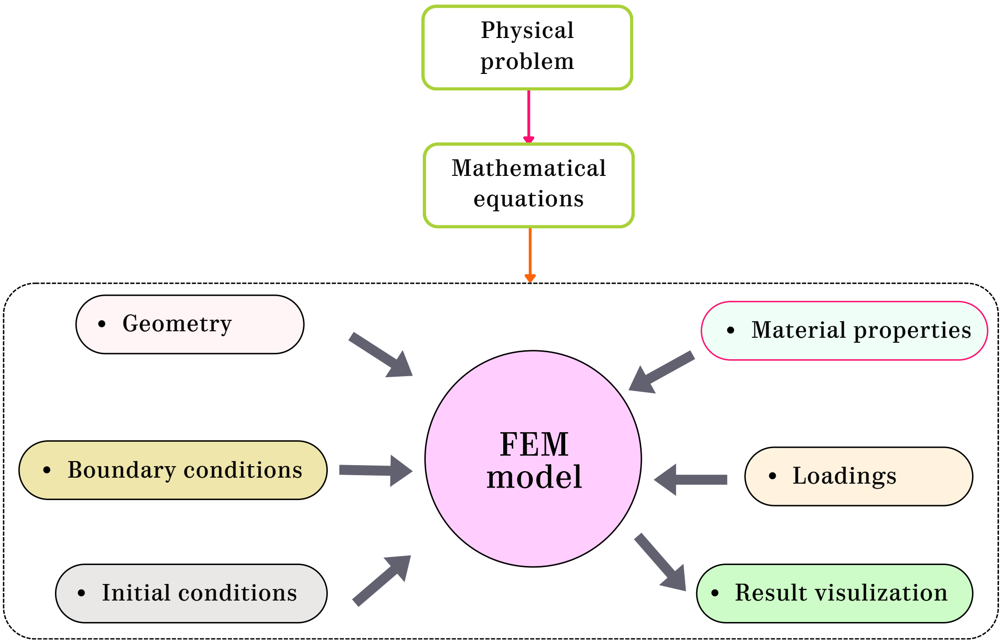

Figure 4.1: From the physical problem to the FEM model.

As highlighted in the Figure 4.1, the accuracy of the results obtained by FEM is closely linked to the definition and properties of four main components: the creation of the domain and its topology, the identification of the material properties of the components, the imposition of boundary and initial conditions, and the judicious choice of the solver. Therefore, we present in this chapter the proposed FEM model for tire simulation under dynamic loads.

4.1.2 Assumptions

The model proposed in this thesis is grounded on the following assumptions:

1. The interlayer contact is perfectly bonded: No debonding or delamination is sought in this work.
2. The rim is assumed rigid. The deformation of the rim is infinitesimal compared to that of the tire. Thus, for computational reasons, we consider the rim as a rigid body.
3. Deformation of the road is also neglected, so that the road can be modeled as a rigid body.
4. Tire parts failure mechanism is not the target of this work; thus, material failure criteria were disregarded.
5. Only the phenomena pertaining to mechanical sources are analyzed in this work. Thus, thermal, acoustic, or multiphysics responses are not investigated.

4.2 Tire geometry creation:

In order to obtain tire geometry, the common practice in the field combines tire scanning (cross-section and tread pattern) and CAD creation of the tire digital geometry, including tread, sidewalls, inner liner, bead regions, and reinforcements, as investigated by Liu et al. [174], who proposed a MATLAB build-in tool that uses image processing techniques to automatically help the user identify rubber domain as well as the location, dimension, and number of reinforcements (steel cords, textile cords, carcass, and bead) in the cross-section. The creation of the digital cross-section from the real tire cross-section is conducted following the process shown in Figure 4.2.

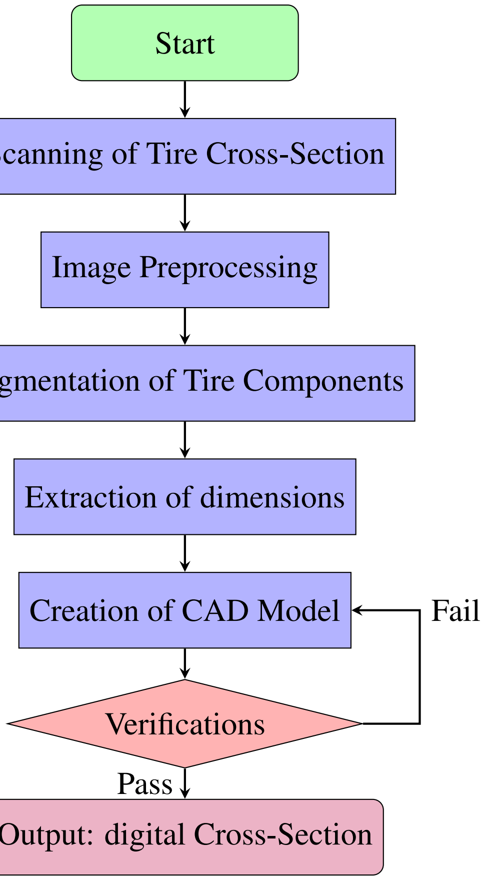

Figure 4.2: Flowchart for creating a digital tire cross-section from cross-section scanning.

4.3 Proposed material parameter identification method:

During the design and manufacturing processes, tire manufacturers must ensure that each component of the tire meets necessary structural requirements to ensure optimal functioning, stability, and durability of the final product. These requirements have been reviewed in Sadjiep Tchuigwa et al. [20] (also referred to as P2).

Aside from the above-mentioned experimental observations, the complexity of material parameter identification and experimental cost are of significant concern. In the current practice, three tests, volumetric, deviatoric, and relaxation/creep tests, are required to determine visco-hyperelastic material parameters. In light of the review of existing models in the literature section and the interpretation of experimental data collected on rubber and textile cord specimens extracted from tires, we have identified the following limitations of existing material behaviors:

- *The Mullins effect*: analysis of the stress-strain curves obtained on rubber (specimens extracted from tires) during cyclic mechanical testing reveals that, in addition to the visco-hyperelastic response, progressive damage inevitably occurs, denoted by a decrease in strength (called Mullins softening), highlighted graphically in the figure, by the fact that below the maximum stress of all previous cycles, the loading path of the current cycle does not coincide with the unloading path of the previous cycle. This characteristic phenomenon of filled rubbers was first studied by Mullins and described mathematically by Ogden and Roxburgh [57]. However, an examination of the research carried out to date on tire simulation reveals that it has not been taken into account. Given that in the tire, dynamic forces involve loading-unloading sequences, such as those performed in the cyclic test on rubber specimens, it is essential to include this damage in the constitutive law.

- In recent tire finite element models, *three tests are commonly required* to characterize the visco-hyperelastic behavior of rubber elements: a monotonic loading test (uniaxial, equibiaxial, or shear), a volumetric test, and a relaxation/creep test. Depending on the model chosen from those mentioned in the section, the corresponding parameters are determined after calibration with the experimental data. However, this approach is costly in terms of both materials and equipment, as it requires three different machines, which is beyond our reach in the VVCD laboratory, where there is a single equipment for both monotonic and cyclic tests.

- Similar to rubber compounds, textile cords also exhibit a visco-hyperelastic response type with Mullins damage, unlike the linear elastic model considered in numerous works in the literature.

Thanks to the recent identification scheme proposed in [133] and [134], it is now possible to determine these parameters (including Mullins damage parameters) with solely the cyclic tensile test. In these articles, the authors proposed a material identification procedure that enable to determine material mechanical properties using only the cyclic test.

In the next section, we describe the material parameter determination procedure adopted in this project.

4.3.1 Material constitutive behavior:

Based on the interpretation of cyclic tensile test of rubber compounds, their constitutive behaviors are, in fact, **visco-hyperelastic+Mullins effect**. This suggests the simultaneous coexistence of three important phenomena:

1. *Hyperelasticity*: described mathematically in Section 3.2.2.

2. *Viscoelasticity*: outlined mathematically in Section 3.2.2.

3. *Mullins damage*: introduced kinematically in Section 3.2.2.

Regarding tire reinforcements, including steel cords, textile cords, and carcass, they experimentally exhibit a linear elastic response, as highlighted in the Section 2.3.1. Therefore, the material properties used for tire components in this dissertation are summarized in Table 4.1.

Table 4.1: Constitutive laws and parameters of tire components.

Parts	**Components**	**Models**	**Parameters**	**Tests**
Tire	rubber compounds (tread, sidewall, inner liner, undertread, bead filler}	Mooney–Rivlin	C_{01} and C_{10}	Cyclic tensile test
		simple volumetric model	D_1	
		Generalized Maxwell model	g_i and τ_i	
		Mullins effect	r, m and β	
	Steel cords	Linear elastic	E_{steel} and ν_{steel}	Uniaxial tensile test
	Textile cords	Linear elastic	$E_{textile\ cap}$ and $\nu_{textile\ cap}$	Uniaxial tensile test
	carcass cords	Linear elastic	$E_{carcass}$ and $\nu_{carcass}$	Uniaxial tensile test

Among the existing phenomenological material models, the Mooney–Rivlin model was selected due to its simplicity and good balance between computational cost and accuracy. Additionally, it is reliable for deformation ranges of up to 200% [175]. Another advantage of this model is that the incompressibility parameter D_1 can be determined using C_{10}, C_{01} and ν as follows:

$$D_1 = \frac{2(1-2\nu)}{C_{10}(5\nu-2)+C_{01}(11\nu-5)} \tag{4.1}$$

Where ν is Poisson's ratio. Rubber compounds used in tire manufacturing are generally nearly incompressible, with a Poisson's ratio (ν) typically falling within the range of 0.480 to 0.499.

4.3.2 Material parameter identification

Cyclic test on rubber compound The tensile cyclic test procedure for rubber-like material can be carried out within the guidance provided in the standard ISO 37:2017[127] entitled *Rubber, vulcanized or thermoplastic elastomer - Determination of tensile properties*. During this test, dumb-bell specimen type 3 is preliminarily cut from tire's part to be tested and then tested as

per the procedure above:
Test procedure:

1. At room temperature, the specimen should be mounted in the machine grips;
2. Positioning of elongation measuring device (video-extensometer or contact extensometer);
3. After an initial preload of 0.1 N, the specimen has to undergo four cycles with loading and unloading up to 25% and 2.5 % of the engineering strain, respectively;
4. Then, followed with four cycles of loading and unloading up to 75 % and 5% of the engineering strain, respectively;
5. Subsequently, four cycles of loading-unloading up to 150 % and 7.5% of the engineering strain, respectively;
6. Finally, four cycles of loading-unloading up to 250 % and 10% of the engineering strain, respectively.

In each of the four loop cycles above, we avoid to unload up to the final state of the last loop to avoid compressive stresses in the specimen. A graphic representation of the engineering strain spectrum is depicted in Figure 4.3.

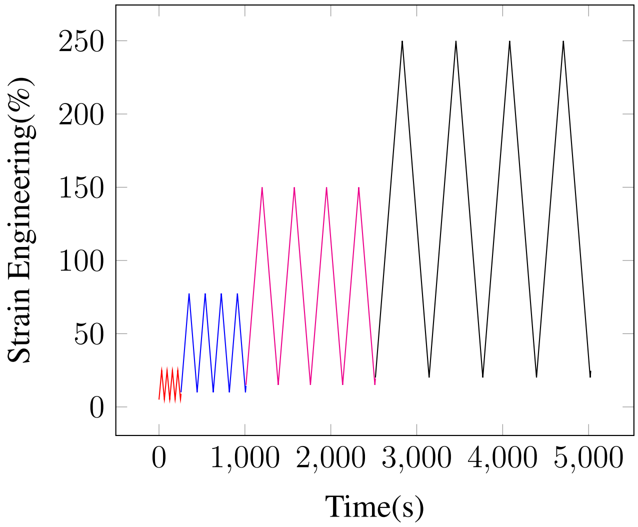

Figure 4.3: Spectrum of the loading sequence.

Steel cords:
According to experimental results existing in the literature, steel cords are predominantly solicited in the lower region of the stress-strain where Hooke's law suffices to account for their contribution. Thus, no plastic deformation is expected here, as depicted in Figure 2.8. In this regard, a simple uniaxial tensile test (as per ASTM D2969) is enough to determine Young's

modulus (E_{st}) and Poisson's ratio (ν_{st}), which are the only parameters we need from this component.

$$\sigma_{st} = E_{st}\ \epsilon \tag{4.2}$$

Textile overlap cords and carcass cords:
Similar to steel cords, the mechanical properties of textile and carcass cords are determined using a uniaxial tensile test. However, it is conducted in accordance with the ASTM D885 standards.

4.3.3 Temperature influence on material parameters:

Definition 1. *let us consider* n *set of experiments in which the prescribed variable* $\mathfrak{T}_\alpha = \langle \mathfrak{T}_{1\alpha}, \mathfrak{T}_{2\alpha}, \dots, \mathfrak{T}_{n\alpha} \rangle$ *generates the response* $\mathfrak{B}_\alpha = \langle \mathfrak{B}_{1\alpha}, \mathfrak{B}_{2\alpha}, \dots, \mathfrak{B}_{n\alpha} \rangle$ *at the temperature* $(\theta_\alpha)_{\alpha \in \langle 1,2,..,t \rangle}$ *for the range of times* $t_\alpha = \langle t_{1\alpha}, t_{2\alpha}, \dots, t_{n\alpha} \rangle$*. With the help of the time-temperature superposition principle, it is possible to estimate material parameters at a temperature* $(\theta_\alpha)_{\alpha \in \langle 1,2,..,t \rangle}$ *from parameters at reference temperature or room temperature using master curves by interpolating as shown in Figure 4.4.*

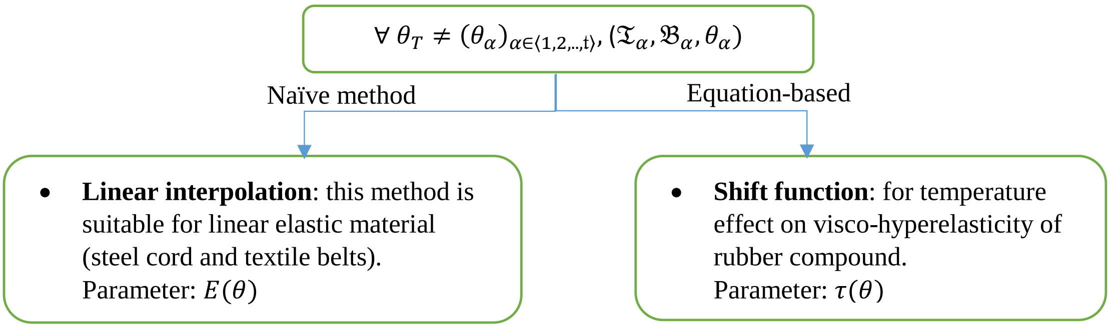

- **Linear interpolation**: this method is suitable for linear elastic material (steel cord and textile belts). Parameter: $E(\theta)$

- **Shift function**: for temperature effect on visco-hyperelasticity of rubber compound. Parameter: $\tau(\theta)$

Figure 4.4: Adjustment of the mechanical properties in response to changes in temperature.

The mathematical process behind this process is described in Section 3.3.

4.4 Creation of the topology:

The accuracy of results obtained from the finite element method heavily depends on the quality of the topology or geometry being analyzed. In the tire industry, the creation of tire topology begins with cross-section scanning. This is effective since the tire construction, or casing, is symmetric with respect to the wheel's axle. The scanned image is then imported into a CAD program, where it serves as a layout for sketching each layer that forms the tire casing. Once this is completed, the file is imported into simulation software such as ABAQUS or ANSYS as a reference.

At this stage, there are two methods for creating a 3D tire mesh:

1. **Method 1**: $\mathrm{One - time\ Mesh}$
   This method is entirely performed in the CAE interface. It involves first creating the 3D geometry and then meshing it. Each rubber compound is modeled separately in this approach. While this method results in a denser mesh, it is computationally expensive. In this method, rubber compounds are meshed with the following finite element:

2. **Method 2**: $\mathrm{axisymmmetric - based}$
   This method takes advantage of the tire's symmetry about the wheel axle. It begins with a 2D axisymmetric model of the tire, which is then meshed. Within ABAQUS, the built-in symmetric model function is utilized to generate the 3D profile. This function allows the creation of equally spaced mesh sectors ($Type\ 1$) or locally refined mesh sectors ($Type\ 2$) in the circumferential direction. The resulting mesh is illustrated in Figure 4.5. This method is computationally efficient; however, it has a drawback: it can only be applied using input files and requires familiarity with the script language.

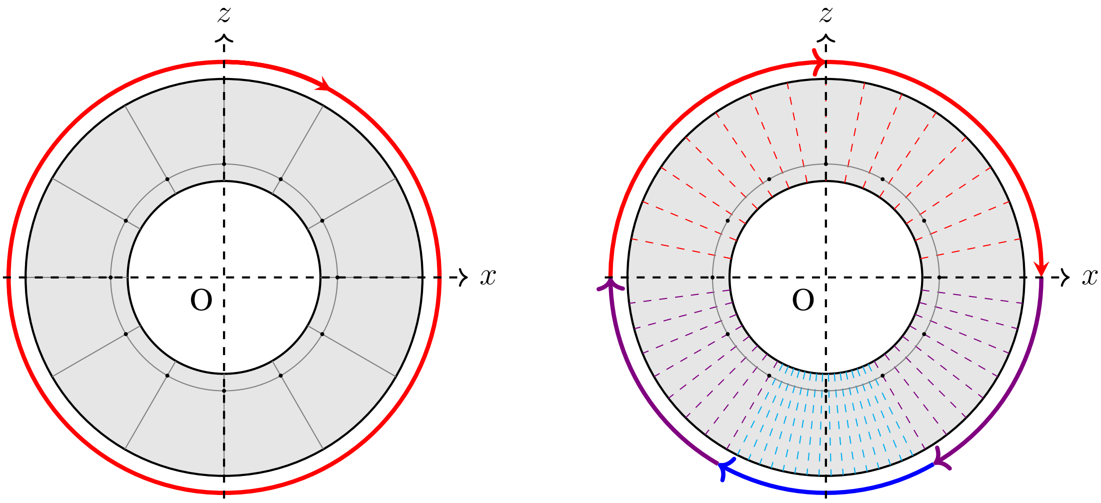
(a) Type 1 (b) Type 2

Figure 4.5: Possible circonferential mesh of tire from 2D axisymmetric tire model. (b) Type 1: Equally spaced sector mesh and (a) Type 2: Sectorized mesh.

Before meshing, the choice of element types depends on the material constitutive laws, the level of deformation the structure may undergo, and the type of solver to be used—whether implicit or explicit—based on the specifics of the problem.

- Given the incompressibility of tire rubber, a mixed variational formulation needs to be adopted. In this formulation, the hydrostatic field p is introduced as a supplementary unknown along with the displacement field u.

- For simplicity, linear elements are generally preferred over quadratic elements. Therefore, reduced integration must be activated to address volumetric locking during the deformation process.

- Finally, for static, quasi-static, and moderately dynamic problems, implicit solvers are suitable, whereas explicit solvers are more effective for impact, transient rolling, and strongly dynamic problems.

While the meshing **method 1** was utilized at the conceptual level, **method 2** was used for validation of the model.

4.4.1 Modeling of rubber compounds and beads

The finite elements listed in Table 4.2 can be utilized for creating a 3D mesh of rubber compounds and tire beads.

Table 4.2: Element type configurations for different parts.

Parts	Dimension	Element type	
		Implicit solver	Explicit solver
Rubber	3D	$C3D6H$	$C3D6R$
		$C3D8RH$	$C3D8R$
Bead	3D	$C3D8RH$	$C3D8R$

Where
$C3D8$: 8-node linear brick element.
$C3D6$: 6-node linear pentahedron element.
H: hybrid element
R: reduced integration
A spatial representation of these elements is shown in Figure 4.7.

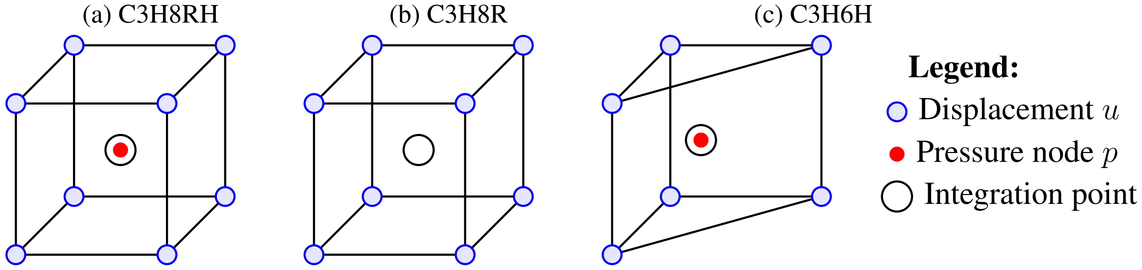
(a) C3H8RH
(b) C3H8R
(c) C3H6H

Figure 4.6: 3D finite element types for meshing rubber compounds and beads.

Since *hybrid* elements (denoted with H) are not supported in the ABAQUS explicit solver, it is necessary to activate the *enhanced strain formulation* to manage instabilities caused by material incompressibility. Enhanced strain formulations address issues such as shear locking, incompatible modes, and hourglassing, particularly in bending-dominated or nonlinear materials.

4.4.2 Modeling of reinforcements

Reinforcements such as steel cords, textile cap cords and carcass are incorporated into rubber matrix to rigidify the tire and absorb stresses and deformation resulting from loads. Their modeling is also of major interest. In ABAQUS, one distinguishes two modeling techniques for reinforcements:

- **Surface element**: Mostly used with axisymmetric modeling, it offers to use a zero-thickness element of type $SFMGAX1$ in 2D and $SFM3D4R$ in 3D to model rebars. These elements (see Fig) have three active degrees of freedom namely 1, 2, 5. Which corresponds to two translations (about u_r, u_z) and one rotation (θ), given in cylindrical coordinates.
- **Beam element**: this type of element is used for modeling individual rebars in a realistic reinforcement model. In ABAQUS, $B21$ and $B31$ are used in 2D and 3D, respectively. In terms of degrees of freedom, $B21$ has three active degrees of freedom (u_x,u_y and θ), while $B31$ has six active degrees of freedom (u_x,u_y,u_z,θ_x,θ_y and θ_z).
- **Solid element**:

For simplicity, linear elements are preferred for computational motivations. In both cases, a single integration point is needed as depicted in the illustration shown in Figure 4.7.

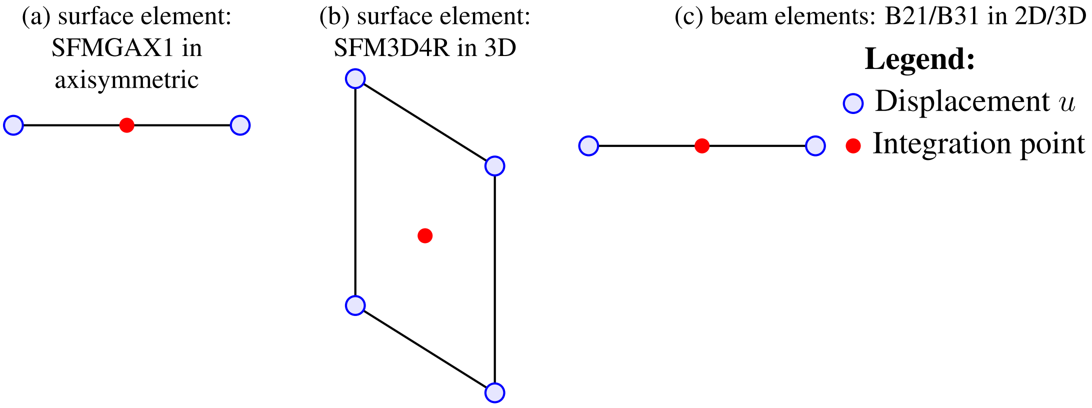

Figure 4.7: Possible FE elements for reinforcements.

In a 3D tire model with realistic reinforcements, the problem size becomes significantly larger due to the doubling of the number of degrees of freedom when compared to surface elements, which only have three degrees of freedom per node. As a result, the computational cost associated with a realistic model is high.

4.4.3 Modeling of reinforced layers

In order to capturing an accurate response in dynamic loading, it is important to thoroughfully model reinforced layers. Actually, there are three modeling possibilities:

- The **laminate** approach which is governed by homogenization theory and enables to replace the composite layer by an homogenized layer with mechanical properties function of the rubber and rebar individual mechanical properties. Under this theory, two popular approaches exist: the orthotropic solid model and the shell ($S4R$) or membrane composite-based model. In the orthotropic solid model [83], [176], a biaxial test is used to determine the material mechanical properties, which are assigned to the whole domain of concern.

- The **materially realistic or hybrid** approach: In this approach, mechanical properties of the matrix and the rebar are determined separately. Within FE commercial software such as ABAQUS, matrix domain (rubber) is modeled seperately (in 2D axisymmetric with $CGA3RH$ /$CGA4RH$ elements and in 3D with $C3H6H/C3H6/$ $C3H8RH/C3H8R$ elements) and assign its individual material constitutive law. On the other hand, reinforcement layers are modeled as a surface elements ($SFMGAX1$ in 2D and $SFM3D4R$ in 3D) with embedded rebars and assign its properties namely, the constitutive behavior, the spacing of rebars and the aspect ratio between the volume of rebars over that of the rubber. This approach has been extensively utilized and validated by authors like.
- The **realistic** approach with embedded rebars: In this model, both matrix and rebars are modeled with the real geometry and material constitutive laws. That is to say, unlike with the previous two approaches, each rebar is modeled as a linear beam element.

Geometry and material law considerations for these models are graphically illustrated in Figure 4.8

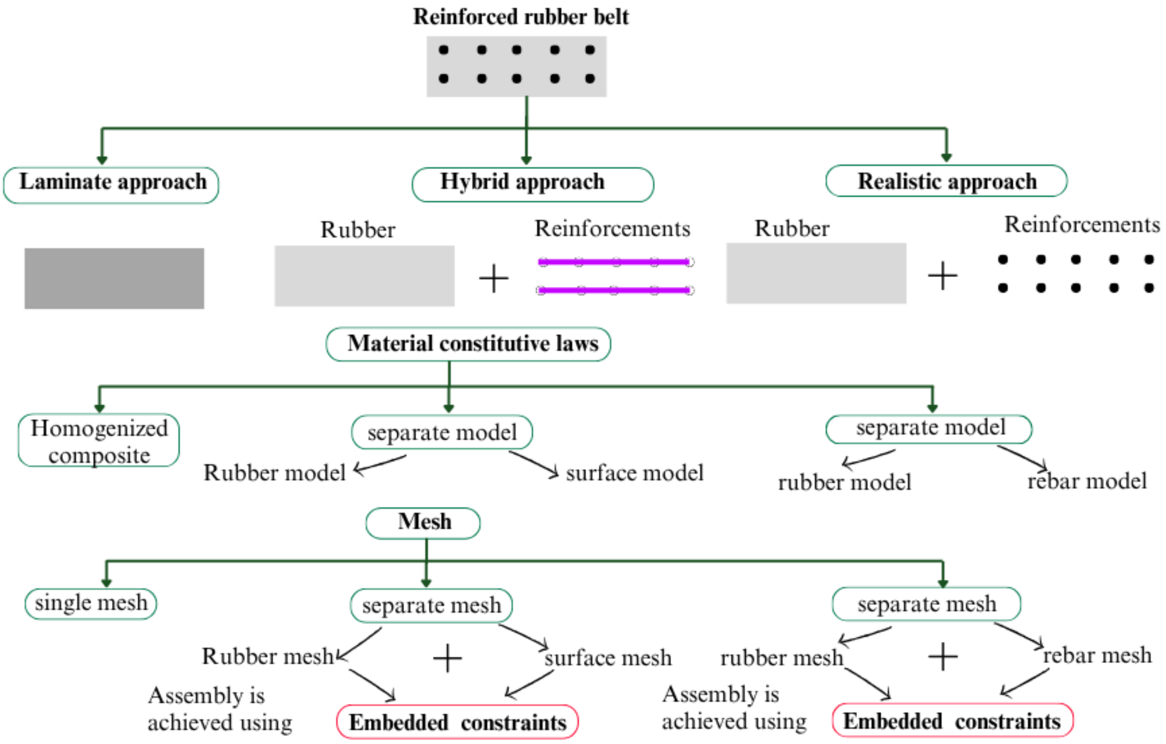

Figure 4.8: Graphical illustration of modeling approaches for reinforced rubber belts.

A comparison of the existing modeling approaches for rubber reinforced layers is summarized, considering factors such as accuracy, computational cost, validity, and the advantages and disadvantages in Table 4.3.

Table 4.3: Comparison of modeling approaches for tire reinforced layers.

$factor$	Reinforced layer modelling approaches		
	Laminate	**Hybrid**	**Realistic**
Validity	Only small deformation under static loading	small and large deformation in under static and dynamic loads	small and large deformation in under static and dynamic load
Accuracy	very low	high	very high
Advantage	reduces the problem size.	Best trade of between accuracy and computational cost	Can predict stress/strain and individual rebar failure mode
Disadvantage	Does not account for rebar aspect ratio and large deformations. Cannot incorporate rubber and rebar real material law	Predict stress / strain in the layer as a whole not on individual rebar	Requires a denser mesh
Computational cost	very low	low	very high

In the scope of this dissertation, both the realistic (see author's articles P5, P6, and P8) and hybrid approaches (see author's articles P3 and P4) were utilized at the conceptual and model validation stages, respectively.

4.5 Modeling of interactions

4.5.1 Tire-rim interaction modeling

Under operational conditions, the tire is mounted on the rim and is secured through the rim cushion in the rim jaws. There are three modeling concepts for tire-rim interaction:

- **Tire-center kinematic coupling** approach: A kinematic coupling is a constraint that ensures the kinematic state of a reference point (such as a wheel's axle) is imposed on a set of points (like part of the rim cushion). In this constraint, the degrees of freedom of the dependent nodes are controlled by the reference point.

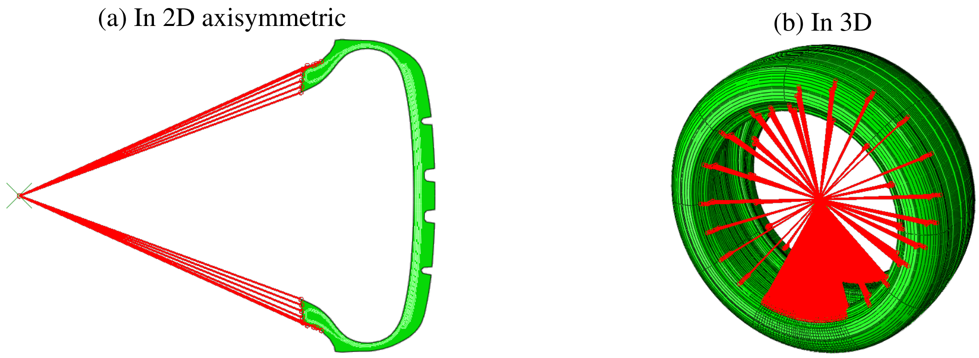
(a) In 2D axisymmetric

(b) In 3D

Figure 4.9: Tire-center kinematic interaction.

- **Tire-center rigid body interaction** approach: This constraint establishes a rigid body deformation type between the reference point (the wheel's axle) and the set of points on the rim cushion. It is similar to a kinematic constraint and has the advantage of being supported during the transition from the 2D axisymmetric model to the 3D model, as described in Method 2 above.

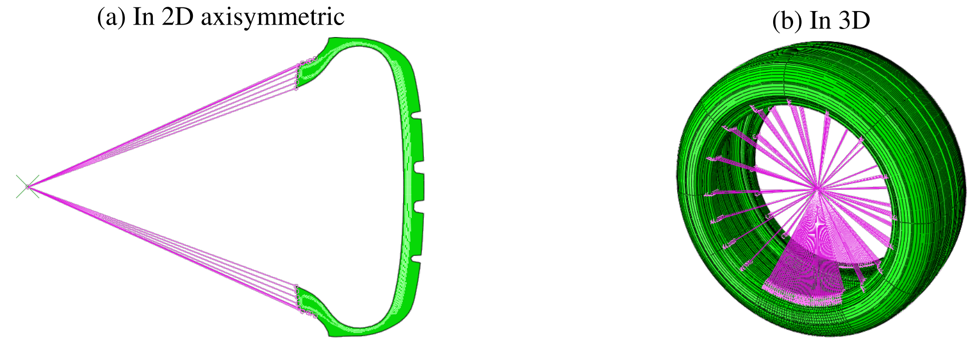
(a) In 2D axisymmetric

(b) In 3D

Figure 4.10: Tire-center rigid body interaction.

- The **realistic tire-rim interaction** approach: In this approach, the rim surface is modeled using a parametric analytical rigid element. Next, a surface-to-surface contact type is defined, using the tire rim cushion surface and rim surface as contact pairs.

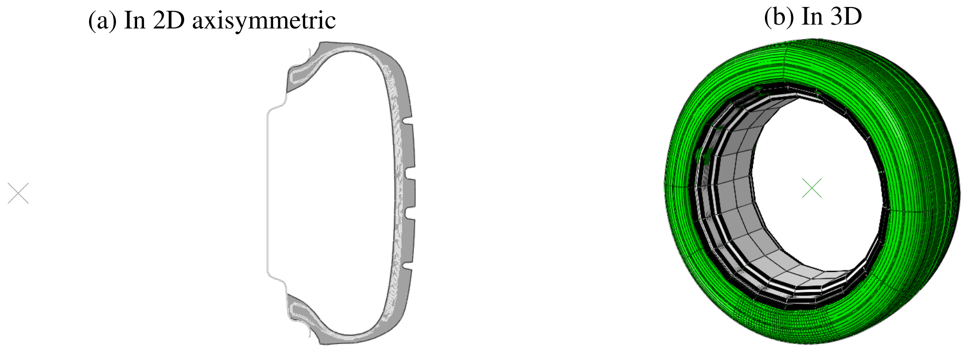
(a) In 2D axisymmetric

(b) In 3D

Figure 4.11: Tire-rim surface interaction.

For computational simplicity, the **tire-center rigid body** interaction and **Tire-center kinematic coupling** approaches were used in this dissertation.

4.5.2 Tire-road interaction modeling

FEM demonstrates versatility in efficiently modeling interactions between contacting bodies. There are two formulations for modeling the contact between tire tread (slave surface) and road surface (master surface).

- **Node-to-surface** contact formulation:In this approach, the slave nodes are restricted from penetrating the master surface, while the nodes from the master surface are permitted to do so. As a result, the distribution of the contact output such as contact stresses and slip, is not ideal. However, this method is computationally inexpensive.
- **Surface-to-surface** contact formulation: Unlike the previous contact formulation, surface-to-surface contact ensures the non-penetration of nodes from both surfaces. As a result, the contact outputs are more accurate, though it comes at a higher computational cost.

Concerning the numerical treatment of contact interactions, both normal and tangential formulations such as penalty methods, Lagrange multipliers, and augmented Lagrange multipliers are commonly used in commercial software like ABAQUS. More recent approaches, including the mortar method [167], [169] and Third Medium Contact (TMC) [177], have not yet gained widespread adoption in commercial FE software. A brief definition of contact properties is outlined in Section 3.5.

4.5.3 Rubber-reinforcements interaction

Within ABAQUS, the *embedded constraint* is used to constrain reinforcements to remain inside their host rubber domain. When an element is embedded into a host region, the displacement nodal degrees of freedom are used as constraints to enrich the displacement of the host region. This constraint is similar to the displacement enrichment used in the Generalized Finite Element Method (GFEM).

4.6 Static/Dynamic loads on tire

In operating conditions, tires are subjected to various loads from the vehicle's body loads or from contact with road asperities or irregularities. These loads can be classified as either static or dynamic. Static loads remain constant over time, while dynamic loads change. In forced dynamic vibrations, applied forces on the tire can be either deterministic (see Figure 4.12(b) and

4.12(c)) or nondeterministic. In the first case, the history sequence of the excitation can be described with a mathematical expression. In the second case, the loading sequence is stochastic. In all existing works, there is no tire model that accounts for dynamic loads (see Figure 4.12(b) and Figure 4.12(c)).

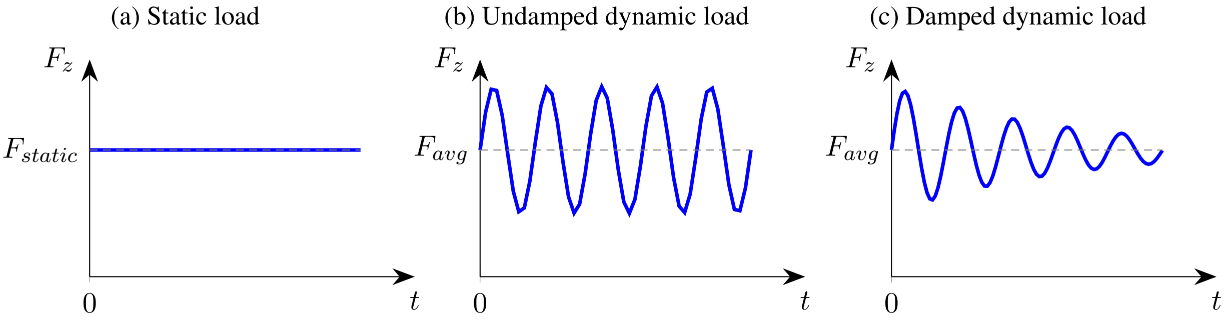

Figure 4.12: Types of loads applied to the tire.

4.7 Kinematics

In this section, we focus our attention of kinematics of rubber compounds in tire casing.

Domain and Boundaries

The boundary value problem of the rubber domain consists of:

$\Omega \subset \mathbb{R}^3$: Tire rubber domain

$\Gamma = \Gamma_u \cup \Gamma_\sigma \cup \Gamma_c$: Boundary

Γ_u : Prescribed displacement (Dirichlet)

Γ_σ : Prescribed traction (Neumann)

Γ_c : Potential contact surface with rigid road

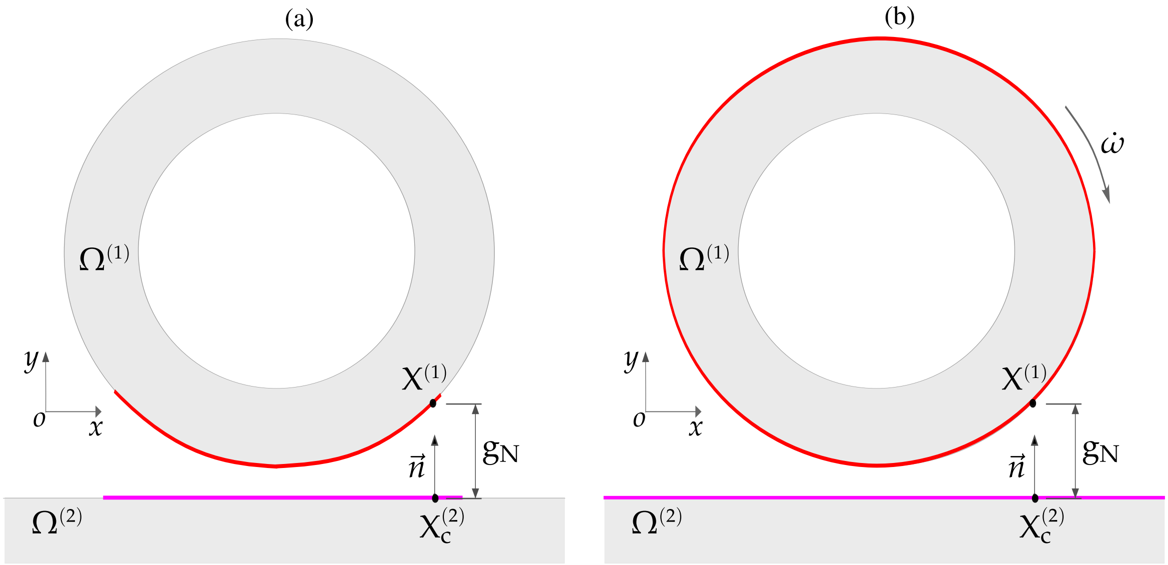

Figure 4.13: Basic representation of the contact gap and potential contact surfaces between the tire and the road. (a) in Static, (b) in rolling.

Deformation Measures

Let us recall $\Omega_0 \subset \mathbb{R}^3$ be the reference configuration and Ω_t the current configuration at time t. The deformation map $\boldsymbol{\varphi} : \Omega_0 \times [0, T] \to \mathbb{R}^3$ defines:

$$\mathbf{F} = \nabla_{\mathbf{X}}\boldsymbol{\varphi}, \quad J = \det(\mathbf{F}) \tag{4.3}$$

$$\dot{\boldsymbol{\varphi}} = \frac{\partial \boldsymbol{\varphi}}{\partial t}, \quad \ddot{\boldsymbol{\varphi}} = \frac{\partial^2 \boldsymbol{\varphi}}{\partial t^2} \tag{4.4}$$

4.7.1 Governing Equations

For all $\mathbf{x} \in \Omega_t$ and $t > 0$, the equilibrium of rubber compound is governed by:

Linear Momentum Balance

$$\rho\ddot{\mathbf{u}}(\mathrm{x}, \mathrm{t}) = \nabla \cdot \boldsymbol{\sigma}(\mathrm{x}, \mathrm{t}) + \mathbf{b}, \qquad \forall(\mathrm{x}, \mathrm{t}) \in \Omega_t \times [0, \mathrm{T}] \tag{4.5}$$

where:

- ρ: Material density
- $\ddot{\mathbf{u}}(\mathrm{x}, \mathrm{t})$: Acceleration field
- $\boldsymbol{\sigma}(\mathrm{x}, \mathrm{t})$: Total Cauchy stress tensor
- $\mathbf{b}$: Body force per unit volume

Nearly-to Incompressibility Constraint

$$\det(\mathbf{F}) - 1 = 0 \tag{4.6}$$

where $\mathbf{F} = \mathbf{I} + \nabla \mathbf{u}$ is the deformation gradient.

3. Constitutive Law: visco-hyperelastic-mullins effect

$$\boldsymbol{\sigma}(\mathrm{x}, \mathrm{t}) = -p\mathbf{I} + \boldsymbol{\sigma}_{\text{eq,dev}}(\mathrm{x}, \mathrm{t}) + \boldsymbol{\sigma}_{\text{neq}}(\mathrm{x}, \mathrm{t}, \mathrm{Q}) \tag{4.7}$$

where:

- p: Hydrostatic pressure (Lagrange multiplier for incompressibility)
- $\boldsymbol{\sigma}_{\text{dev,eq}}(\mathrm{x}, \mathrm{t})$: Deviatoric part of the equilibrium stress component
- $\boldsymbol{\sigma}_{\text{neq}}(\mathrm{x}, \mathrm{t}, \mathrm{Q})$: Non-equilibrium stress component

A simpler form can then be derived by exploiting expressions from Eq.(3.75b) and (3.87b).

Equilibrium Stress (Ogden-Roxburgh)

$$\boldsymbol{\sigma}_{\text{eq}} = \frac{1}{J}\mathbf{F}\frac{\partial W_{\text{eq}}}{\partial \mathbf{C}}\mathbf{F}^{\mathsf{T}} = -p_{\text{vol}}\mathbf{I} + \boldsymbol{\sigma}_{\text{eq,dev}}(\mathrm{x}, \mathrm{t}); \quad J = \det(\mathbf{F}) \tag{4.8}$$

with strain energy density:

$$W_{\text{eq}}(\bar{\mathbf{C}}, J, \eta) = \eta \hat{W}_{\text{dev}}(\bar{\mathbf{C}}) + U(J) \tag{4.9}$$

and softening function:

$$\eta(\zeta) = 1 - \frac{1}{r}\,\text{erf}\left(\frac{\zeta - W_{\text{max}}}{m + \beta\zeta}\right) \tag{4.10}$$

History variable evolution:

$$\zeta(\mathbf{x}, t) = \max_{s \in [0,t]} W_{\text{dev}}(\mathbf{x}, s) \tag{4.11}$$

Non-Equilibrium Stress (Prony Series)

Non-equilibrium stress is due to rubber viscoelasticity and is defined as

$$\boldsymbol{\sigma}_{\text{neq}} = \sum_{k=1}^{M} \mathbf{Q}_k \tag{4.12}$$

with evolution equations:

$$\dot{\mathbf{Q}}_k + \frac{1}{\tau_k}\mathbf{Q}_k = g_k \dot{\boldsymbol{\varepsilon}}_{\text{dev}}, \quad k = 1, \ldots, M \tag{4.13}$$

where:

- $\boldsymbol{\varepsilon}$: Hencky (logarithmic) strain tensor
- $\boldsymbol{\varepsilon}_{\text{dev}} = \boldsymbol{\varepsilon} - \frac{1}{3}(\operatorname{tr}\boldsymbol{\varepsilon})\mathbf{I}$: Deviatoric part of Hencky strain
- g_k, τ_k: Prony series parameters

Hencky Strain Definition:
The Hencky strain tensor is given by:

$$\boldsymbol{\varepsilon} = \frac{1}{2}\ln \mathbf{b}, \quad \mathbf{b} = \mathbf{F}\mathbf{F}^T \quad \text{(left Cauchy-Green tensor)} \tag{4.14}$$

where $\ln$ denotes the tensor logarithm.

Contact Conditions on Γ_c

$\forall$t $\in [0, T]$, contact compatibility conditions between tread surface and road have to be satisfied in the normal direction and tangential plane:

1. **Normal Contact Conditions**

$$g \geq 0 \tag{4.15a}$$

$$\boldsymbol{\lambda}_n \leq 0 \tag{4.15b}$$

$$\boldsymbol{\lambda}_n g = 0 \tag{4.15c}$$

   where $g = (\mathbf{x} - \mathbf{x}_{\text{road}}) \cdot \mathbf{n}_{\text{road}}$ is the gap function.

2. **Frictional Contact Conditions (Coulomb Model)**

$$\|\boldsymbol{\lambda}_\tau\| \leq \mu|\boldsymbol{\lambda}_n| \tag{4.16a}$$

$$\boldsymbol{\lambda}_\tau \cdot \mathbf{v}_T + \mu|\boldsymbol{\lambda}_n|\|\mathbf{v}_T\| = 0 \tag{4.16b}$$

$$\mathbf{v}_T = \dot{\mathbf{u}}_T - \mathbf{v}_{\text{road},T} \tag{4.16c}$$

   where:

   - $\mathbf{t}_T$: Tangential traction vector

- $\mathbf{v}_T$: Relative tangential velocity
- μ: Coefficient of friction
- $\dot{\mathbf{u}}_T$: Tangential component of material velocity
- $\mathbf{v}_{\text{road},T}$: Tangential component of road velocity

3. **Traction Decomposition**

$$\boldsymbol{\sigma}\mathbf{n} = \boldsymbol{\lambda}_n \mathbf{n}_{\text{road}} + \boldsymbol{\lambda}_\tau \tag{4.17}$$

Boundary Conditions

1. **Dirichlet Condition on Γ_u:** This type of boundary conditions is used to enforce the contact between the rim and tire rim cushion or the rigid body constraint between wheel axle and tire.

$$\mathbf{u} = \bar{\mathbf{u}} \tag{4.18}$$

2. **Neumann Condition on Γ_σ:** This type of boundary condition is used to prescribe the inflation pressure on tire inner surface.

$$\boldsymbol{\sigma}\mathbf{n} = \bar{\mathbf{t}} \tag{4.19}$$

Initial Conditions (at $t = 0$)

Besides spatial conditions, there is also initial conditions. At $t = 0$, we have the following conditions:

$$\mathbf{u}(\mathbf{x}, 0) = \mathbf{u}_0(\mathbf{x}) \tag{4.20a}$$

$$\dot{\mathbf{u}}(\mathbf{x}, 0) = \mathbf{v}_0(\mathbf{x}) \tag{4.20b}$$

$$\mathbf{Q}_k(\mathbf{x}, 0) = \mathbf{0}, \quad k = 1, \ldots, M \qquad \textit{No residual viscous stress} \tag{4.20c}$$

$$\zeta(\mathbf{x}, 0) = 0 \qquad \textit{No residual damage} \tag{4.20d}$$

$$\boldsymbol{\varepsilon}(\mathbf{x}, 0) = \mathbf{0} \qquad \textit{No residual strain} \tag{4.20e}$$

Summary of the Strong Form for tire rubber-road BVP

Find fields $\mathbf{u}(\mathbf{x},t)$, $p(\mathbf{x},t)$, $\boldsymbol{\lambda}_n(\mathbf{x},t)$, and $\boldsymbol{\lambda}_\tau(\mathbf{x},t)$ such that:

$$\rho\ddot{\mathbf{u}} = \nabla\cdot\boldsymbol{\sigma} + \mathbf{b} \text{ in } \Omega\times(0,T] \tag{4.21a}$$

$$\det(\mathbf{F}) - 1 = 0 \text{ in } \Omega\times(0,T] \tag{4.21b}$$

$$\boldsymbol{\sigma} = -p\mathbf{I} + \boldsymbol{\sigma}_{\text{dev,eq}} + \boldsymbol{\sigma}_{\text{neq}} \text{ in } \Omega\times(0,T] \tag{4.21c}$$

$$\dot{\mathbf{Q}}_k + \tau_k^{-1}\mathbf{Q}_k = g_k\dot{\boldsymbol{\varepsilon}}_{\text{dev}} \text{ in } \Omega\times(0,T];\ k=1,\ldots,M \tag{4.21d}$$

$$\boldsymbol{\sigma}\mathbf{n} = p_c\mathbf{n}_{\text{road}} + \mathbf{t}_T \text{ on } \Gamma_c\times(0,T] \tag{4.21e}$$

$$g\geq 0, \boldsymbol{\lambda}_n \leq 0, \boldsymbol{\lambda}_n g = 0 \text{ on } \Gamma_c\times(0,T] \tag{4.21f}$$

$$\|\boldsymbol{\lambda}_\tau\| \leq \mu|\boldsymbol{\lambda}_n| \text{ and } \boldsymbol{\lambda}_\tau\cdot\mathbf{v}_T + \mu|\boldsymbol{\lambda}_n|\|\mathbf{v}_T\| = 0 \text{ on } \Gamma_c\times(0,T] \tag{4.21g}$$

$$\mathbf{u} = \bar{\mathbf{u}} \text{ on } \Gamma_u\times(0,T] \tag{4.21h}$$

$$\boldsymbol{\sigma}\mathbf{n} = \bar{\mathbf{t}} \text{ on } \Gamma_\sigma\times(0,T] \tag{4.21i}$$

$$\mathbf{u}(\mathbf{x},0)\mathbf{u}_0(\mathbf{x}) \tag{4.21j}$$

$$\dot{\mathbf{u}}(\mathbf{x},0) = \mathbf{v}_0(\mathbf{x}) \tag{4.21k}$$

$$\mathbf{Q}_k(\mathbf{x},0) = \mathbf{0}, \quad k=1,\ldots,M \tag{4.21l}$$

$$\zeta(\mathbf{x},0) = 0 \tag{4.21m}$$

$$\varepsilon(\mathbf{x},0) = \mathbf{0} \tag{4.21n}$$

4.8 Challenges:

Although an enhancement with the above-mentioned method of identifying tire material parameters overcomes the limitations associated with existing models, it is imperative to note that the accuracy, performance and robustness of the resulting model are closely conditioned by certain constraints inherent to its deployment within the framework of the finite element method, which entails the following challenges:

- **Nonlinearity related challenges**: Tire modeling involves three major types of nonlinearities, which require a deep understanding of the problem we are dealing with and also the capabilities of the computer program we want to use since all this is to be involved in a dynamic contest.
  - Geometrical nonlinearity: the fact that the material undergoes large deformation inevidently implies that in the course of the dynamic loading the geometry or domain significantly changes which in the context of Finite element method can result in *mesh distortion*. Even more, this is accentuated when the loading rate is relatively

high. That is to say there happens a huge change in shape in a single load increment. Latter, we discuss solutions to overcome this challenge;

  - Material nonlinearity: viscoelasticity behavior of the material is responsible for this type of nonlinearity and drives the strain rate dependence of the material. As the *strain state* in such materials is *time dependent*, so does the stress state via the constitutive law. This key information is very important for the choice of the numerical solver in dynamics;
  - Contact nonlinearity: given that the tire is permanently in contact with the road through its tread, we must ensure that at each time step there is contact compatibility, which is enforced with boundary conditions by choosing an appropriate numerical scheme among those integrated in the software. This imposes a requirement on the mesh size, which must be densified in the vicinity of potential contact pairs. However, in the case of dynamic explicit solver the refinement of the mesh leads to a decrease in *stable characteristic time increment*, resulting in a very long computational time.

- **Mesh distortion**: Depending on the loading rate, tire mesh shape and size can significantly change due to hyperelasticity in the course of deformation between two instants t_n and t_{n+1}, leading to spurious or inaccurate results. This deterioration of mesh quality is called *mesh distortion* and is a major problem to be addressed when choosing either an implicit or explicit solver for solving dynamic problems. Thus, for stability reasons, a suitable procedure is to be implemented to work this problem around and guarantee that the mesh quality is permanently verified at each time step or increment.
- **Computational cost**: FEA can be very expensive when the size of the topology is large and when many sources of nonlinearities are involved, like in tire simulation. In order to improve the runtime of the model, parallel computing has to be utilized and also the mesh size has to be optimized.

Thus, the proposed computer model is expected to efficiently deal with these challenges while ensuring accuracy, reliability, and efficiency for more convenient practical deployment for further innovation in the field.

4.9 Design of the modeling road-map

In the literature, the standard modeling process of tire consists in four main phases (see Figure 4.14): the generation of the 3D geometry, Mounting of the tire on rim, Inflation of the tire and the loading of the tire with axle load.

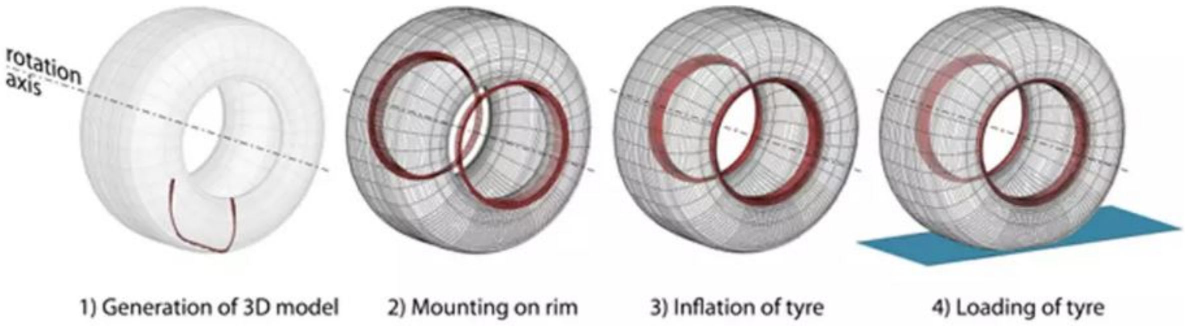

Figure 4.14: Standard tire modeling process [178].

For a concrete case study of tire modeling and given all the challenges it involves, we have adopted a progressive improvement of the model, starting from the simplest case to the targeted one, as illustrated in the flowchart in Figure 4.15.

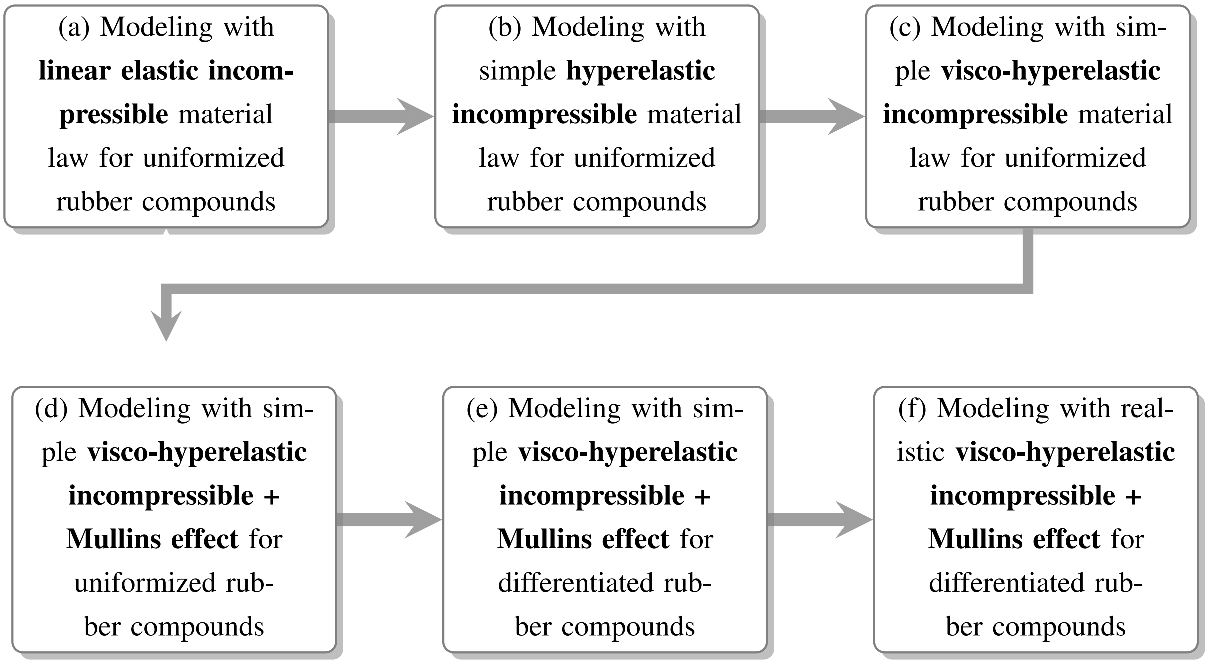

Figure 4.15: Modeling road-map adopted: progressive improvement.

In the following two chapters, stages (a) to (d) were used to implement and refine the proposed model. Then, the validation with laboratory experiments was conducted in stage (f).

5 Implementation of the method

5.1 Case study 1: a proof of concept analysis

This section summarizes outcomes from the published conference proceedings [179] and [180], respectively referred to as P5 and P6:

P5: **B. S. Sadjiep Tchuigwa**, J. Krmela, and J. Pokorny, “Toward detailed modeling of tires with linear elastic rubber compounds using finite element method,” IOP Conference Series: Earth and Environmental Science, vol. 1380, no. 1, p. 012 018, Aug. 2024. DOI:10.1088/1755-1315/1380/1/012018. (indexed in Scopus and Web of Science).

P5: **B. S. Sadjiep Tchuigwa**, J. Krmela, and J. Pokorný, “A numerical study of the influence of the choice of rubber material behavior on the static response of tires,” IOP Confer- ence Series: Earth and Environmental Science, vol. 1380, no. 1, p. 012 019, Aug. 2024. DOI: 10.1088/1755-1315/1380/1/012019. (indexed in Scopus and Web of Science).

5.1.1 Motivations

The tire response under static and dynamic loads is intrinsically linked with rubber compounds; thus, as observed with the experimental data, the constitutive law of the rubber part has to be chosen accordingly. Although Mullins’s damage is intricately associated with rubber compound response captured experimentally, as mentioned, there is no existing tire simulation inventoried with hyper-pseudoelastic rubber behavior in the literature. So, for the completeness of our comparison, we also consider it in this study. Thereby, in this work, a dynamic explicit FE-based comparative study is conducted on a static tire using ABAQUS[38] and considering four types of incompressible constitutive laws for rubber compounds: elastic(EL), hyperelastic(HE), visco-hyperelastic(VH), and hyper-pseudoelastic(HM). The selected comparison variables are radial deformation, maximum Von Mises stress, CPU time, contact patch, and contact pressure, respectively.

5.1.2 Material and method

Before going further, it is worth defining the hypothesis under which the current study was conducted:

- Rubber compounds, namely tread, inner liner, sidewall, undertread, and apex, are assumed to have the same mechanical behavior so that the unique rubber matrix model holds;
- The rim is modeled as a rigid body using coupling contact with the wheel's center;
- The simplified bead approach with a homogenized property is adopted [181];
- The rigid road model is considered;
- Since only the static vertical loading setup is treated here, frictional effects are disregarded.

5.1.3 Geometry of the tire:

The geometry of the tire 175/75R14, whose half cross-section is depicted in Figure 5.1, was selected for this study and was drawn out from [182]. It is a radial passenger tire with 618mm diameter and 175mm tread width. It is designed to be mounted on a 355.6mm rim diameter.

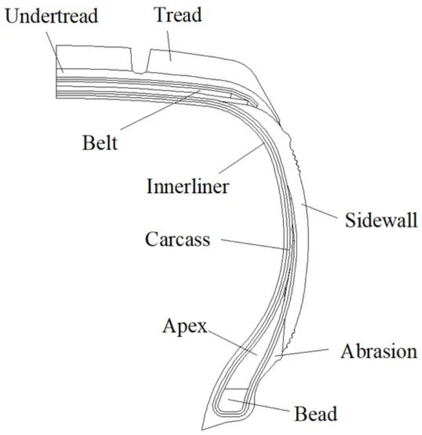

Figure 5.1: half cross-section of 175/75R14 tire [182]

This scanned image was utilized as a layout to sketch a cross-section in the software AUTOCAD. Subsequently, the DXF file was imported into ABAQUS and used to draw the 3D tire using a combination of commands such as revolution, symmetry, and mirror. Based on the cross-section in Figure 5.2(f), beads in Figure 5.2(a) and rubber compounds Figure 5.2(f) were generated from their respective cross-sections using a 360° revolution along the transversal axis passing through the wheel's center(O). As for carcass parts in Figure 5.2(d), a single element was first drawn, and the other 299 were generated using a radial pattern feature around the transversal axis.

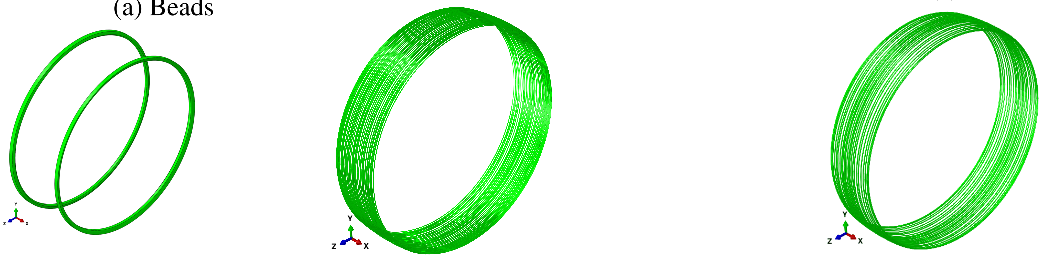
(a) Beads (b) Steel cords (c) Textile cords

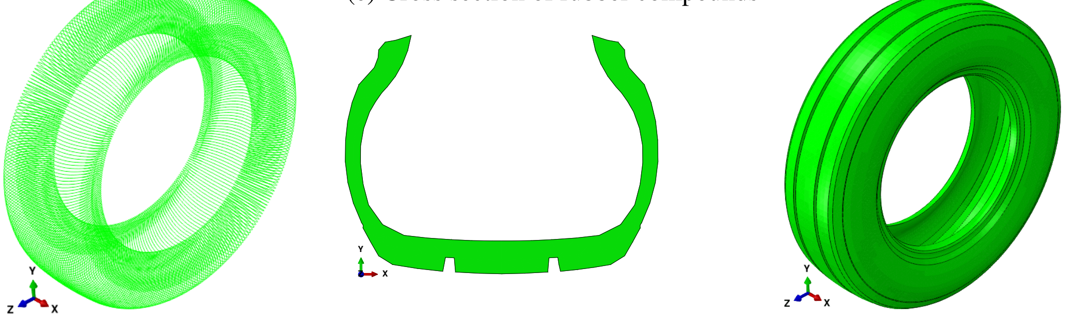
(d) Carcass (e) Cross section of rubber compounds (f) 3D view of rubber compounds

Figure 5.2: Parts of the tire

5.1.4 Material properties:

Another important input needed for building the FE model is the mechanical properties of parts or structural components of the problem. For this sake, a combination of uniaxial tensile tests is usually performed in laboratory conditions on steel cords, textile cords, and beads in compliance with the relevant test standards. Similarly, a cyclic tensile test is needed to capture the dynamic response of rubber compounds as investigated by authors in [133], [134]. Hence, the mechanical properties of the reinforcements adopted in this study are highlighted in Table 5.1.

Table 5.1: Reinforcement material propeties

Tire parts	E [MPa]	ν	$\varnothing$ [mm]	ρ [Kg/m^3]
Steel cords	15.724	0.3	0.60	7 850
Textile cords	1 900	0.35	0.80	1 250
Carcass	1 900	0.40	1.00	1 250
Bead	164 499	0.29		7 850

Aside from that, with data extracted from [133], [182], [183], we consider four (04) cases of incompressible rubber material behavior, ranging from elastic (EL), hyperelastic (HE), visco-hyperelastic (VH), to hyper-pseudoelastic (HM), all with mechanical properties reported in Table 5.2.

Table 5.2: Material properties of rubber compounds

Elastic	
Density ρ [Kg/m^3]	1200
E [MPa]	100
ν	0.485

a **Case 1**: linear elastic material model

Hyperelastic	
Density ρ [Kg/m^3]	1200
C_{01} [MPa]	15.724
C_{10} [MPa]	1.111
D_1 [MPa^{-1}]	0.0018

b **Case 2**: Hyperelastic material model

Hyperelastic		viscoelastic	
Density ρ [Kg/m^3]	1200	g_1	0.1433
C_{01} [MPa]	15.724	g_2	0.0852
C_{10} [MPa]	1.111	τ_1 [s]	7.6125
D_1 [MPa^{-1}]	0.0018	τ_2 [s]	235.62

c **Case 3**: Visco-hyperelastic material model

Hyperelastic		Mullins damage	
Density ρ [Kg/m^3]	1200		
C_{01} [MPa]	15.724	r	2.18
C_{10} [MPa]	1.111	m	0.38
D_1 [MPa^{-1}]	0.0018	β	0.5

d **Case 4**: Hyper-pseudoelastic material model

5.1.5 Mesh properties:

Bearing in mind that the time step in a dynamic explicit scheme is closely conditioned by a stable time increment, which in turn depends on mesh properties, special care must be taken when creating the mesh. The best procedure is to mesh each entity separately. Furthermore, it prevents us from ending up with densified mesh in the rubber domain in the vicinity of reinforcements. However, for the sake of reducing the problem size, knowing that the contact zone between the tire and the road is located in the lower portion of the tire throughout the test, the rubber part in Figure 5.2(f) was partitioned into two parts: the lower part is bounded by an angle of 35° on either side of the vertical axis centered at O and the second part the remainder. The mesh size of the former part is smaller than that of the latter. Except for beads that were meshed using C3D8R elements, all the other fibers were meshed as B32H elements, which correspond to 1D beam elements (with 3 translations and 3 rotations degrees of freedom per node). Table 5.3 summarizes the details of the mesh of the tire's parts.

Table 5.3: Mesh properties

Parts	**Elements**	**Element type**	**Number of elements**
Rubber parts	3D solid	C3D8R: 8-node linear brick, reduced integration with hourglass control	20 090
Bead	3D solid	C3D8R: 8-node linear brick, reduced integration with hourglass control	3 248
Textile cords	1D beam	B32H: 3-node quadratic hybrid elements	3 082
Carcass	1D beam	B32H: 3-node quadratic hybrid elements	19 800
Steel cords	1D beam	B32H: 3-node quadratic hybrid elements	5 768
Road	2D Shell	S4R: 4-node linear shell with hourglass control	16 950

In addition, enhanced hourglass control together with distortion was activated to prevent mesh distortion arising from large deformation. Also, reduced integration was selected to avoid volumetric locking, mostly in the rubber part. The created mesh is shown in Figure 5.3.

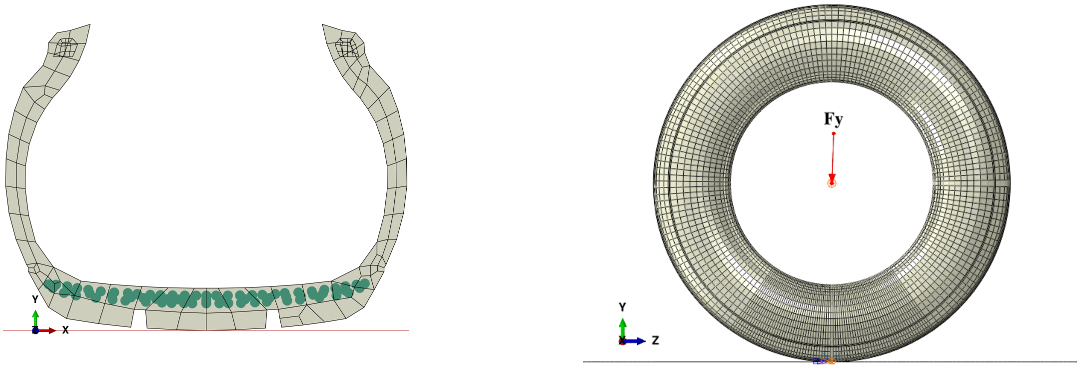
(a) Mesh view on the cross-section

(b) Longitudinal view on the tire

Figure 5.3: Parts of the tire

5.1.6 Boundary conditions:

Three types of boundary conditions were enforced: Prior to this, the so-called hard contact type was created.

- *Rim-tire interaction*: As assumed in the introduction, the rim is a rigid body, so we enforce this condition by linking the rim's center (reference point) to its contact zone with the tire through a coupling constraint. To maintain consistency with this concept, we activated kinematic coupling under the coupling window and enabled all degrees of freedom;

- *Tire-road interaction*: This contact constraint was enforced using a combination of general contact interaction and surface-to-surface contact. While the former helps handle contact in general, including self-contact, which prevents contact violations in a body's interaction with itself, the second formulation helps restrict the contacting surface to the specified master (road) and slave (tread outermost face);
- *Embedded constraints*: all fibers, namely carcass, steel cords, textile cords and bead were connected to rubber matrix (hosting domain) using embedded constraints;
- all the degrees of freedom of road's nodes were blocked through the reference point at the center of the road;
- For stability reasons, U_x at the wheel's center was fixed.
- *Vertical applied load* F_y was applied linearly at the reference point located at wheel's center in Figure 5.3(b) up to the value of 7500N;
- *Inflation pressure*: a uniformly distributed pressure of 0.35MPa was applied on the inner liner surface;
- *Tire self-weight* was taken into account thanks to gravity effects defined on all model's elements except the road.

The abovementioned loads were applied in a single load step of $1s$, as represented in time history in Fig. 5.4

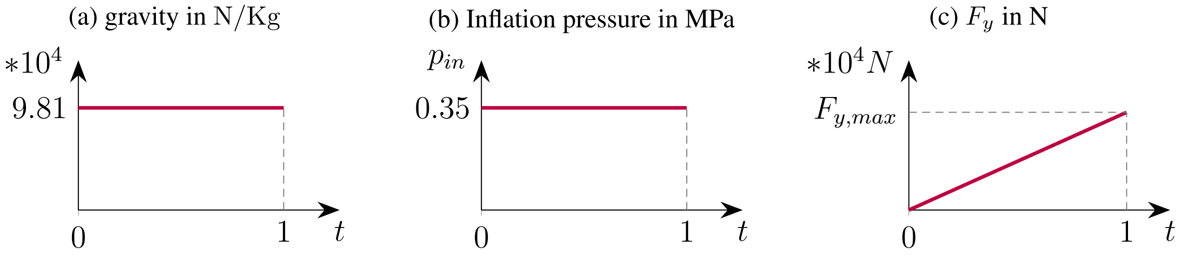

Figure 5.4: Load definition

With the help of a dynamic explicit scheme, it is possible to solve this equation without strictly enforcing equilibrium like in the implicit scheme through Newton-Raphson algorithm. Therefore, the former method is faster, but its drawback is that it necessitates choosing a stable time step Δt that fulfills the stability condition given as

$$\Delta t_{stable} = \frac{h}{c_L} \tag{5.1}$$

where h is the characteristic length of the element and $c_L = \sqrt{\frac{E}{\rho}}$. An alternative to this approach defined the critical time step as a function of the maximal eigenfrequency of the mesh and reads as follows

$$\Delta t_{stable} \leq \frac{2}{\omega_{max}} \tag{5.2}$$

Depending on the size of the finite elements, Δt_{stable} can be very small and lead to very long execution times. For the sake of getting the highest value possible, hexahedral elements were chosen over tetrahedral elements, and the mesh feature was set to comply with contact conditions and stability reasons. Under the details provided in Table 5.3, an initial time increment of $\Delta t_{stable} = 1.0128 \times 10^{-6} s$ was obtained. Among possible acceleration strategies, mass scaling is considered here to increase the time step. So, after many stability verifications, we obtained an acceptable mass scaling factor of 100, which means that in virtue of Eq. (5.1), we ended up with $\Delta t = 1.0128 \times 10^{-5} s$.

5.2 Results and discussion

All of the four tire models with rubber compounds outlined in Table 5.2, were computed separately, and the corresponding distribution of Mixes stress, vertical displacement U_y and normal contact stress are presented below in Figure 5.5 to 5.8, Figure 5.9 to 5.12 and Figure 5.13, respectively.

5.2.1 Von Mises stress distribution in $[\mathrm{MPa}]$

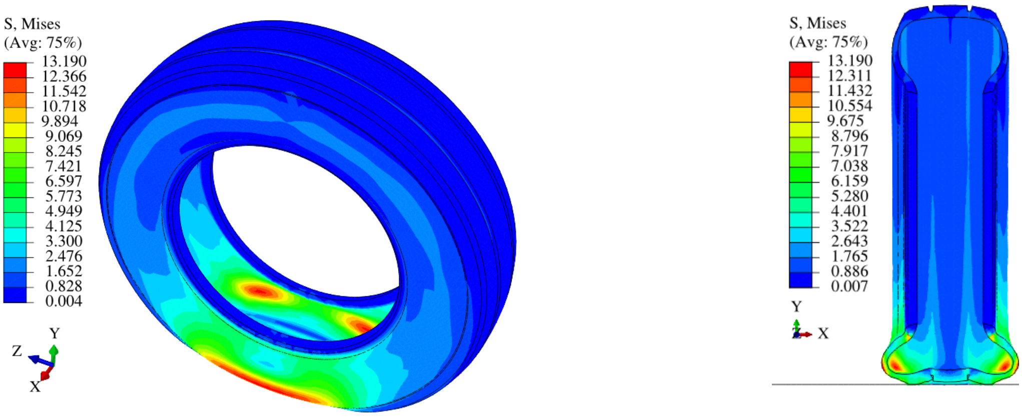
(a) 3D view

(b) rear view

Figure 5.5: σ_{VM} at $t = 1\ s$ in the tire with **incompressible linear elastic** rubber materials.

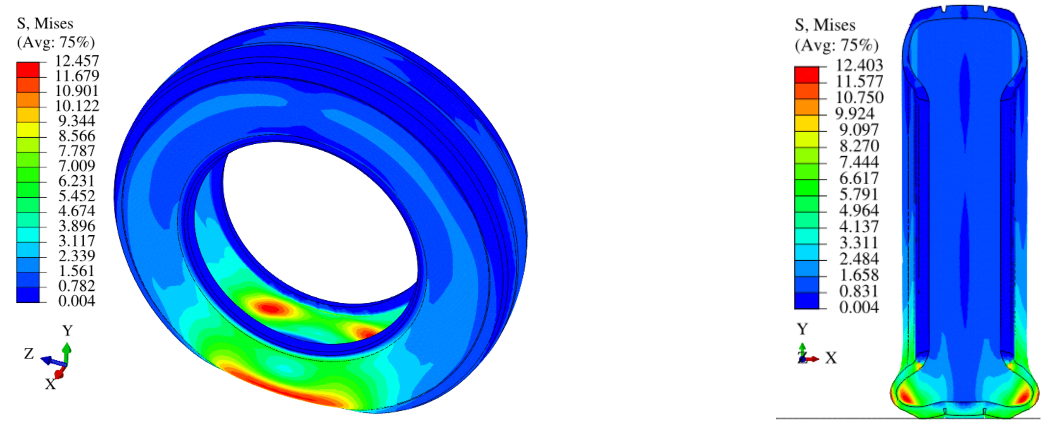
(a) 3D view

(b) rear view

Figure 5.6: σ_{VM} at $t = 1\ s$ in the tire with **incompressible hyperelastic** rubber materials.

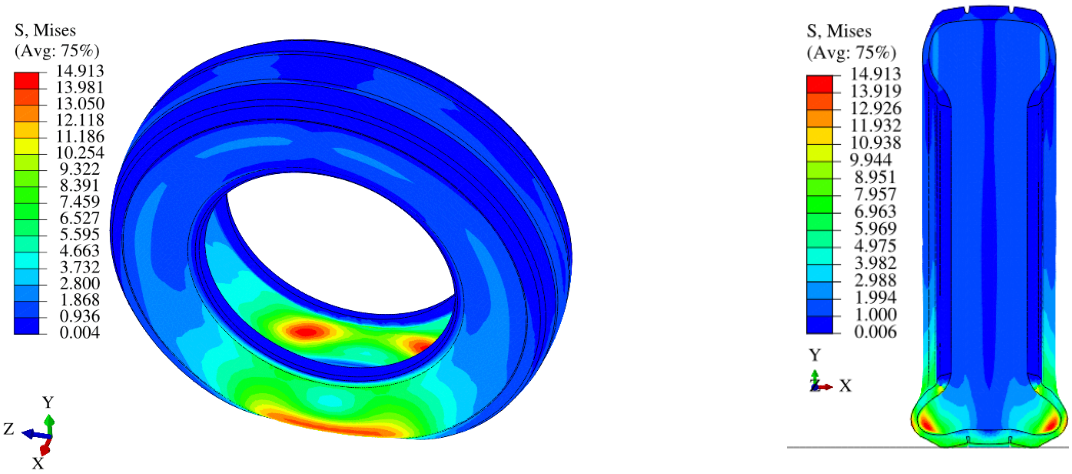
(a) 3D view

(b) rear view

Figure 5.7: σ_{VM} at $t = 1\ s$ in the tire with **incompressible visco-hyperelastic** rubber materials.

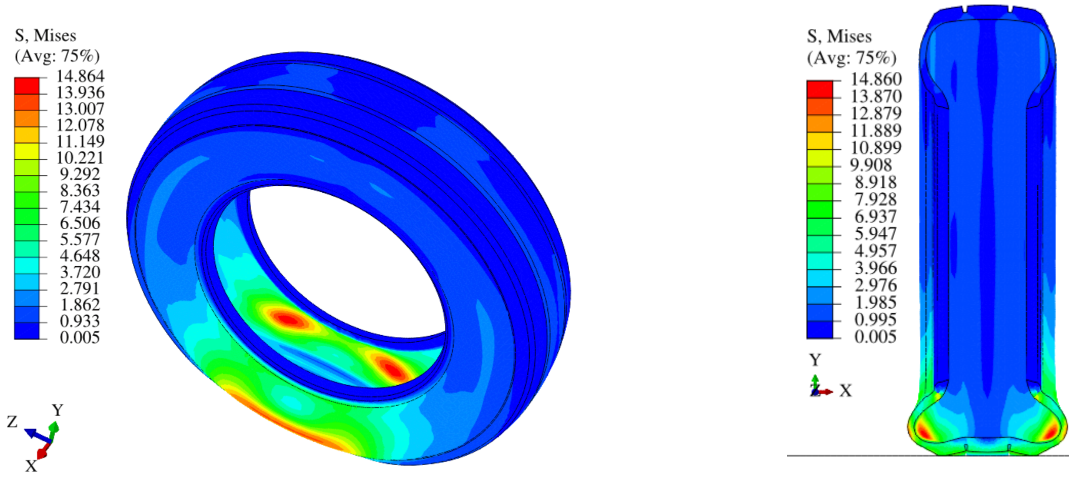
(a) 3D view

(b) rear view

Figure 5.8: σ_{VM} at $t = 1\ s$ in the tire with **incompressible hyper-pseudoelastic** rubber materials.

As expected, we observe that Von Mises stress is not the same for all the models, of which the values of the visco-hyperelastic and hyper-pseudoelastic models are closer to each other. The hyperelastic model has the lowest values and is followed by the elastic model.

5.2.2 Distribution of the vertical displacement U_y [mm]

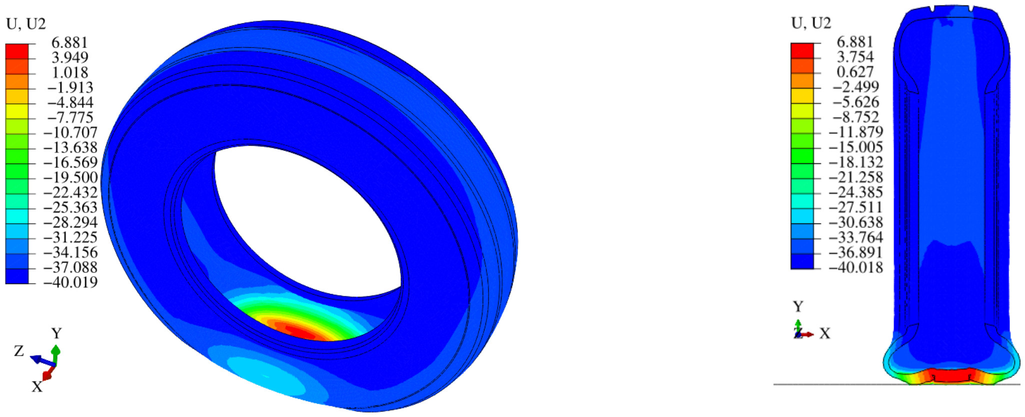

(a) 3D view (b) rear view

Figure 5.9: U_Y [mm] at $t = 1\ s$ in the tire with **incompressible linear elastic** rubber materials.

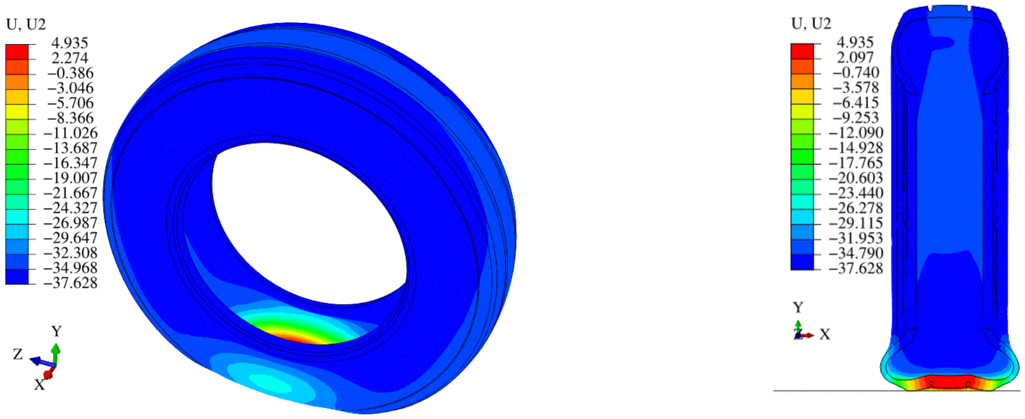

(a) 3D view (b) rear view

Figure 5.10: U_Y [mm] at $t = 1\ s$ in the tire with **incompressible hyperelastic** rubber materials.

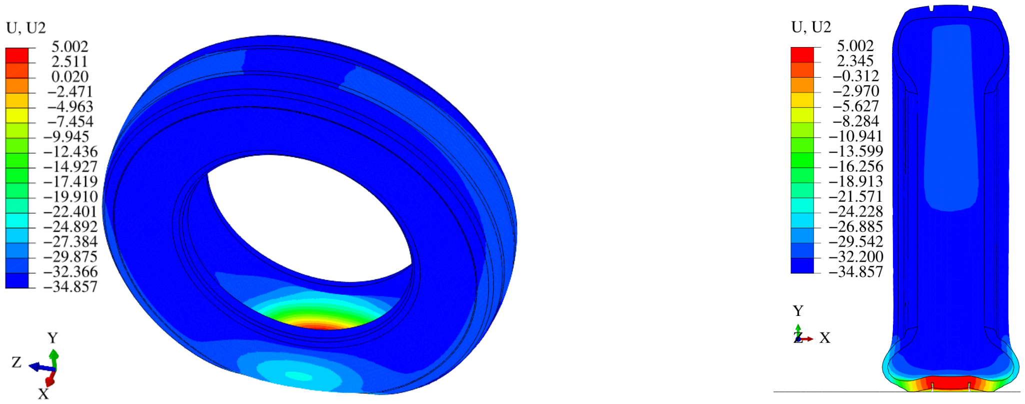

(a) 3D view (b) rear view

Figure 5.11: U_Y [mm] at $t = 1\ s$ in the tire with **incompressible visco-hyperelastic** rubber materials.

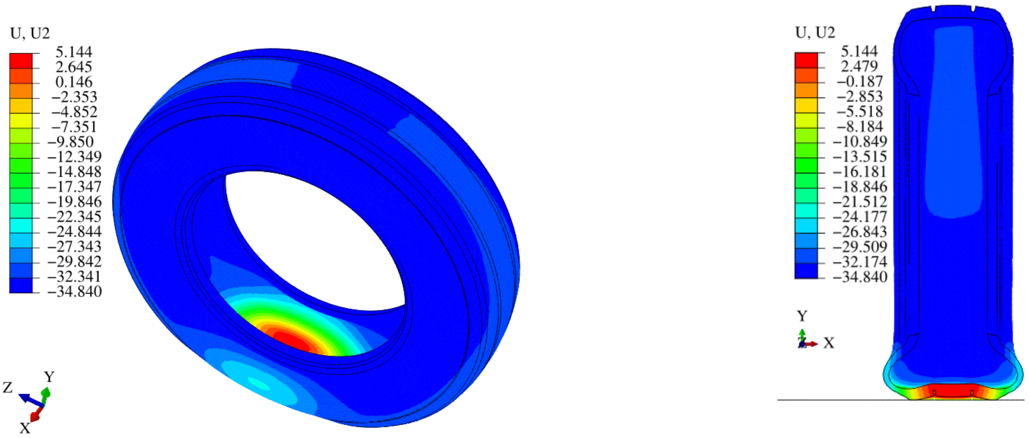

(a) 3D view

(b) rear view

Figure 5.12: U_Y [mm] at $t = 1\ s$ in the tire with **incompressible hyper-pseudoelastic** rubber materials.

When it comes to the comparison of vertical displacement U_y, we observe that the elastic model witnesses the highest vertical deformation $U_y = 40.019mm$ and is followed by the hyperelastic model with $U_y = 37.857mm$. After the previous ones, the visco-hyperelastic and hyper-pseudoelastic models come with almost the same value of U_y.

5.2.3 Distribution of the normal contact stress p_N [MPa]

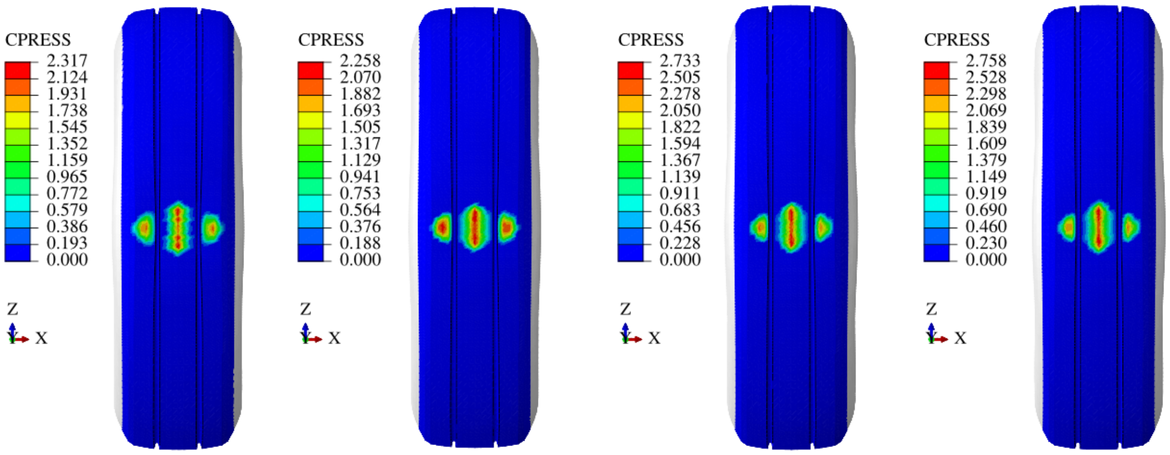

(a) Elastic

(b) Hyperelastic

(c) Visco-hyperelastic

(d) Hyper-pseudoelastic

Figure 5.13: Normal contact stress p_n at $t = 0.46\ s$ for different rubber material constitutive laws.

We see that, for instance, at $t = 0.46$, the contact patch shape is nearly the same for all models. However, there is a higher normal contact stress (circa 18%) with the visco-hyperelastic and hyper-pseudoelastic models than the elastic model.

5.2.4 Comparison of results

At the end of the simulation, we collected σ_{VM}, U_y, p_N and $CPU\ time$ for all of the four models and summarized them in Table 5.4 below

Table 5.4: results and performance

Model	**Elastic**	**Hyperelastic**	**Visco-hyperelastic**	**Pseudo-hyperelastic**
σ_{VM} [MPa]	13.190	12.460	14.910	14.864
U_y [mm]	40.02	37.63	34.86	34.65
p_N [MPa]	6.783	9.502	11.230	11.385
$CPU\ time$ [min]	82.00	70.53	100.30	68.82

It is more convenient to compare these models using a bar chart of the data in Table 5.4 and depicted in Fig. 5.14.

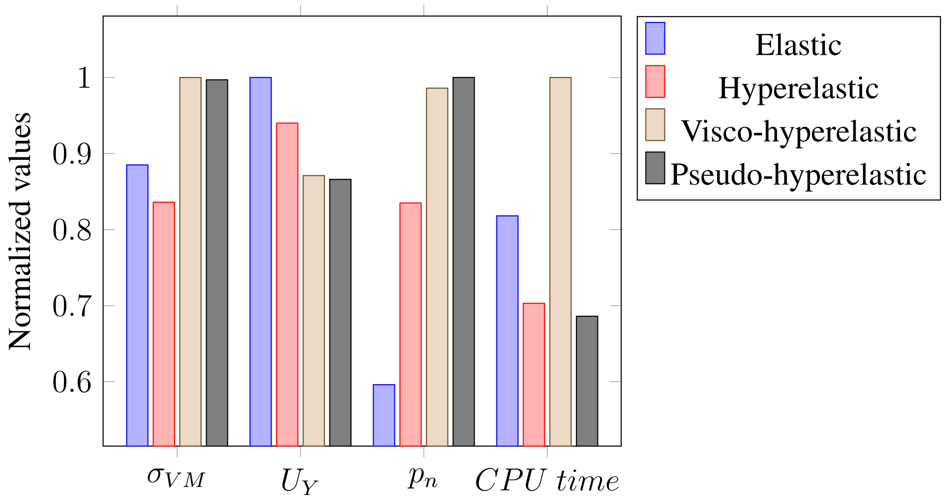

Figure 5.14: Performance analysis of the different models

5.3 Conclusion

This study has explored different approaches to modeling static tire response using different rubber constitutive behaviors, including elastic, hyperelastic, visco-hyperelastic, and unexplored hyper-pseudoelastic rubber behaviors. The comparative analysis was conducted on the results obtained using dynamic explicit FEM in ABAQUS, taking into account tire performance metrics such as radial deformation, maximum Von Mises stress, contact patch, and contact pressure. In light of the findings of this study, we demonstrate that the choice of rubber compound material behavior has to be made judiciously in accordance with the real material response recorded in laboratory testing so as to mimic the mechanical contribution of the element in the FE model. In such a way, there should be a good tradeoff between computational complexity and mod el accuracy. So, as long as the vertical displacement is the only target of the study, the visco-hyperelastic suffices, but when extended results such as stress distribution, contact pressure and CPU time are concerned, the model with Hyper-pseudoelastic rubber compound has to be prioritized. Furthermore, this model is better than the others since it is computationally less intensive and gives better results. The knowledge gained in this study paves the way for a more in-depth consideration of the constitutive behavior of rubber compounds for more accurate prediction of tire response, which is essential for the optimal use of materials but also for improving tire energy performance.

The remaining bottleneck to the industrial deployment of the proposed method is inherent in the considerable computational cost associated with the finite element method. In fact, the design of the tire involves, in reality, dynamic loads in more complex scenarios, such as transient rolling, steady state rolling and steady state dynamic. Therefore, in the next section, we introduce a numerical solution to improve FEM computational time.

5.4 Case study 2: a solution to computational cost

This section summarizes outcomes from the published journal article [184] and the conference paper [185], respectively referred to as P1 and P7:

P1: **B. S. Sadjiep. Tchuigwa**, J. Krmela, J. Pokorny, V. Krmelová, and P. Jilek, "Vectfem: A generalized MATLAB-based vectorized algorithm for the computation of global matrix/-force for finite elements of any type and approximation order in linear elasticity," Zeitschrift für angewandte Mathematik und Physik, vol. 75, no. 4, p. 150, 2024, ISSN: 1420-9039. DOI: 10.1007/s00033-024-02293-w, **WoS Q2 (SCOPUS Q1/D2) Jimp**.

P7: **B. S. Sadjiep. Tchuigwa**, J. Krmela, J. Pokorny, and V. Krmelová, "Improved and vectorised MATLAB-based algorithms for serial and parallel implementation of finite element method in linear elasticity," in Proceedings of the 23rd International Scientific Conference on Engineering for Rural Development, Jelgava, May 2024, pp. 1–6. DOI: 10.22616/ERDev.2024.23.TF212 (indexed in Web of Science and Scopus).

5.4.1 Motivations

In the context of the implementation of the finite element method, one of the major problems encountered is the computational cost. In order to speed up the computation of matrices and forces arising from FE formulation, we introduce a vectorized algorithm that drastically reduces the computational cost while maintaining the same memory usage as the existing algorithms.

This method can be implemented in any vector object-oriented language, such as Python, Fortran, and Julia.

6 Simulation, results and validation of the model

In this chapter, we have proceeded with the implementation and experimental validation of the computer model proposed in this thesis. The structure of the chapter is as follows: First, Section 6.1, the finite element model (FEM) of the selected tire was introduced. Next, in Section 6.2, we utilized this model for simulations and validated it against experimental results obtained from laboratory tests. Subsequently, in Section 6.3, we conducted further analyses to assess the tire's response under various operating conditions, such as steady-state rolling, random vibrations, and transient rolling.

6.1 Methodology

6.1.1 Model presentation

In this study, we have chosen the Matador $165/65\mathrm{R}13$ $77\mathrm{T}$ $\mathrm{MP}16$ tire for the analysis and validation of the proposed model. This tire, specifically designed for passenger vehicles, has a width of $165\mathrm{mm}$, an aspect ratio of 65%, and goes with a rim of diameter $330.2\mathrm{mm}$. More details are provided in Appendix 7, and its cross-section is shown in Figure 6.1. The tire's casing consists of rubber components, two layers of steel cords, one layer of textile cord, and one layer of ply, as depicted in the figure. The load index (LI) and maximum inflation pressure of this tire are equal to 412 Kg and $300\mathrm{kPa}$, respectively.

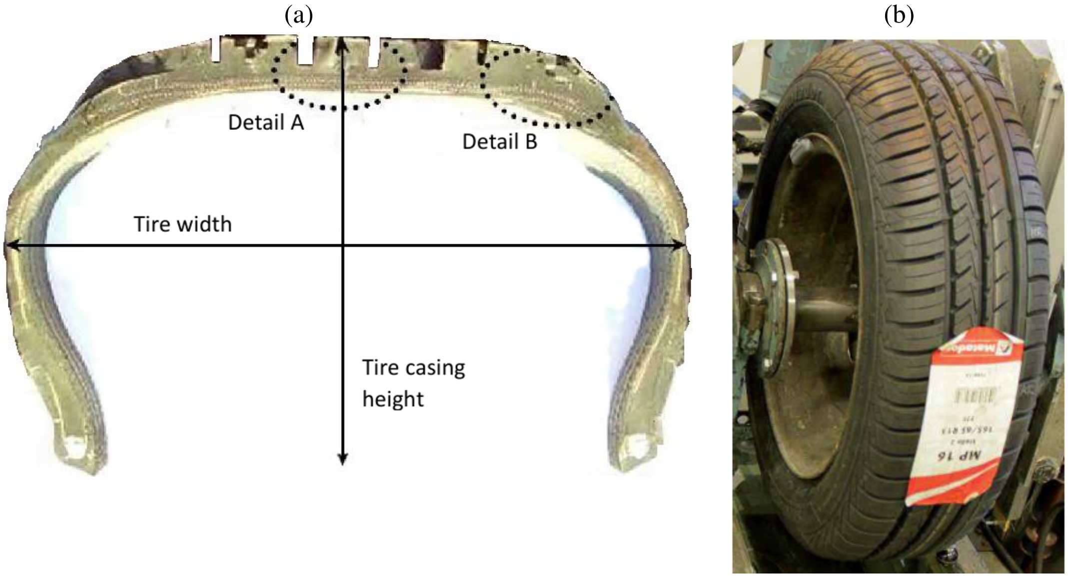

Figure 6.1: Cross-section and 3D view on $165/65\mathrm{R}13\ 77\mathrm{T}\ \mathrm{MP}16$ tire.

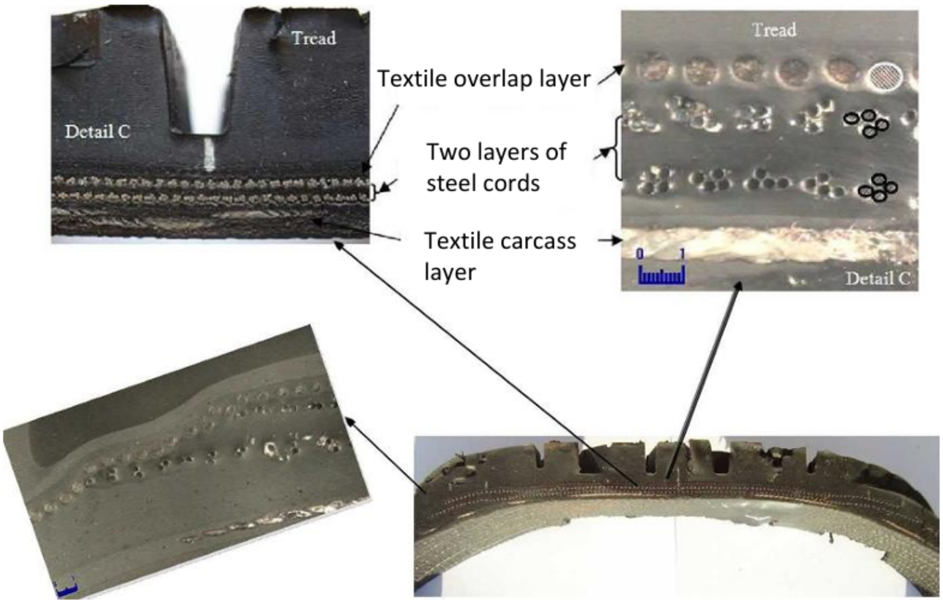

Figure 6.2: Details of casing.

This tire is made up of several rubber-like components, including the tread, sidewall, rim cushion (also known as bead rubber), inner liner, bead bundle (or bead filler), rubber for steel-cord belts, and rubber for textile-cord belts. In terms of tire reinforcement orientation, the carcass angle is set at zero degrees, while the steel cords are embedded at an angle of 23 degrees. The textile overlaps are oriented at 90 degrees. A better view of these components is shown in Figure 6.1.

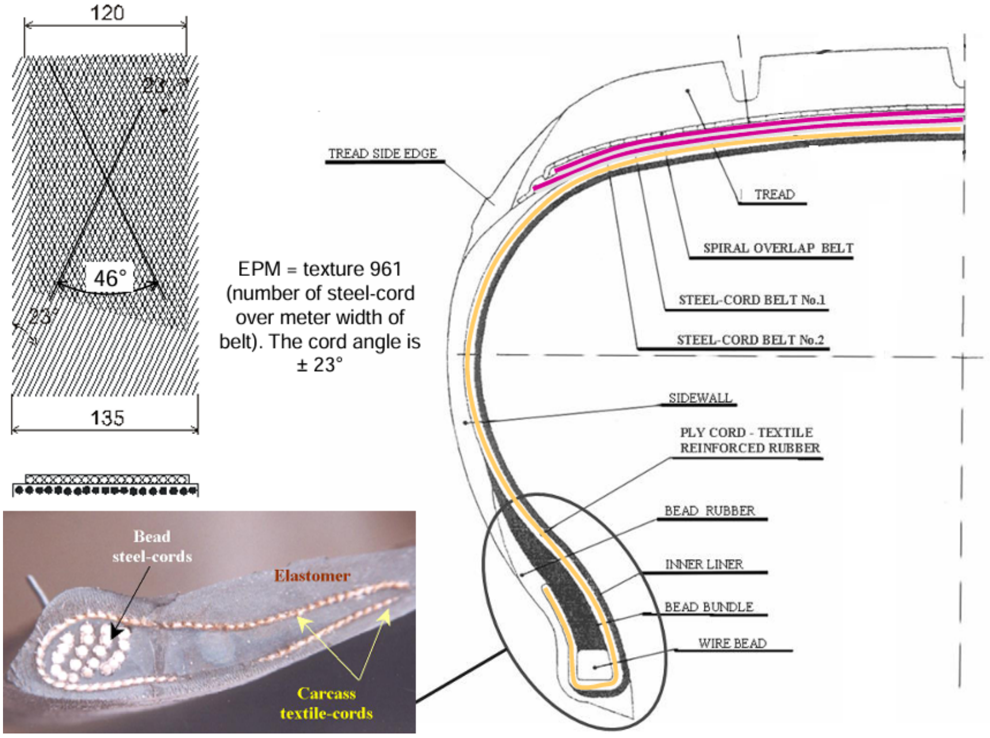

Figure 6.3: Tire casing parts.

Besides the internal components of the tire casing, the rolling surface of this tire is designed with patterns to ensure stability in adverse rolling conditions, as shown in Figure 6.1(b).

6.1.2 Topology

The creation of the tire topology (geometry) started with scanning of the cross section (see Figure 6.3), then the generated image was imported into AUTOCAD as a reference for the sketching of the cross-section layers and components. Afterward, the obtained sketch was imported with the extension $.stp$ into ABAQUS. Next, this sketch was used to create the cross-section of the tire in 2D axisymmetric. In this context, rubber compounds were modeled using CGA3RH and CGA4RH elements, while all reinforcements (steel cords, textile cap cords, and carcass) were modeled with SFMGAX1 surface elements. Subsequently, the 3D mesh of the tire was generated following the workflow in Figure 6.4.

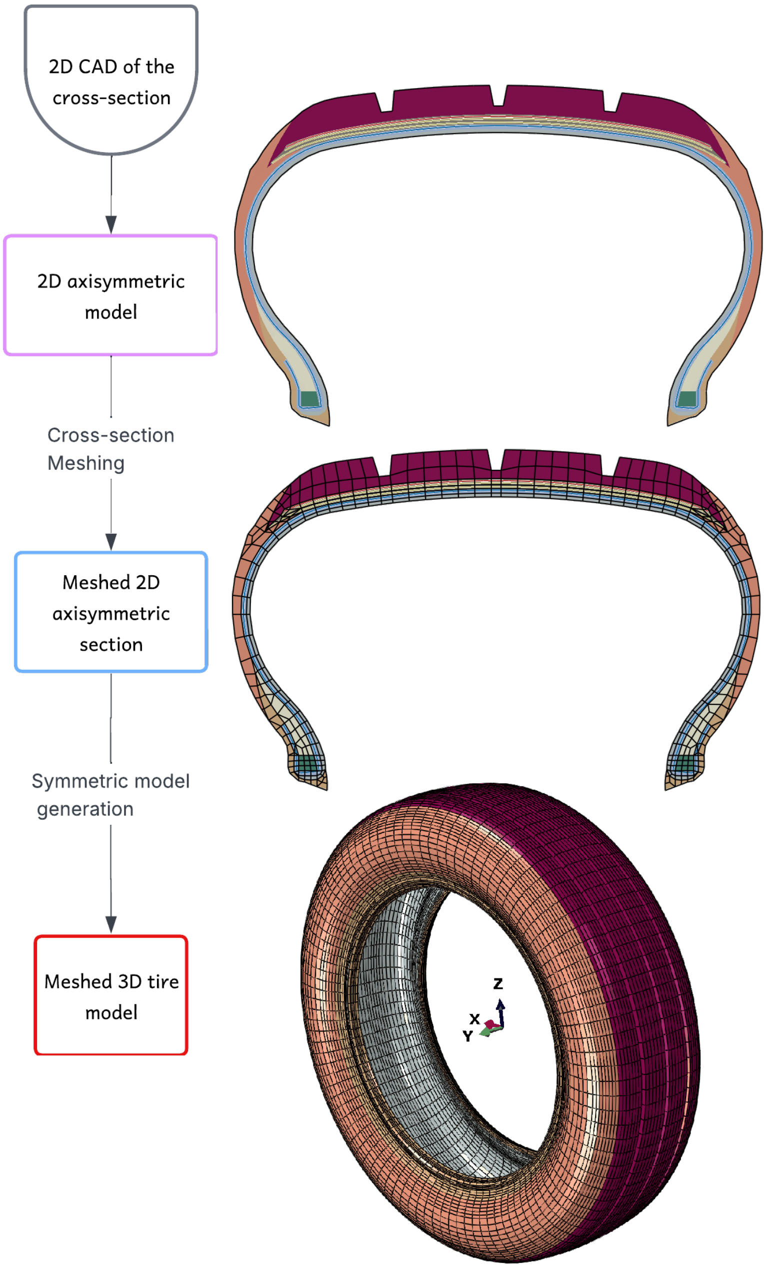

Figure 6.4: Full 3D model for static analysis.

Figure 6.5 provides a 3D view of the tire components along with their mesh. It should be noted that each reinforcement layer is created individually and then assembled with its host rubber component using embedded constraints.

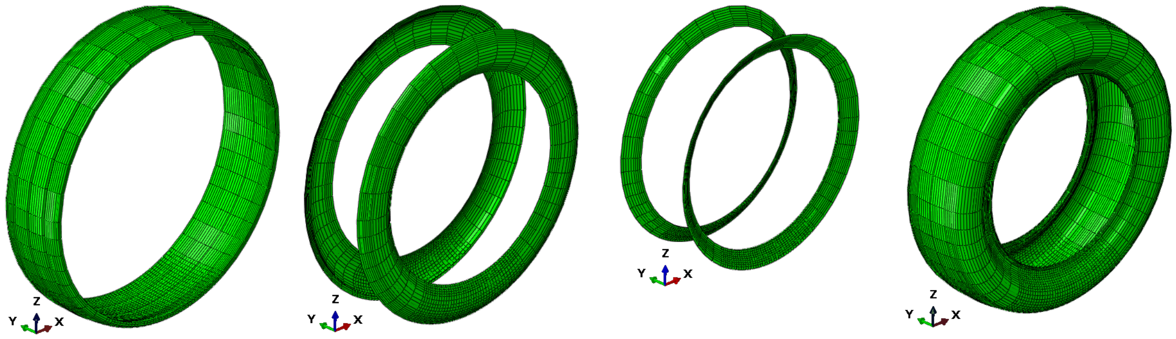

(a) Tread (b) Sidewall (c) Bead filler (d) Inner liner

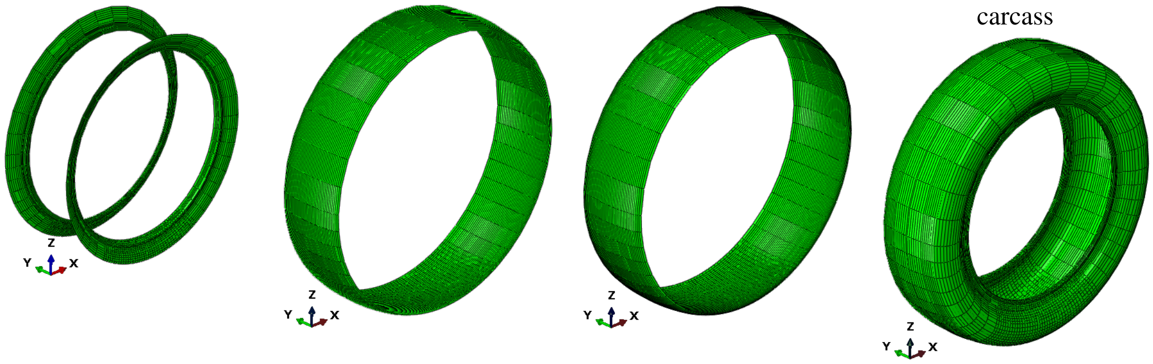

(e) Rim cushion (f) Steel cords layer 1 (g) Steel cords layer 2 (h) Rubber layer for carcass

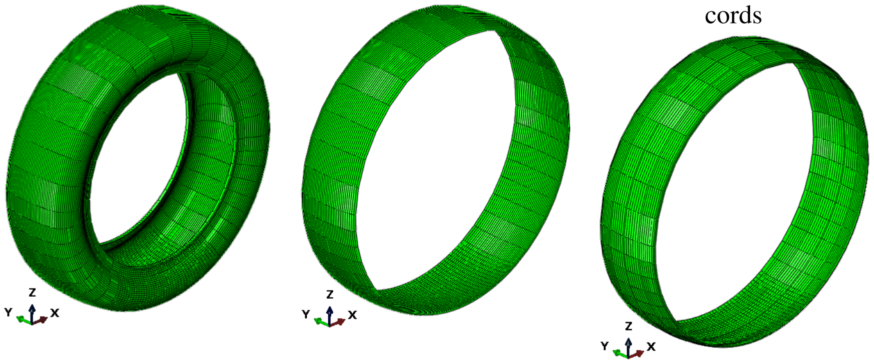

(i) Carcass cords layer (j) Textile cord layer (k) Rubber layer for textile cords

Figure 6.5: Discretized parts of the finite element model.

For simplicity, we assume that the road is a non-deformable body and model it as an analytical rigid surface (see Figure 6.6).

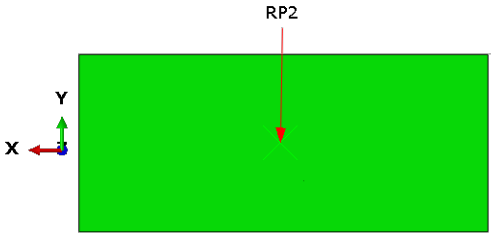

Figure 6.6: Road

After assembling everything, we obtained the complete finite element model depicted in Figure 6.7.

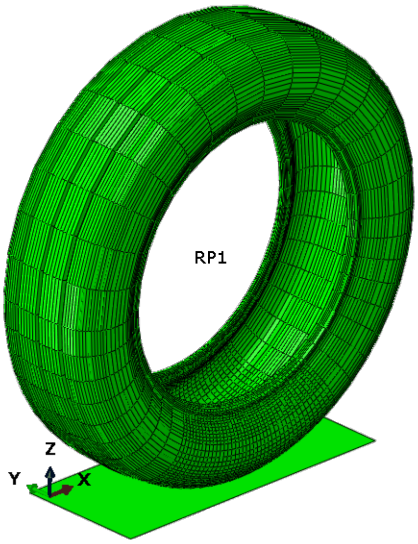

Figure 6.7: Full 3D model for static analysis.

Throughout the analysis, surface-to-surface interaction was used to model the contact between the tread surface (slave surface) and the road (master surface). Apart from the above topology created with sectorized mesh (referred to as mesh *Type 2* in Section), we also utilized a topology created with equally spaced sector mesh (*Type 1*).

6.1.3 Material properties

Input parameters, such as mechanical properties, are essential data in a finite element model. Therefore, experimental tests were conducted on specimens extracted from the tire. Rubber compounds underwent uniaxial tensile cyclic testing according to standard ISO 37:2017[127], following the procedure outlined in Section 4.3.1 and conducted experimentally as described in Krmela et al. [186] (also referred to as P10, part of the author's contribution). Meanwhile, reinforcements, including steel cord, textile cord, and carcass, were tested using a uniaxial tensile test as specified in ASTM D2969 and ASTM D7269, respectively. After calibration with the constitutive laws detailed in Section 4.3.1, we obtained the material properties listed in Table 6.1 and Table 6.2.

Table 6.1: Reinforcement material propeties.

Tire parts	E [MPa]	ν	$\varnothing$ [mm]	spacing [mm]	ρ [Kg/m^3]	Orientation [°]
Steel cords	160 000	0.30	0.60	1.09	5 600	23
Textile cap cords	3 400	0.40	0.69	0.9	950	90
Carcass	11 000	0.40	0.49	1.0	950	0
Bead	180 000	0.30	/	/	6 800	/

Table 6.2: Material properties of rubber compounds.

	Hyperelasticity				**Mullins effect**		
Parts	ρ [Kg.m^{-3}]	C_{01} [MPa]	C_{10} [MPa]	D_1 [MPa^{-1}]	r	m	β
Bead filler	801	-0.111	1.945	0.01097	10.25	0.8	1.25
Inner liner	801	0.109	0.259	0.05471	13.2	0.92	1.91
Rim cushion	801	0.692	0.0371	0.01894	8.36	1.08	2.52
Sidewall	801	0.532	0.065	0.03372	21.67	0.732	1.151
Tread	801	0.417	0.519	0.02151	17.37	1.19	1.05
Rubber[a]	801	0.328	0.119	0.04504	12.18	0.987	2.349
Rubber[b]	801	0.548	0.112	0.03051	26.94	1.03	1.102
Rubber[b]	801	0.638	0.284	0.02183	21.615	0.89	3.25

	Viscoelasticity: Prony series					
Parts	g_1	τ_1 [s]	g_2	τ_2 [s]	g_3	τ_3 [s]
Bead filler	0.00498	0.000265	0.1082	258.341	0.207	1786.528
Inner liner	0.0835	0.0321	0.264	128.341	0.172	2185.35
Rim cushion	0.217	0.0108	0.3897	108.836	0.0428	1152.719
Sidewall	0.0137	0.512	0.124	204.534	0.0587	2431.25
Tread	0.0207	0.012	0.315	317.654	0.0934	1386.241
Rubber[a]	0.0125	3.464	0.137	148.26	0.223	2124.201
Rubber[b]	0.0231	0.0231	0.225	187.054	0.127	1350.16
Rubber[c]	0.0364	0.726	0.135	238.780	0.0605	2057.35

[a] rubber part for steel cords.

[b] rubber part for textile cap cords.

[c] rubber part for carcass cords.

We should bear in mind that the orientation of steel cords given in Table 6.1 is measured with respect to the local axis 2 of the layer. Since angles were defined with respect to the local axis 1 in axisymmetric, we calculate the angle as follows: $90° - 23° = 67°$.

6.1.4 Analysis flowchart

With all the ingredients of our model prepared, we proceeded with simulations. In this context, we have conducted several simulations and utilized various equipment and experimental tests to validate the model:

- Quasi-static validation on the static adhesor.
- Quasi-static and dynamic validation on the dynamic adhesor.
- Modal vibration validation.

After validation, we conducted a comprehensive analysis to evaluate tire response with the proposed model during steady-state rolling, post-steady-state rolling vibration, random vibration, and transient rolling. The workflow implemented for these analyses is summarized in Figure 6.8.

Figure 6.8: Workflow for model deployment and validation.

6.2 Results and Validation of the model

6.2.1 Quasi-static state validation using static adhesor setup:

Experimental setup

The laboratory test for this study was conducted on the static adhesor (see Figure 6.10)located within the Alexander Dubček University of Trenčín. On this machine, it is possible to test passenger tires with rim ranging from R13 to R18 and with a maximum width of 235 mm. The loading capacity goes up to 1 tonne and it is equipped with:

- Three force tensiometer sensors EMSYST EMS40 2.0kN (see Figure 6.9(b)).
- A linear potentiometer (see Figure 6.9(b)) and three sensors with an X-Y recorder for the orientation of the force-deformation relationship.
- A data logger system (see Figure 6.10(b)): during the test, data are recorded thanks to the data logger system DataQ DI-718B-US equipped with three strain gage input modules DI-8B38 and one Potentiometer input module DI-8B360.

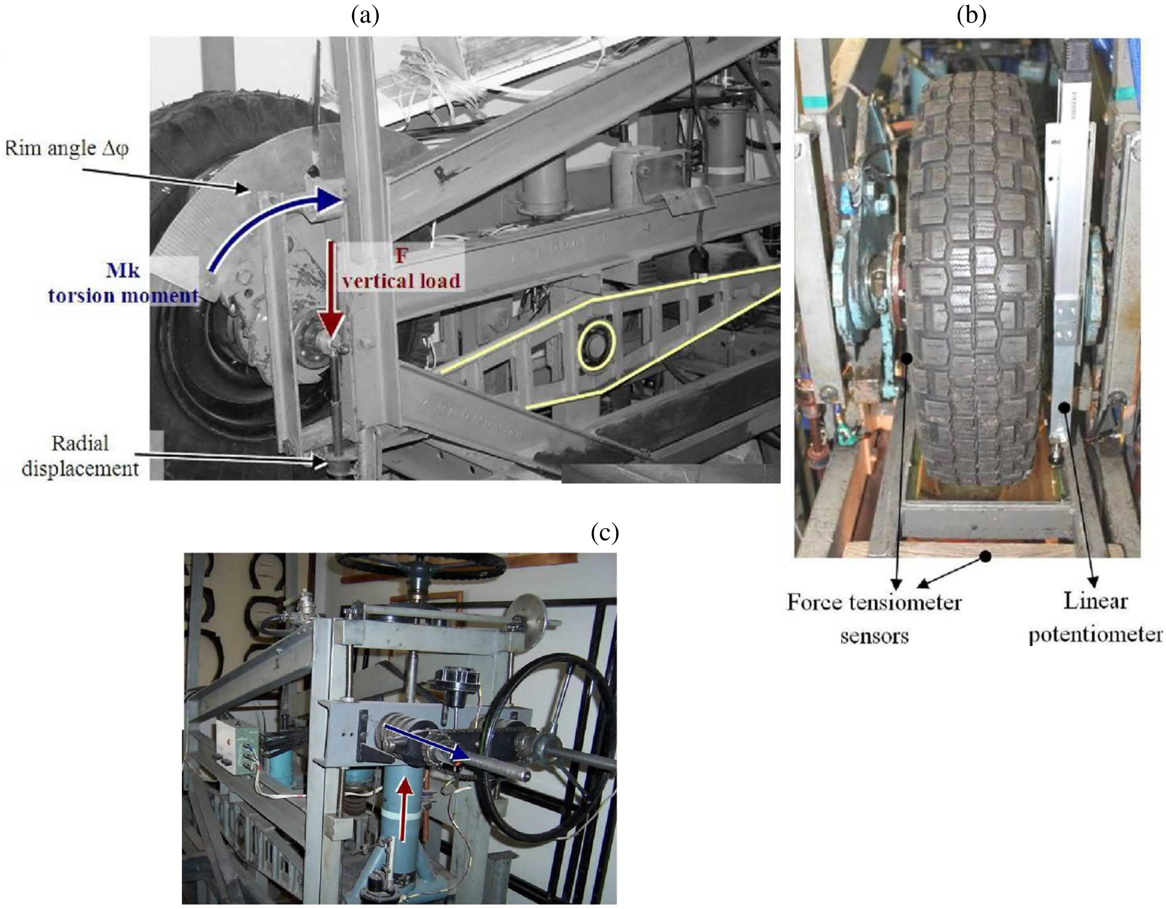

Figure 6.9: Views of the static adhesor [183].

This data logger is connected to a computer and using the software WinDaq/Lite, data are visualized and stored on the computer.

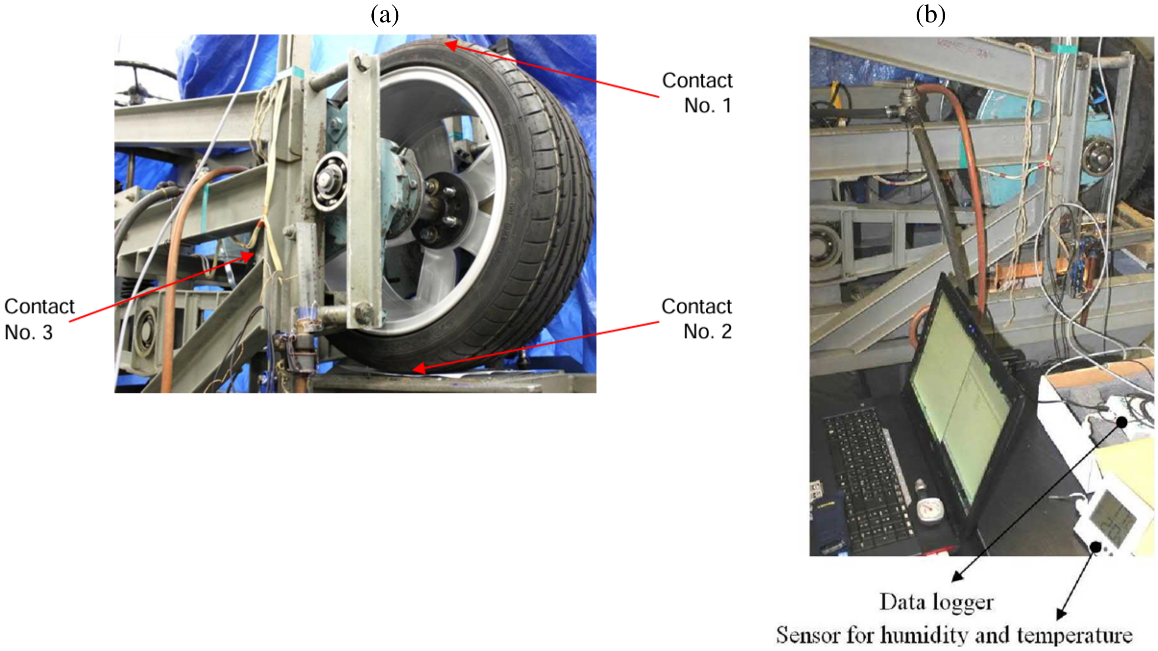

Figure 6.10: Views of the static adhesor [183].

Procedure of the test:

- Firstly, the selected tire is mounted on the rim.
- Then, it is inflated up to the chosen inflation pressure.
- The wheel is mounted on the test rig indicated in Figure 6.10. At this stage, the wheel is only subjected to its self weight and leads to a zero state equilibrium.
- Afterward, the quasi-static application of the vertical load starts.

Since two inflation pressures were chosen, this procedure was followed for testing at each of these pressures.The data were recorded and stored in the computer.

Finite element Model

The tire-road interaction in this analysis was considered frictionless in the tangential contact and hard contact type, in the normal direction. The Abaqus standard solver was selected, and given that hyperelastic materials are involved, the NLGEOM keyword was added to activate the Newton-Raphson scheme. The following three steps were created:

1. **Inflation**: In this step, the tire is inflated at the specified inflation pressure. Here, the rim is fixed as well as the road, though not in contact.
2. **Equilibrium**: In order to avoid convergence issues, we must leave a small gap between the deformed shape of the tire and the road. In this step, a small displacement is applied at the reference point of the road towards the tire. This helps close the gap.
3. **Preloading with selfweight**: as pointed out in the experimental setup, before the loading starts, the tire sits on the contact 2 (see Figure 6.10(a)) under its self-weight. Thus, a load

of 140 N representing the wheel's load (tire+rim) is applied on the reference point of the road towards the tire. The rim remains fixed.

4. **Static test loading**: Here begins the static loading up to $135\%LI$. This load is applied on the reference point RP1 downward towards the road surface. The road is fixed in this step.

Experimental data were collected following the experimental setup outlined on the static adhesor at different inflation pressures ($180\mathrm{kPa}$ and $250\mathrm{kPa}$) and under a vertical load varying from 0 to 125% of the LI. We recall that for the selected tire, $LI = 412$ Kg, which corresponds to a load of 4041.72 N.

Results and validation

The simulation with the proposed model was efficient and cost-effective. The total CPU time for this analysis was approximately 10 minutes.

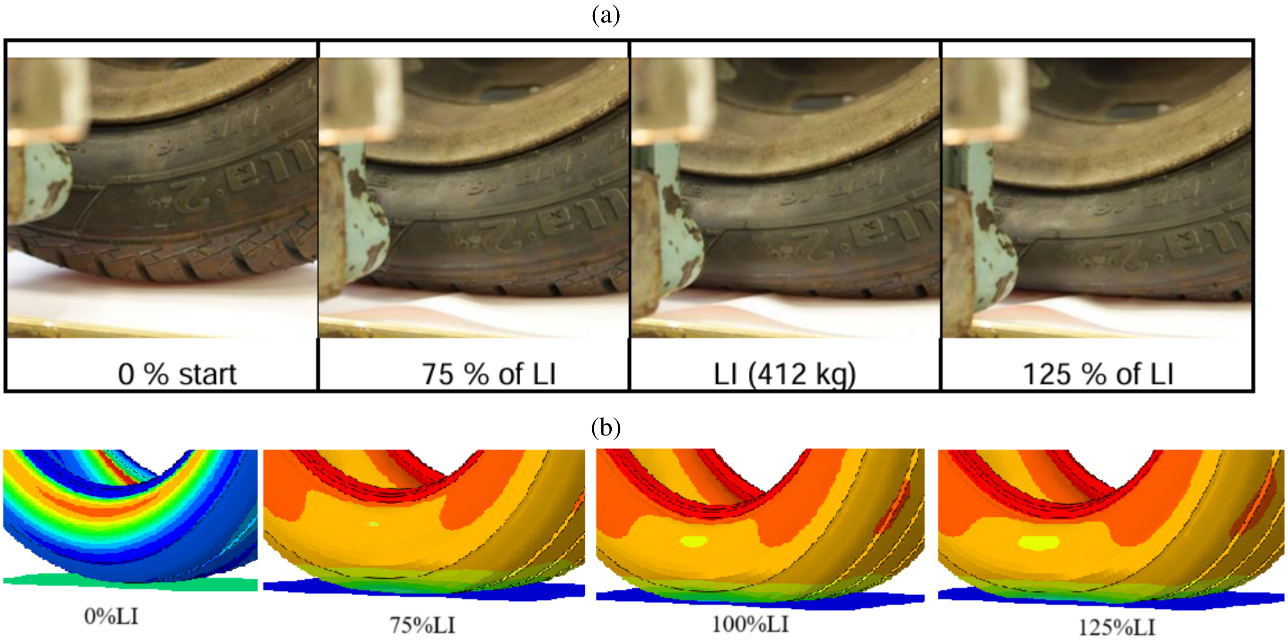

Figure 6.11: Visualization of tire deformation during vertical static loading. (a) Experiment and (a) FE model.

Particularly, Figure 6.12 displays the distribution of Von Mises stresses $\boldsymbol{\sigma}_{VM}$ (MPa) and normal force (MPa) at $F_z = 100\%LI$ in both rubber parts and reinforcements. Especially, we note that the rim cushion experiences the highest stress value of 2.86 MPa, followed by the rubber part for the steel cords layer 1 and the textile cords, with 1.97 MPa and 1.71 MPa, respectively. Concerning reinforcements, steel cords layer 2 sustain the highest force of magnitude 53.82 N.

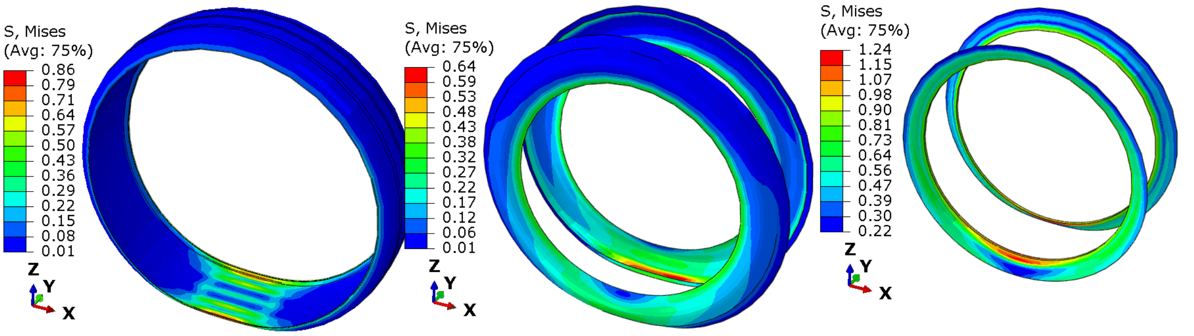

(a) Tread

(b) Sidewall

(c) Bead filler

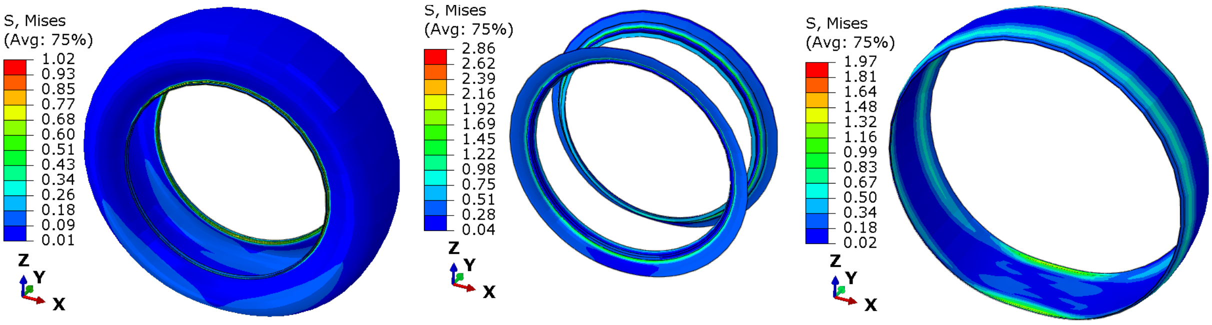

(d) Inner liner

(e) Rim cushion

(f) Rubber for steel cord layer 1

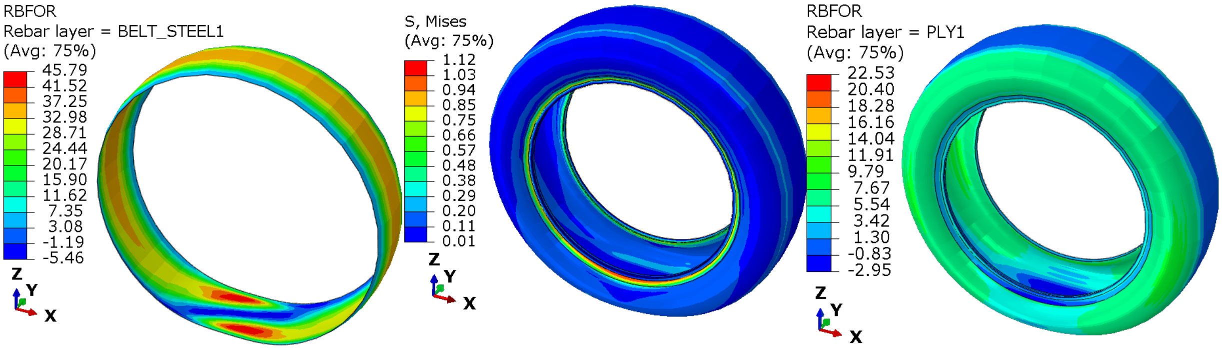

(g) Steel cords layer 1

(h) Rubber layer for carcass

(i) Carcass cords layer

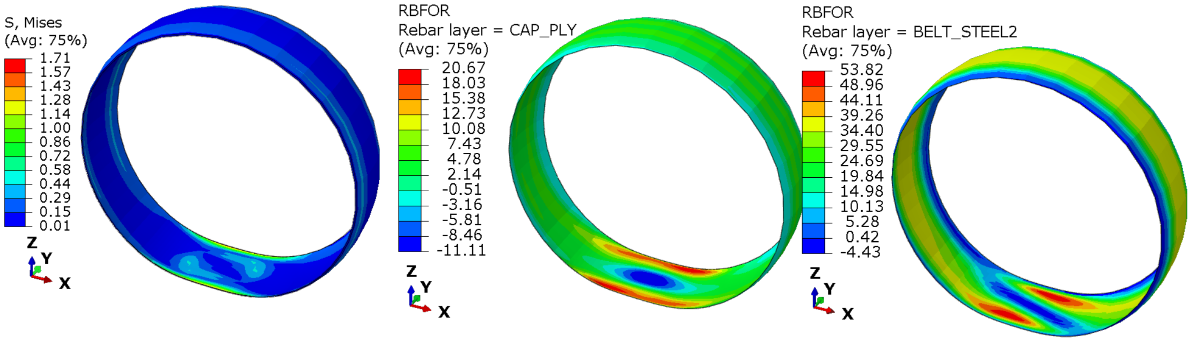

(j) Rubber for textile cords

(k) Textile cords layer

(l) Steel cords layer 2

Figure 6.12: Distribution of Von Mises stress (in rubber parts) and normal force (in reinforcements).

A 3D visualization of the distribution of the vertical displacement on the tire is presented in Figure 6.13.

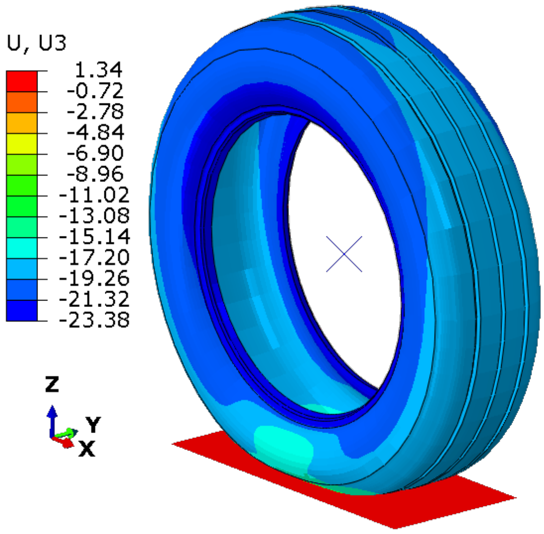

Figure 6.13: 3D view on the deformed tire at $p_{in} = 250$ kPa and under $100\% LI$.

Comparison between u_z^{exp} and u_z^{FEM}

After executing the jobs with the created Abaqus input file, the dependence of force versus deflection at the node $RP1$ (wheel center) was retrieved and plotted in a Figure 6.14 alongside the curve of force versus displacement measured experimentally.

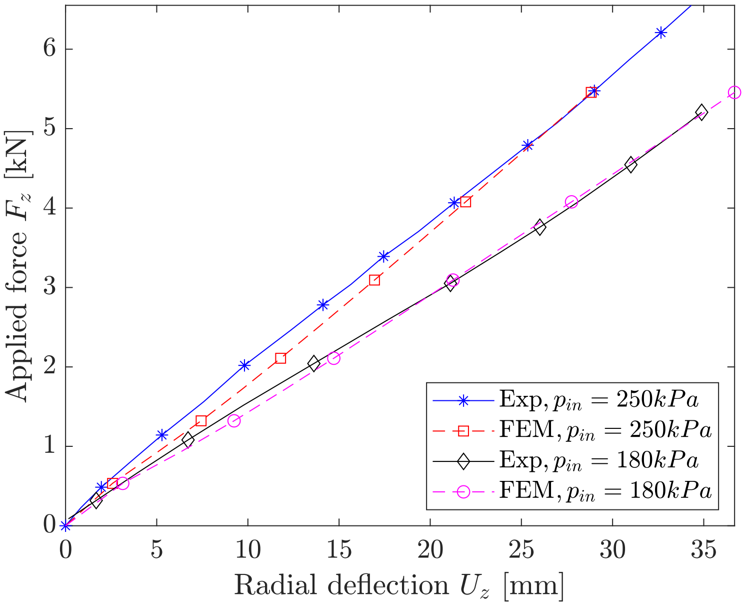

Figure 6.14: Numerical and experimental results of the applied load F_z versus the radial deflection u_z on the static adhesor.

Now, talking quantitatively about the data from Figure 6.14, Table 6.3 compares the experimental and numerical values obtained for an inflation pressure of 180 and 250 kPa, considering a load F_z equal to 100% of the load index. Here, the absolute relative error (%) is utilized as the metric for this comparison.

Table 6.3: Comparison of radial deformation between the numerical model and experiment at 100%LI

p_{in} [kPa]	Radial deformation $\mathrm{U_z}$ (in mm) at 100%LI		
	Simplified model	Experimental	Relative error (%)
180	27.75	27.00	2.78
250	21.76	21.50	1.16

We observe that the resulting relative error is less than 5% in both cases. Consequently, the proposed model is accurate with respect to the prediction of the radial deflection on the static adhesor.

Comparison of the contact patch from experiments and FEM results

Another important output we can obtain from the numerical model is the variation of contact area with applied force F_z as depicted in Figure 6.15.

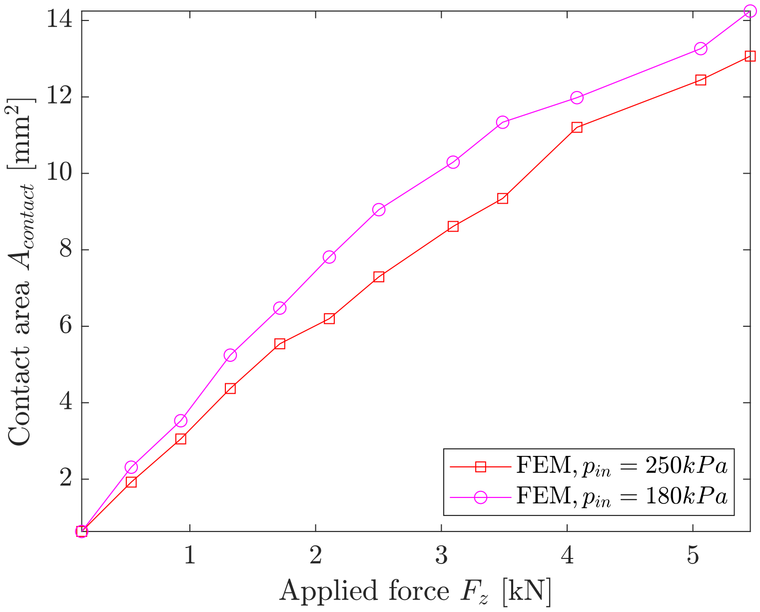

Figure 6.15: Numerical and experimental results of the applied load F_z versus the radial deflection u_z on the static adhesor.

During the experimental tests with an inflation pressure of 250kPa, the contact patch on the ground was captured at 100%LI using a thin film, and the resulting dimensions were also measured. In addition, the contact shape was recorded as output from the numerical model on both the simplified and the complex models. The visualization of these contact patches is displayed in Figure 6.16(a).

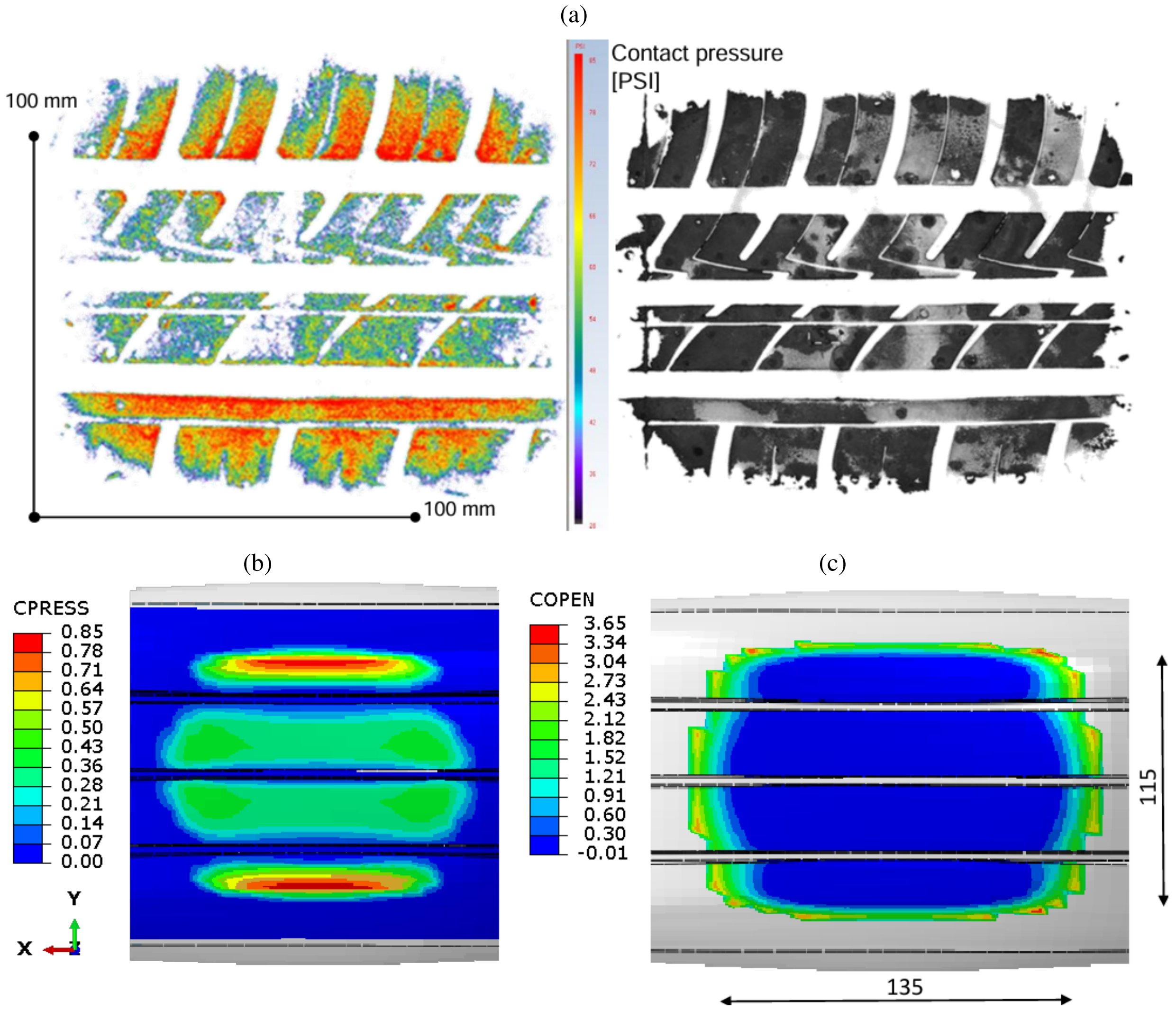

Figure 6.16: Visualization of contact stress and contact patch from FE model and expriment at 100%LI. (a) Experiment, (b) and (c) are respectively the contact pressure and contact patch from FE model.

The examination of the contact patches reveals a similarity in the distribution of the contact imprints, which is especially noticeable towards the edges. Additionally, it is observed that the effective contact surface is larger in the FE model. This is evident because, in this model, the actual shape of the grooves has been simplified. The resulting contact areas are summarized in the Table 6.4.

Table 6.4: Comparison of contact area between the numerical (simplified) and experimental results at 100%LI

p_{in} [kPa]	Contact area A_{contact} (in mm^2) at 100%LI		
	Simplified model	Experimental	Relative error (%)
180	11840	11820	0.2
250	11200	10125	10.6

We observe that at an inflation pressure p_{in} of 180 [kPa], the experimental and numerical contact areas are consistent at 100% load index (LI). However, at an inflation pressure of 180 [kPa], the contact area from the finite element (FE) model is approximately 10% larger than the experimental measurement. This difference makes sense because a tire model with a smooth or simplified tread surface will have a greater contact area with the road compared to a tire with a real tread pattern. At 180 kPa inflation and under a radial force (F_z) of 100%LI, the tire is under-inflated.This indicates that the effective contact area is concentrated on the longitudinal edges of the tire.

A more accurate contact area can be obtained for the case with $p_{in} = 250\text{kPa}$ by using instead the tire model with a real tread pattern and a friction coefficient of 0.70. The resulting contact area is summarized in Table 6.5.

Table 6.5: Comparison of contact area between the numerical model and experiment at 100%LI

p_{in} [kPa]	Contact Area (in mm^2) at 100%LI		
	Complex model	Experimental	Error(%)
250	10015	10125	1.1

The obtained contact patch is displayed in Figure 6.17.

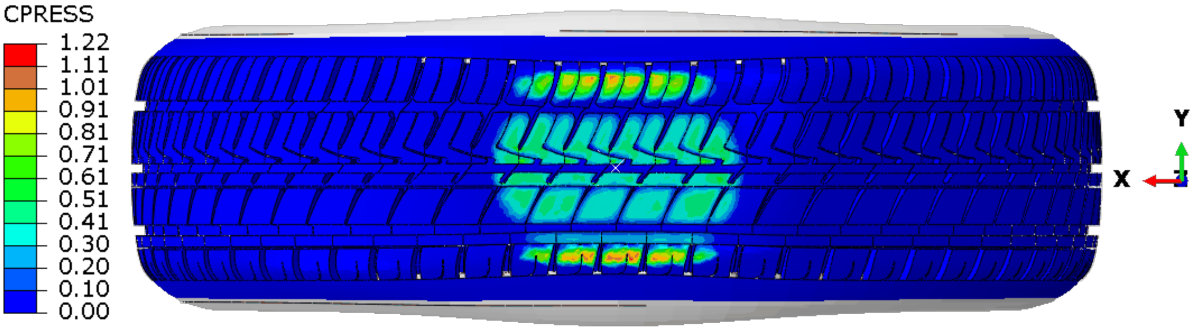

Figure 6.17: Contact patch obtained on the tire with tread pattern.

Comparison of the radial stiffness from experiment and FEM

Based on the dependence of the applied force on the deflection, it is possible to compute the radial stiffness k_z.

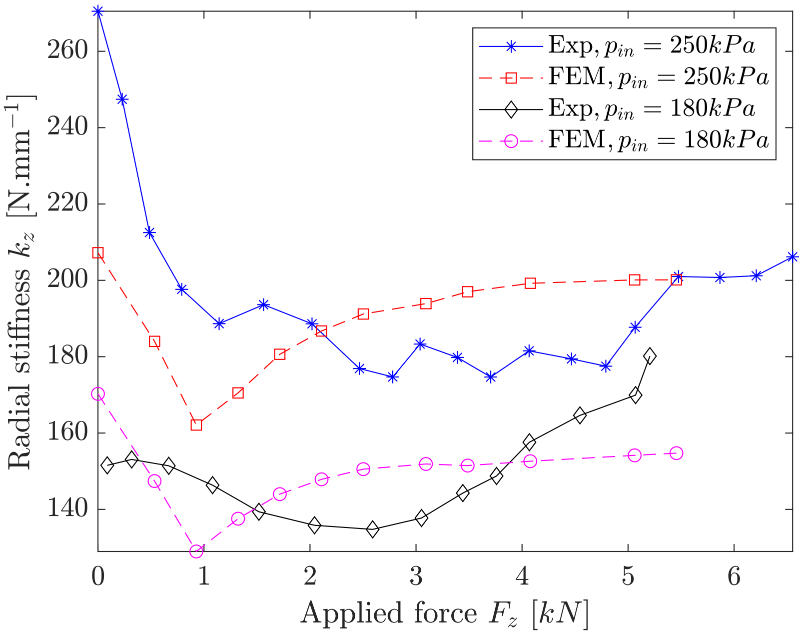

Figure 6.18: Numerical versus experimental radial stiffness k_z.

For vehicle dynamic analysis, it is a common practice to estimate a single value of k_z rather than having it dependent on the applied force. According to ČSN 63 1511 standard [187], this value is given as

$$k_z = \frac{F_{z,125\%LI} - F_{z,75\%LI}}{u_{z,125\%LI} - u_{z,75\%LI}} \tag{6.1}$$

The main drawback of this formula is that it does not take into account some features related to the loading process. Thus, Krmela and Michal [188] alleviated this limit with the formula below

$$k_z = \frac{F_{z,100\%LI} - F_{z,60\%LI}}{u_{z,100\%LI} - u_{z,60\%LI}} \tag{6.2}$$

Therefore, using the formula in Eq.(6.2), we can compare the experimental and numerical values in Table 6.6.

Table 6.6: Comparison of radial stiffness between the numerical model and experiment

p_{in} [kPa]	Radial stiffness $\mathrm{k_z}$ (in [N.mm^{-1}])		
	Simplified model	Experimental	Relative error (%)
180	151.29	153	1.11
250	194.97	185	5.38

In view of the results, it can be seen that the absolute relative error is acceptable.

6.2.2 Quasi-static and dynamic state validation using the dynamic adhesor setup:

Static testing on the dynamic adhesor (see Figure 6.19) involves using a stationary drum (of diameter $\phi_{drum} = 1.705m$), which remains at zero speed, onto which the tire is moved through a force-driven sequence. This sequence is regulated by a hydraulic system, which is monitored on the control board located in the control room. The outcome of this testing procedure measures the radial deformation in response to the applied force.

Figure 6.19: View on the dynamic adhesor.

A schematic illustration of this testing setup is shown in Figure 6.20.

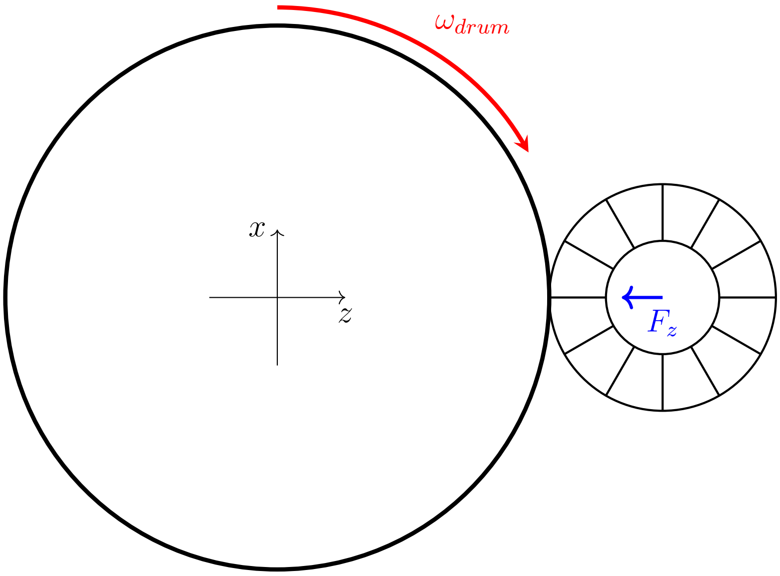

Figure 6.20: Schematic view of tire testing on dynamic adhesor: drum on the left and tire on the right.

Three inflation pressures $p_{in} \in \{160\text{kPa}, 250\text{kPa}, 300\text{kPa}\}$ were considered, and the applied load varying monotonically such that $F_z \in [0, 135\%\text{LI}]$. The drum was modeled as a rigid surface.

Static test validation: At zero speed

The simulation was completed very quickly, taking approximately 10 minutes for each inflation level. The experimental and numerical results are shown in Figure 6.21.

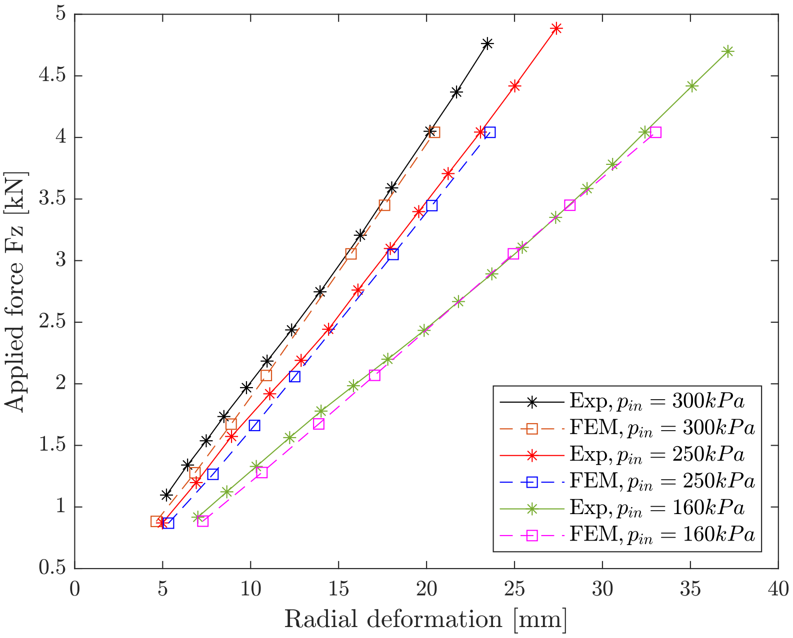

Figure 6.21: Numerical and experimental results of the applied load F_z versus the radial deflection u_z at zero speed on the dynamic adhesor.

It can be seen from the curves that the numerical model predicts the response of the tire to vertical loads very well. More concretely, at $100\%LI$, the absolute error is less than 5% as summarized in Table 6.7.

Table 6.7: Comparison of radial deflection on dynamic adhesor at $300\mathrm{kPa}$ inflation and $0\ \mathrm{Km.h^{-1}}$ speed.

p_{in} [kPa]	Radial deformation $\mathrm{U_z}$ (in mm)		
	Simplified model	Experimental	Relative error (%)
160	33.03	32.40	1.9
250	23.60	23.05	2.4
300	20.45	20.15	1.5

Dynamic test validation: with a rotating drum

On the dynamic adhesor, it is also possible to carry out the radial test with a rotating drum. Thus, the tire was tested with a drum rotating at a speed of $V = 120\ \mathrm{Km.h^{-1}}$, which corresponds to an angular speed of $\omega_{drum} = \frac{V}{R_{drum}} = 19.55\ \mathrm{rad.s^{-1}}$. The visualization of the experimental and numerical results is presented in Figure 6.22.

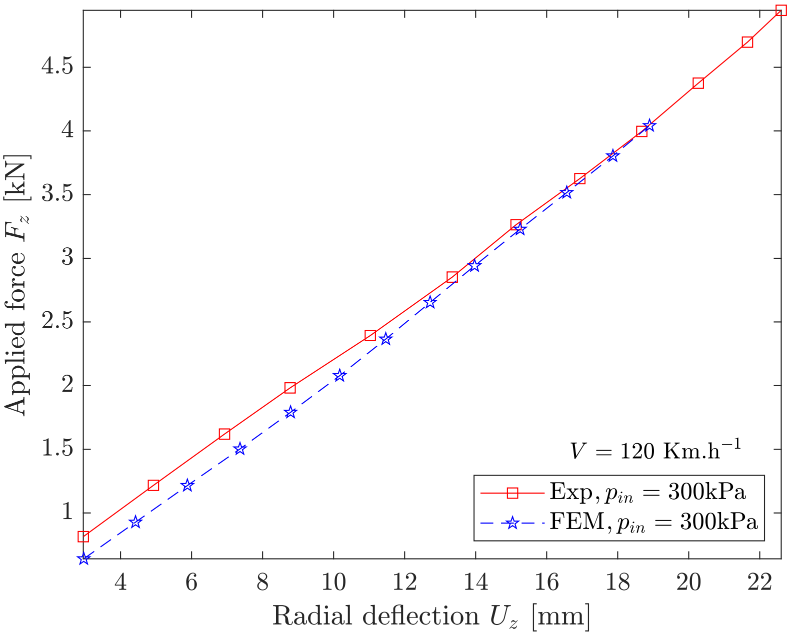

Figure 6.22: Numerical and experimental results of the applied load F_z versus the radial deflection u_z on the dynamic adhesor at a speed of $120\ \mathrm{Km.h^{-1}}$.

We observe that both results are very similar, despite a small difference at low force. The comparison at $100\%LI$ is reported in Table 6.8.

Table 6.8: Comparison of the radial deflection on the dynamic adhesor at $300\mathrm{kPa}$ inflation and $120\ \mathrm{Km.h}^{-1}$ speed.

p_{in} [kPa]	Radial deformation $\mathrm{U_z}$ (in mm) under 100%LI		
	Simplified model	Experimental	Relative error (%)
300	18.90	18.87	0.16

Although the absolute error under low force ($F_z < 45\%LI$) is about 7%, under higher load, the error is less than 2%. The greater relative error observed under lower forces may be attributed to the *influence of temperature*. When the tire is pressed against the rotating drum, the frictional energy is converted into thermal energy (heat). This effect, along with the errors stemming from the hyperelastic material model, likely contributes to increased relative error under lower loads. Nevertheless, the relative error is still acceptable. Thus, we conclude that the model effectively predicts tire deformation under dynamic load.

6.2.3 Modal analysis

The purpose of this section is to analyze the natural vibration of the unloaded tire under an inflation pressure of $250\mathrm{kPa}$ and use experimental results to validate the accuracy of simulation results.

Experimental setup

Under laboratory conditions, the tire was inflated to $250\mathrm{kPa}$ and mounted on the test rig, as shown in Figure 6.23.

Figure 6.23: Wheel mounted on a fixed rig.

An Electronic Speckle Pattern Interferometer (ESPI) system was utilized to measure tire surface deformation, as well as modal frequencies and shapes. The components of the ESPI system are illustrated in Figure 6.24. Basically, the ESPI system is a laser-based and non-destructive technique utilized for capturing and analyzing the intricate vibration patterns of the surfaces of a structure subjected to an excitation. By illuminating a surface with coherent laser light, ESPI generates a speckle pattern that is exploited to measure the structure's response. With this system, it is also possible to measure fatigue response, stress-deformation response and detect internal defects and cracks in materials.

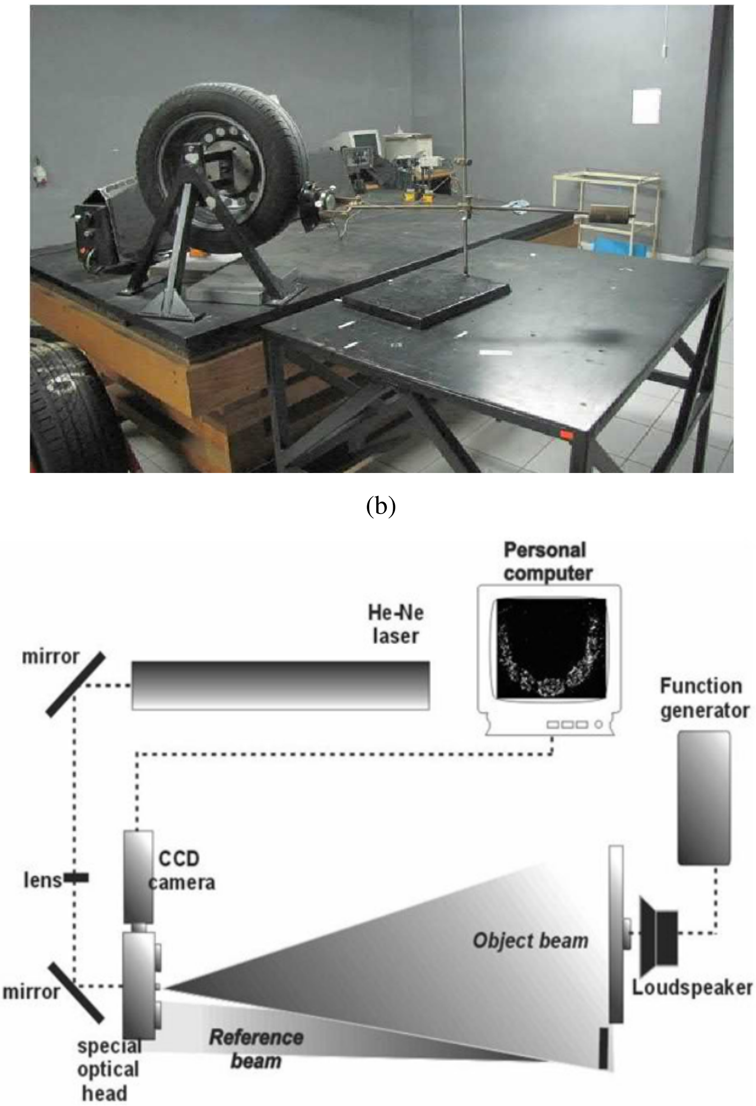

(a)

(b)

Figure 6.24: Experimental setup for measuring modal vibration of unloaded tire. (a) View on the experimental setup (b) Apparatus and its components [189].

FEM model

Kinematics basis

In the presence of material, geometrical, and contact nonlinearity, modal analysis can be performed at a specific deformed configuration. In this context, the modal analysis of the tire must be conducted after applying the inflation pressure preload.

Problem formulation: A Two-Stage Solution Strategy

Unloaded tire model analysis involves two stages: the first stage being a nonlinear static analysis (under the inflation pressure) and the second stage is the extraction of natural frequencies from the deformed configuration.

- **Stage 1: Nonlinear Static Analysis**
  From the weak form, in Section 4.7.1, we solve for mean displacement $\boldsymbol{u}_0$ under static loads:

  $$\int_{\Omega_0} \boldsymbol{P}(\boldsymbol{u}_0, \xi_0) : \delta \boldsymbol{F} \mathrm{d}\Omega_0 = \int_{\Omega_0} \rho_0 \bar{\boldsymbol{b}} \cdot \delta \boldsymbol{u} \mathrm{d}\Omega_0 + \int_{\Gamma_N} \bar{\boldsymbol{t}} \cdot \delta \boldsymbol{u} \mathrm{d}\Gamma_N \tag{6.3}$$

  Here the damage effect is frozen at $\xi_0 = \max \Psi_0(\boldsymbol{C}(\boldsymbol{u}_0))$.

- **Stage 2: Linearized Dynamic Analysis**
  The weak form of the problem in dynamics is given by:

  $$\underbrace{\int_{\Omega_0} \rho_0 \ddot{\boldsymbol{u}} \cdot \delta \boldsymbol{u} \, dV}_{\text{Inertial term}} + \int_{\Omega_0} \boldsymbol{P}(\boldsymbol{u}_0, \xi_0) : \delta \boldsymbol{F} \mathrm{d}\Omega_0 = \int_{\Omega_0} \rho_0 \bar{\boldsymbol{b}} \cdot \delta \boldsymbol{u} \mathrm{d}\Omega_0 + \int_{\Gamma_N} \bar{\boldsymbol{t}} \cdot \delta \boldsymbol{u} \mathrm{d}\Gamma_N \tag{6.4}$$

  Let us now linearize this weak form around the pre-deformed state $(\mathbf{F}_0, \mathbf{C}_0, \mathbf{D}_0)$ with static equilibrium $\mathbf{P}_0 = 0.$. We assume that the displacement u can be decomposed in terms of its mean value $\boldsymbol{u}_0$ and $\tilde{\boldsymbol{u}}$ (the perturbed part), we can linearize it around $\boldsymbol{u}_0$ as follows:

  $$\delta \boldsymbol{F} \approx \nabla_{\boldsymbol{X}} \delta \boldsymbol{u} \tag{6.5}$$

  $$\delta \mathbf{E} = \mathbf{F}_0^T \delta \mathbf{F} \quad \text{(Symmetric part)} \tag{6.6}$$

  $$\boldsymbol{P} \approx \boldsymbol{P}_0 + \mathbb{C}_{\text{tang}} : \Delta \boldsymbol{E} + \mathbb{D} : \Delta \dot{\boldsymbol{E}} \tag{6.7}$$

  where $\mathbb{C}_{\text{tang}}$ is tangent modulus and $\mathbb{D}$ is damping modulus.

Consistent Material Tangent Modulus

The consistent tangent modulus relates stress and strain variations:

$$\delta \mathbf{S} = \mathbf{C}_{\text{tang}} : \delta \mathbf{E} \tag{6.8}$$

where:

$$\mathbf{C}_{\text{tang}} = \underbrace{\eta \mathbf{C}_{\text{eq}}}_{\text{Damaged elastic}} + \underbrace{\sum_{k=1}^{N} \mathbf{C}_{\text{neq}}^{k}}_{\text{Viscoelastic}} - \underbrace{\left(\frac{\partial \eta}{\partial \mathbf{C}} \otimes \mathbf{S}_{\text{eq},0} \right)}_{\text{Damage effect}} + \underbrace{\mathbf{C}_{\text{geo}}}_{\text{Geometric stiffness}} \tag{6.9}$$

Components:

- Elastic tangent: $\mathbf{C}_{\text{eq}} = 4 \frac{\partial^2 \psi_{\text{eq}}}{\partial \mathbf{C} \partial \mathbf{C}}$
- Damage derivative: $\frac{\partial D}{\partial \mathbf{C}} = \frac{\partial D}{\partial \psi_{\text{eq}}} \frac{\partial \psi_{\text{eq}}}{\partial \mathbf{C}}$
- Geometric stiffness: $\mathbf{C}_{\text{geo}}^{ijkl} = S_0^{jl} \mathcal{G}^{ik}$ (where $\mathcal{G}^{ik}$ is the contravariant metric tensor)

Viscoelastic Material Response in Frequency Domain

Prony series time dependent material properties can be converted into frequency-dependent viscoelastic response by the complex modulus tensor $\mathbb{D}(\omega)$ as follows

$$\mathbb{D}(\omega) = \mathbb{C}_0 \left[g_\infty + \sum_{k=1}^{m} g_k \frac{i\omega\tau_k}{1 + i\omega\tau_k} \right] \tag{6.10}$$

where:

- $g_\infty = 1 - \sum g_k$ is the equilibrium modulus fraction
- g_k and τ_k are Prony series parameters
- $\mathbb{C}_0$ is the instantaneous elastic modulus

The damping matrix $\boldsymbol{C}(\omega)$ is then computed as:

$$\boldsymbol{C}(\omega) = \int_{\Omega_0} \boldsymbol{B}^T \mathbb{D}_{\text{imag}}(\omega) \boldsymbol{B} d\Omega_0 \tag{6.11}$$

where $\mathbb{D}_{\text{imag}}$ is the imaginary part of $\mathbb{D}(\omega)$, representing energy dissipation.

Frequency Domain Formulation

Let us apply Fourier transform $\mathcal{F}\{\tilde{\boldsymbol{u}}\} = \hat{\tilde{\boldsymbol{u}}}(\omega)$ and rewrite the weak form accordingly:

$$\int_{\Omega_0} \left[-\omega^2 \rho_0 \hat{\tilde{\boldsymbol{u}}} + i\omega \hat{\boldsymbol{\sigma}}_{\text{visco}} + \hat{\boldsymbol{\sigma}}_{\text{el}} \right] : \delta\hat{\boldsymbol{\epsilon}} \mathrm{d}\Omega_0 = 0 \tag{6.12}$$

where:

- $\hat{\boldsymbol{\sigma}}_{\text{el}} = \mathbb{C}(\eta(\xi_0)) : \hat{\boldsymbol{\epsilon}}$ is the linearized elastic stress
- $\hat{\boldsymbol{\sigma}}_{\text{visco}} = \mathbb{D}_{\text{real}}(\omega) : \hat{\boldsymbol{\epsilon}}$ is the viscoelastic stress

Discretized Finite Element Equations

After FEM discretization using $\hat{\hat{\boldsymbol{u}}} = \boldsymbol{N}\hat{\hat{\boldsymbol{d}}}$ and $\mathrm{B}_a = \frac{\partial N_a}{\partial \mathrm{X}}\mathbf{F}_0$ (strain-displacement matrix), we obtain

$$\left(-\omega^2\boldsymbol{M} + i\omega\boldsymbol{C}(\omega) + \boldsymbol{K}\right)\hat{\hat{\boldsymbol{d}}}(\omega) = 0 \tag{6.13}$$

where:

$$\boldsymbol{M} = \int_{\Omega_0} \rho_0 \boldsymbol{N}^T\boldsymbol{N}\mathrm{d}\Omega_0 \quad \text{and} \quad \boldsymbol{K} = \int_{\Omega_0} \boldsymbol{B}^T\mathbb{C}_{\mathrm{tang}}(\eta(\xi_0))\boldsymbol{B}\mathrm{d}\Omega_0 \tag{6.14}$$

$$\boldsymbol{C}(\omega) = \int_{\Omega_0} \boldsymbol{B}^T\mathbb{D}(\omega)\boldsymbol{B}\mathrm{d}\Omega_0 \quad \text{and} \quad \mathbb{D}(\omega) = \sum_{k=1}^{m} \frac{i\omega\tau_k g_k}{1 + i\omega\tau_k}\mathbb{C}_0 \tag{6.15}$$

$\mathbb{D}$, $\boldsymbol{M}$, $\boldsymbol{K}$ and $\mathbb{C}$ are the damping modulus matrix, mass matrix, the stiffness matrix and the damping stiffness. Also,

- ω_k: are Natural frequencies (rad/s)
- $\hat{\hat{\boldsymbol{d}}}(\omega)$: are eigenvectors

In the Static Preload Analysis step, the tire is inflated to a specified pressure and securely fixed to its axle. Next, in this deformed configuration, we calculate the consistent stiffness matrix, damping matrix, and mass matrix for use in the subsequent modal analysis. The flowchart for the whole analysis is shown in Figure 6.25.

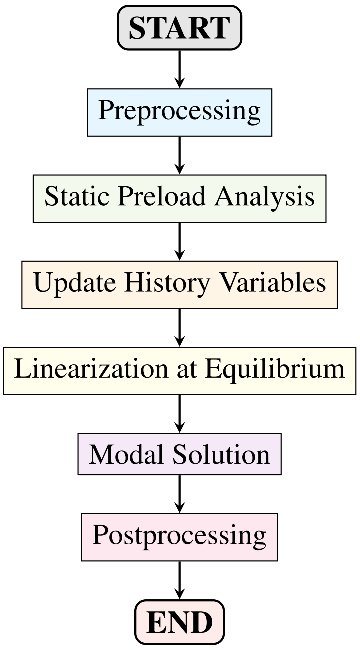

Figure 6.25: Flowchart for the modal vibration analysis of the unloaded tire.

The 16 lowest natural frequencies were extracted using LANCOZ solver in a frequency step. In accordance with the experimental setup, the tire is fixed at its wheel center. In terms of topology (mesh), the tire was meshed equally into n sectors in the circumference (see Figure 6.26) and generated using `symmetric model generation` function in ABAQUS input file procedure.

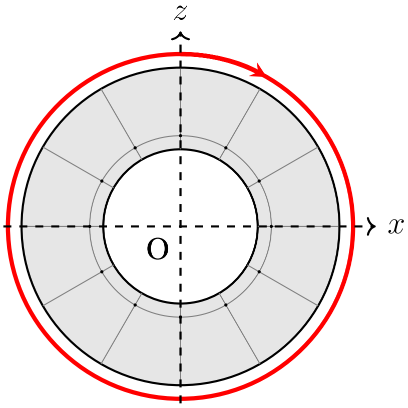

Figure 6.26: Equally space circumferential meshing of the tire

The workflow exploited for this analysis is highlighted in Figure 6.27.

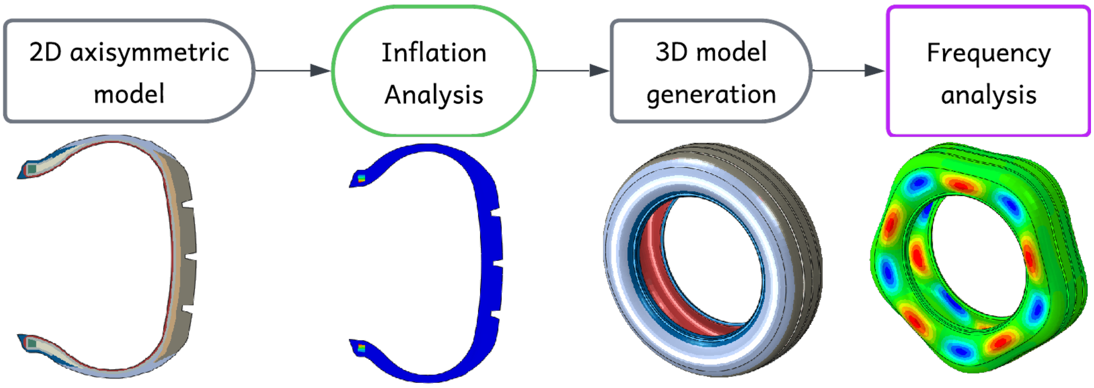

Figure 6.27: Flowchart of the Modal analysis

Results and discussions

In order to select the suitable mesh, a sensitivity mesh analysis was performed on the set of meshes reported in Table 6.9.

Table 6.9: Set of meshes selected for mesh sensitivity analysis.

Mesh index	n_{node}	$n_{elements}$
1	13450	11950
2	26900	23900
3	40350	35850
4	53800	47800
5	67250	59750
6	80700	71700

After running the program using the created input file, we obtained the frequencies versus mesh size data points plotted in Figure 6.28.

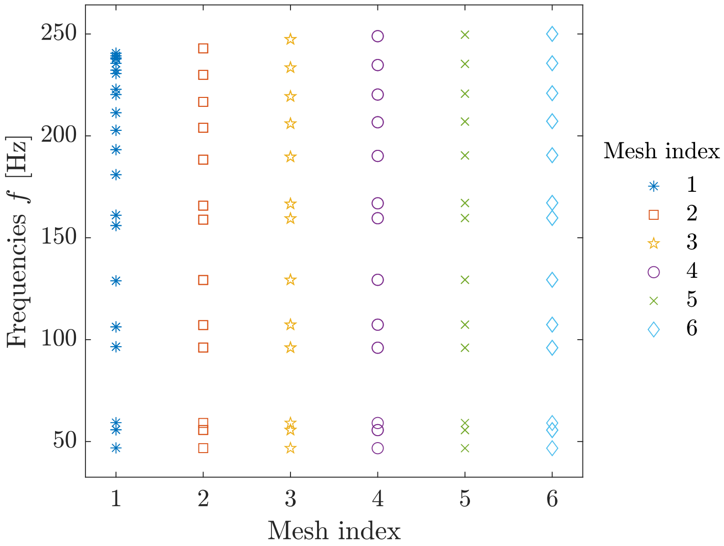

Figure 6.28: Mesh sensitivity analysis for frequency extraction

We observe that beyond mesh 4, the frequencies are almost the same. Hence, mesh 4 was adopted for the remainder. After the simulation, we obtained a set of modes, which we classified into two categories: in-plane and out-of-plane modes. A visualization of in-plane vibration modes is presented in Table 6.10.

Table 6.10: Eight (08) lowest in-plane natural vibration modes of the unloaded tire.

Mode	f[Hz]	X − Z view	Y − Z view	Mode	f[Hz]	X − Z view	Y − Z View
R0	59.09	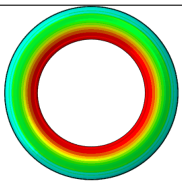	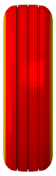	R1	96.03	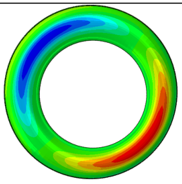	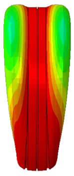
R2	129.36	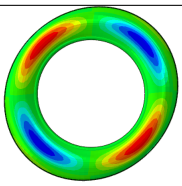	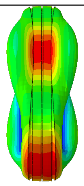	R3	160.00	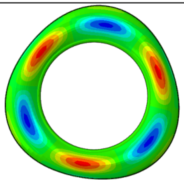	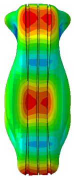
R4	190.17	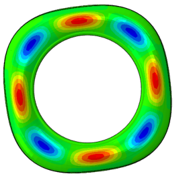	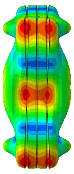	R5	220.27	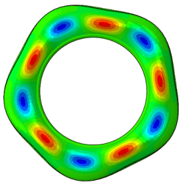	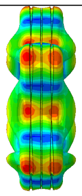
R6	248.93	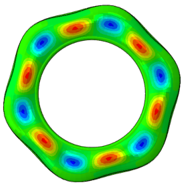	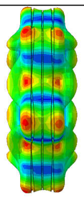	R7	275.37	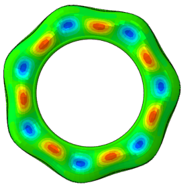	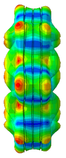

Natural out-of-plane vibration modes are reported in Table 6.11.

Table 6.11: Eight(08) lowest out-of-plane natural vibration modes of the unloaded tire

Mode	f[Hz]	X − Z view	Y − Z View	Mode	f[Hz]	X − Z view	Y − Z View
A0	46.73	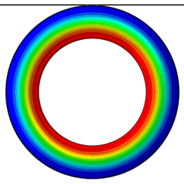	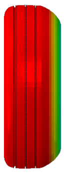	A1	59.09	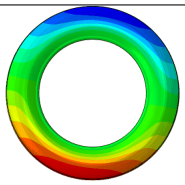	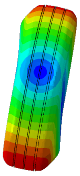
A2	107.34	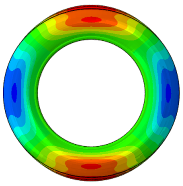	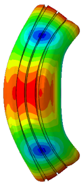	A3	166.92	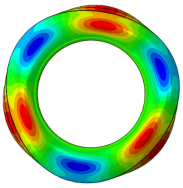	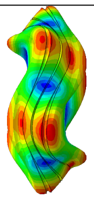
A4	206.70	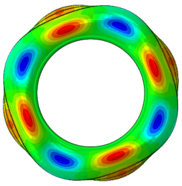	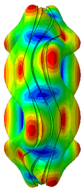	A5	234.76	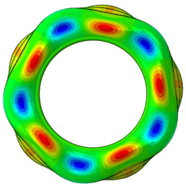	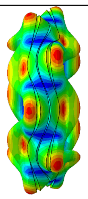
A6	258.27	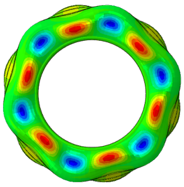	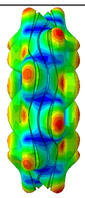	A7	279.92	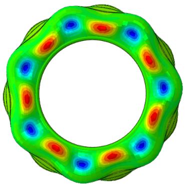	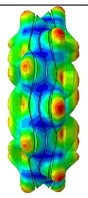

Validation of modal analysis

Now that we have frequencies and mode shapes obtained using the proposed FEM model and experiment, we proceed with the comparison of both results. The obtained frequencies are summarized in Table 6.12.

Table 6.12: Comparison between FEM calculated and experimentally measured frequencies.

Radial modes			
Code	f_{FEM} [Hz]	$f_{\text{Experimental}}$ [Hz]	Relative Error (%)
R2	129.36	136	4.88
R3	160.00	166	3.61
R4	190.17	188	1.15
R5	219.27	208	5.89
R6	248.93	239	4.15

Axial modes			
Code	f_{FEM} [Hz]	$f_{\text{Experimental}}$ [Hz]	Relative Error (%)
A1	108.34	120	9.72
A2	166.92	179	6.75

Besides the axial mode A1 and A2, the relative error between calculated and measured modes is less than 6%. Thus, we conclude that the accuracy of the model is verified.

Furthermore, ESPI system also enables to capture modal vibration shapes. Thus, we organized them into radial and axial mode shapes, then compared them with those obtained from the simulation. Table 6.13 compares radial modes from FEA results with those measured.

Table 6.13: Comparison of in-plane shapes between the FE and experiment results

Name	Experiment		FEM	
	f_{Exp}[Hz]	Mode shape	f_{FEM}[Hz]	Mode shape
R2	136	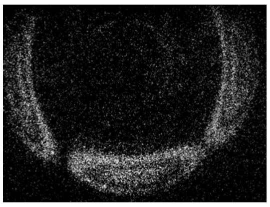	129.36	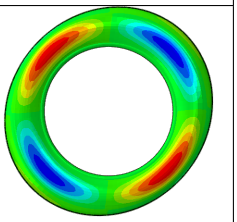
R3	166	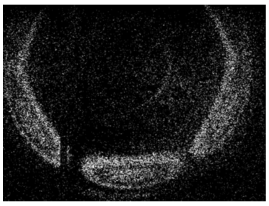	160.00	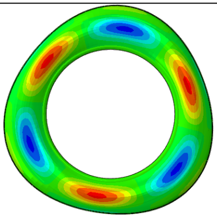
R4	188	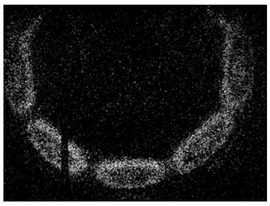	190.17	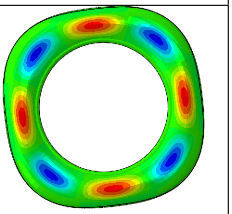
R5	208	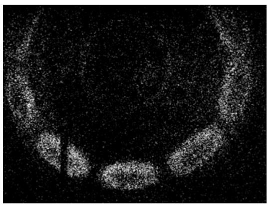	220.27	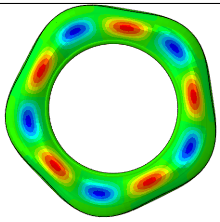
R6	239	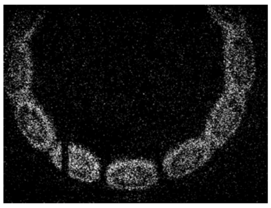	248.93	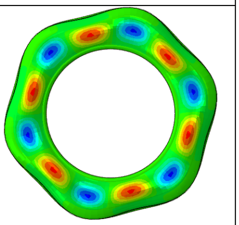

Equally, Table 6.14 presents the visualization of the computed and measured axial mode shapes.

Table 6.14: Comparison of out-of-plane mode shapes between the FE and experiment results

Name	Experiment		FEM	
	f_{Exp}[Hz]	Modeshape	f_{FEM}[Hz]	Modeshape
A2	120	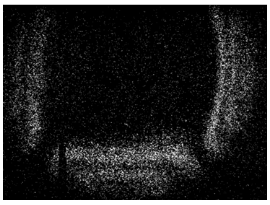	107.34	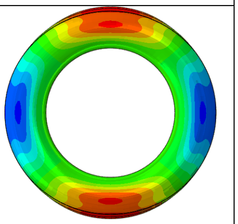
A3	179	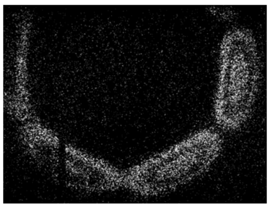	166.92	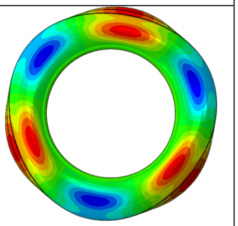

The analysis of the mode shapes reveals that the vibration patterns exhibit great similarity across the FE model and experiment. Specifically, the number of vibration lobes or fields remains consistent for each mode, underscoring a strong correlation between both results.

Influence of the inflation pressure on the natural vibration

In the previous section, the unloaded vibration was examined considering an inflation pressure of 250kPa. However, given that the tire is made of highly nonlinear materials, the natural frequencies are not constant. They are influenced by many other factors such as the temperature and the inflation pressure. That is why the frequency extraction takes place considering the deformed shape from the inflation analysis step. Thereby, the purpose of this section is to investigate the influence of the inflation pressure on the frequencies.

To this end, we consider 05 inflation pressures, namely 175kPa, 200kPa, 250kPa, 275kPa, and 300kPa. Afterward, the 05 separate input files were created with these values, and the obtained frequencies (12 lowest) versus mesh size data points are plotted in Figure 6.29.

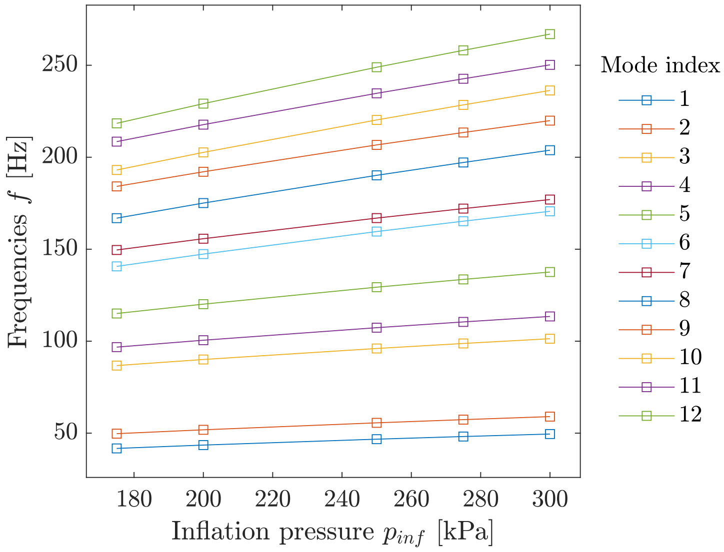

Figure 6.29: Modal frequency sensitivity analysis

It can be observed that all frequencies increased linearly with inflation pressure. In particular, the rate of increase is much higher for modes 8 to 12.

6.3 Further analysis on numerical model

6.3.1 Steady state rolling

As mentioned in the Section 3.1 the finite element method (FEM) is a highly versatile technique that allows modeling a wide range of problems, among which is the tire-road steady state rolling. Basically, the steady-state rolling of a tire analyzes its rolling response when subjected to a constant velocity and applied load, which simulates real-life driving conditions. The main objective is to gather data on tire characteristics, such as axle loads and their interaction with the road. Key data collected during these simulations encompass various forces, including lateral and longitudinal forces during cornering, braking, and traction. Additionally, the analysis targets moments (torques) that affect the tire's maneuverability and the distribution of contact stresses on the tire-road interface. These factors significantly determine tire handling performance under different driving conditions, such as during acceleration, braking, and cornering maneuvers.

Problem definition: an Arbitrary Lagrangian-Eulerian (ALE)

We consider a rolling tire $\Omega \subset \mathbb{R}^3$ rotating with angular velocity $\boldsymbol{\omega}$. The boundary $\partial\Omega = \Gamma_u \cup \Gamma_t \cup \Gamma_c$ consists of Dirichlet (Γ_u), Neumann (Γ_t), and contact (Γ_c) surfaces.

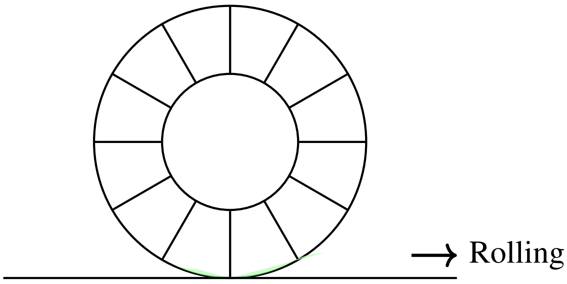

Figure 6.30: Illustration of tire rolling.

Governing Equations

Momentum Balance

At any time $t \in [0, T]$ and for $M \in \Omega_t$, in a rotating reference frame, the momentum balance fulfills:

$$\nabla \cdot \boldsymbol{\sigma} + \rho \boldsymbol{b}_{\text{eff}} = \boldsymbol{0} \quad \text{in} \quad \Omega \subset \mathbb{R}^3 \tag{6.16}$$

Where effective body force includes:

$$\boldsymbol{b}_{\text{eff}} = \boldsymbol{b} + \boldsymbol{b}_{\text{cent}} + \boldsymbol{b}_{\text{cor}} \tag{6.17}$$

$$\boldsymbol{b}_{\text{cent}} = -\underline{\boldsymbol{\omega}} \times (\underline{\boldsymbol{\omega}} \times \boldsymbol{x}) \qquad \textit{Centrifugal force} \tag{6.18}$$

$$\boldsymbol{b}_{\text{cor}} = -2\underline{\boldsymbol{\omega}} \times \boldsymbol{v}_{\text{rel}} \qquad \textit{Coriolis force} \tag{6.19}$$

$\boldsymbol{v}_{\text{rel}} = \underline{\boldsymbol{\omega}} \times (\boldsymbol{x} - \boldsymbol{x}_0) - \dot{\boldsymbol{u}}$ is relative velocity. $\underline{\omega}$ is the angular velocity vector.

Constitutive Equations

Cauchy stress derives from the fundamental expressions introduced in Section 3.2.2, which can be decomposed into:

$$\boldsymbol{\sigma} = \boldsymbol{\sigma}_{\text{eq}} + \boldsymbol{\sigma}_{\text{neq}} \tag{6.20}$$

- **Ogden-Roxburgh damage[57]:**

$$\eta = 1 - \frac{1}{r} \operatorname{erf}\left(\frac{W_{\text{eq}}^{\max} - W_{\text{eq}}}{m}\right) \tag{6.21}$$

- **Equilibrium stress**:

$$\boldsymbol{\sigma}_{\text{eq}} = -p\mathbf{I} + \boldsymbol{\sigma}_{\text{eq}}^{\text{dev}}, \quad \boldsymbol{\sigma}_{\text{eq}}^{\text{dev}} = \frac{2}{J}\mathbf{F}\frac{\partial W_{\text{eq}}^{\text{dev}}}{\partial \mathbf{C}}\mathbf{F}^T \tag{6.22}$$

- **Volumetric constraint**:

$$p = -\frac{\partial U(J)}{\partial J} \tag{6.23}$$

- **Viscoelastic stress**: Evolves according to

$$\overset{\circ}{\boldsymbol{\sigma}}_{\text{neq},k} + \frac{\boldsymbol{\sigma}_{\text{neq},k}}{\tau_k} = \dot{\gamma}_k \tag{6.24}$$

Mixed Variational Formulation

Due to the incompressibility of rubber, a mixed variational formulation must be employed. In this formulation, the hydrostatic pressure p is introduced as an additional unknown variable in the problem. Various variants of mixed formulations can be found in the literature, with detailed discussions provided in the works of J.C. Simo [102] and Brezzi and Fortin [190]. In the following, we briefly introduce a weak form in the context of steady state rolling.

Function Spaces

Let us define the functional spaces $\mathcal{U}$, $\mathcal{Q}$ and $\mathcal{U}$, such that:

$$\begin{aligned} \mathcal{U} &= \left\{ \boldsymbol{u} \in [H^1(\Omega)]^3 : \boldsymbol{u} = \boldsymbol{u}_0 \text{ on } \Gamma_u \right\} \\ \mathcal{Q} &= \left\{ p \in L^2(\Omega) \right\} \\ \mathcal{U}_0 &= \left\{ \boldsymbol{w} \in [H^1(\Omega)]^3 : \boldsymbol{w} = \mathbf{0} \text{ on } \Gamma_u \right\} \end{aligned}$$

Weak Form Residuals

Based on Eq.(6.16) and Eq.(6.23), we use the (u, p) and the test functions (w, q) to derive the residuals R_u and R_p :

- **Momentum residual** (R_u):

$$\begin{aligned} R_u(\boldsymbol{u}, p; \boldsymbol{w}) = &\int_\Omega \left[\eta\left(-p\mathbf{I} + \boldsymbol{\sigma}_{\text{eq}}^{\text{dev}}\right) + \boldsymbol{\sigma}_{\text{neq}}\right] : \nabla \boldsymbol{w} \mathrm{d}\Omega \\ &- \int_\Omega \rho\left[\boldsymbol{b} - \boldsymbol{\omega} \times (\boldsymbol{\omega} \times \boldsymbol{x}) - 2\boldsymbol{\omega} \times \boldsymbol{v}_{\text{rel}}\right] \cdot \boldsymbol{w} \mathrm{d}\Omega \\ &- \int_{\Gamma_t} \boldsymbol{t} \cdot \boldsymbol{w} \mathrm{d}\Gamma - \underbrace{\int_{\Gamma_c} \left[\epsilon_n \langle g \rangle_- (\boldsymbol{w} \cdot \boldsymbol{n}) + \boldsymbol{t}_t \cdot \boldsymbol{w}_t\right] \mathrm{d}\Gamma}_{\text{Contact term}} \end{aligned} \tag{6.25}$$

- **Volumetric constraint residual** (R_p):

$$R_p(\boldsymbol{u}, p; q) = \int_\Omega \left[p + \frac{\partial U(J)}{\partial J} \right] q \mathrm{d}\Omega \tag{6.26}$$

Variational Statement

Now, we seek $(\boldsymbol{u}, p) \in \mathcal{U} \times \mathcal{Q}$ such that:

$$\begin{aligned} R_u(\boldsymbol{u}, p; \boldsymbol{w}) = 0 \quad \forall \boldsymbol{w} \in \mathcal{U}_0 \\ R_p(\boldsymbol{u}, p; q) = 0 \quad \forall q \in \mathcal{Q} \end{aligned} \tag{6.27}$$

Finite Element Discretization

With the weak form at hand, we proceed with the discretization of u, p, w and q.

Field Approximations

$$\boldsymbol{u} = \sum_{i=1}^{n_u} N_i^u \boldsymbol{u}_i, \quad \boldsymbol{w} = \sum_{i=1}^{n_u} N_i^u \boldsymbol{c}_i, \quad p = \sum_{j=1}^{n_p} N_j^p p_j, \quad q = \sum_{j=1}^{n_p} N_j^p d_j \tag{6.28}$$

Matrix Formulation

After replacing Eq.(6.28) into Eq.(6.27) and rewriting everything out, we obtain the discrete system in the form:

$$\begin{bmatrix} \mathbf{K}_{uu} & \mathbf{K}_{up} \\ \mathbf{K}_{pu} & \mathbf{K}_{pp} \end{bmatrix} \begin{bmatrix} \Delta \boldsymbol{u} \\ \Delta \boldsymbol{p} \end{bmatrix} = - \begin{bmatrix} \boldsymbol{R}_u \\ \boldsymbol{R}_p \end{bmatrix} \tag{6.29}$$

Where Sub-Matrix Definitions are:

- **Displacement tangent stiffness**:

$$\mathbf{K}_{uu} = \int_\Omega \mathbf{B}^T \left[\eta \mathbb{C}_{\text{eq}}^{\text{dev}} + \mathbb{C}_{\text{neq}} \right] \mathbf{B} \mathrm{d}\Omega + \mathbf{K}_{\text{inertia}} + \mathbf{K}_{\text{contact}} \tag{6.30}$$

- **Displacement-pressure** (up) **coupling stiffness**:

$$\mathbf{K}_{up} = - \int_\Omega \eta (\nabla \cdot \boldsymbol{w})^T \boldsymbol{N}^p \mathrm{d}\Omega \tag{6.31}$$

- **Pressure-displacement** (pu) **coupling stiffness**:

$$\mathbf{K}_{pu} = \int_\Omega \frac{\partial^2 U}{\partial J^2} \frac{\partial J}{\partial \boldsymbol{u}} (\boldsymbol{N}^p)^T \mathrm{d}\Omega \tag{6.32}$$

- **Pressure stiffness**:

$$\mathsf{K}_{pp} = \int_\Omega (\boldsymbol{N}^p)^T \boldsymbol{N}^p \mathrm{d}\Omega \tag{6.33}$$

Constitutive Update Algorithm

In the numerical implementation of the above discretized form, the following computations are carried out at each integration point:

1. Compute kinematics: F, J, $\overline{\mathsf{C}}$
2. Calculate strain energies:

$$W_{\text{eq}} = U(J) + W_{\text{eq}}^{\text{dev}}(\overline{\mathsf{C}}) \tag{6.34}$$

3. Update damage variable:

$$W_{\text{eq}}^{\max} \leftarrow \max(W_{\text{eq}}^{\max}, W_{\text{eq}}), \quad \eta = 1 - \frac{1}{r}\operatorname{erf}\left(\frac{W_{\text{eq}}^{\max} - W_{\text{eq}}}{m}\right) \tag{6.35}$$

4. Compute stresses:

$$\boldsymbol{\sigma}_{\text{eq}}^{\text{dev}} = \frac{2}{J}\mathsf{F}\frac{\partial W_{\text{eq}}^{\text{dev}}}{\partial \mathsf{C}}\mathsf{F}^T, \quad p = -\frac{\partial U(J)}{\partial J} \tag{6.36}$$

5. Update viscoelastic stress:

$$\boldsymbol{\sigma}_{\text{neq}}^{n+1} = \mathcal{F}(\boldsymbol{\sigma}_{\text{neq}}^{n}, \dot{\gamma}, \Delta t) \tag{6.37}$$

Contact-Friction Implementation

Contact enforcement has to be achieved numerically for each contact element:

1. Compute normal gap:

$$g = (\boldsymbol{x} - \boldsymbol{x}_c) \cdot \boldsymbol{n} \tag{6.38}$$

2. Calculate normal pressure:

$$p_n = \epsilon_n \langle g \rangle_- \tag{6.39}$$

3. Determine tangential traction:

$$\boldsymbol{t}_t = \begin{cases} \epsilon_t \boldsymbol{\xi} & \text{if } \|\epsilon_t \boldsymbol{\xi}\| \leq \mu |p_n| \quad \text{(stick)} \\ \mu |p_n| \dfrac{\boldsymbol{\xi}}{\|\boldsymbol{\xi}\|} & \text{otherwise} \quad \text{(slip)} \end{cases} \tag{6.40}$$

Steady-State Advection

- Material velocity field:

$$\boldsymbol{v} = \boldsymbol{\omega} \times \boldsymbol{x} - \dot{\boldsymbol{u}} \tag{6.41}$$

- History variable advection:

$$\frac{DW_{\text{eq}}^{\max}}{Dt} = 0 \quad \text{(Advect along streamlines)} \tag{6.42}$$

- ALE formulation for mesh motion:

$$\boldsymbol{v}_{\text{mesh}} = \boldsymbol{\omega} \times \boldsymbol{x} \tag{6.43}$$

Stabilization Techniques

Throughout the numerical implementation, instability may arise from the pressure constraint, the Coriolis force, and the contact constraint; thus, stabilization techniques are introduced to handle them.

- **Inf-sup stabilization**:

$$R_p^{\text{stab}} = R_p + \int_\Omega \kappa \nabla p \cdot \nabla q \mathrm{d}\Omega \tag{6.44}$$

- **Coriolis stabilization**:

$$\boldsymbol{b}_{\text{cor}}^{\text{stab}} = \boldsymbol{b}_{\text{cor}} + \zeta h (\boldsymbol{v}_{\text{rel}} \cdot \nabla) \dot{\boldsymbol{u}} \tag{6.45}$$

- **Contact regularization**:

$$\langle g \rangle_- \approx -\frac{g}{2} \left(1 - \tanh(kg)\right), \qquad \frac{\boldsymbol{\xi}}{\|\boldsymbol{\xi}\|} \approx \frac{\boldsymbol{\xi}}{\|\boldsymbol{\xi}\| + \epsilon_{\text{reg}}} \tag{6.46}$$

Solution Algorithm

1. Initialize: $\eta = 1$, $W_{\text{eq}}^{\max} = 0$, $\boldsymbol{\sigma}_{\text{neq}} = \boldsymbol{0}$
2. For each load increment:
   (a) Update mesh position (ALE framework)
   (b) Advect history variables $W_{\text{eq}}^{\max}$
   (c) Newton-Raphson iteration:
      i. Compute deformation measures
      ii. Update constitutive state
      iii. Calculate contact forces
      iv. Assemble residuals $\boldsymbol{R}_u$, $\boldsymbol{R}_p$

v. Construct tangent matrix K
vi. Solve linear system for $\Delta \boldsymbol{u}$, $\Delta \boldsymbol{p}$
vii. Update solution: $\boldsymbol{u} \leftarrow \boldsymbol{u} + \Delta \boldsymbol{u}$, $p \leftarrow p + \Delta p$
viii. Check convergence: $\|\Delta \boldsymbol{u}\| < \epsilon_u$, $\|\Delta \boldsymbol{p}\| < \epsilon_p$

It is important to note that there are different formulations for the steady-state rolling problem, specifically the Eulerian and Lagrangian formulations. In the Lagrangian formulation, the reference configuration used to describe motion is tied to the material itself. In contrast, the Eulerian formulation describes the problem based on the current configuration.

In ABAQUS[38], a mixed Eulerian/Lagrangian approach is implemented to reduce computational costs. Specifically, in the analysis of tire-road steady-state transport, the tire is modeled using the Eulerian frame, while the rigid road is modeled using the Lagrangian formulation.

Results and discussions

In this section, we performed steady-state rolling analysis of $165/65R13$ tire using input script language in ABAQUS. We chose an inflation pressure of 250kPa, a speed of $80\ \text{Km.h}^{-1}$ and considered three loading levels, namely $50\%\text{LI}$, $75\%\text{LI}$, and $100\%\text{LI}$. The basic Coulomb Friction Model (see Figure 3.16(b)) was adopted by setting the friction coefficient (μ) and the slip rate to 0.8 and 0.02, respectively.

Free rolling analysis

In rolling conditions, the contact patch and stress distribution have an impact on the rolling and grip resistance of the tire as well as fuel consumption. The aim of this analysis is to find the free rolling angular velocity, where, particularly, the torque is equal to zero. The Eulerian formulation introduced in Section 3.1 was utilized for this purpose. Since the footprint analysis was conducted assuming a frictionless contact, contact properties were modified in the script with the `*contact change` option.

Under the above-described conditions, the free rolling was performed for each level of load using the footprint analysis result as a restart file. The recorded longitudinal resistance force and the rolling resistance moment (wheel torque) are shown in Figure 6.31.

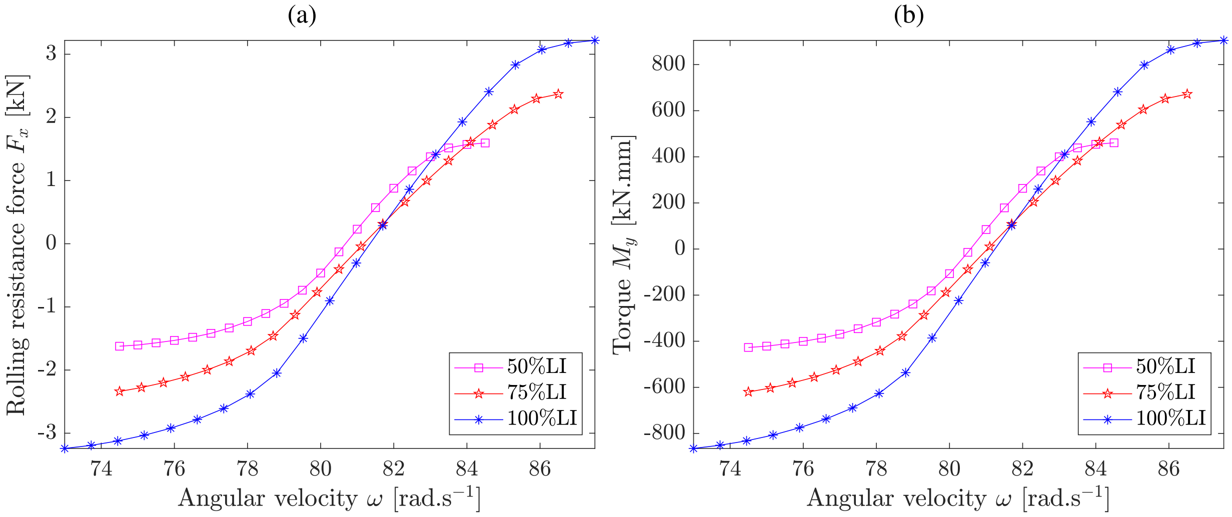

Figure 6.31: Dependence of the tire rolling resistance force and wheel torque on the angular velocity ω and applied load F_z at a rolling velocity of 80Km.h^{-1}. (a) longitudinal resistance force F_x and (b) wheel torque M_y.

With this result at hand, the free rolling position was computed using the results in Figure 6.31(b) as illustrated with the red marker in the curves in Figure 6.32.

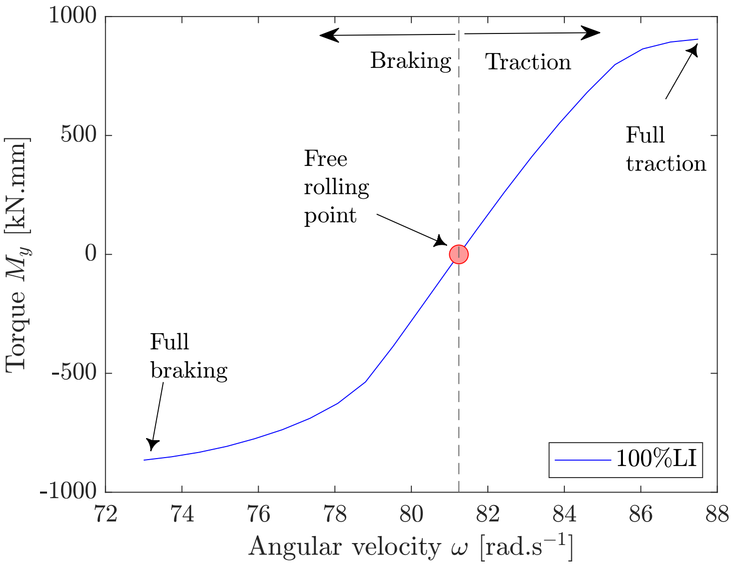

Figure 6.32: Identification of the free rolling angular velocity ω_0.

At full traction and full braking, the rolling resistance force reaches the threshold value of μF_z, in absolute value, as can be seen in Figure 6.31(a). For example, when $F_z = 100\%LI = 4041.72$ N, the maximum rolling resistance force is $F_{x,friction} = 3233, 38$ N.
At free rolling point, the distribution of the contact patch and stress is shown in Figure 6.33. The maximum contact stress rises from 0.46 MPa at $50\%LI$ to 0.64 MPa at $75\%LI$, then to 0.85 MPa at $100\%LI$. Furthermore, as a consequence of the fact that M_y yields zero, the

contact patch has approximately two axes of symmetry with respect to the center of the contact patch.

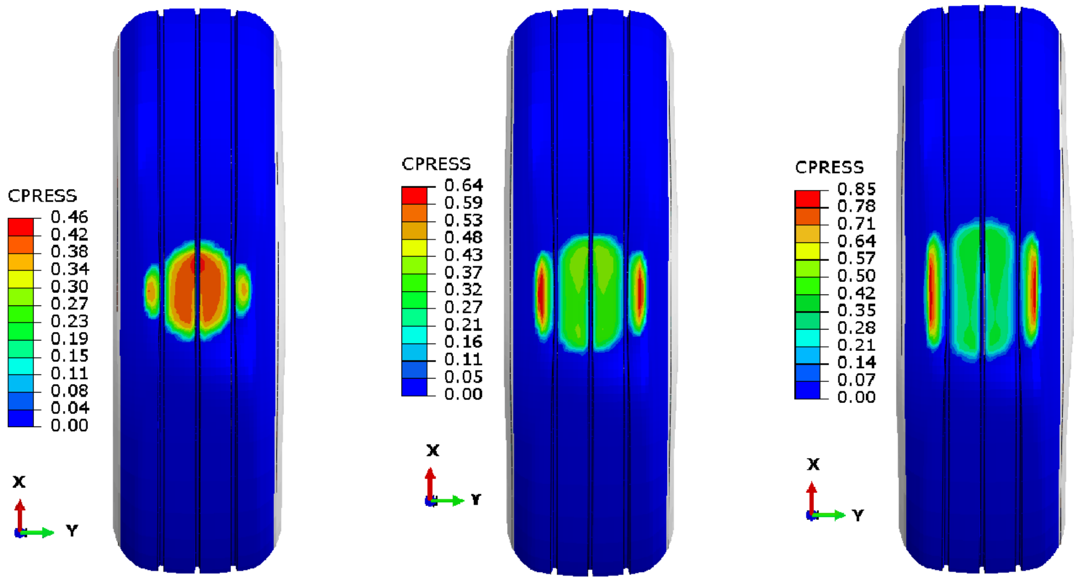
(a) at $50\%LI$ (b) at $75\%LI$ (c) at $100\%LI$

Figure 6.33: Distribution of the contact stress $[\mathrm{MPa}]$ at free rolling with a velocity of $80\mathrm{Km.h}^{-1}$.

The figure is completely different at full braking, where the contact stress peak shifts toward the front zone of the contact area in the heading direction as shown in Figure 6.34.

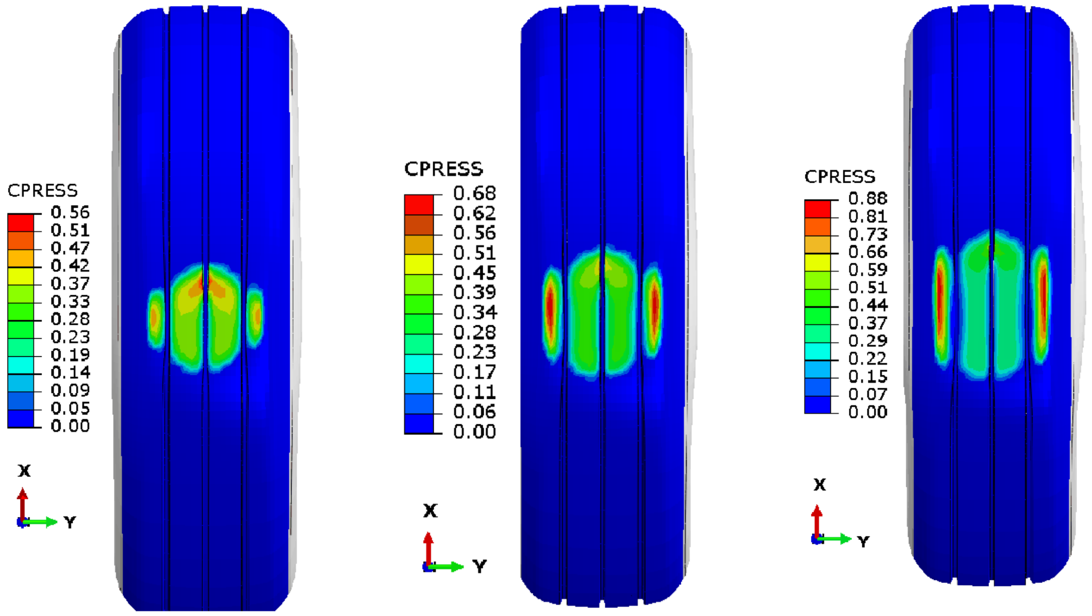
(a) at $50\%LI$ (b) at $75\%LI$ (c) at $100\%LI$

Figure 6.34: Distribution of the contact stress $[\mathrm{MPa}]$ at full braking from a speed of $80\mathrm{Km.h}^{-1}$.

At full acceleration, however, the opposite situation occurs, with the concentration of the contact stress being shifted towards the rear of the contact patch, as illustrated in Figure 6.35.

Similarly, the maximum value of the contact stress increases with the load applied.

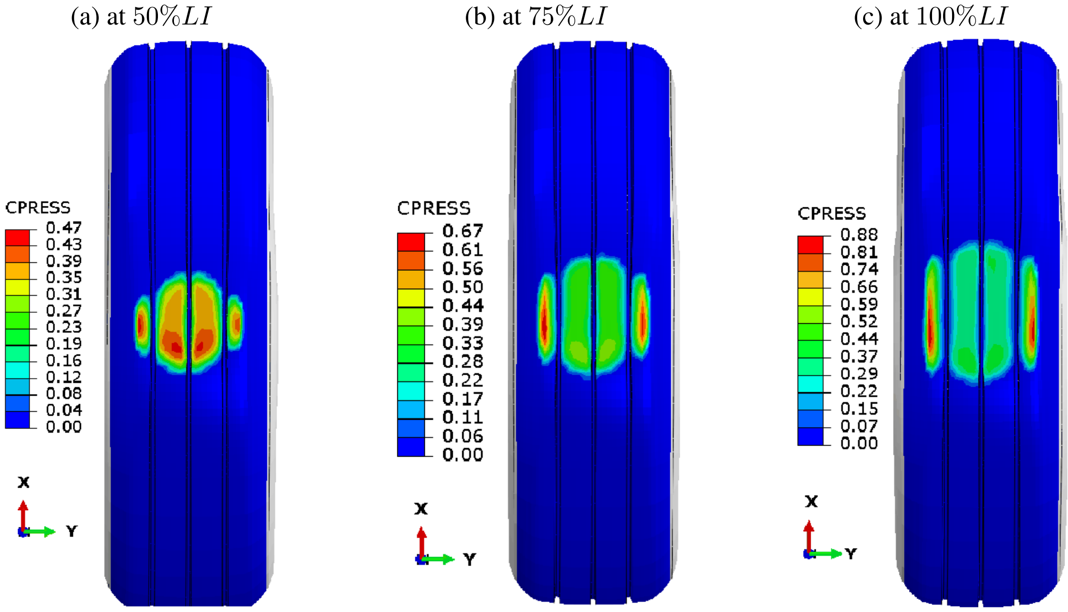
(a) at 50%LI (b) at 75%LI (c) at 100%LI

Figure 6.35: Distribution of the contact stress $[\mathrm{MPa}]$ at full acceleration from a speed of $80\mathrm{Km.h}^{-1}$.

After finding the angular velocity corresponding to free rolling (0 torque), the next step was to analyze the cornering and camber response of the tire.

Camber effect analysis

The effect of camber on tire-road interaction forces/moments was studied considering a camber angle $\gamma \in [0, 8°]$. Figure 6.36 represents resulting tire characteristics

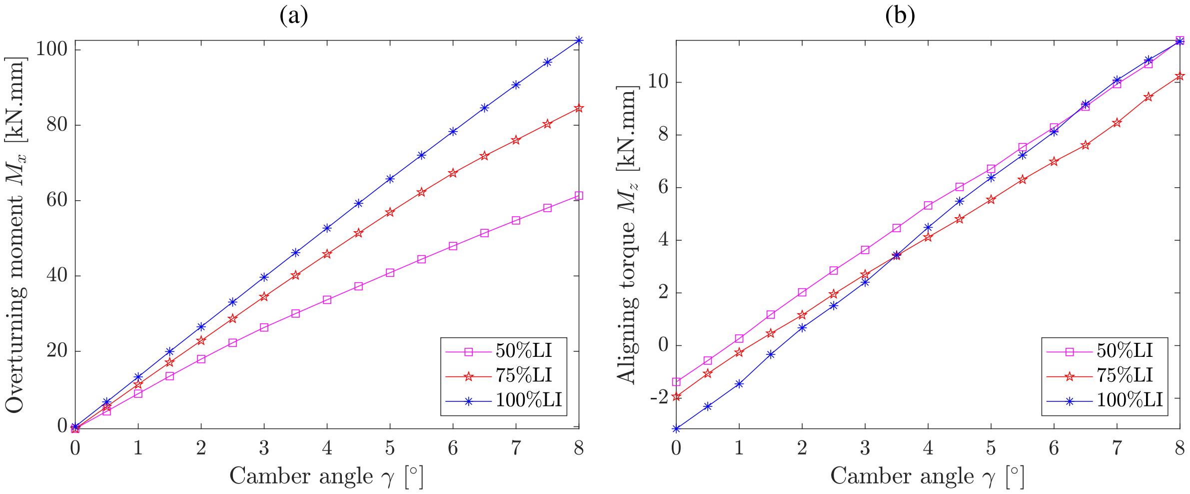
(a) (b)

Figure 6.36: Dependence of the tire forces/moments on the camber angle γ and applied load F_z at a velocity of $80\mathrm{Km.h}^{-1}$. (a) overturning moment M_x and (b) Aligning torque M_z.

It should be noted that in the case of $\gamma \in [-8°, +8°]$, the full curves of M_x and M_z can be obtained by symmetry with respect to the origin, as illustrated with M_x in Figure 6.37.

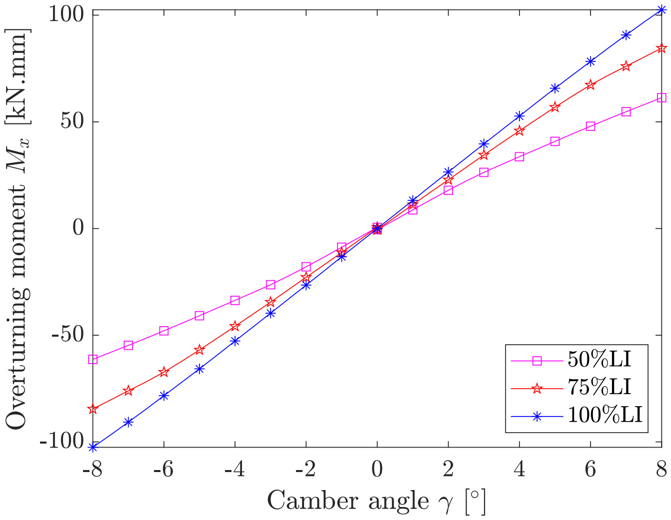

Figure 6.37: M_x versus $\gamma \in [-8°, +8°]$.

When the $\gamma = 8°$, the resulting contact patch and contact stress is depicted in Figure 6.38.

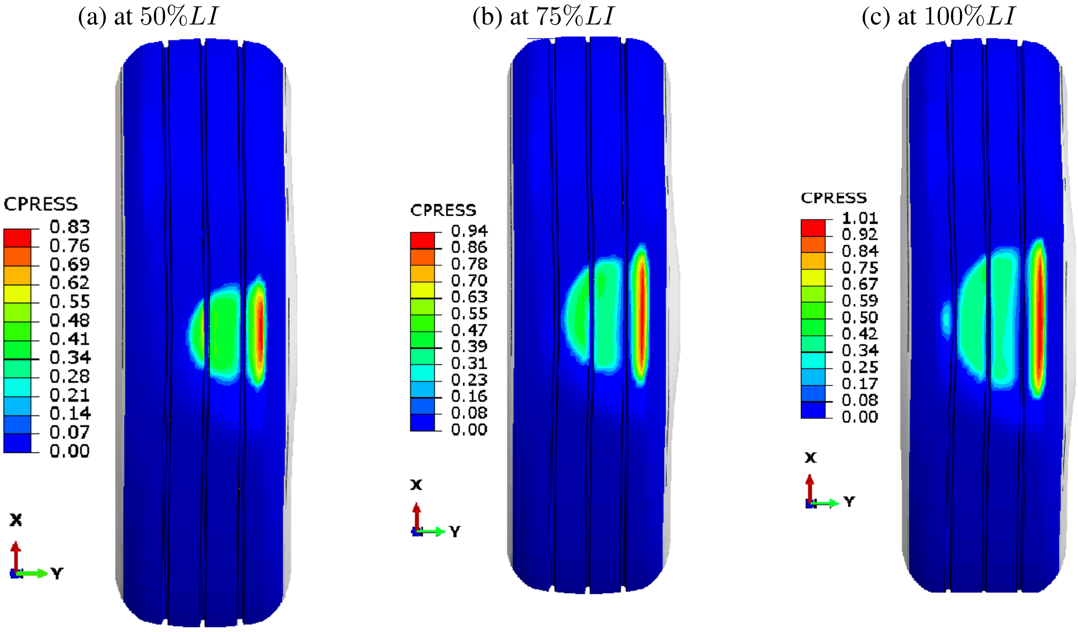
(a) at $50\%LI$

(b) at $75\%LI$

(c) at $100\%LI$

Figure 6.38: Distribution of the contact stress [MPa] at cambering with $\gamma = 8°$ and a velocity of 80 Km.h^{-1}.

Cornering effect analysis

When tire direction deviates from the direction of driving, such as in cornering, there is an angle called the slip angle between these directions. These conditions generate forces/moments that affect tire maneuverability and stability. Hence, in this section, we analyze the handling characteristics of the 165/65R13 tire in pure cornering with a slip angle $\alpha \in [0, 15°]$. Figure 6.39

shows the resulting tire rolling forces/moments.

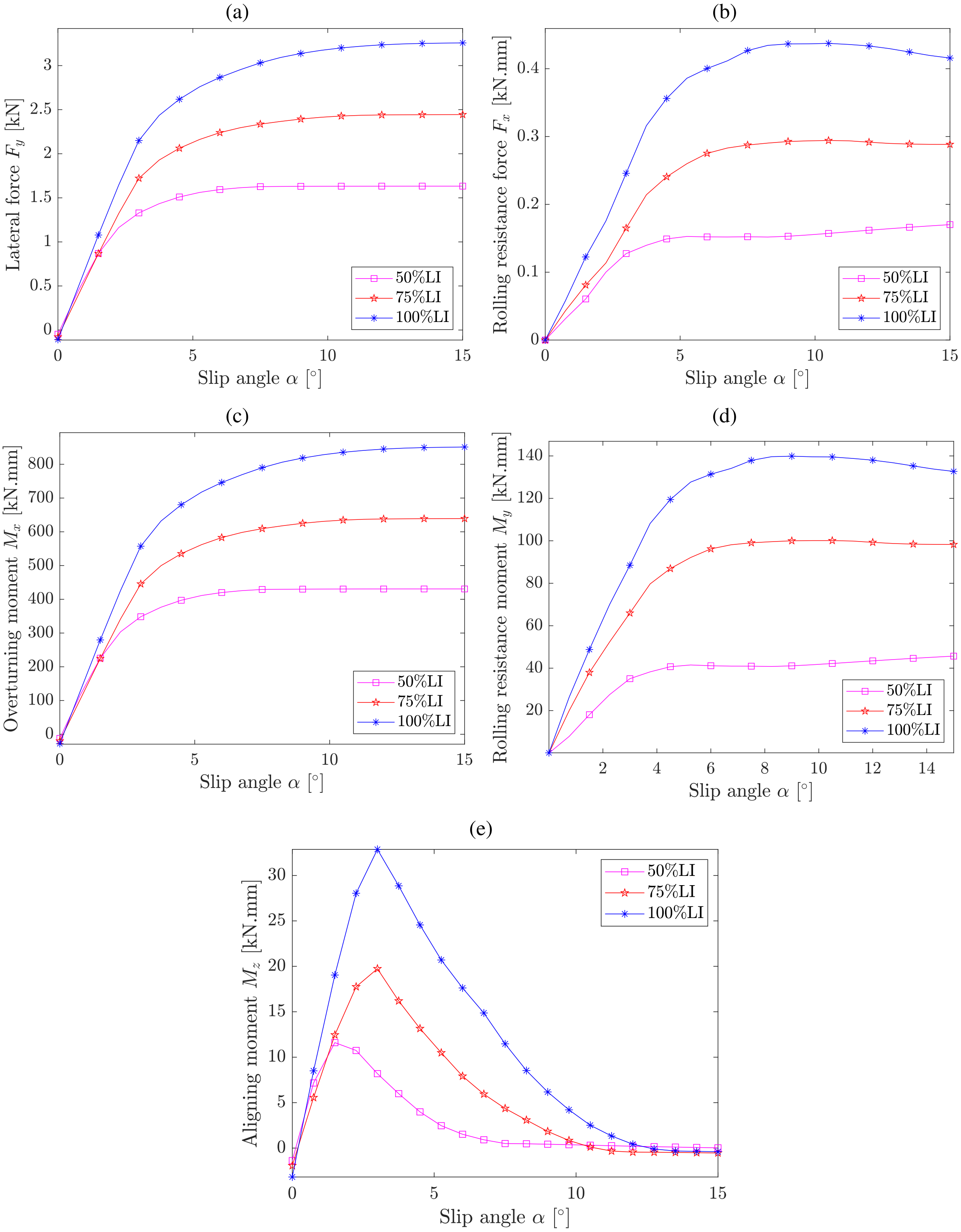

Figure 6.39: Dependence of the tire forces/moments on the slip angle α and applied load F_z at a velocity of 80 $\mathrm{Km.h}^{-1}$. (a) Lateral force F_y and (b) Longitudinal force F_x, (c) overturning moment M_x, (d) rolling resistance moment M_y and (e) Aligning torque M_z.

Similarly, these characteristics can be easily deduced for the negative/positive slip angle as shown in Figure 6.40.

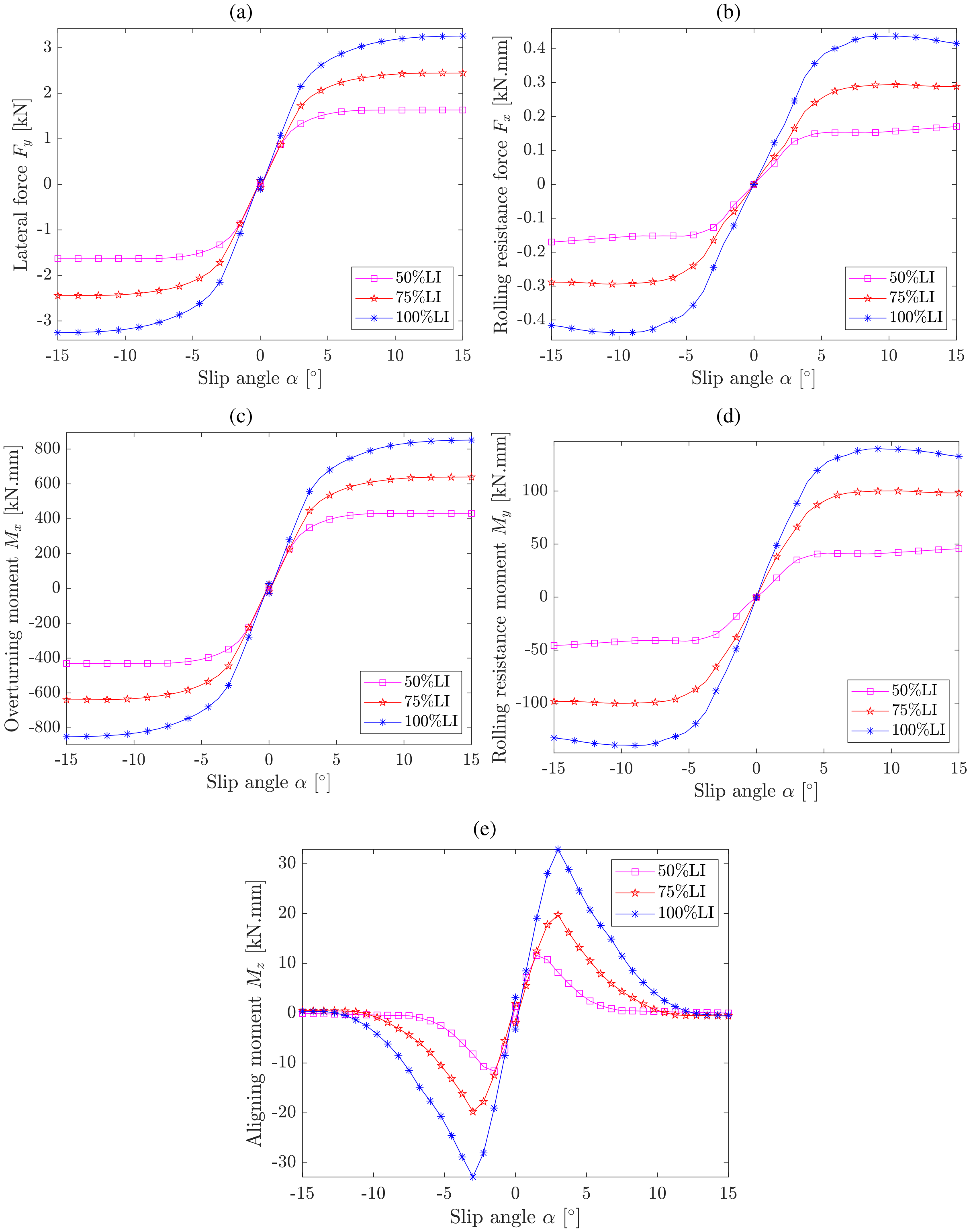

Figure 6.40: Dependence of the tire forces/moments on the slip angle $\gamma \in [-15°, +15°]$ and applied load F_z at a velocity of 80 $\mathrm{Km.h^{-1}}$. (a) Lateral force F_y, (b) Lateral force F_x, (c) overturning moment M_x, (d) rolling resistance moment M_y and (e) Aligning torque M_z.

From the above results, it is possible to make use of the numerical derivative to compute the cornering stiffness C_α based on the formula defined in Eq.(2.2). Figure 6.41 shows the variation of the cornering stiffness as a function of $\alpha \in [0, 15°]$ at the same velocity of $80\ \mathrm{Km.h}^{-1}$.

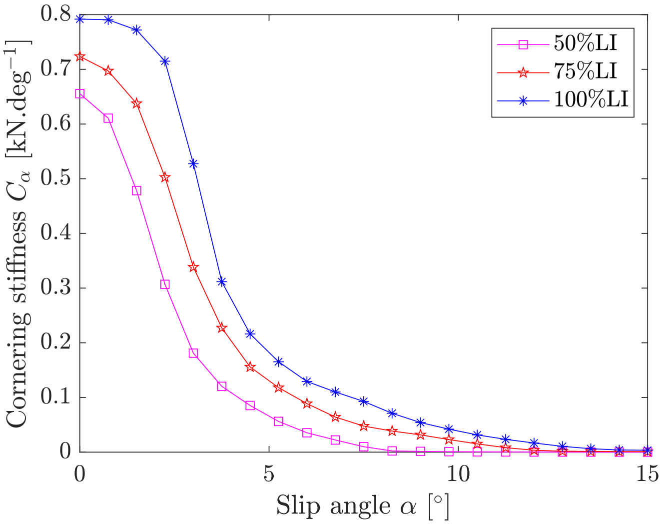

Figure 6.41: Cornering stiffness C_α for $\alpha \in [0, 15°]$.

For completeness, it is very common to obtain C_α with $\alpha \in [-15, +15°]$. According to the definition of the derivative, the left-hand side portion of C_α can be obtained by making a symmetry of the initial portion with respect to the vertical axis. The result is shown in Figure 6.42.

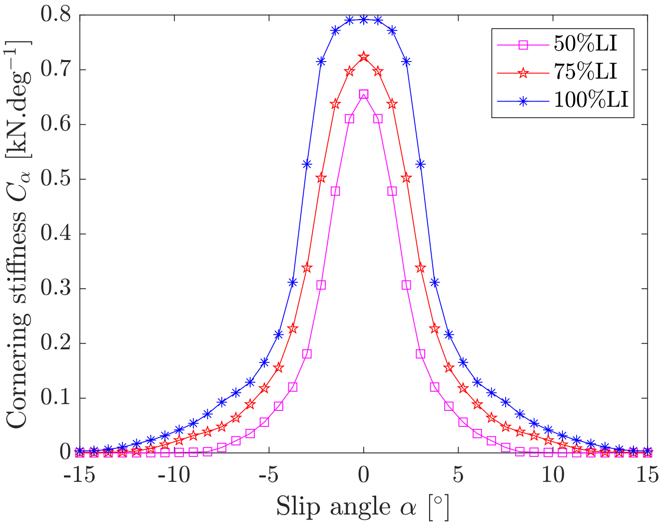

Figure 6.42: Variation of the cornering stiffness C_α as function of $\alpha \in [-15°, +15°]$ and applied load.

As can be seen in Figure 6.41 and Figure 6.42, C_α reaches its maximum at 0 slip angle for each level of load applied. Particularly at $100\%LI$, $C_\alpha^{FEM}\ |_{max,\alpha=0} = 791.81\ \mathrm{N}.^{\circ -1}$. Physically, this value means that at a rolling speed of $80\ \mathrm{Km.h}^{-1}$ and under $100\%LI$, one degree slip angle generates the lateral contact force between the tire and the road of magnitude $791.81\ \mathrm{N}$. This parameter is very important to counteract centrifugal forces. Therefore, the higher this parameter is, the stronger the tire is to guarantee the stability and grip during cornering.

Validation of the steady state rolling analysis:

In Gillespie's book[191] entitled *"Fundamentals of vehicle dynamics"*, a reference in the field, it is established that for PCR tires, the cornering stiffness at 100% Load Index (LI) can be approximated using the formula provided in Eq. (6.47)

$$C^{emp}{}_{\alpha}\ |_{max,\alpha=0} = 0.2 * 100\% LI = 808.34\ \mathrm{N.}^{\circ -1} \tag{6.47}$$

The comparison between the calculated and empirical values at $100\% LI$ and 0 slip angle is summarized in Table 6.15.

Table 6.15: Comparison between the calculated and empirical cornering Stiffness at $100\% LI$, 0° slip angle and $80\ \mathrm{Km.h}^{-1}$ rolling velocity.

$C_{\alpha}^{FEM}{}_{\alpha=0,max}\ [\mathrm{N.}^{\circ -1}]$	$C_{\alpha}^{emp}{}_{\alpha=0,max}\ [\mathrm{N.}^{\circ -1}]$	Relative error(%)
791.81	808.34	2.04

Given that the relative error is very small, we validate the accuracy of the model.

The resulting tire-road contact interaction (contact stress and patch) is depicted in Figure 6.43.

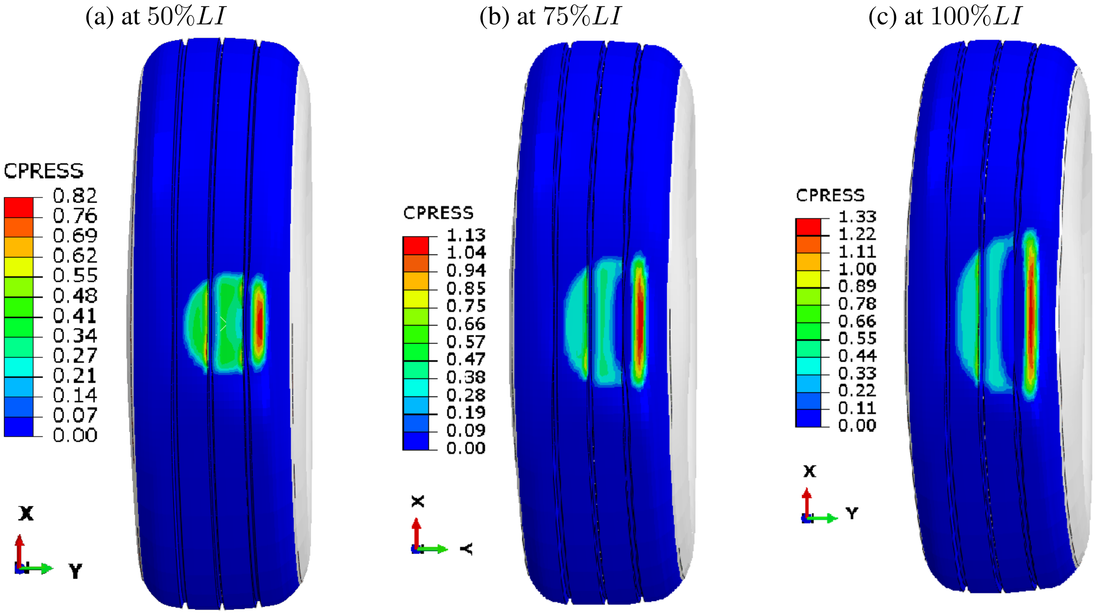
(a) at $50\% LI$ (b) at $75\% LI$ (c) at $100\% LI$

Figure 6.43: Distribution of the contact stress $[\mathrm{MPa}]$ at cornering with $\alpha = 15°$ and a velocity of $80\ \mathrm{Km.h}^{-1}$.

6.3.2 Post-steady state rolling modal analysis

The purpose of this analysis is to study the modal vibration of the tire at free rolling state (see Figure 6.32) at the velocity of $v_x = 80\ \mathrm{Km.h}^{-1}$. The mathematical formulation and the resolution procedure are the same as explained in Section 6.2.3 for unloaded modal analysis.

However, here the deformed configuration at the free rolling state is used instead as the base configuration for the modal analysis. Therefore, the free rolling input file was utilized as a restart file for this analysis. Only the case with $F_z = 100\% LI$ was investigated in this section.

Results and discussions

The obtained vibration frequencies and mode shapes are reported in Table 6.16 and Table 6.17 for in-plane (radial) and out-of-plane(axial) modes, respectively.

Table 6.16: Ten (10) lowest in-plane vibration modes of the free rolling tire at $80\ \mathrm{Km.h^{-1}}$.

Mode	f[Hz]	X – Z view	Mode	f[Hz]	X – Z view
R0	49.43	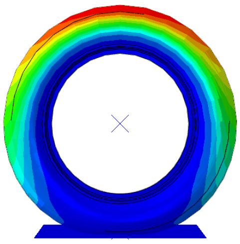	R1	71.37	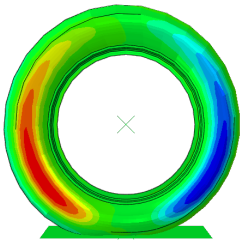
R1′	82.40	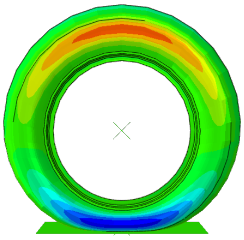	R2	109.61	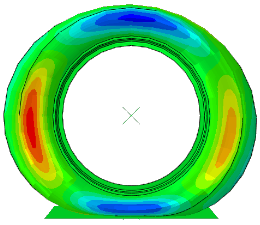
R3	134.50	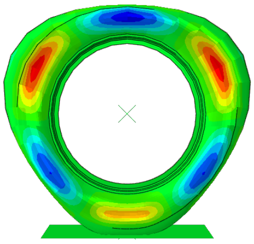	R3′	137.46	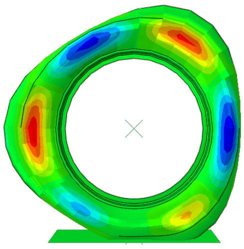
R4	158.98	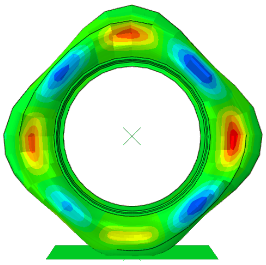	R4′	163.11	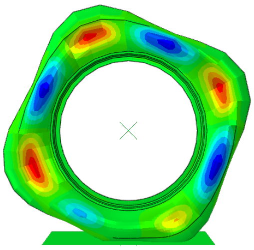

Continued on next page

Table 6.16: Ten (10) lowest in-plane vibration modes of the free rolling tire at 80 $\mathrm{Km.h^{-1}}$. (Continued)

Mode	f[Hz]	X – Z view	Mode	f[Hz]	X – Z view
R5	182.22	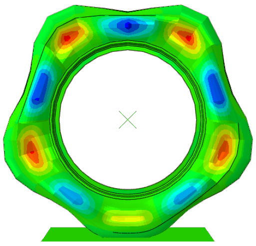	R6	203.03	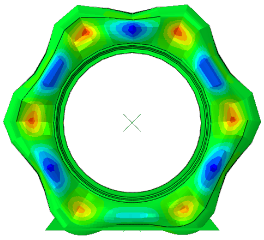

Natural out-of-plane vibration modes are reported in Table 6.17.

Table 6.17: Eight (08) lowest out-of-plane vibration modes of the free rolling tire at 80 $\mathrm{Km.h^{-1}}$.

Mode	f[Hz]	X – Z view	Mode	f[Hz]	X – Z view
A1	60.83	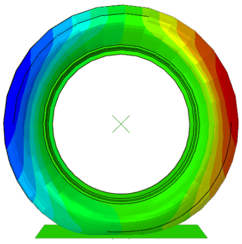	A2	88.43	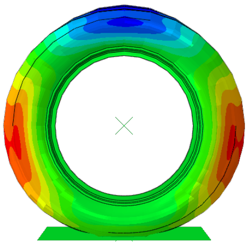
A2′	109.19	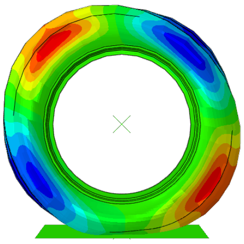	A3	145.86	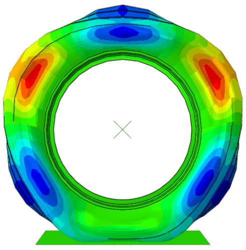
A3′	158.08	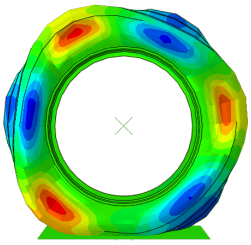	A4	183.75	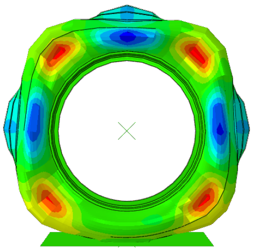
A5	187.53	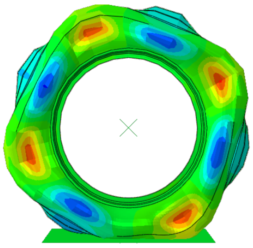	A6	204.12	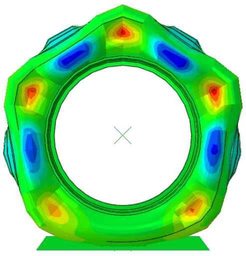

Partial conclusion

When comparing the results of the natural vibrations of the unloaded tire to those of the tire under steady-state free rolling conditions, the following characteristics of modal vibrations can be observed:

- Several vibration modes appear in pairs but oscillate at different frequencies. The specific pairs identified include modes $\mathrm{R1}$ and $\mathrm{R1}'$, modes $\mathrm{R3}$ and $\mathrm{A3}'$, modes $\mathrm{R4}$ and $\mathrm{A4}'$, modes $\mathrm{A2}$ and $\mathrm{A2}'$ or modes $\mathrm{A3}$ and $\mathrm{A3}'$.
- With the exception of radial mode $\mathrm{R2}$ and the axial mode $\mathrm{A2}'$, the frequencies of the tire in free rolling conditions are smaller.

6.3.3 Random Vibration Analysis via PSD

Random vibration analysis based on Power Spectral Density (PSD) is a convolutional technique for studying a system's response to nondeterministic loads or excitations. This method utilizes PSD along with Mode Superposition to statistically predict displacements, strains, and stresses.

Problem formulation: A Two-Stage Solution Strategy

The implementation of this method typically involves two stages. The first stage involves nonlinear static analysis (with contact), which assesses the system's behavior under static loads while considering the inherent nonlinearities in material properties, geometry, and contact conditions. Following this, the frequency extraction is conducted. Finally, the calculation of the Power Spectral Density (PSD) response is carried out.

- **Stage 1: Nonlinear Static Analysis**

  From the strong form, in Section 4.7.1, we solve for mean displacement $\boldsymbol{u}_0$ under static loads:

  $$\int_{\Omega_0} \boldsymbol{P}(\boldsymbol{u}_0, \xi_0) : \delta\boldsymbol{F}\mathrm{d}\Omega_0 = \int_{\Omega_0} \rho_0 \bar{\boldsymbol{b}} \cdot \delta\boldsymbol{u}\mathrm{d}\Omega_0 + \int_{\Gamma_N} \bar{\boldsymbol{t}} \cdot \delta\boldsymbol{u}\mathrm{d}\Gamma_N + \int_{\Gamma_C} \boldsymbol{t}_{c0} \cdot \delta\boldsymbol{u}\mathrm{d}\Gamma_C \quad (6.48)$$

  Here the damage effect is frozen at $\xi_0 = \max \Psi_0(\boldsymbol{C}(\boldsymbol{u}_0))$.

- **Stage 2: Linearized Dynamic Analysis**

  The weak form of the problem in dynamics is given by:

  $$\underbrace{\int_{\Omega_0} \rho_0 \ddot{\boldsymbol{u}} \cdot \delta\boldsymbol{u}\, dV}_{\text{Inertial term}} + \int_{\Omega_0} \boldsymbol{P}(\boldsymbol{u}_0, \xi_0) : \delta\boldsymbol{F}\mathrm{d}\Omega_0 = \int_{\Omega_0} \rho_0 \bar{\boldsymbol{b}} \cdot \delta\boldsymbol{u}\mathrm{d}\Omega_0 + \int_{\Gamma_N} \bar{\boldsymbol{t}} \cdot \delta\boldsymbol{u}\mathrm{d}\Gamma_N + \int_{\Gamma_C} \boldsymbol{t}_{c0} \cdot \delta\boldsymbol{u}\mathrm{d}\Gamma$$

  (6.49)

Recalling that the displacement u can be decomposed in terms of its mean value $\boldsymbol{u}_0$ and $\tilde{\boldsymbol{u}}$ (the random part), we can linearize it around $\boldsymbol{u}_0$ as follows:

$$\delta \boldsymbol{F} \approx \nabla_{\boldsymbol{X}} \delta \boldsymbol{u} \tag{6.50}$$

$$\boldsymbol{P} \approx \boldsymbol{P}_0 + \mathbb{C} : \Delta \boldsymbol{E} + \mathbb{D} : \Delta \dot{\boldsymbol{E}} \tag{6.51}$$

where $\mathbb{C}$ is tangent modulus and $\mathbb{D}$ is damping modulus.

Viscoelastic Material Response in Frequency Domain

Prony series time dependent material properties can be converted into frequency-dependent viscoelastic response by the complex modulus tensor $\mathbb{D}(\omega)$ as follows

$$\mathbb{D}(\omega) = \mathbb{C}_0 \left[g_\infty + \sum_{k=1}^{m} g_k \frac{i\omega\tau_k}{1 + i\omega\tau_k} \right] \tag{6.52}$$

where:

- $g_\infty = 1 - \sum g_k$ is the equilibrium modulus fraction
- g_k and τ_k are Prony series parameters
- $\mathbb{C}_0$ is the instantaneous elastic modulus

The damping matrix $\boldsymbol{C}(\omega)$ is then computed as:

$$\boldsymbol{C}(\omega) = \int_{\Omega_0} \boldsymbol{B}^T \mathbb{D}_{\text{imag}}(\omega) \boldsymbol{B} d\Omega_0 \tag{6.53}$$

where $\mathbb{D}_{\text{imag}}$ is the imaginary part of $\mathbb{D}(\omega)$, representing energy dissipation.

Frequency Domain Formulation

Let us apply Fourier transform $\mathcal{F}\{\tilde{\boldsymbol{u}}\} = \hat{\tilde{\boldsymbol{u}}}(\omega)$ and rewrite the weak form accordingly:

$$\int_{\Omega_0} \left[-\omega^2 \rho_0 \hat{\tilde{\boldsymbol{u}}} + i\omega \hat{\boldsymbol{\sigma}}_{\text{visco}} + \hat{\boldsymbol{\sigma}}_{\text{el}} \right] \quad : \quad \delta \hat{\boldsymbol{\epsilon}} \mathrm{d}\Omega_0 \quad = \quad - \int_{\Omega_0} \rho_0 \hat{\ddot{\boldsymbol{u}}}_b(\omega) \quad \cdot \quad \delta \hat{\tilde{\boldsymbol{u}}} \mathrm{d}\Omega_0 \tag{6.54}$$

where:

- $\hat{\boldsymbol{\sigma}}_{\text{el}} = \mathbb{C}(\eta(\xi_0)) : \hat{\boldsymbol{\epsilon}}$ is the linearized elastic stress
- $\hat{\boldsymbol{\sigma}}_{\text{visco}} = \mathbb{D}_{\text{real}}(\omega) : \hat{\boldsymbol{\epsilon}}$ is the viscoelastic stress
- $\hat{\tilde{g}}$ is the dynamic gap variation

Discretized Finite Element Equations

After FEM discretization using $\hat{\tilde{\boldsymbol{u}}} = \boldsymbol{N} \hat{\tilde{\boldsymbol{d}}}$, we obtain

$$\left(-\omega^2 \boldsymbol{M} + i\omega \boldsymbol{C}(\omega) + \boldsymbol{K} \right) \hat{\tilde{\boldsymbol{d}}}(\omega) = -\boldsymbol{M} \hat{\ddot{\boldsymbol{u}}}_b(\omega) \tag{6.55}$$

where:

$$\boldsymbol{M} = \int_{\Omega_0} \rho_0 \boldsymbol{N}^T \boldsymbol{N} \mathrm{d}\Omega_0 \tag{6.56}$$

$$\boldsymbol{K} = \int_{\Omega_0} \boldsymbol{B}^T \mathbb{C}(\eta(\xi_0)) \boldsymbol{B} \mathrm{d}\Omega_0 + \boldsymbol{K}_{\text{contact}} \tag{6.57}$$

$$\boldsymbol{C}(\omega) = \int_{\Omega_0} \boldsymbol{B}^T \mathbb{D}(\omega) \boldsymbol{B} \mathrm{d}\Omega_0 \tag{6.58}$$

$$\mathbb{D}(\omega) = \sum_{k=1}^{m} \frac{i\omega\tau_k g_k}{1 + i\omega\tau_k} \mathbb{C}_0 \tag{6.59}$$

$\mathbb{D}$, $\boldsymbol{M}$, $\boldsymbol{K}$ and $\mathbb{C}$ are the damping modulus matrix, mass matrix, the stiffness matrix and the damping stiffness.

Contact Linearization in Frequency Domain

For active contact regions identified during static analysis, the contact stiffness contribution remains constant in the linearized analysis:

$$\boldsymbol{K}_{\text{contact}} = \int_{\Gamma_C} \gamma_c \boldsymbol{N}^T \boldsymbol{n}_c \otimes \boldsymbol{n}_c \boldsymbol{N} d\Gamma_C \quad \text{(for } g_0 < 0) \tag{6.60}$$

This represents a constant spring-like constraint in the frequency domain for regions in contact during static equilibrium.

PSD Response Calculation

From Eq.(6.55), we can easily compute the following key expressions:

- **Frequency Response Function (FRF)**

  The FRF matrix $\boldsymbol{H}(\omega)$ maps input excitation to output response:

  $$\boldsymbol{H}(\omega) = \left(-\omega^2 \boldsymbol{M} + i\omega \boldsymbol{C}(\omega) + \boldsymbol{K}\right)^{-1} \tag{6.61}$$

  Thus, the displacement response to the excitation is then:

  $$\hat{\tilde{\boldsymbol{d}}}(\omega) = -\boldsymbol{H}(\omega) \boldsymbol{M} \Gamma \hat{\ddot{\boldsymbol{u}}}_b(\omega) \tag{6.62}$$

- **Force Power Spectral Density (PSD)**

  Force PSD represents the distribution of force's energy across different frequencies and given by the expression

  $$\mathrm{S}_{ff}(\omega) = \boldsymbol{M} \mathrm{S}_{bb}(\omega) \boldsymbol{M}^T \tag{6.63}$$

- **Response Power Spectral Density (PSD)**

Response PSD stands for the distribution of force's energy across different frequencies when subjected to a random excitation.

$$\mathrm{S}_{uu}(\omega) = \boldsymbol{H}(\omega)\mathrm{S}_{ff}(\omega)\boldsymbol{H}^*(\omega); \quad \mathbf{H}^*(\omega) = \overline{\mathbf{H}(\omega)}^T = \mathbf{H}^H(\omega) \tag{6.64}$$

where:

- The Hermitian adjoint $\mathbf{H}^*(\omega) \in \mathcal{C}^{n \times n}$
- $\overline{\mathbf{H}(\omega)}$ denotes the complex conjugate (all elements $h_{ij} \to \bar{h}_{ij}$)
- ^{T} denotes the matrix transpose

- **Root Root Mean Square(RMS) displacement:**

  The RMS displacement is the effective displacement under the random vibrations. It is the square root of the area under the response power spectral density function.

$$\mathrm{RMS}_u = \sqrt{\int_{-\infty}^{\infty} \mathrm{diag}(\mathrm{S}_{uu}(\omega))\mathrm{d}\omega} \tag{6.65}$$

Computational Algorithm

The flowchart below breaks down the numerical implementation of the procedure described above.

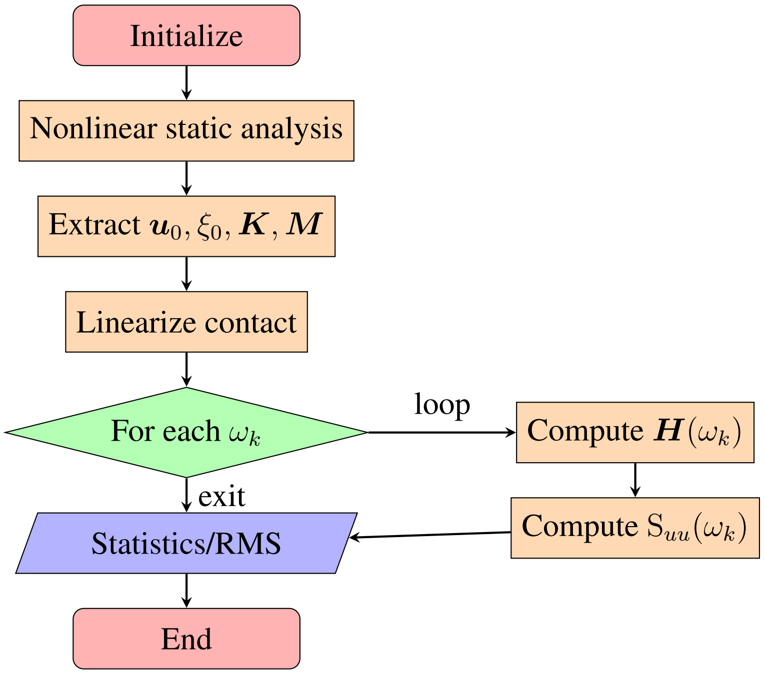

Figure 6.44: PSD-based random vibration analysis workflow

Further insights into this formulation for random vibration analysis can be found in the works of Newland [192], Liu and Zhao [193], and Pashaei et al. [194].

6.3.4 Steady State dynamic

Tire steady-state dynamic analysis examines the vibration response of a tire under periodic applied loads. The procedure is akin to random vibration analysis and utilizes natural vibration modes to determine the tire's vibration response.

Implementation procedure

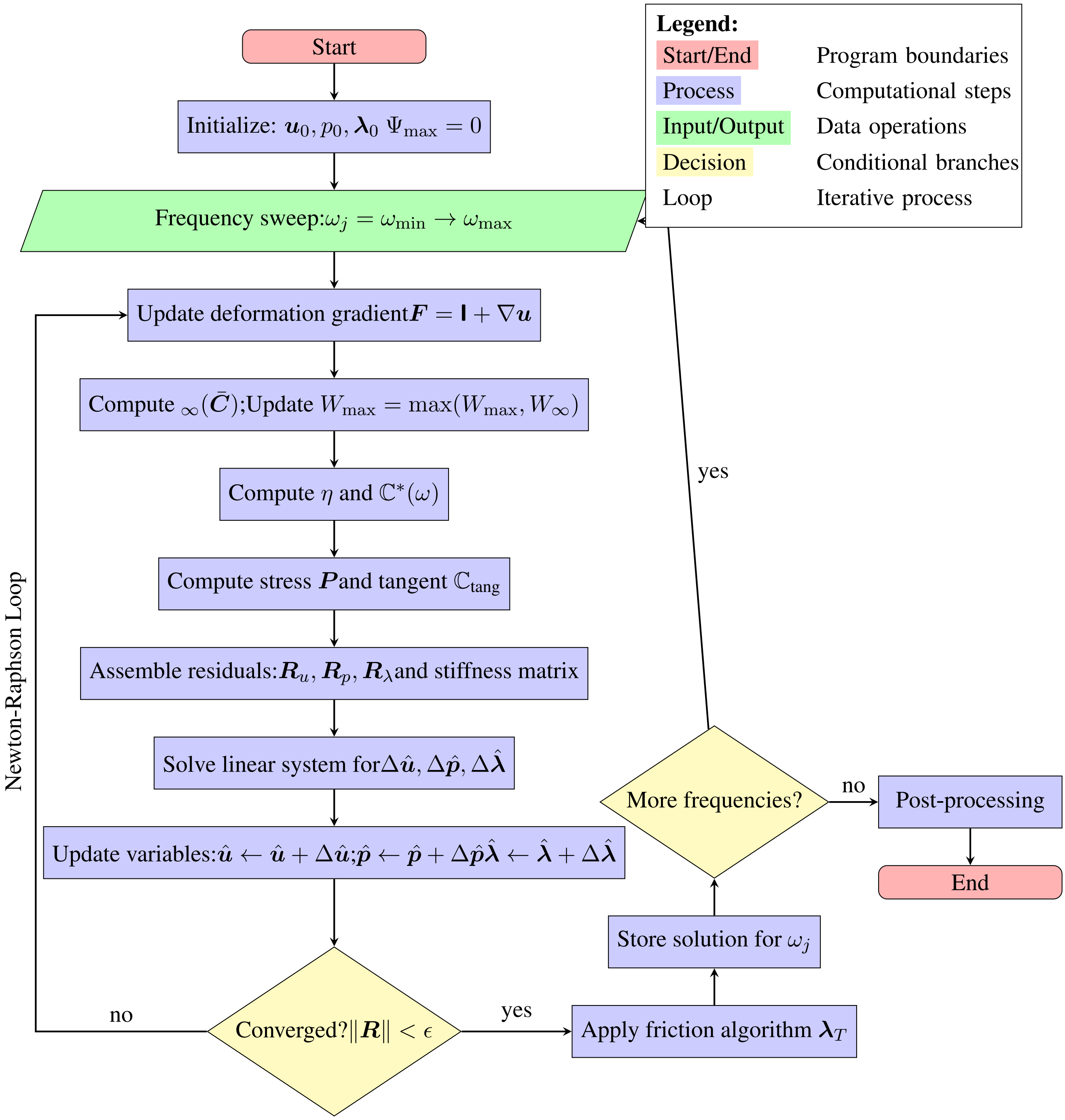

Figure 6.45: Solution algorithm for steady-state dynamic analysis of tire in contact with road

Algorithm Description

1. **Initialization:** Set initial values for displacement ($\boldsymbol{u}_0$), pressure (p_0), contact multipliers ($\boldsymbol{\lambda}_0$), and maximum strain energy ($\Psi_{\text{max}} = 0$)
2. **Frequency sweep:** Loop through frequency range $\omega_j = \omega_{\text{min}}$ to ω_{max}
3. **Newton-Raphson loop:**
   (a) Compute deformation gradient $\boldsymbol{F}$ and isochoric right Cauchy-Green tensor $\bar{\boldsymbol{C}}$
   (b) Calculate equilibrium strain energy Ψ_∞ and update Ψ_{max}
   (c) Evaluate Ogden-Roxburgh damage function η
   (d) Compute complex modulus $\mathbb{C}^*(\omega)$ from Prony series
   (e) Calculate stress $\boldsymbol{P}$ and tangent modulus $\mathbb{C}_{\text{tang}}$
   (f) Assemble residual vectors and tangent matrix
   (g) Solve linear system for variable increments
   (h) Update displacement, pressure, and multiplier fields
   (i) Check convergence; repeat if needed
4. **Contact friction:** Apply return mapping algorithm for tangential contact
5. **Solution storage:** Save solution for current frequency
6. **Post-processing:** compute displacement, stress, contact pressure distributions, etc.

Results and discussion

The application of this scheme was conducted considering a loaded tire at $100\% LI$ and inflated with a pressure of 250 MPa, then two periodic impulse loads with respective amplitudes 500N and 1000N were considered. These loads are assumed to vibrate at a frequency $f \in [0, 275]$ Hz such that:

$$F_z = F_{z,max} \cos(\omega t) \tag{6.66}$$

Where $F_{z,max} \in \{500, 1000\}$ [N] and $\omega = 2\pi f$. The circumference equally spaced mesh (see Figure 6.26) with 450 sectors was used. The simulation was quite straightforward. The footprint analysis took about 28 minutes, and the steady state dynamic analysis with both periodic impulses took about 18 minutes. The vertical deflection of the center of the tire was extracted and depicted in Figure 6.56.

(a) under $F_z = 500\cos(\omega t)$ [N]

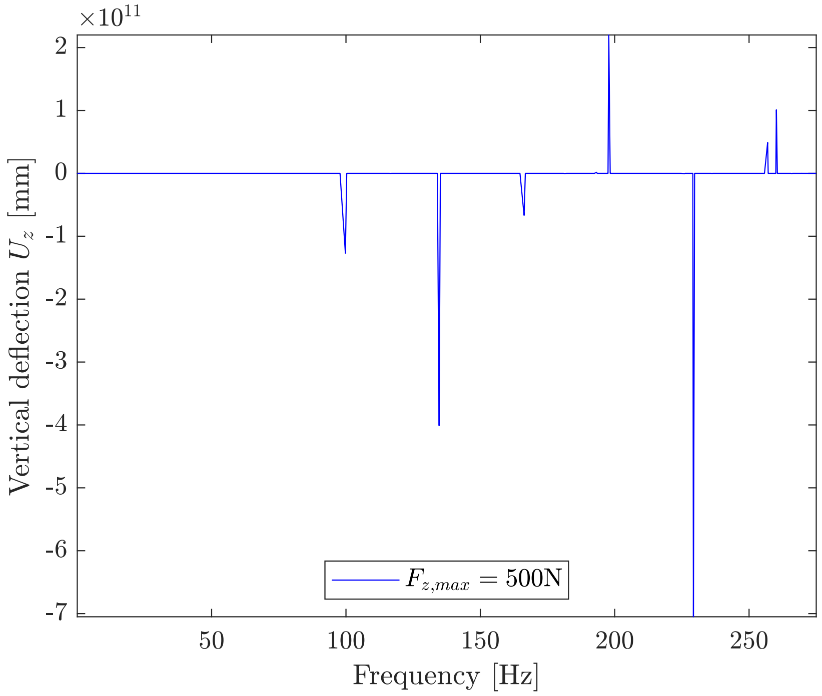

(b) under $F_z = 1000\cos(\omega t)$ [N]

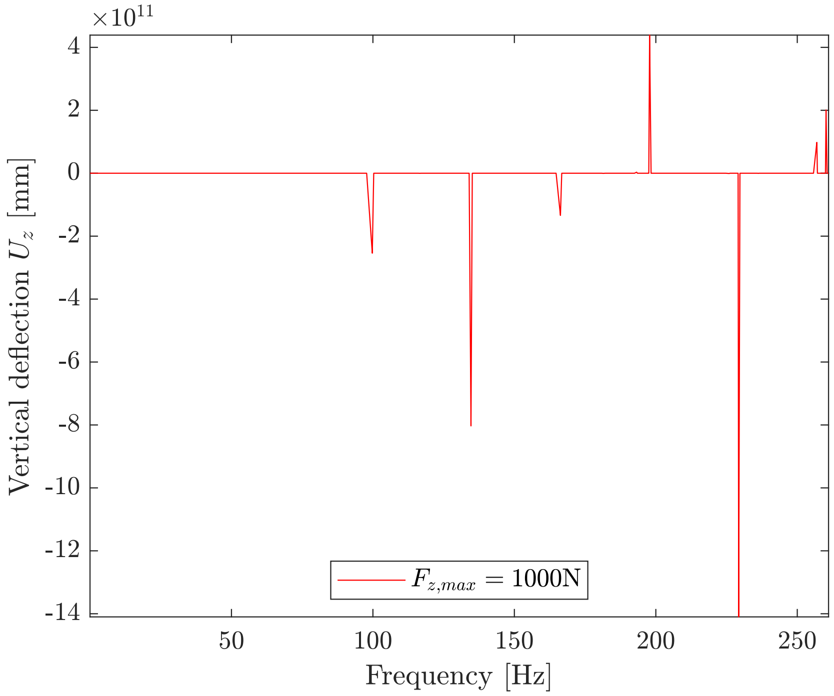

Figure 6.46: Vertical displacement at tire center as per the excitation frequency.

In the curves above, the peaks indicate the points where the excitation frequencies align with the natural frequencies of the tire, resulting in resonance. Now, we want to determine the vertical displacements of the tire at other frequencies. To achieve this, we removed the resonance points and plotted the remaining data in Figure 6.47.

(a) under $F_z = 500\cos(\omega t)$ [N]

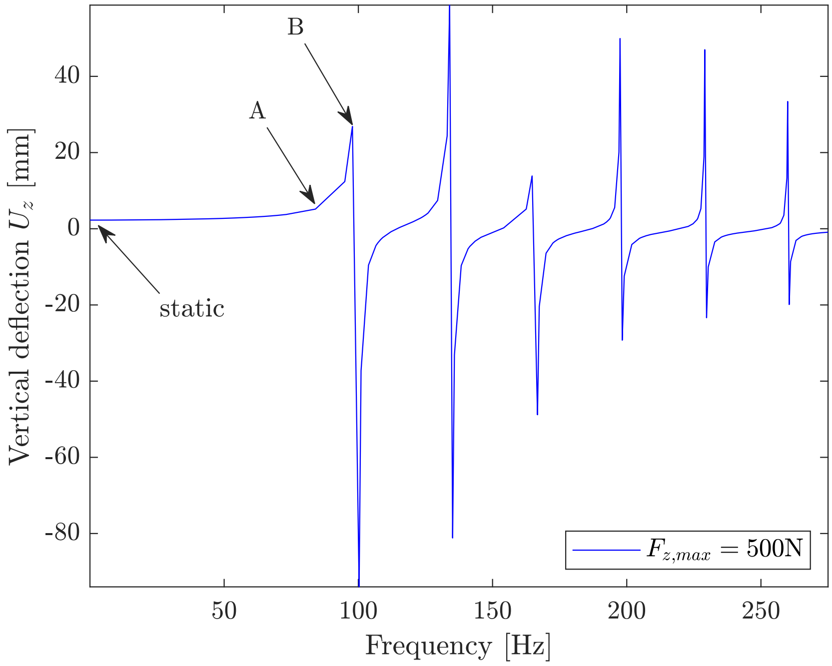

(b) under $F_z = 1000\cos(\omega t)$ [N]

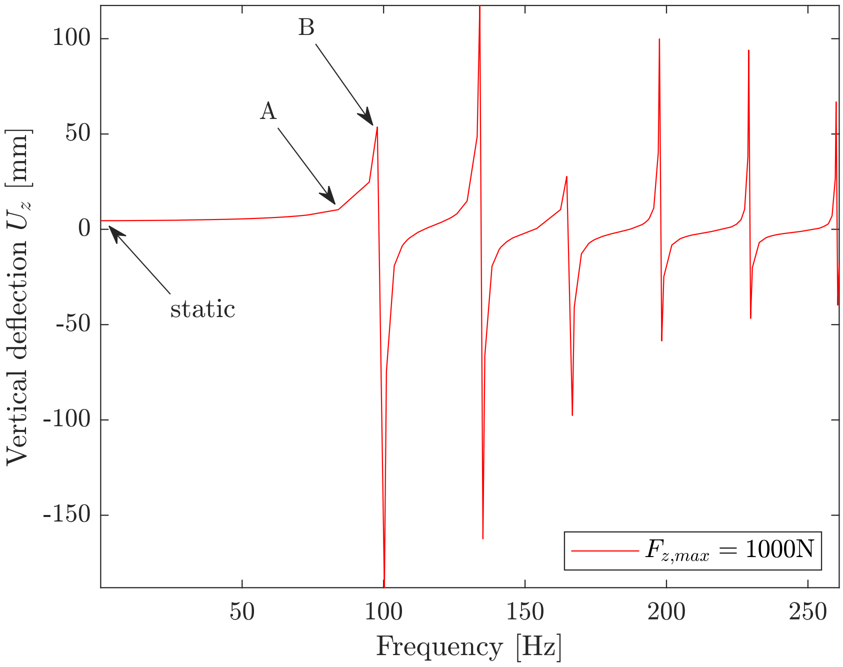

Figure 6.47: Vertical displacement at tire center as per the excitation frequency. **Without the natural frequencies**.

Let us now analyze the above figures. When $f = 0$, i.e. $\omega = 0$, the load is *static*, ($F_z = 500$ N), and the resulting displacement is 2.4 mm. However, it can be seen that when $f > 0$, the applied impulse generates a vertical displacement that is higher than that of a static load. Specifically, at point A, an applied impulse force with amplitude 500 N and a frequency of $f = 84$ Hz induces a displacement of 5.3 mm. Similarly, at point B, the same load amplitude oscillating at a frequency of $f = 97.80$ Hz generates a displacement of 26.9 mm. The same observation can be made when the amplitude of the load impulse is 1000 N (see Figure 6.47(b)).

Furthermore, we observe that when comparing the results for both impulses, doubling the amplitude of the load impulse results in a doubling of the resulting displacement. This is clearly shown in Figure 6.48, where both results are plotted together.

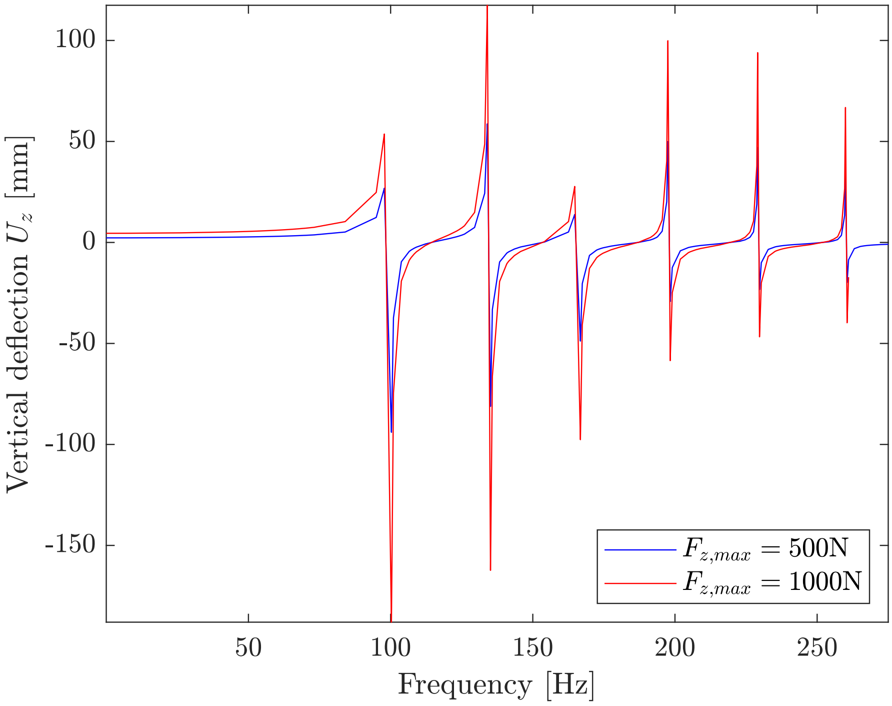

Figure 6.48: Visualization of the effect of amplitude and the frequencies of the impulse force on the vertical displacement of the tire.

6.3.5 Transient rolling state

Problem formulation

In this section, we briefly present a four-field mixed finite element formulation for the transient rolling contact analysis of a tire composed of a visco-hyperelastic rubber material with Mullins effect and frictional road contact. We assume a decomposition of the contact stress in its normal part $\boldsymbol{\lambda}_n(\mathbf{X}, t)$ and tangential part $\boldsymbol{\lambda}_t(\mathbf{X}, t)$. The independent unknowns of the BVP are the following:

- Displacement field: $\mathbf{u}(\mathbf{X}, t) \in \mathbb{R}^3$
- Hydrostatic pressure: $p(\mathbf{X}, t) \in \mathbb{R}$
- Normal contact multiplier: $\lambda_n(\mathbf{X}, t) \in \mathbb{R}$
- Tangential (frictional) contact multiplier: $\boldsymbol{\lambda}_t(\mathbf{X}, t) \in \mathbb{R}^2$

In the following, we use the strong form given in Section 4.7.1.

Weak Formulation

The boundary value problem can be formulated as the task of finding the quadruple $(\boldsymbol{u}, p, \boldsymbol{\lambda}_n, \boldsymbol{\lambda}_t) \in \mathcal{V} \times \mathcal{Q} \times \mathcal{M}_n \times \mathcal{M}_t$ such that the following weak form holds for all admissible variations $(\delta\mathbf{u}, \delta p, \delta\lambda_n, \delta\boldsymbol{\lambda}_t)$:

Momentum Balance (Virtual Work)

$$\underbrace{\int_{\Omega_0} \rho_0 \ddot{\mathbf{u}} \cdot \delta\mathbf{u}\, dV}_{\text{Inertial term}} + \underbrace{\int_{\Omega_0} [\mathbf{P}_{dev} - \int_{\Omega_0} pJ\mathbf{F}^{-T}] : \nabla\delta\mathbf{u}\, dV}_{\text{Internal term}} - \underbrace{\int_{\Gamma_C} \lambda_n(\delta\mathbf{u}\cdot\mathbf{n}_0)\, dA}_{\text{normal contact term}} - \underbrace{\int_{\Gamma_C} \boldsymbol{\lambda}_t \cdot \mathbf{P}_t(\delta\mathbf{u})\, dA}_{\text{tangential contact term}} \tag{6.67}$$

$$= \underbrace{\int_{\Omega_0} \rho_0 \mathbf{b} \cdot \delta\mathbf{u}\, dV}_{\text{body term}} + \underbrace{\int_{\partial\Omega_N} \mathbf{t} \cdot \delta\mathbf{u}\, dA}_{\text{traction term}} \tag{6.68}$$

Incompressibility Constraint

$$\int_{\Omega_0} \delta p (J-1)\, dV = 0 \tag{6.69}$$

Normal Contact Constraint

$$\int_{\Gamma_C} \delta\lambda_n\, g_n(\mathbf{u})\, dA = 0 \tag{6.70}$$

Frictional Contact Constraint

$$\int_{\Gamma_C} \delta\boldsymbol{\lambda}_t \cdot \mathbf{g}_t(\mathbf{u})\, dA = 0 \tag{6.71}$$

with friction constraint:

$$\|\boldsymbol{\lambda}_t\| \leq \mu\lambda_n, \quad \text{(equality in sliding)} \tag{6.72}$$

Discretized Matrix Form

After replacing all discretized variables and their admissible variations into the weak form, we end up with the global system of equations of the form:

$$\underbrace{\begin{bmatrix} \mathbf{M} & 0 & 0 & 0 \\ 0 & 0 & 0 & 0 \\ 0 & 0 & 0 & 0 \\ 0 & 0 & 0 & 0 \end{bmatrix}}_{\text{Inertial terms}} \begin{bmatrix} \ddot{\mathbf{u}} \\ \ddot{\mathbf{p}} \\ \ddot{\boldsymbol{\lambda}}_n \\ \ddot{\boldsymbol{\lambda}}_t \end{bmatrix} + \underbrace{\begin{bmatrix} \mathbf{K}_{uu} & \mathbf{K}_{up} & \mathbf{K}_{u\lambda_n} & \mathbf{K}_{u\lambda_t} \\ \mathbf{K}_{pu} & 0 & 0 & 0 \\ \mathbf{K}_{\lambda_n u} & 0 & 0 & 0 \\ \mathbf{K}_{\lambda_t u} & 0 & 0 & 0 \end{bmatrix}}_{\text{Tangent stiffness and coupling}} \begin{bmatrix} \mathbf{u} \\ \mathbf{p} \\ \boldsymbol{\lambda}_n \\ \boldsymbol{\lambda}_t \end{bmatrix} = \begin{bmatrix} \mathbf{F}^{\text{ext}} \\ 0 \\ 0 \\ 0 \end{bmatrix} \tag{6.73}$$

Matrix Definitions

$$\mathbf{M} = \int_{\Omega_0} \rho_0 \mathbf{N}_u^T \mathbf{N}_u \, dV \tag{6.74}$$

$$\mathbf{K}_{uu} = \int_{\Omega_0} \mathbf{B}^T \mathbb{C}_{\text{eff}} \mathbf{B} \, dV \tag{6.75}$$

$$\mathbf{K}_{up} = -\int_{\Omega_0} \mathbf{G}_p^T \mathbf{D}_p \, dV \tag{6.76}$$

$$\mathbf{K}_{u\lambda_n} = -\int_{\Gamma_C} \mathbf{N}_{\lambda_n}^T (\mathbf{N}_u \cdot \mathbf{n}_0) \, dA \tag{6.77}$$

$$\mathbf{K}_{u\lambda_t} = -\int_{\Gamma_C} \mathbf{N}_{\lambda_t}^T \mathbf{P}_t(\mathbf{N}_u) \, dA \tag{6.78}$$

with $\mathbb{C}_{\text{eff}} = \eta \mathbb{C}_{\text{dev}}^{\text{eq}} + \mathbb{C}_{\text{iso}}^{\text{eq}} + \sum_k \mathbb{C}^{(k)}$, including softening and visco-hyperelasticity via internal variables.

Friction Law (Regularized)

It is not computationally always feasible to strictly enforce the pure Coulomb friction law. Therefore, a smoothening is introduced to address discontinuity and contact instabilities. For instance, the following regularized Coulomb friction model may be used:

$$\boldsymbol{\lambda}_t = -\mu \lambda_n \frac{\mathbf{g}_t}{\|\mathbf{g}_t\| + \epsilon} + k_t \mathbf{g}_t \tag{6.79}$$

with regularization $\epsilon > 0$, and penalty stiffness k_t. Alternatively, KKT-based active set methods or Augmented Lagrangian schemes[195], [196] can be employed.

Time Integration

The resolution of Eq.(6.78) demands also to choose a time integration scheme. In ABAQUS explicit solver, time integration is implemented via central-difference integration scheme. This scheme is given by the formula:

$$\ddot{\mathbf{u}}^n = \mathbf{M}^{-1}\left[\mathbf{f}^n_{\text{ext}} - \mathbf{K}_{\text{eff}}\mathbf{u}^n - \mathbf{G}_n^\top \lambda_n^n - \mathbf{G}_t^\top \boldsymbol{\lambda}_t^n\right] \tag{6.80}$$

$$\mathbf{u}^{n+1} = 2\mathbf{u}^n - \mathbf{u}^{n-1} + \Delta t^2 \ddot{\mathbf{u}}^n \tag{6.81}$$

It is worth to bear in mind that this scheme is conditionally stable. Thus every time increment Δt must satisfy the stability condition below:

$$\Delta t \leq \frac{L_{min}}{c_L} \tag{6.82}$$

where:

- L_{min} is the smallest characteristic length of element mesh.
- c_L is the characteristic speed in the material.

Choosing a time step that meets the aforementioned condition does not completely eliminate stability issues. In fact, for complex problems involving contact, it is still likely to encounter stability challenges. To address this, a predictor-corrector approach is implemented to enhance the stability of the scheme. For further details, the reader is referred to the work of [197], [198].

Post steady-state transient rolling on an uneven surface

This analysis comprises four steps:

1. Inflation analysis in ABAQUS Standard.
2. Footprint analysis in ABAQUS Standard.
3. Steady-state rolling via $visco$ step in ABAQUS Standard.
4. Transient rolling analysis with ABAQUS explicit.

In order to avoid deformation instability during transient analysis, we utilized an enhanced strain formulation. The road shape was represented as an analytical rigid surface with a curb height of $30\ \mathrm{mm}$. The horizontal distance from the tire axle to the curb is equal to $250\ \mathrm{mm}$.

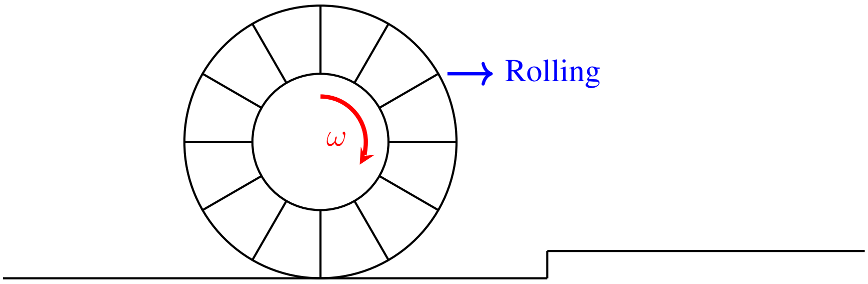

Figure 6.49: Schematic view on Tire transient rolling setup

Pure Coulomb friction model was considered with $\mu = 0.8$. A vertical preload of $100\% LI$ was chosen as load level for the analysis. In terms of velocity, three longitudinal velocity v_x were chosen : $10\ \mathrm{Km.h^{-1}}$, $40\ \mathrm{Km.h^{-1}}$ and $80\ \mathrm{Km.h^{-1}}$. The corresponding free rolling speeds ω were computed during the steady state rolling analysis. For each analysis, v_x and ω were applied in a ramp-like manner, as shown in Figure 6.50.

Figure 6.50: Definition of (a) the longitudinal velocity v_x and (b) the angular velocity ω.

Throughout this analysis, the vertical load F_z remained constant. The tire was permitted to rotate freely around its axle (the y axis) and move vertically about the z axis, while all other degrees of freedom were fixed. Also, the road was fixed.

The critical time step of $\Delta t = 1.867 * 10^{-7}\ s$ computed by the software was maintained. Thus, no increase in time step through mass scaling was utilized. The simulation was launched in parallel with 7 CPUs and 1 GPU. The computational time of the transient analysis was about 5 hours.

Results and discussions

During the simulation, we recorded history outputs of displacement, velocity and acceleration components at the tire axle, along with field outputs such as deformation and stress at various points. Figure 6.53 shows the evolution of the vertical deformation ε_{zz} over time.

(a) at $t = 0$ ms (b) at $t = 5.0$ ms

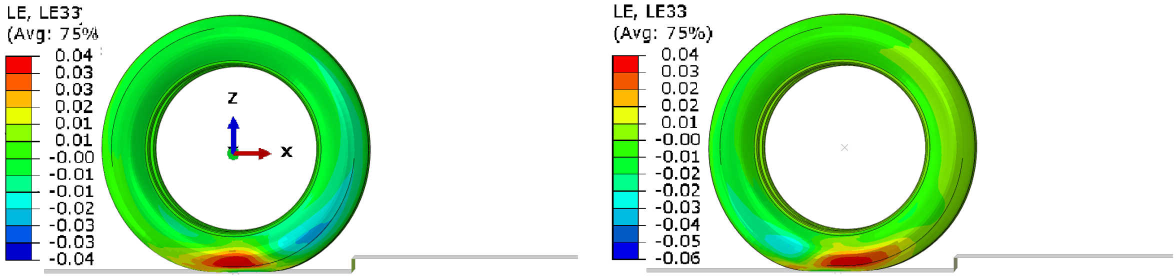

(c) at $t = 50.0$ ms (d) at $t = 60.0$ ms

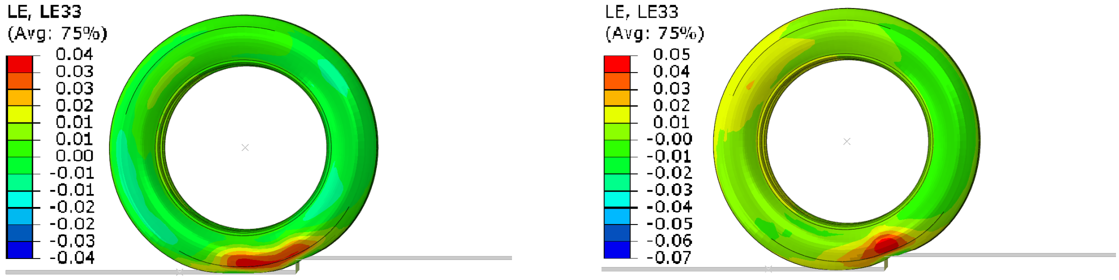

(e) at $t = 72.5$ ms (f) at $t = 117.5$ ms

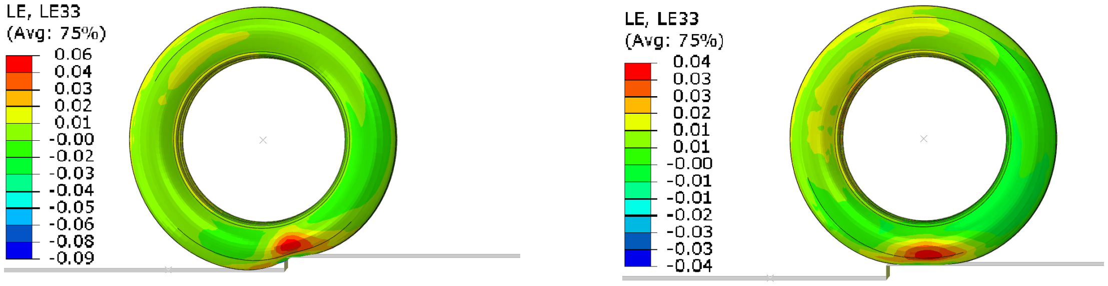

Figure 6.51: Evolution of the strain component ε_{zz} over the time at a rolling speed of $v_x = 10\ \mathrm{Km.h^{-1}}$.

Notably, at time $t = 0$, the maximum vertical deformation is $\varepsilon_{zz} = 0.04$. As the speed increases to $v_x = 10\ \mathrm{Km.h^{-1}}$, this value rises to 0.07. After reaching a steady speed, the deformation returns to its initial value. However, at full contact with the curb, the maximum deformation dramatically increases to 0.09. Afterwards, beyond the curb, it drops back to the initial value of 0.04. Additionally, we observe that, in contrast to the initial position (steady state free rolling), the peak of the maximum deformation slightly shifts toward the front bottom of the tire.

The lateral displacement (u_y) was also analyzed. In Figure 6.52, we note that the maximum lateral displacement is located at the bottom and moves similarly as above with the vertical strain.

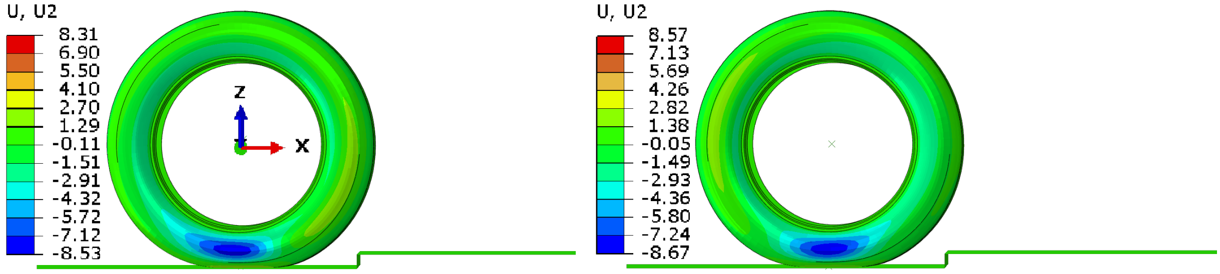
(a) at $t = 0$ ms (b) at $t = 2.5$ ms

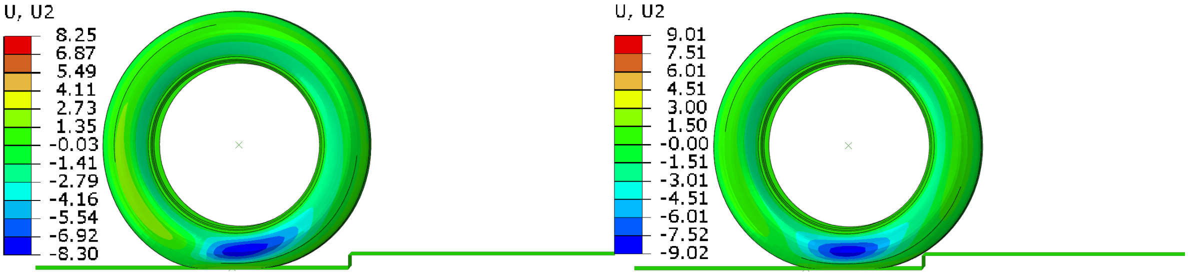
(c) at $t = 5.0$ ms (d) at $t = 32.5$ ms

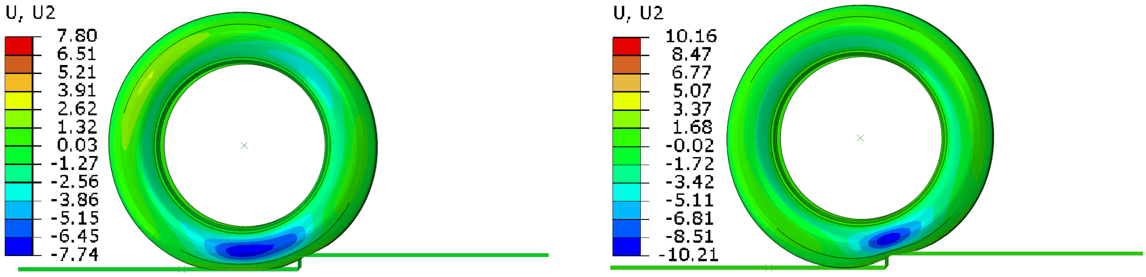
(e) at $t = 47.5$ ms (f) at $t = 70.0$ ms

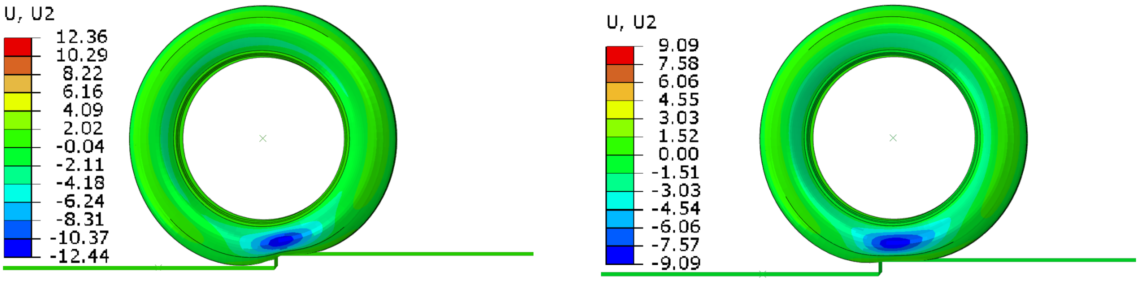
(g) at $t = 80.0$ ms (h) at $t = 100.0$ ms

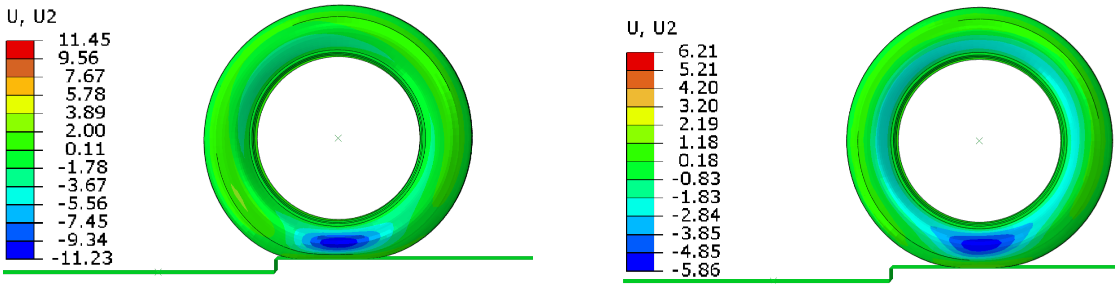
(i) at $t = 137.5$ ms (j) at $t = 157.5$ ms

Figure 6.52: Evolution of the transversal displacement u_y over the time at a rolling speed of $v_x = 10\ \mathrm{Km.h^{-1}}$.

One should note that the positive values of u_y ($u_y > 0$) are for nodes located on the opposite face of the tire.

We also scrutinized the evolution of the forces and stresses in rebar surface layers (steel cords, textile cap cords, and carcass) and noticed that steel cords are the most solicited reinforcements during the rolling. Mainly when the contact with the curb occurs, steel cords sustain the highest efforts while the other reinforcements are unaffected. Even beads are not affected.

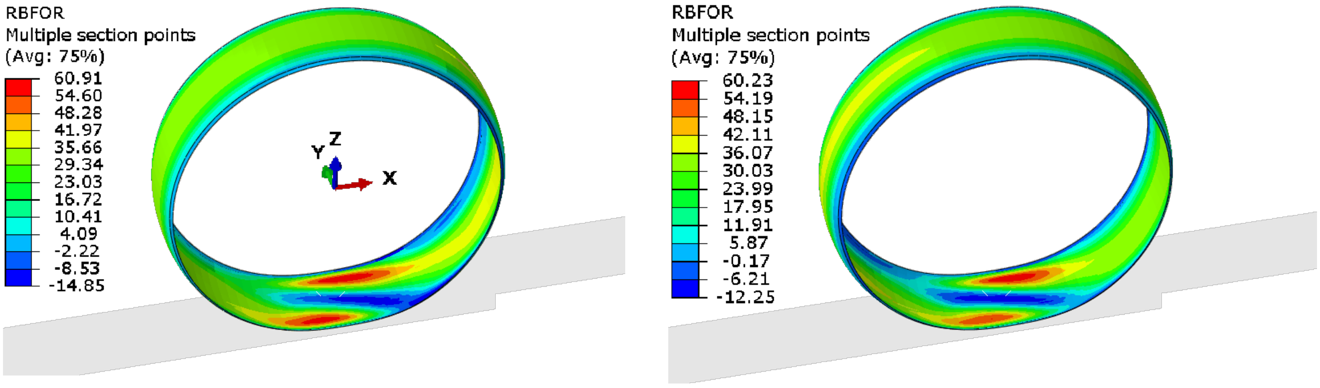

(a) at $t = 0$ ms

(b) at $t = 2.5$ ms

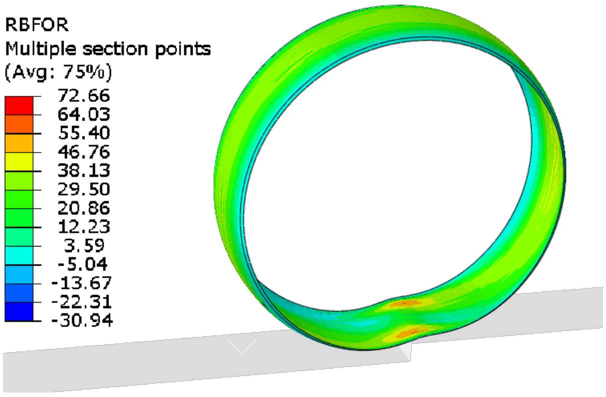

(c) at $t = 80.5$ ms

Figure 6.53: Evolution of the normal force (in Newton) in steel cords surface layer over the time at a rolling speed of $v_x = 10$ Km.h^{-1}.

In this figure, we see that due to the contact, this force increases by a factor of approximately 1.5 in comparison with its initial value.

Influence of the velocity on tire transient rolling

Now, we focus our attention on how the increase of rolling longitudinal velocity affects tire transient rolling response. For this sake, we also consider a speed of $v_x = 40$ Km.h^{-1} and $v_x = 80$ Km.h^{-1}. Figure 6.56 depicts the response of the tire at full acceleration and a contact with the curb.

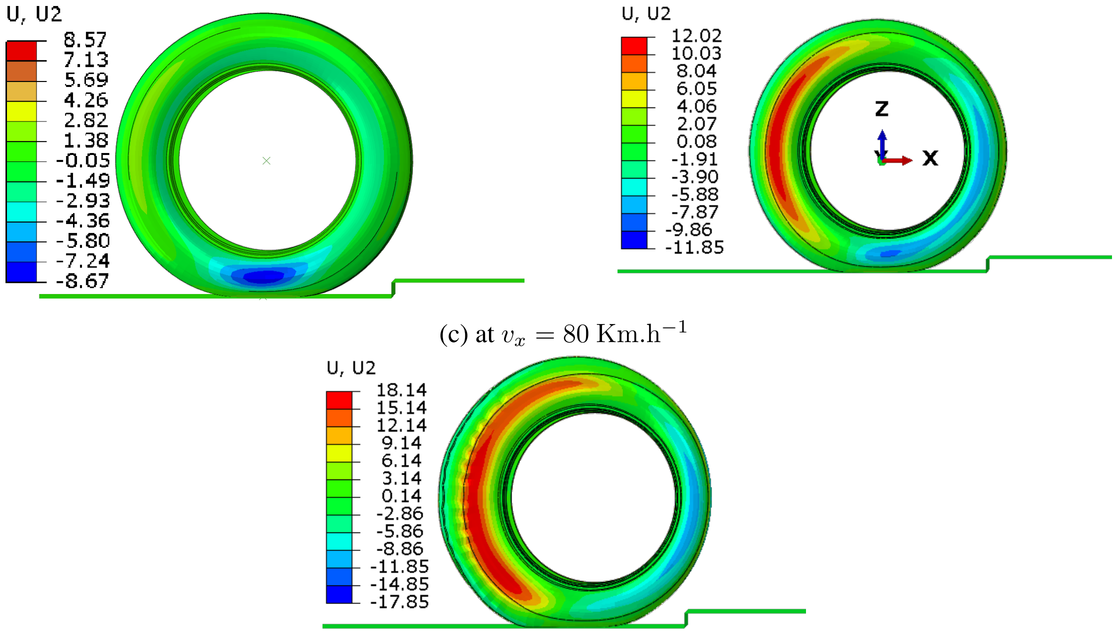

(a) at $v_x = 10\ \mathrm{Km.h^{-1}}$

(b) at $v_x = 40\ \mathrm{Km.h^{-1}}$

(c) at $v_x = 80\ \mathrm{Km.h^{-1}}$

Figure 6.54: Visualization of the influence of the rolling velocity on the lateral deformation of the tire at $t = 2.5$ ms.

At first glance at Figure 6.56, it is important to note that the sudden acceleration to the targeted longitudinal velocity leads to an increase in lateral deformation of the tire, even though the radial force remains constant. Additionally, we observe that at velocities of 40 and $80\ \mathrm{Km.h^{-1}}$, there are two zones on each side of the tire that deform in opposite directions. This contrasts with the deformation seen at $10\ \mathrm{Km.h^{-1}}$, which is unidirectional on each side.

Furthermore, we notice that at velocities of 40 and $80\ \mathrm{Km.h^{-1}}$, the sidewall surface exhibits some undulations or waves in the same two zones of concentrated lateral deformation. The amplitude of these waves increases with the velocity.

(a) at $v_x = 10\ \mathrm{Km.h^{-1}}$ (b) at $v_x = 40\ \mathrm{Km.h^{-1}}$

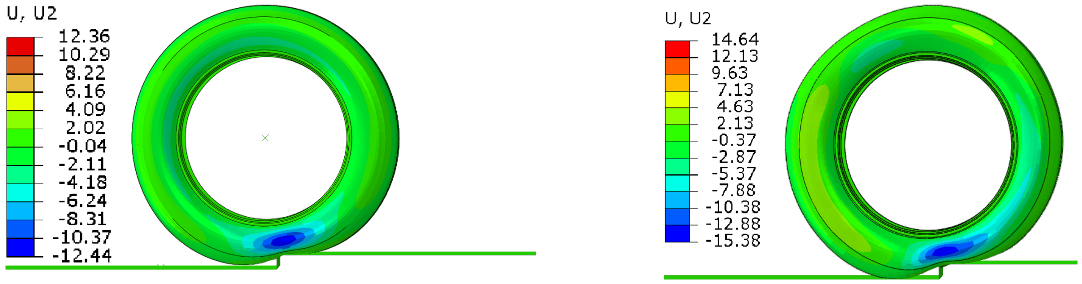

(c) at $v_x = 80\ \mathrm{Km.h^{-1}}$

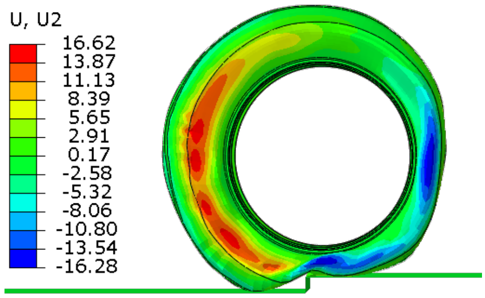

Figure 6.55: Visualization of the influence of the rolling velocity on the lateral deformation of the tire at the contact with the curb.

As expected, the lateral sinkage of the tire at contact with the curb increases with tire rolling velocity. However, at $80\ \mathrm{Km.h^{-1}}$ velocity, the tire loses its structural integrity when it comes into contact with the curb.

Now, let us dive deeper into why this happens and why there are undulations on the sidewall surface at higher velocities. For this purpose, the data of the wheel axle's acceleration, velocity, and displacement were extracted and plotted as a function of time.

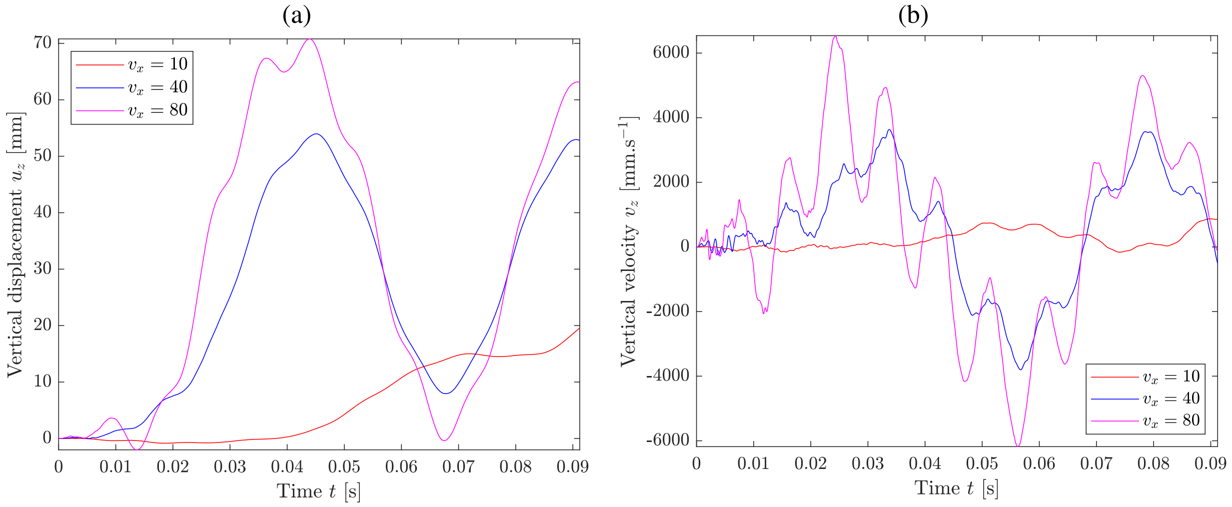

Figure 6.56: Visualization of the evolution of the vertical velocity, vertical displacement and distance traveled over the time. v_x given in $\mathrm{Km.h^{-1}}$.

Also, the distance traveled u_x was retrieved and plotted in Figure 6.57. A linear relationship between u_x and t was established for all the studied velocities.

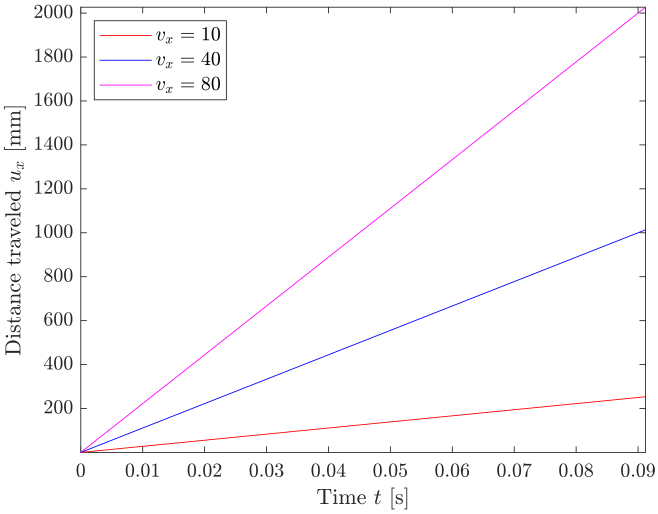

Figure 6.57: Visualization of the evolution of distance covered over the time. v_x given in $\mathrm{Km.h}^{-1}$.

Then, we focus our attention on the range $t \in [0, 5]\mathrm{ms}$, where the full acceleration takes place. In Figure 6.58, the variation of the vertical displacement u_z at the tire center is shown.

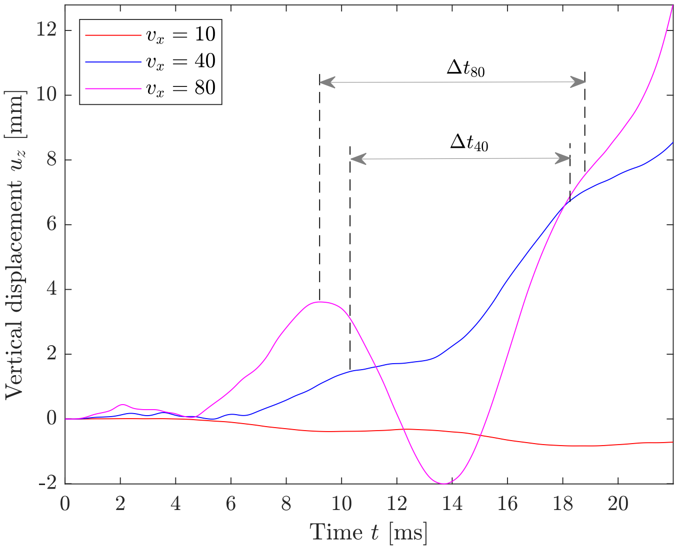

Figure 6.58: Identification of generated vibration.

We observe that the sudden jump in velocity up to the targeted value induces vibrations within the tire. It is noted that the amplitude of the resulting signal increases with the velocity, while the vibration frequency decreases as the velocity increases. Indeed, with the period $\Delta t_{40} = 9\text{x}10^{-3}\mathrm{s}$ and $\Delta t_{80} = 12\text{x}10^{-3}\mathrm{s}$ calculated as illustrated in Figure 6.58, we can compute the corresponding frequencies.

$$\boldsymbol{f}_{v_{40}} = \frac{1}{\Delta t_{40}} = 109.89 \text{ Hz} \tag{6.83}$$

$$\boldsymbol{f}_{v_{80}} = \frac{1}{\Delta t_{80}} = 82.64 \text{ Hz} \tag{6.84}$$

When we compare $\boldsymbol{f}_{v_{80}}$ with the frequencies obtained from the post-steady state rolling vibration analysis (see Section6.3.2), we discover that it closely matches the frequency $f_{\mathrm{R1}} = 71.37$ Hz of the radial mode $\mathrm{R1}$. Furthermore, we observe that the locations of the two vibration fields (in red and blue) are identical. Therefore, we can conclude that the instability observed is due to the onset of resonance.

7 Conclusions

Summary

This study focused on developing a finite element model to simulate car tires subjected to dynamic loads. After evaluating the limitations of existing literature, we constructed a finite element (FE) model based on the consistent natural dynamic responses of tire components and the dynamic nature of the loads encountered in real-world operations. We proposed a fine-tuned, multistage modeling methodology that outlines the necessary inputs, such as topology, mechanical properties, loads, and solution schemes, along with its implementation in ABAQUS.

The application of the model for simulating Matador $165/65\mathrm{R}13$ $77\mathrm{T}$ $\mathrm{MP}16$ tire demonstrated an accurate agreement with experimental data results under both static and dynamic loads. The validation was performed in a static adhesion setup, a dynamic adhesion setup (both with and without speed), and a free vibration setup using collected quantities such as displacement, contact area, natural frequencies, and mode shapes. The maximum absolute relative error between the experimental and numerical results is 5%, except for the axial natural frequencies, which is about 9%.

In industrial practices, the characterization of a tire's vibrational response often focuses solely on extracting natural frequencies, under the assumption that under dynamic loads, failures occur only when the structure resonates. However, it is necessary to go beyond this approach. As evidence, we examined the case of a dynamic periodic load and used steady-state dynamic analysis to determine the tire's response. After assessing the deflection of the tire's center under a periodic load and isolating displacements at resonance frequencies, we found that failure can also occur in resonance-free modes. Furthermore, our assessment of the displacement spectrum revealed that even under a small amplitude load impulse, the induced displacement was significantly larger than that under static loads.

In addition, in explicit transient analysis of the same tire rolling on an uneven surface has brought out a key finding:

- A sudden acceleration can make the tire enter into resonance. This result brings a very likely explanation to tire blowouts and structural disintegration in rolling conditions.
- In rolling conditions, dynamic deformation, stresses, and strains induced by the contact with road asperities are critical for tire stability and durability.

In terms of computational efficiency, the model is very efficient. While the computational time for footprint analysis was about 69 minutes on the preliminary model, with the final model, it is about 10 minutes on a similar mesh size. The analyses that require significant computation time (several hours on a medium-sized mesh) include transient analysis, steady state rolling analysis, and dynamic footprint analysis in the time domain. The major limitation of the model is the computational cost associated with these demanding analyses when fine meshes are used. As a solution, a vectorized algorithm has been proposed. This algorithm can be integrated to fully leverage the computer's vectorized architecture, thereby reducing computation time.

Based on the results obtained, we can conclude that this work contributes to the advancement of tire modeling design. Its application at an industrial scale can provide engineers with a deeper understanding of tire dynamics, ultimately leading to the development of safer and more efficient car tires.

Future work

Future work could concentrate on validating the steady-state rolling analysis and incorporating material failure criteria to simulate and experimentally validate tire failure mechanics.

Recommendations

Based on the findings from this work, the following recommendations are provided:

- Because of its computational robustness and accuracy, the creation of tire geometry and topology based on the axisymmetric approach is the most optimal choice. As demonstrated in the experimental and numerical results, it leads to accurate results.
- More accurate results in dynamic analysis can be obtained by incorporating thermal effects, specifically through thermo-mechanical analysis.
- To minimize mesh refinement in specific areas and significantly reduce mesh size, it is recommended to partition the cross-section into smaller regions before meshing.
- The addition of Mullins damage not only enhances the prediction of material response from the structural point of view but also improves the convergence of the numerical scheme.
- When it comes to modal extraction, it is more suitable to use the so-called rebar-continuum approach to account for reinforcement mechanical contribution.
- A more accurate result can be achieved by utilizing advanced phenomenological material models such as Ogden [124], Yeoh [119], or Gent [125].

Appendix A

Physical Interpretation in Viscoelastic Systems

For viscoelastic materials, the FRF matrix has significant imaginary components due to:

$$\mathbf{C}(\omega) = \int_{\Omega_0} \mathbf{B}^T \mathbb{D}_{\text{imag}}(\omega) \mathbf{B} d\Omega_0 \tag{7.1}$$

The Hermitian adjoint $\mathbf{H}^*$ ensures:

- Phase lead/lag relationships are preserved
- Dissipated energy is correctly accounted for
- Cross-correlations between different material points maintain physical consistency

Properties of the Response PSD

The Hermitian adjoint guarantees $\mathbf{S}_{uu}(\omega)$ has these mathematical properties:

$$\mathbf{S}_{uu}^*(\omega) = \mathbf{S}_{uu}(\omega) \quad \text{(Hermitian)} \tag{7.2}$$

$$\mathbf{v}^H \mathbf{S}_{uu}(\omega) \mathbf{v} \geq 0 \quad \forall \mathbf{v} \in \mathbb{C}^n \quad \text{(Positive semi-definite)} \tag{7.3}$$

$$\int_{-\infty}^{\infty} \text{tr}[\mathbf{S}_{uu}(\omega)] d\omega < \infty \quad \text{(Finite energy)} \tag{7.4}$$

These are essential for physical realizability of the stochastic response.

Appendix B: tire specifications

The technical specifications for the Matador tire, model $165/65R13\ 77T\ MP16$, are provided in Table 7.2 and Table 7.1.

Table 7.1: Basic specification [199] as per EU 2020/740 standard.

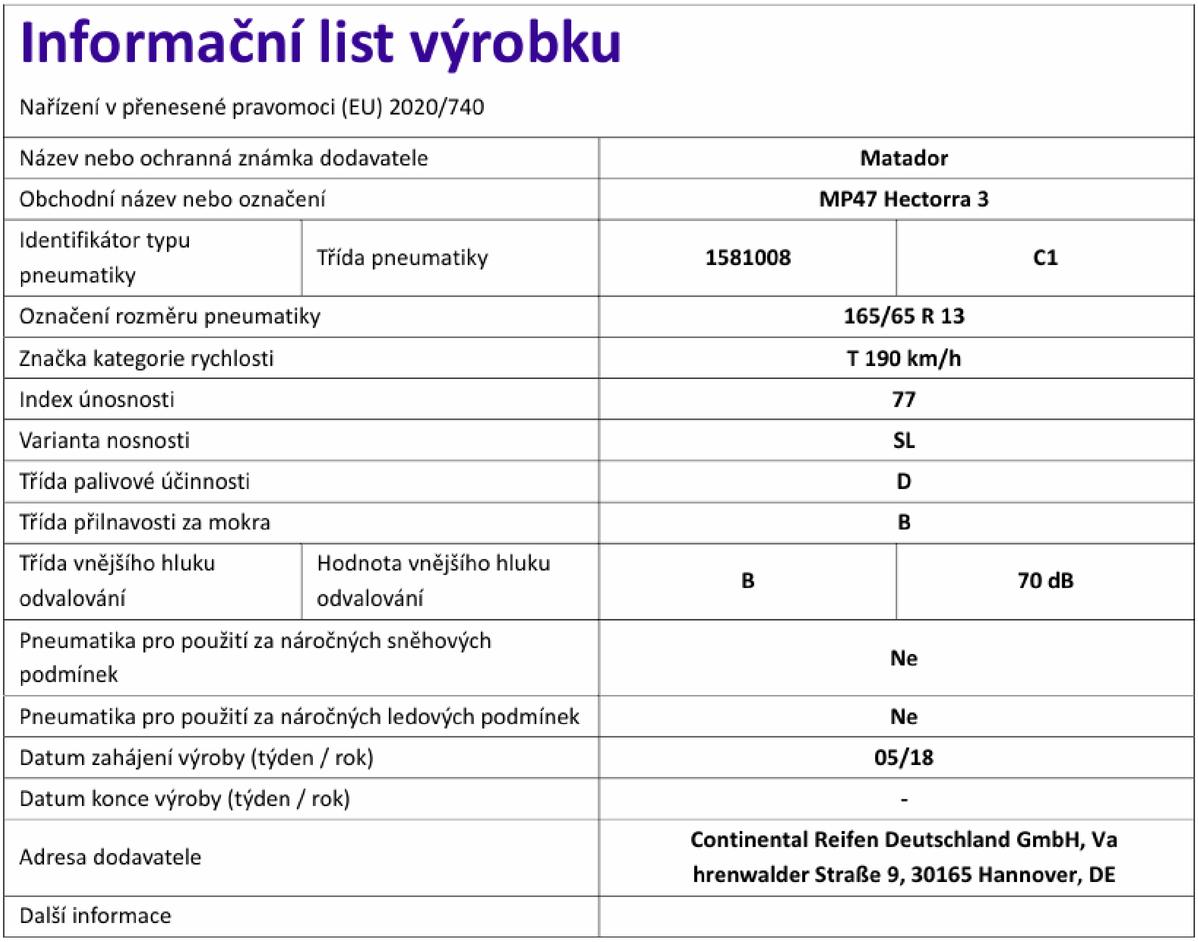

Informační list výrobku

Nařízení v přenesené pravomoci (EU) 2020/740

Název nebo ochranná známka dodavatele		**Matador**	
Obchodní název nebo označení		**MP47 Hectorra 3**	
Identifikátor typu pneumatiky	Třída pneumatiky	**1581008**	**C1**
Označení rozměru pneumatiky		**165/65 R 13**	
Značka kategorie rychlosti		**T 190 km/h**	
Index únosnosti		**77**	
Varianta nosnosti		**SL**	
Třída palivové účinnosti		**D**	
Třída přilnavosti za mokra		**B**	
Třída vnějšího hluku odvalování	Hodnota vnějšího hluku odvalování	**B**	**70 dB**
Pneumatika pro použití za náročných sněhových podmínek		**Ne**	
Pneumatika pro použití za náročných ledových podmínek		**Ne**	
Datum zahájení výroby (týden / rok)		**05/18**	
Datum konce výroby (týden / rok)		**-**	
Adresa dodavatele		**Continental Reifen Deutschland GmbH, Va hrenwalder Straße 9, 30165 Hannover, DE**	
Další informace			

Table 7.2: General specifications

Type of tires	Personal tires (PCR)
Brand	MATADOR
Tread pattern	MP16 STELLA 2
Parameters	165/65 R 13
Period	Summer
Segment	Economy class
Width	165
Profile	65
Construction	R
Diameter	13
Weight / Speed Index	77T

References

[1] E. Kriegler et al., “Will economic growth and fossil fuel scarcity help or hinder climate stabilization?: Overview of the RoSE multi-model study,” *Climatic Change*, vol. 136, no. 1, pp. 7–22, 2016, ISSN: 15731480. DOI: 10.1007/s10584-016-1668-3.

[2] E. U. Commission, “Study assessing consumer understanding of tyre labels,” Tech. Rep., 2023. DOI: 10.2833/210444.

[3] UK Department for Transport, “Transport and Environment Statistics 2021: Annual Report,” Tech. Rep. May, 2021, pp. 1–17. [Online]. Available: https://assets.publishing.service.gov.uk/government/uploads/system/uploads/attachment_data/file/984685/transport-and-environment-statistics-2021.pdf.

[4] OECD and ITF, *ITF Transport Outlook 2015* (ITF Transport Outlook). OECD, Jan. 2015, p. 172, ISBN: 9789282107645. DOI: 10.1787/9789282107782-en.

[5] J. Krmela, L. Beneš, and V. Krmelová, “Statical experiments of tire as complex long-fibre composite for obtaining material parameters and deformation characteristics,” *Materials Engineering*, vol. 19, p. 12, May 2012.

[6] U.S. Tire Manufacturers Association, “What’s in a tire,” Washington, DC.,USA, Tech. Rep., Accessed: 05.09.2023. [Online]. Available: https://www.ustires.org/whats-tire-0.

[7] I. Japan Automobile Tyre Manufacturers Association (JATMA), “Preventing global warming,” Tokyo,Japan, Tech. Rep., 2021. [Online]. Available: https://www.jatma.or.jp/english/environment_recycle/globalwarming.html#LCA.

[8] S. K. Clark and R. N. Dodge, “A handbook for the rolling resistance of pneumatic tires,” Tech. Rep., 1979.

[9] European Comission, “on the labelling of tyres with respect to fuel efficiency and other parameters, amending Regulation (EU) 2017/1369 and repealing Regulation (EC) No 1222/2009,” Luxembourg, Tech. Rep. 05/06/2020, 2020, pp. 1–62. [Online]. Available: http://eur-lex.europa.eu/legal-content/EN/TXT/PDF/?uri=OJ:L:2014:015:FULL&from=EN.

[10] M. SCA, “15th-annual-industrials-autos-week,” Michelin SCA, Tech. Rep., Dec. 2023.

[11] Continental GmbH, *Sustainability*, Accessed: 15.06.2024. [Online]. Available: https://www.continental-tires.com/about/sustainability/our-ambition/#:~:text=All%20our%20tires%20will%20be,sustainable%20re%2Duse%20of%20tires..

[12] P. Research, *TBR Tire Market*, Jul. 2023. [Online]. Available: https://www.precedencere
com/tbr-tire-market.

[13] Promodo, "Global tire market research 2022," May, 2022, Accessed: 04-05-2024, pp. 1–56. [Online]. Available: https://www.promodo.com/blog/tire-market-trends-to-succeed-in-2023.

[14] Statista. "Size of the automotive tire market worldwide 2022-2027. "[Online]. Available: https://www.statista.com/statistics/1228044/global-automotive-tire-market-size/.

[15] J. R. Meijer, M. A. J. Huijbregts, K. C. G. J. Schotten, and A. M. Schipper, "Global patterns of current and future road infrastructure," *Environmental Research Letters*, vol. 13, no. 6, p. 064 006, May 2018. DOI: 10.1088/1748-9326/aabd42.

[16] M. D. Freeman and W. M. Leith, "An Epidemiologic Analysis of Causal Factors in Tire Failure-Related Traffic Crashes," Aug. 2018. DOI: 10.4271/2018-01-5031. [Online]. Available: https://www.sae.org/content/2018-01-5031/.

[17] Q. Chen, J. M. Weaver, and G. Xu, "Research on Real-time Identification for Tire Failure," *American Journal of Mechanical Engineering*, vol. 2, no. 3, pp. 54–57, May 2014, ISSN: 2328-4102. DOI: 10.12691/ajme-2-3-1. [Online]. Available: http://pubs.sciepub.com/ajme/2/3/1/index.html.

[18] A. N. Gent and J. D. Walter, *Pneumatic tire*. Mechanical Engineering Faculty Research, 2006, p. 854.

[19] J. Gardner and B. Queise, "Introduction to tire safety, durability and failure analysis," *The Pneumatic Tire*, pp. 618–640, 2005.

[20] B. S. Sadjiep Tchuigwa, J. Krmela, and J. Pokorny, "Literature review on tire component requirements," *Perner's Contacts*, vol. 16, p. 6, Dec. 2021. DOI: 10.46585/pc.2021.2.1740.

[21] Bridgestone Corporation. "Bridgestone develops new sensor technology for autonomous vehicles smart strain sensor gathers tire wear and load information, even at low speeds news | bridgestone." Accessed: 14-06-2024. [Online]. Available: https://www.bridgestone.com/corporate/news/2019121801.html.

[22] J. Hooker, A. Rose, and G. Roberts, "A holistic approach to vehicle simulation," *Mathematics and Computers in Simulation*, vol. 25, no. 3, pp. 259–267, 1983, ISSN: 0378-4754. DOI: `10.1016/0378-4754(83)90102-7`.

[23] N. Kalantzis, T. Fletcher, A. Pezouvanis, and K. Ebrahimi, "Holistic simulation for integrated vehicle design," *International Journal of Powertrains*, vol. 10, no. 1, pp. 27–53, 2021. DOI: `10.1504/IJPT.2021.114736`.

[24] Y. Han, B. Xu, Q. Wang, Y. Liu, and Z. Duan, "Topology optimization of material nonlinear continuum structures under stress constraints," *Computer Methods in Applied Mechanics and Engineering*, vol. 378, p. 113 731, 2021, ISSN: 0045-7825. DOI: `10.1016/j.cma.2021.113731`.

[25] J. Liang, X. Zhang, B. Zhu, R. Wang, C. Cui, and H. Zhang, "Topology optimization of geometrically nonlinear structures based on a self-adaptive material interpolation scheme," *Machines*, vol. 11, no. 12, 2023, ISSN: 2075-1702. DOI: `10.3390/machines11121047`.

[26] Dhrangdhariya, Priyankkumar, Maiti, Soumyadipta, and Rai, Beena, "Topological optimization of non-pneumatic unique puncture-proof tire system spoke design for tire performance," *SAE International Journal of Passenger Vehicle Systems*, vol. 17, no. 1, pp. 3–23, Jul. 2023, ISSN: 2770-3460. DOI: `10.4271/15-17-01-0001`.

[27] X. Y. Yang, Y. M. Xie, G. P. Steven, and O. M. Querin, "Bidirectional evolutionary method for stiffness optimization," *AIAA journal*, vol. 37, no. 11, pp. 1483–1488, 1999.

[28] M. P. Bendsøe, "Optimal shape design as a material distribution problem," *Structural Optimization*, vol. 1, no. 4, pp. 193–202, 1989, ISSN: 09344373. DOI: `10.1007/BF01650949`.

[29] G. Zhang, "Topology optimization of nonlinear structural and material systems," Ph.D. dissertation, University of Notre Dame, 2019, p. 423. DOI: `10.7274/8g84mk64s91`.

[30] M. Habashneh and M. Movahedi Rad, "Reliability based geometrically nonlinear bidirectional evolutionary structural optimization of elasto-plastic material," *Scientific Reports*, vol. 12, no. 1, p. 5989, 2022. DOI: `10.1038/s41598-022-09612-z`.

[31] A. H. Frederiksen, O. Sigmund, and K. Poulios, "Topology optimization of self-contacting structures," *Computational Mechanics*, vol. 73, no. 4, pp. 967–981, 2024. DOI: `10.1007/s00466-023-02396-7`.

[32] Kenda Americana Tire and Wheel, "Difference between radial and bias trailer tires," Reynoldsburg, Tech. Rep., 2018, p. 20. [Online]. Available: `https://americanatire.com/differences-between-radial-and-bias-tires/`.

[33] V. Ievleva and V. Hammatova, "Analysis of technical textiles used for automobile tires," *Bulletin of Kazan Technological University*, vol. 20, no. 16, pp. 64–8, 2017.

[34] Y. Li, X. Sun, J. Song, S. Zhang, and S. Han, "Topological structure and experimental investigation of a novel whole tire bead," *Materials and Design*, vol. 203, p. 109 592, 2021, ISSN: 18734197. DOI: `10.1016/j.matdes.2021.109592`. [Online]. Available: `https://doi.org/10.1016/j.matdes.2021.109592`.

[35] Discounted Wheel Warehouse, *Parts of a Wheel Guide - Discounted Wheel Warehouse*. Accessed: Jun. 3, 2023. [Online]. Available: `https://www.discountedwheelwarehous` `com/parts-of-a-wheel`.

[36] Tyroola, *Your Guide To Tyre Tread Patterns | Tyroola*. Accessed: Jun. 3, 2023. [Online]. Available: `https://www.tyroola.com.au/guides/tyre-tread-pattern-guide/`.

[37] S. Jansen, A. Schmeitz, S. Maas, and R. Carmen, "Study on some safety-related aspects of tyre use," European Union, Helmond, Tech. Rep. 2, 2014, p. 193. DOI: `10.2832/67191`.

[38] Dassault Systemes Simulia Corpia Corp, *ABAQUS/Standard User's Manual, Version 6.9*, 2020.

[39] ANSYS, *Ansys® academic research—mechanical, 2024 release 2*, 2024.

[40] A. Hackl, "Enhanced Tyre Modelling for Vehicle Dynamics Control Systems," Ph.D. dissertation, 2019, p. 182. [Online]. Available: `http://marefateadyan.nashriyat.ir/node/150`.

[41] P. Gruber, R. S. Sharp, and A. D. Crocombe, "Friction and camber influences on the static stiffness properties of a racing tyre," *Proceedings of the Institution of Mechanical Engineers, Part D: Journal of Automobile Engineering*, vol. 222, no. 11, pp. 1965–1976, Nov. 2008, ISSN: 0954-4070. DOI: `10.1243/09544070JAUTO872`. [Online]. Available: `http://journals.sagepub.com/doi/10.1243/09544070JAUTO872`.

[42] A. Kongo Kondé et al., "Thermomechanical Couplings in Aircraft Tire Rolling/Sliding Modeling," *Advanced Materials Research*, vol. 274, pp. 81–90, Jul. 2011, ISSN: 1662-8985. DOI: `10.4028/www.scientific.net/AMR.274.81`. [Online]. Available: `https://www.scientific.net/AMR.274.81`.

[43] J. Yunta, D. Garcia-Pozuelo, V. Diaz, and O. Olatunbosun, "A Strain-Based Method to Detect Tires' Loss of Grip and Estimate Lateral Friction Coefficient from Experimental Data by Fuzzy Logic for Intelligent Tire Development," *Sensors*, vol. 18, no. 2, p. 490, Feb. 2018, ISSN: 1424-8220. DOI: `10.3390/s18020490`. [Online]. Available: `http://www.mdpi.com/1424-8220/18/2/490`.

[44] C. Ahn, H. Peng, and H. E. Tseng, “Robust estimation of road friction coefficient using lateral and longitudinal vehicle dynamics,” *Vehicle System Dynamics*, vol. 50, no. 6, pp. 961–985, Jun. 2012, ISSN: 0042-3114. DOI: 10.1080/00423114.2012.659740. [Online]. Available: http://www.tandfonline.com/doi/abs/10.1080/00423114.2012.659740.

[45] N. Korunović, C. Fragassa, D. Marinković, N. Vitković, and M. Trajanović, “Performance evaluation of cord material models applied to structural analysis of tires,” *Composite structures*, vol. 224, p. 111 006, 2019, ISSN: 0263-8223. DOI: 10.1016/j.compstruct.2019.111006.

[46] C. Wei and O. A. Olatunbosun, “The effects of tyre material and structure properties on relaxation length using finite element method,” *Materials Design*, vol. 102, pp. 14–20, 2016, ISSN: 0264-1275. DOI: https://doi.org/10.1016/j.matdes.2016.04.014.

[47] P. Bogusz, D. Miedzińska, and M. Wieczorek, “Experimental investigation of the tensile behavior of selected tire cords using novel testing equipment,” *Materials*, vol. 15, no. 12, 2022, ISSN: 1996-1944. DOI: 10.3390/ma15124163. [Online]. Available: https://www.mdpi.com/1996-1944/15/12/4163.

[48] M. H. R. Ghoreishy, M. Alimardani, R. Z. Mehrabian, and S. T. Gangali, “Modeling the hyperviscoelastic behavior of a tire tread compound reinforced by silica and carbon black,” *Journal of Applied Polymer Science*, vol. 128, no. 3, pp. 1725–1731, 2013. DOI: https://doi.org/10.1002/app.38242. eprint: https://onlinelibrary.wiley.com/doi/pdf/10.1002/app.38242. [Online]. Available: https://onlinelibrary.wiley.com/doi/abs/10.1002/app.38242.

[49] X. Yang, O. A. Olatunbosun, and E. O. Bolarinwa, “Materials testing for finite element tire model,” *SAE Technical Papers*, vol. 3, no. 1, pp. 211–220, 2010, ISSN: 26883627. DOI: 10.4271/2010-01-0418.

[50] S. Ma, G. Huang, K. Obaia, S. W. Moon, and W. V. Liu, “Hysteresis loss of ultra-large off-the-road tire rubber compounds based on operating conditions at mine sites,” *Proceedings of the Institution of Mechanical Engineers, Part D: Journal of Automobile Engineering*, vol. 236, no. 2-3, pp. 439–450, 2022. DOI: 10.1177/09544070211015525. eprint: https://doi.org/10.1177/09544070211015525. [Online]. Available: https://doi.org/10.1177/09544070211015525.

[51] Y. Liu, Z. Qian, C. Liu, and Q. Huang, "Investigation on hydroplaning behaviors of a patterned tire on a steel bridge deck pavement," *Applied Sciences*, vol. 11, no. 22, 2021, ISSN: 2076-3417. DOI: `10.3390/app112210566`. [Online]. Available: `https://www.mdpi.com/2076-3417/11/22/10566`.

[52] J. Krmela, M. Michna, Z. Růžička, V. Krmelová, and A. Artyukhov, "Cyclic testing of polymer composites and textile cords for tires," *Polymers*, vol. 15, no. 10, 2023, ISSN: 2073-4360. DOI: `10.3390/polym15102358`. [Online]. Available: `https://www.mdpi.com/2073-4360/15/10/2358`.

[53] L. Mullins, "Softening of rubber by deformation," *Rubber Chemistry and Technology*, vol. 42, no. 1, pp. 339–362, Mar. 1969, ISSN: 1943-4804. DOI: `10.5254/1.3539210`. [Online]. Available: `https://meridian.allenpress.com/rct/article/42/1/339/87399/Softening-of-Rubber-by-Deformation`.

[54] L. Mullins and N. Tobin, "Theoretical model for the elastic behavior of filler-reinforced vulcanized rubbers," *Rubber chemistry and technology*, vol. 30, no. 2, pp. 555–571, 1957.

[55] F. Bueche, "Molecular basis for the mullins effect," *Journal of Applied Polymer Science*, vol. 4, no. 10, pp. 107–114, 1960.

[56] S. Govindjee and J. Simo, "Transition from micro-mechanics to computationally efficient phenomenology: Carbon black filled rubbers incorporating mullins' effect," *Journal of the Mechanics and Physics of Solids*, vol. 40, no. 1, pp. 213–233, 1992.

[57] R. W. Ogden and D. G. Roxburgh, "A pseudo–elastic model for the Mullins effect in filled rubber," *Proceedings of the Royal Society of London. Series A: Mathematical, Physical and Engineering Sciences*, vol. 455, no. 1988, pp. 2861–2877, Aug. 1999, ISSN: 1364-5021. DOI: `10.1098/rspa.1999.0431`.

[58] J. Lemaitre, *A course on damage mechanics*. Springer science & business media, 2012.

[59] E. D. S. Neto, D. Perić, and D. Owen, "A phenomenological three-dimensional rate-idependent continuum damage model for highly filled polymers: Formulation and computational aspects," *Journal of the Mechanics and Physics of Solids*, vol. 42, no. 10, pp. 1533–1550, 1994.

[60] A. Dorfmann and R. Ogden, "A constitutive model for the Mullins effect with permanent set in particle-reinforced rubber," *International Journal of Solids and Structures*, vol. 41, no. 7, pp. 1855–1878, Apr. 2004, ISSN: 00207683. DOI: `10.1016/j.ijsolstr.2003.11.014`. [Online]. Available: `https://linkinghub.elsevier.com/retrieve/pii/S0020768303006504`.

[61] S. Göktepe, *Micro-macro approaches to rubbery and glassy polymers: Predictive micromechanic based models and simulations*. 2007.

[62] M. Rafei, M. H. R. Ghoreishy, and G. Naderi, "Thermo-mechanical coupled finite element simulation of tire cornering characteristics—effect of complex material models and friction law," *Mathematics and Computers in Simulation*, vol. 144, no. July 2020, pp. 35–51, 2018, ISSN: 03784754. DOI: 10.1016/j.matcom.2017.05.011.

[63] W. Wang, S. Yan, and S. Zhao, "Experimental verification and finite element modeling of radial truck tire under static loading," *Journal of Reinforced Plastics and Composites*, vol. 32, no. 7, pp. 490–498, 2013, ISSN: 07316844. DOI: 10.1177/0731684412474998.

[64] J. Laine, "Measurement, analysis and modelling of the vibrations of a tyre by using a single embedded accelerometer," M.S. thesis, Aalto university, 2016.

[65] W. Wang, S. Yan, and Y. Zhao, "Numerical and experimental studies of a radial truck tire with tread pattern," *Simulation*, vol. 91, no. 11, pp. 970–979, 2015, ISSN: 17413133. DOI: 10.1177/0037549715608434.

[66] Y. Li, C. Liu, Y. Sun, Y. Li, C. Xu, and M. Xie, "Modeling Methods and Simulation Analysis of Radial Tire with Different Tread Patterns," vol. 9, no. 1, pp. 20–30, 2020.

[67] H. Pacejka, *Tire and vehicle dynamics*. Elsevier, 2005. DOI: 10.1016/C2010-0-68548-8.

[68] E. Fiala, "Lateral forces on rolling pneumatic tires," *Zeitschrift VDI*, vol. 96, no. 29, pp. 973–979, 1954.

[69] H. Dugoff, P. S. Fancher, and L. Segel, "Tire performance characteristics affecting vehicle response to steering and braking control inputs," Highway Safety Research Institute, The University of Michigan, Tech. Rep., 1970.

[70] A. O'Neill, J. Prins, J. F. Watts, and P. Gruber, "Enhancing brush tyre model accuracy through friction measurements," *Vehicle System Dynamics*, vol. 60, no. 6, pp. 2075–2097, 2022. DOI: 10.1080/00423114.2021.1893766.

[71] S. Chae, "Nonlinear finite element modeling and analysis of a truck tire," Ph.D. dissertation, Pennsylvania State University, State College, 2006, p. 206. [Online]. Available: https://etda.libraries.psu.edu/catalog/7047.

[72] K. Khanse, Y. Siramdasu, and S. Taheri, "Development of a simulink-carsim interaction package for abs simulation of discrete tire models," *Tire Science and Technology*, vol. 44, pp. 2–21, Jan. 2016. DOI: 10.2346/tire.16.440101.

[73] M. Gipser, "Ftire–the tire simulation model for all applications related to vehicle dynamics," *Vehicle System Dynamics*, vol. 45, no. S1, pp. 139–151, 2007.

[74] M. Matsubara, A. Saito, C. Po-Siang, and S. Kawamura, “Tire vibration analysis of three-dimensional flexible ring with brush model under static contact conditions by using frequency-based substructuring,” *Archive of Applied Mechanics*, vol. 95, no. 1, p. 10, 2025.

[75] I. Lopez, S. Kersjes, N. Roozen, A. Schmeitz, and H. Nijmeijer, “Green’s functions for a rotating tyre: A semi-analytical approach,” in *Proceedings of Euronoise*, 2006.

[76] A. K. Noor, C. M. Andersen, and J. A. Tanner, “Exploiting symmetries in the modeling and analysis of tires,” *Computer Methods in Applied Mechanics and Engineering*, vol. 63, no. 1, pp. 37–81, 1987, ISSN: 0045-7825. DOI: `10.1016/0045-7825(87)90123-X`.

[77] S. Shokouhfar, S. Rakheja, and M. El-Gindy, “Verification of the part-composite approach for modeling the multi-layered structure of a rolling truck tire,” in *10th European LS-DYNA Conference 2015*, Jun. 2015. DOI: `10.13140/RG.2.1.2453.1048`.

[78] Z. Shida, M. Koishi, T. Kogure, and K. Kabe, “A Rolling Resistance Simulation of Tires Using Static Finite Element Analysis,” *Tire Science and Technology*, vol. 27, no. 2, pp. 84–105, Apr. 1999, ISSN: 0090-8657. DOI: `10.2346/1.2135980`.

[79] A. Burke and O. Olatunbosun, “Static tyre/road interaction modelling,” *Meccanica*, vol. 32, pp. 473–479, 1997.

[80] V. Alkan, S. Karamihas, and G. Anlas, “Finite element modeling of static tire enveloping characteristics,” *International Journal of Automotive Technology*, vol. 12, pp. 529–535, 2011.

[81] H. Golbakhshi and M. Namjoo, “An efficient numerical scheme for evaluating the rolling resistance of a pneumatic tire,” vol. 5, pp. 1009–1015, Jul. 2015.

[82] J. Phromjan and C. Suvanjumrat, “Belt layer effects on non-pneumatic tire performance by finite element analysis,” in *Recent Advances in Manufacturing Engineering and Processes*, R. K. Agarwal, Ed., Singapore: Springer Nature Singapore, 2023, pp. 149–157, ISBN: 978-981-19-6841-9.

[83] A. Mohsenimanesh, S. Ward, and M. Gilchrist, “Stress analysis of a multi-laminated tractor tyre using non-linear 3d finite element analysis,” *Materials & Design*, vol. 30, no. 4, pp. 1124–1132, 2009. DOI: `https://doi.org/10.1016/j.matdes.2008.06.040`.

[84] M. Fontaine et al., “Static in-tire circumferential strain signature using rayleigh-scattering fiber optic technology: Preliminary results,” in *Transport Research Arena TRA 2020*, Helsinki, Finland: Proceedings of 8th Transport Research Arena TRA 2020, 2020, pp. 149–157. [Online]. Available: https://univ-eiffel.hal.science/hal-04486233.

[85] J. T. Tielking, “A Finite Element Tire Model,” *Tire Science and Technology*, vol. 11, no. 1, pp. 50–63, Jan. 1983, ISSN: 0090-8657. DOI: 10.2346/1.2150979.

[86] A. K. Noor, “Nonlinear analysis and modeling of tires. final report, 12 september 1990-31 december 1995,” Virginia University, Tech. Rep., May 1996. [Online]. Available: https://www.osti.gov/biblio/382988.

[87] P. Baranowski and J. Malachowski, “Numerical study of selected military vehicle chassis subjected to blast loading in terms of tire strength improving,” *Bulletin of the Polish Academy of Sciences, Technical Sciences*, vol. 63, pp. 867–878, Dec. 2015. DOI: 10.1515/bpasts-2015-0099.

[88] P. Baranowski, J. Malachowski, J. Janiszewski, and J. Wekezer, “Detailed tyre fe modelling with multistage validation for dynamic analysis,” *Materials Design*, vol. 96, pp. 68–79, 2016, ISSN: 0264-1275. DOI: https://doi.org/10.1016/j.matdes.2016.02.029.

[89] P. Baranowski, J. Malachowski, and L. Mazurkiewicz, “Numerical and experimental testing of vehicle tire under impulse loading conditions,” *International Journal of Mechanical Sciences*, vol. 106, pp. 346–356, Jan. 2016. DOI: 10.1016/j.ijmecsci.2015.12.028.

[90] A. Abu-Odeh, “Application of new concrete model to roadside safety barriers,” in *Proc. of the 9th International LS-DYNA Users’ Conference*, 2006.

[91] J. O. Hallquist, “Theoretical manual for dyna3d,” Lawrence Livermore National Lab., CA (USA), Tech. Rep., 1983.

[92] LS-DYNA, *Livermore software technology corporation*.

[93] J.-R. Cho, H.-W. Lee, and W.-B. Jeong, “Numerical simulation of radiation noise of 3-d smooth tire using the rebound excitation force at the bending front,” *Journal of Mechanical Science and Technology*, vol. 31, pp. 3371–3377, 2017.

[94] T. Kuraishi, T. Terahara, K. Takizawa, and T. E. Tezduyar, “Computational flow analysis with boundary layer and contact representation: I. tire aerodynamics with road contact,” *Journal of Mechanics*, vol. 38, pp. 77–87, 2022.

[95] J. Krmela and V. Krmelova, “Tire casings and their material characteristics for computational modeling of tires,” May 2017. DOI: 10.22616/ERDev2017.16.N043.

[96] S. N. Ali, "Rolling resistance estimation for pcr tyre design using the finite element method," in *Finite Element Methods and Their Applications*, M. Baccouch, Ed., Rijeka: IntechOpen, 2020, ch. 9. DOI: `10.5772/intechopen.94144`.

[97] T. M. Inc., *Matlab version: 9.13.0 (r2022b)*, Natick, Massachusetts, United States, 2022. [Online]. Available: `https://www.mathworks.com`.

[98] G. Van Rossum and F. L. Drake Jr, *Python tutorial*. Centrum voor Wiskunde en Informatica Amsterdam, The Netherlands, 1995.

[99] X. Hu, X. Liu, X. Wan, Y. Shan, and J. Yi, "Experimental analysis of sound field in the tire cavity arising from the acoustic cavity resonance," *Applied Acoustics*, vol. 161, p. 107 172, 2020, ISSN: 0003-682X. DOI: `https://doi.org/10.1016/j.apacoust.2019.107172`. [Online]. Available: `https://www.sciencedirect.com/science/article/pii/S0003682X19300234`.

[100] S. S. Rao, *The Finite Element Method in Engineering: Fifth Edition*. 2010, vol. 79, pp. 1–710, ISBN: 9781856176613. DOI: `10.1016/C2009-0-04807-7`. [Online]. Available: `https://www.sciencedirect.com/book/9781856176613/the-finite-element-method-in-engineering`.

[101] O. Zienkiewicz, R. Taylor, and J. Zhu, "The finite element method: Its basis and fundamentals," in *The Finite Element Method: its Basis and Fundamentals*. Elsevier, 2013, p. 714. DOI: `10.1016/B978-1-85617-633-0.00020-4`.

[102] T. H. J.C. Simo, *Computational inelasticity*. 1999, vol. 37, p. 392. DOI: `10.1016/s0898-1221(99)90413-3`.

[103] O. Bauchau, "Dymore user's manual," p. 10, Jan. 2010. Accessed: Jan. 6, 2024. [Online]. Available: `https://zbmath.org/software/11481`.

[104] *Rubber Caster Wheels - Hysteresis - Bulldog Castors Blog — bulldogcastors.co.uk*, `https://www.bulldogcastors.co.uk/blog/rubber-caster-wheels-hysteresis/`, [Accessed 20-06-2025].

[105] K. Akutagawa, "Nano-mechanical modeling for rubbery materials," no. January 2019, pp. 593–596, Aug. 2017. DOI: `10.1201/9781315223278-91`. [Online]. Available: `https://www.taylorfrancis.com/books/9781351840408/chapters/10.1201/9781315223278-91`.

[106] J. Krmela, L. Beneš, and V. Krmelová, "Interaction of Steel Cord – Elastomer in Radial Tires for Passenger Vehicle," *Production Engineering Archives*, vol. 5/4, no. June 2020, pp. 10–13, 2014, ISSN: 23535156. DOI: `10.30657/pea.2014.05.03`.

[107] K. Miller, “Experimental Loading Conditions Used to Implement Hyperelastic and Plastic Material Models,” *Axel Products Inc*, no. January 2000, pp. 1–14, 2000. [Online]. Available: `http://axelproducts.com/downloads/ExpLoadings.pdf`.

[108] E. Wiechert, “Gesetze der elastischen Nachwirkung für constante Temperatur,” *Annalen der Physik*, vol. 286, no. 11, pp. 546–570, 1893, ISSN: 00033804. DOI: `10.1002/andp.18932861110`. [Online]. Available: `https://onlinelibrary.wiley.com/doi/10.1002/andp.18932861110`.

[109] S. M. Clarke, F. Elias, and E. M. Terentjev, “Ageing of natural rubber under stress,” *European Physical Journal E*, vol. 2, no. 4, pp. 335–341, 2000, ISSN: 12928941. DOI: `10.1007/s101890050015`. arXiv: `0005092 [cond-mat]`.

[110] C. Donolato, “Analytical and numerical inversion of the Laplace-Carson transform by a differential method,” *Computer Physics Communications*, vol. 145, no. 2, pp. 298–309, 2002, ISSN: 00104655. DOI: `10.1016/S0010-4655(02)00281-3`.

[111] W. M. Rust, “A Theorem on Volterra Integral Equations of the Second Kind With Discontinuous Kernels,” *The American Mathematical Monthly*, vol. 41, no. 6, p. 346, Jun. 1934, ISSN: 00029890. DOI: `10.2307/2301549`. [Online]. Available: `http://www.jstor.org/stable/2301549?origin=crossref`.

[112] J. Bonet and A. J. Burton, “A simple orthotropic, transversely isotropic hyperelastic constitutive equation for large strain computations,” *Computer Methods in Applied Mechanics and Engineering*, vol. 162, no. 1-4, pp. 151–164, 1998, ISSN: 00457825. DOI: `10.1016/S0045-7825(97)00339-3`.

[113] J. E. Bischoff, E. M. Arruda, and K. Grosh, “Orthotropic hyperelasticity in terms of an arbitrary molecular chain model,” *Journal of Applied Mechanics, Transactions ASME*, vol. 69, no. 2, pp. 198–201, 2002, ISSN: 00218936. DOI: `10.1115/1.1432664`.

[114] R. Ortigosa, A. J. Gil, J. Bonet, and C. Hesch, “A computational framework for polyconvex large strain elasticity for geometrically exact beam theory,” *Computational mechanics*, vol. 57, pp. 277–303, 2016.

[115] J. Bonet and R. D. Wood, *Nonlinear continuum mechanics for finite element analysis*. Cambridge university press, 1997.

[116] P. H. Mott, J. R. Dorgan, and C. M. Roland, “The bulk modulus and Poisson’s ratio of "incompressible" materials,” *Journal of Sound and Vibration*, vol. 312, no. 4-5, pp. 572–575, 2008, ISSN: 0022460X. DOI: `10.1016/j.jsv.2008.01.026`.

[117] P. H. Mott and C. M. Roland, "Limits to Poisson's ratio in isotropic materials," *Physical Review B - Condensed Matter and Materials Physics*, vol. 80, no. 13, pp. 1–4, 2009, ISSN: 10980121. DOI: 10.1103/PhysRevB.80.132104.

[118] I. Castañar, J. Baiges, and R. Codina, "A stabilized mixed finite element approximation for incompressible finite strain solid dynamics using a total Lagrangian formulation," *Computer Methods in Applied Mechanics and Engineering*, vol. 368, p. 113 164, 2020, ISSN: 00457825. DOI: 10.1016/j.cma.2020.113164. [Online]. Available: https://doi.org/10.1016/j.cma.2020.113164.

[119] C. Miehe, "Aspects of the formulation and finite element implementation of large strain isotropic elasticity," *International Journal for Numerical Methods in Engineering*, vol. 37, no. 12, pp. 1981–2004, Jun. 1994, ISSN: 0029-5981. DOI: 10.1002/nme.1620371202. [Online]. Available: https://onlinelibrary.wiley.com/doi/10.1002/nme.1620371202.

[120] J. C. Simo, R. L. Taylor, and K. S. Pister, "Variational and projection methods for the volume constraint in finite deformation elasto-plasticity," *Computer Methods in Applied Mechanics and Engineering*, vol. 51, no. 1-3, pp. 177–208, 1985, ISSN: 00457825. DOI: 10.1016/0045-7825(85)90033-7.

[121] S. Reese, P. Wriggers, and B. D. Reddy, "A New Locking-Free Brick Element Formulation For Continuous Large Deformation Problems," *Computational Mechanics*, pp. 1–21, 1998.

[122] D. Al Akhrass, S. Drapier, J. Bruchon, and S. Fayolle, "Stabilized finite element methods to deal with incompressibility in solid mechanics in finite strains," in *ECCOMAS 2012 - European Congress on Computational Methods in Applied Sciences and Engineering, e-Book Full Papers*, 2012, pp. 3781–3793, ISBN: 9783950353709.

[123] R. S. Rivlin, "Large elastic deformations of isotropic materials. I. Fundamental concepts," *Philosophical Transactions of the Royal Society of London. Series A, Mathematical and Physical Sciences*, vol. 240, no. 822, pp. 459–490, Jan. 1948, ISSN: 0080-4614. DOI: 10.1098/rsta.1948.0002. [Online]. Available: https://royalsocietypubl
org/doi/10.1098/rsta.1948.0002.

[124] R. OGDEN, "Elastic Deformations of Rubberlike Solids," in *Mechanics of Solids*, Elsevier, 1982, pp. 499–537. DOI: 10.1016/B978-0-08-025443-2.50021-5. [Online]. Available: https://linkinghub.elsevier.com/retrieve/pii/B9780080254432500215.

[125] A. N. Gent, "A new constitutive relation for rubber," *Rubber Chemistry and Technology*, vol. 69, no. 1, pp. 59–61, 1996, ISSN: 00359475. DOI: 10.5254/1.3538357.

[126] C. O. Horgan, “The remarkable Gent constitutive model for hyperelastic materials,” *International Journal of Non-Linear Mechanics*, vol. 68, pp. 9–16, Jan. 2015, ISSN: 00207462. DOI: 10.1016/j.ijnonlinmec.2014.05.010. [Online]. Available: https://linkinghub.elsevier.com/retrieve/pii/S0020746214001127.

[127] R. Rivlin and D. Saunders, “Large elastic deformations of isotropic materials VII. Experiments on the deformation of rubber,” *Philosophical Transactions of the Royal Society of London. Series A, Mathematical and Physical Sciences*, vol. 243, no. 865, pp. 251–288, Apr. 1951, ISSN: 0080-4614. DOI: 10.1098/rsta.1951.0004. [Online]. Available: https://royalsocietypublishing.org/doi/10.1098/rsta.1951.0004.

[128] L. Vergori, M. Destrade, P. Mcgarry, and R. W. Ogden, “On anisotropic elasticity and questions concerning its Finite Element implementation,” *Computational Mechanics*, pp. 1185–1197, 2013. DOI: 10.1007/s00466-013-0871-6.

[129] G. Chagnon, J. Ohayon, J. L. Martiel, and D. Favier, “Hyperelasticity Modeling for Incompressible Passive Biological Tissues,” *Biomechanics of Living Organs: Hyperelastic Constitutive Laws for Finite Element Modeling*, pp. 3–30, 2017. DOI: 10.1016/B978-0-12-804009-6.00001-8.

[130] J. D. Humphrey and F. C. Yin, “On constitutive relations and finite deformations of passive cardiac tissue: I. A pseudostrain-energy function,” *Journal of Biomechanical Engineering*, vol. 109, no. 4, pp. 298–304, 1987, ISSN: 15288951. DOI: 10.1115/1.3138684.

[131] G. A. Holzapfel, T. C. Gasser, and R. W. Ogden, “A new constitutive framework for arterial wall mechanics and a comparative study of material models,” *Journal of Elasticity*, vol. 61, no. 1-3, pp. 1–48, 2000, ISSN: 03743535. DOI: 10.1023/A:1010835316564.

[132] G. A. Holzapfel, G. Sommer, C. T. Gasser, and P. Regitnig, “Determination of layer-specific mechanical properties of human coronary arteries with nonatherosclerotic intimal thickening and related constitutive modeling,” *American Journal of Physiology-Heart and Circulatory Physiology*, vol. 289, no. 5, H2048–H2058, Nov. 2005, ISSN: 0363-6135. DOI: 10.1152/ajpheart.00934.2004. [Online]. Available: https://www.physiology.org/doi/10.1152/ajpheart.00934.2004.

[133] B. Fazekas and T. J. Goda, “Constitutive modelling of rubbers: Mullins effect, residual strain, time-temperature dependence,” *International Journal of Mechanical Sciences*, vol. 210, p. 106 735, Nov. 2021, ISSN: 00207403. DOI: 10.1016/j.ijmecsci.2021.106735. [Online]. Available: https://linkinghub.elsevier.com/retrieve/pii/S0020740321004665.

[134] B. Fazekas and T. J. Goda, “Closed-form and numerical stress solution-based parameter identification for incompressible hyper-viscoelastic solids subjected to various loading modes,” *International Journal of Mechanical Sciences*, vol. 151, pp. 650–660, Feb. 2019, ISSN: 00207403. DOI: 10.1016/j.ijmecsci.2018.12.011. [Online]. Available: https://linkinghub.elsevier.com/retrieve/pii/S0020740318335781.

[135] H. Khajehsaeid, J. Arghavani, R. Naghdabadi, and S. Sohrabpour, “A visco-hyperelastic constitutive model for rubber-like materials: A rate-dependent relaxation time scheme,” *International Journal of Engineering Science*, vol. 79, pp. 44–58, Jun. 2014, ISSN: 00207225. DOI: 10.1016/j.ijengsci.2014.03.001. [Online]. Available: https://linkinghub.elsevier.com/retrieve/pii/S0020722514000561.

[136] A. Kossa, “Closed-form stress solutions for incompressible visco-hyperelastic solids in uniaxial extension,” *ZAMM - Journal of Applied Mathematics and Mechanics / Zeitschrift für Angewandte Mathematik und Mechanik*, vol. 97, no. 10, pp. 1268–1282, Oct. 2017, ISSN: 00442267. DOI: 10.1002/zamm.201600182. [Online]. Available: https://onlinelibrary.wiley.com/doi/10.1002/zamm.201600182.

[137] B. Fazekas and T. J. Goda, “Determination of the hyper-viscoelastic model parameters of open-cell polymer foams and rubber-like materials with high accuracy,” *Materials Design*, vol. 156, pp. 596–608, Oct. 2018, ISSN: 02641275. DOI: 10.1016/j.matdes.2018.07.010. [Online]. Available: https://linkinghub.elsevier.com/retrieve/pii/S0264127518305409.

[138] J. Simo and M. Ortiz, “A unified approach to finite deformation elastoplastic analysis based on the use of hyperelastic constitutive equations,” *Computer Methods in Applied Mechanics and Engineering*, vol. 49, no. 2, pp. 221–245, 1985, ISSN: 0045-7825. DOI: https://doi.org/10.1016/0045-7825(85)90061-1. [Online]. Available: https://www.sciencedirect.com/science/article/pii/0045782585900611.

[139] J. S. Bergström and M. C. Boyce, “Constitutive modeling of the time-dependent and cyclic loading of elastomers and application to soft biological tissues,” *Mechanics of materials*, vol. 33, no. 9, pp. 523–530, 2001.

[140] J. Diani, B. Fayolle, and P. Gilormini, “A review on the Mullins effect,” *European Polymer Journal*, vol. 45, no. 3, pp. 601–612, Mar. 2009, ISSN: 00143057. DOI: 10.1016/j.eurpolymj.2008.11.017. [Online]. Available: https://linkinghub.elsevier.com/retrieve/pii/S0014305708006332.

[141] J. Simo, "On a fully three-dimensional finite-strain viscoelastic damage model: Formulation and computational aspects," *Computer Methods in Applied Mechanics and Engineering*, vol. 60, no. 2, pp. 153–173, Feb. 1987, ISSN: 00457825. DOI: `10.1016/0045-7825(87)90107-1`. [Online]. Available: `https://linkinghub.elsevier.com/retrieve/pii/0045782587901071`.

[142] L. Bartolini, D. Iannuzzi, and G. Mattei, "Comparison of frequency and strain-rate domain mechanical characterization," *Scientific Reports*, vol. 8, no. 1, p. 13 697, Sep. 2018, ISSN: 2045-2322. DOI: `10.1038/s41598-018-31737-3`. [Online]. Available: `https://www.nature.com/articles/s41598-018-31737-3`.

[143] J. C. Simo and R. L. Taylor, "A simple three dimensional model accounting for damage effects," *Rept. No. UCB/SESM/83-10, Department of Civil Engineering, University ofCalifornia, Berkeley*, 1983.

[144] J. Simo and R. Taylor, "J.C. Simo and R.L. Taylor, A three dimensional finite deformation viscoelastic model accounting for damage effects," *Rept. No. UCBiSESMiG-2. Department of Civil Engineering, University of California, Berkeley, CA*, 1985.

[145] N. A. S. Abdullah, F. F. Abdullah, A. H. Sufian, A. N. S. Z. Abidin, A. S. Jamaludin, and M. N. M. Razali, "Effect of degradation by temperature onto nitrile rubber elastomer mechanical properties," *Materials Today: Proceedings*, vol. 48, pp. 1941–1946, 2021, ISSN: 22147853. DOI: `10.1016/j.matpr.2021.10.247`. [Online]. Available: `https://doi.org/10.1016/j.matpr.2021.10.247`.

[146] B. Yenigun, E. Gkouti, K. Jankowski, and A. Czekanski, "Numerical Validation of The Influence of Temperature on Viscoelastic Behavior of Silicone Rubber at Low Temperatures," *Progress in Canadian Mechanical Engineering*, vol. 3, 2020. DOI: `10.32393/csme.2020.1178`.

[147] T. Rey, G. Chagnon, J. B. Le Cam, and D. Favier, "Influence of the temperature on the mechanical behaviour of filled and unfilled silicone rubbers," *Polymer Testing*, vol. 32, no. 3, pp. 492–501, 2013, ISSN: 01429418. DOI: `10.1016/j.polymertesting.2013.01.008`.

[148] M. Tahir and A. W. Birley, "Stress relaxation of rubbers in compression: the modulus enhancement factor," *Polymer Testing*, vol. 7, no. 1, pp. 3–26, 1987, ISSN: 01429418. DOI: `10.1016/0142-9418(87)90035-3`.

[149] L. Kunheng, C. Zhiyong, and S. Zhiyong, "Rubber aging life prediction based on interpolation and improved time-temperature superposition principle," *Materials Research Express*, vol. 9, no. 1, 2022, ISSN: 20531591. DOI: `10.1088/2053-1591/ac45ba`.

[150] W. Hernández, D. Castello, N. Roitman, and C. Magluta, “Thermorheologically simple materials: A bayesian framework for model calibration and validation,” *Journal of Sound and Vibration*, vol. 402, pp. 14–30, Aug. 2017, ISSN: 0022460X. DOI: `10.1016/j.jsv.2017.05.005`. [Online]. Available: `https://linkinghub.elsevier.com/retrieve/pii/S0022460X17303772`.

[151] N. Tschoegl, *The phenomenological theory of linear viscoelastic behavior: an introduction*. 1989, vol. 35, pp. 3616–8, ISBN: 3540191739. [Online]. Available: `http://scholar.google.com/scholar?hl=en&btnG=Search&q=intitle:the+phenomenological+theory+of+linear+viscoelastic+behavior+an+introduction#0`.

[152] F. J. D., *Viscoelastic Properties of Polymers*. 1980, p. 676, ISBN: 9780471048947. [Online]. Available: `https://login.ezproxy.library.ualberta.ca/login?url=https://search.ebscohost.com/login.aspx?direct=true&db=tdh&AN=TDH0407095198107300&site=eds-live&scope=site`.

[153] S. H. Chae, J. H. Zhao, D. R. Edwards, and P. S. Ho, “Characterization of the Viscoelasticity of Molding Compounds in the Time Domain,” *Journal of Electronic Materials*, vol. 39, no. 4, pp. 419–425, 2010, ISSN: 03615235. DOI: `10.1007/s11664-010-1078-7`.

[154] A. R. Trivedi, R. Whybrow, A. H. Muhr, and C. R. Siviour, “Experimentally characterising the temperature and rate dependent behaviour of unfilled, and glass microsphere filled, natural rubber,” *Polymer*, vol. 270, p. 125 773, Mar. 2023, ISSN: 00323861. DOI: `10.1016/j.polymer.2023.125773`. [Online]. Available: `https://linkinghub.elsevier.com/retrieve/pii/S0032386123001039`.

[155] S. G. Nunes, S. Saseendran, R. Joffe, S. C. Amico, P. Fernberg, and J. Varna, “On Temperature-Related Shift Factors and Master Curves in Viscoelastic Constitutive Models for Thermoset Polymers,” *Mechanics of Composite Materials*, vol. 56, no. 5, pp. 573–590, 2020, ISSN: 15738922. DOI: `10.1007/s11029-020-09905-2`.

[156] J. D. S. Becho and M. Greco, “Influence of Retardation Time on Viscoelastic Behavior of Plane Beams Modeled by the Nonlinear Positional Formulation of the Finite Element Method,” *Mathematical Problems in Engineering*, vol. 2021, 2021, ISSN: 15635147. DOI: `10.1155/2021/2684127`.

[157] G. Gohane et al., “Study Analysis of Tire Wear Characteristics of TATA LPO 1618,” *IOP Conference Series: Materials Science and Engineering*, vol. 1017, no. 1, p. 012 026,

Jan. 2021, ISSN: 1757-8981. DOI: 10.1088/1757-899X/1017/1/012026. [Online]. Available: https://iopscience.iop.org/article/10.1088/1757-899X/1017/1/012026.

[158] H. Jerbi, "Modélisation de l'usure et l'endommagement des contacts nus et revêtus sous chargement de fretting par une méthode semi-analytique," Ph.D. dissertation, Université de Lyon, 2016.

[159] E. Felder and P. Montmitonnet, "Théorie de l'usure - Approches par l'élasticité et les équations de bilan," *Frottement, usure et lubrification*, 2017. DOI: 10.51257/a-v1-tri502.

[160] J. F. Archard, "Contact and rubbing of flat surfaces," *Journal of Applied Physics*, vol. 24, no. 8, pp. 981–988, 1953, ISSN: 00218979. DOI: 10.1063/1.1721448.

[161] K. A. Grosch and A. Schallamach, "Tyre wear at controlled slip," *Wear*, vol. 4, no. 5, pp. 356–371, 1961, ISSN: 00431648. DOI: 10.1016/0043-1648(61)90003-5.

[162] D. Manas, "Wear of Tires," *Encyclopedia of Tribology*, pp. 4073–4086, 2013. DOI: 10.1007/978-0-387-92897-5_908.

[163] T. Wangs, *Analysis on tyre wear: Modelling and simulations*, 2017.

[164] F. Braghin, F. Cheli, S. Melzi, and F. Resta, "Tyre wear model: Validation and sensitivity analysis," *Meccanica*, vol. 41, no. 2, pp. 143–156, 2006, ISSN: 00256455. DOI: 10.1007/s11012-005-1058-9.

[165] R. Ivanov, "Tire wear modeling," Ph.D. dissertation, 2016, pp. 111–120. DOI: 10.20858/tp.2016.11.3.11.

[166] B. Ma, H. G. Xu, Y. Chen, and M. Y. Lin, "Evaluating the tire wear quantity and differences based on vehicle and road coupling method," *Advances in Mechanical Engineering*, vol. 9, no. 5, 2017, ISSN: 16878140. DOI: 10.1177/1687814017700063.

[167] A. Popp, "Mortar methods for computational contact mechanics and general interface problems," Ph.D. dissertation, Technische Universität München, 2012.

[168] J. Harden, *The Mortar Method - an advanced coupling method*, 2016. [Online]. Available: https://online.tugraz.at/tug_online/wbAbs.showThesis?pThesisNr=61478&pOrgNr=37&pPersNr=3969.

[169] P. Farah, W. Wall, and A. Popp, "A mortar finite element approach for point, line, and surface contact," *International Journal for Numerical Methods in Engineering*, vol. 114, no. 3, pp. 255–291, 2018.

[170] M. Gitterle, “A dual mortar formulation for finite deformation frictional contact problems including wear and thermal coupling,” Ph.D. dissertation, Technische Universität München, 2012.

[171] P. Olejnik and S. Ayankoso, “Friction modelling and the use of a physics-informed neural network for estimating frictional torque characteristics,” *Meccanica*, vol. 58, no. 10, pp. 1885–1908, 2023.

[172] M. Wojtyra, “Modeling of static friction in closed-loop kinematic chains—uniqueness and parametric sensitivity problems,” *Multibody System Dynamics*, vol. 39, no. 4, pp. 337–361, 2017.

[173] J. T. Oden and E. B. Pires, “Nonlocal and Nonlinear Friction Laws and Variational Principles for Contact Problems in Elasticity,” *Journal of Applied Mechanics*, vol. 50, no. 1, pp. 67–76, Mar. 1983, ISSN: 0021-8936. DOI: 10.1115/1.3167019. [Online]. Available: https://doi.org/10.1115/1.3167019.

[174] C. Liu, Y. Dong, Y. Wei, J. Wang, and H. Li, “Image detection and parameterization for different components in cross-sections of radial tires,” *Proceedings of the Institution of Mechanical Engineers, Part D: Journal of Automobile Engineering*, vol. 236, no. 2-3, pp. 287–298, 2022.

[175] A. Aldeen, Y. Can, and M. Yazıcı, “Modeling hyperelastic materials by matlab,” *International Journal of Computational and Experimental Science and Engineering*, vol. 6, no. 3, pp. 165–168, 2020. DOI: 10.22399/ijcesen.662707.

[176] J. Krmela, “The computational modelling of tire,” in *International Conference on Economic Engineering and Manufacturing Systems*, vol. Vol. 10, no. 3(27), Recent, Nov. 2009.

[177] P. Wriggers, J. Schröder, and A. Schwarz, “A finite element method for contact using a third medium,” *Computational Mechanics*, vol. 52, pp. 837–847, 2013. DOI: 10.1007/s00466-013-0848-5.

[178] University of Surrey, *Tyre dynamics research*, Accessed: 20.06.2024. [Online]. Available: https://www.surrey.ac.uk/centre-automotive-engineering/research/tyre-dynamics.

[179] B. S. Sadjiep Tchuigwa, J. Krmela, and J. Pokorny, “Toward detailed modeling of tires with linear elastic rubber compounds using finite element method,” *IOP Conference Series: Earth and Environmental Science*, vol. 1380, no. 1, p. 012 018, Aug. 2024. DOI: 10.1088/1755-1315/1380/1/012018.

[180] B. S. Sadjiep Tchuigwa, J. Krmela, and J. Pokorný, “A numerical study of the influence of the choice of rubber material behavior on the static response of tires,” *IOP Conference Series: Earth and Environmental Science*, vol. 1380, no. 1, p. 012 019, Aug. 2024. DOI: `10.1088/1755-1315/1380/1/012019`.

[181] Y. Li, X. Sun, J. Song, S. Zhang, and S. Han, “Topological structure and experimental investigation of a novel whole tire bead,” *Materials Design*, vol. 203, p. 109 592, 2021, ISSN: 0264-1275. DOI: `https://doi.org/10.1016/j.matdes.2021.109592`.

[182] G. Wang, W. Wang, C. Liang, and L. Cao, “Fatigue life prediction of radial tire bead using a maximum strain energy density range method,” *Applied Sciences*, vol. 11, no. 12, p. 5477, 2021, ISSN: 2076-3417. DOI: `10.3390/app11125477`.

[183] J. Krmela, *Experiments and Computational Modelling of Tires: Textbooks for university students*. Zborov, Czech Republic: Jan Krmela, 2020, ISBN: 978-80-270-9020-4.

[184] B. S. Sadjiep Tchuigwa, J. Krmela, J. Pokorny, V. Krmelová, and P. Jilek, “Vectfem: A generalized matlab-based vectorized algorithm for the computation of global matrix/force for finite elements of any type and approximation order in linear elasticity,” *Zeitschrift für angewandte Mathematik und Physik*, vol. 75, no. 4, p. 150, 2024. DOI: `10.1007/s00033-024-02293-w`.

[185] B. S. Sadjiep Tchuigwa, J. Krmela, J. Pokorny, and V. Krmelova, “Improved and vectorised matlab-based algorithms for serial and parallel implementation of finite element method in linear elasticity,” in *23rd International Scientific Conference “Engineering for Rural Development”: proceedings:[Jelgava, Latvia], May 22–24, 2024*, vol. 23, 2024, pp. 1032–1041. DOI: `10.22616/ERDev.2024.23.TF212`.

[186] J. Krmela, V. Krmelova, M. Gavendova, A. Bakosova, A. Kasperovich, and B. S. Sadjiep Tchuigwa, “Methods for determining the physico-mechanical properties of polymers,” in *-2020*, 2020, pp. 168–171.

[187] C. S. Agency, “Standard: Testing of tyres. determination of static radial stiffness and static tyre radius,” International Organization for Standardization, Czech Republic, Standard, Jan. 2000.

[188] J. Krmela and P. Michal, “Determination of radial stiffness of tire from experiments on the static test device called static adhesor,” *Metallurgical Journal (Hutnické listy)*, vol. 7, no. 1, pp. 81–84, 2012, ISSN: 0018-8069.

[189] P. Koštial, Z. Jančíková, D. Bakošová, J. Valícek, M. Harnicarova, and I. Špička, “Artificial neural networks application in modal analysis of tires,” *Measurement Science Review*, vol. 13, Oct. 2013. DOI: `10.2478/msr-2013-0040`.

[190] F. Brezzi and M. Fortin, *Mixed and Hybrid Finite Element Methods*. New York: Springer-Verlag, 1991, ISBN: 978-0-387-97515-3.

[191] T. Gillespie, *Fundamentals of vehicle dynamics*. SAE international, 1992, ISBN: 1-56091-199-9.

[192] D. E. Newland, *Random vibrations, spectral and wavelet analysis*. New York: Dover Publications, 2012.

[193] F. Liu and Y. Zhao, "A hybrid method for analysing stationary random vibration of structures with uncertain parameters," *Mechanical Systems and Signal Processing*, vol. 164, p. 108 259, 2022, ISSN: 0888-3270. DOI: `https://doi.org/10.1016/j.ymssp.2021.108259`.

[194] M. Pashaei, M. Bagheri, and G. Ghodrati Amiri, "Stochastic finite element analysis of nonlinear structures with random properties under random excitation," *Journal of Sound and Vibration*, vol. 485, p. 115 541, 2020. DOI: `10.1016/j.jsv.2020.115541`.

[195] P. W. Farah, "Mortar methods for computational contact mechanics including wear and general volume coupled problems," Ph.D. dissertation, Technische Universität München, 2018.

[196] P. Wriggers and T. A. Laursen, *Computational contact mechanics*. Springer, 2006, vol. 2. DOI: `10.1007/978-3-540-32609-0`.

[197] R. KOLMAN, S. S. CHO, and K. Park, "Accurate explicit finite element method for wave propagation and dynamic contact problems," in *11th World Congress on Computational Mechanics WCCM XI, 5th European Conference on Computational Mechanics ECCM V, 6th European Conference on Computational Fluid Dynamics ECCFD VI*, 2014, pp. 20–25.

[198] R. Kolman, J. Kopačka, J. A. González, S. Cho, and K. Park, "Bi-penalty stabilized technique with predictor–corrector time scheme for contact-impact problems of elastic bars," *Mathematics and Computers in Simulation*, vol. 189, pp. 305–324, 2021, MATCOM Special Issue: Modelling 2019: The 6th International Conference on Mathematical Modelling and Computational Methods in Applied Sciences and Engineering, ISSN: 0378-4754. DOI: `10.1016/j.matcom.2021.03.023`.

[199] *Matador MP16 Stella 2 165/65 R13 77T*, `https://pneumatiky.heureka.cz/matador-mp16-stella-2-165-65-r13-77t/#specifikace/`, [Accessed 12-01-2025].

Author's publications

List of author's published and in review results in relation to PhD thesis

Journal papers: published

P1 **B. S. Sadjiep Tchuigwa**, J. Krmela, J. Pokorny, V. Krmelová, and P. Jilek, "Vectfem: A generalized matlab-based vectorized algorithm for the computation of global matrix/force for finite elements of any type and approximation order in linear elasticity," Zeitschrift für angewandte Mathematik und Physik, vol. 75, no. 4, p. 150, 2024, ISSN: 1420-9039. DOI: 10.1007/s00033-024-02293-w, **WoS Q2 (SCOPUS Q1/D2) Jimp**.

P2 **B. S. Sadjiep. Tchuigwa**, J. Krmela, and J. Pokorny, "A literature review on tire component requirements," Perner's Contacts, vol. 16, p. 6, Dec. 2021, ISSN: 1801-674X, DOI: 10.46585/pc.2021.2.1740.

Journal papers: in review

P3 **B. S. Sadjiep. Tchuigwa**, J. Krmela, J. Pokorný and V. Krmelova, "Numerical and experimental validation of car tire testing on the static and dynamic adhesors: an enhanced tire model with Mullins damage," under review in Composites Communications.

P4 **B. S. Sadjiep. Tchuigwa**, J. Krmela, J. Pokorný and V. Krmelova, "Dynamic loads and their Impact on the Vibration Behavior of Car Tires: A Numerical and Experimental Study," under review in Discover Materials.

Conference proceedings : published

P5 **B. S. Sadjiep Tchuigwa**, J. Krmela, and J. Pokorny, "Toward detailed modeling of tires with linear elastic rubber compounds using finite element method," IOP Conference Series: Earth and Environmental Science, vol. 1380, no. 1, p. 012 018, Aug. 2024, ISSN: 1755-1315. DOI: 10.1088/1755-1315/1380/1/012018. (indexed in Scopus).

P6 **B. S. Sadjiep Tchuigwa**, J. Krmela, and J. Pokorný, "A numerical study of the influence of the choice of rubber material behavior on the static response of tires," IOP Conference Series: Earth and Environmental Science, vol. 1380, no. 1, p. 012 019, Aug. 2024, ISSN: 1755-1315. DOI: 10.1088/1755-1315/1380/1/012019. (indexed in Scopus).

P7 **B. S. Sadjiep Tchuigwa**, J. Krmela, J. Pokorny, and V. Krmelová, "Improved and vectorised matlab-based algorithms for serial and parallel implementation of finite element method in linear elasticity," in Proceeding of the 23rd International Scientific Conference

on Engineering for Rural Development, Jelgava, May 2024, pp. 1–6. DOI: 10.22616/ERDev.2024. (indexed in Web of Science and Scopus).

P8 **B. S. Sadjiep Tchuigwa**, J. Krmela, J. Pokorn‘y, and V. Krmelová, "Finite element modeling and analysis of tire creep test," in IOP Conference Series: Materials Science and Engineering, IOP Publishing, vol. 1319, 2024, p. 012 037.ISSN: 1757-899X, DOI: 10.1088/1757-899X/1319/1/012037. (indexed in Web of Science).

P9 J. Krmela, V. Krmelová, A. Artyukhov, **B. S. Sadjiep Tchuigwa**, and A. Bakošová, "Computational simulation of the shear test of a multi-layered long-fibre composite with a polymer matrix," IOP Conference Series: Materials Science and Engineering, vol. 1199, no. 1, p. 012 075, Nov. 2021, ISSN: 1757-899X, DOI: 10.1088/1757-899X/1199/1/012075. (indexed in Web of Science).

P10 J. Krmela, V. Krmelová, M. Gavendová, A. Bakošová, A Kasperovich, **B. S. Sadjiep Tchuigwa**, "Methods for determining the physico-mechanical properties of polymers". In petrochemistry–2020: proceedings. Minsk: Belarusian State Technological University, 2020. pp. 168-171 pp. ISBN 978-985-530-863-9. URL: Link.

Other publications: not related to the thesis

Journal paper: published

P11 P. Jilek, J. Berg, and **B. S. Sadjiep Tchuigwa**, "Influence of the weld joint position on the mechanical stress concentration in the construction of the alternative skid car system's skid chassis," Applied Sciences, vol. 12, no. 1, 2022, ISSN: 2076-3417. DOI: 2076-3417/12/1/397. **WoS Q3 (SCOPUS Q2/D2) Jimp**.

Conference proceedings : published

P12 J. Krmela, A. Bakosova, V. Krmelova, and **B. S. Sadjiep Tchuigwa**, "Drone propeller blade material optimization using modern computational method," in 20th International Scientific Conference Engineering for Rural Development Proceedings, Latvia University of Life Sciences and Technologies, Faculty of Engineering, May 2021, DOI: 10.22616/ERDev.202 (indexed in Web of Science and Scopus).